Experimental Investigation on Hydrogen Isotope Separation in Nanoporous Materials

Von der Fakultät Chemie der Universität Stuttgart zur Erlangung

der Würde eines Doktors der Naturwissenschaften

(Dr. rer. nat.) genehmigte Abhandlung

vorgelegt von

Linda Zhang

aus Xuzhou, P. R. China

Hauptbericht:	Prof. Dr. Dr. h.c. Guido Schmitz
Mitbericht:	Prof. Dr. Giesla Schütz
Prüfungsvorsitzender:	Prof. Dr. -Ing. Elias Klemm

Tag der mündlichen Prüfung: 23. Juli. 2020

Max–Planck–Institut für Intelligente Systeme, Stuttgart

2020

To my beloved mother

献给我的母亲

Table of Contents

Zusammenfassung

Die Trennung von H_2/D_2-Isotopengemischen ist aufgrund der identischen Größe, Form und thermodynamische Eigenschaften der Isotope sowohl wissenschaftlich als auch technologisch eines der schwierigsten, Trennverfahren. Die konventionelle H/D-Trennung wird entweder mit kryogener Destillation oder mit dem Girdler-Sulfid-Verfahren durchgeführt, jedoch beträgt dabei die Selektivität (Trennfaktor) weniger als 2,5 und weiterhin sind diese Verfahren sehr energieaufwendig und daher kostenintensiv. Eine vielversprechende Alternative kann der Einsatz von porösen Materialien zur direkten Trennung von gasförmigen Isotopengemischen sein. Für eine effiziente Isotopentrennung können dabei zwei unterschiedliche Prinzipien verwendet werden: i) Chemisches Affinitätssieben (CAS) an starken Adsorptionsstellen, an denen das schwerere Isotop aufgrund der niedrigeren Nullpunktsenergie (*ZPE*) eine stärkere Wechselwirkung aufweist. ii) Kinetisches Quantensieben (KQS) in kleinen Porenöffnungen, basiert auf der schnelleren Diffusion des schwereren Isotops mit niedrigerer *ZPE* unter kryogenen Bedingungen. Die Messmethode der kryogenen thermischen Desorptionsspektroskopie (TDS) erlaubt die direkte Bestimmung der Selektivität nach Exposition mit einem äquimolaren H_2/D_2-Isotopengasgemisch.

Der Einsatz des chemischen Affinitätssiebens zur Trennung von Wasserstoffisotopen wird am Zeolith Y, der mit verschiedenen Ionen, Co (II), Ni (II), Cu (II), Ni (II) und Ag (I), ausgetauscht wurde, untersucht, um den Einfluss des verwendeten Kationentyps auf dessen Trennfaktor zu bestimmen. Die Trenn- und Adsorptionsleistung verbessert sich bei allen Ionenaustauschzeolithen aufgrund ihrer höheren Adsorptionsenthalpien und ihres geringen Kationenvolumens, das zusätzlich die Poren vergrößert. Unter den untersuchten Kationen zeigt das ungesättigte Ag^+ eine bevorzugte Adsorption des schwereren Isotops als starke Bindungsstelle bis zu Temperaturen oberhalb des Siedepunkts von flüssigem Stickstoff. Die höchste D_2/H_2-Selektivität von 10 wird bei 90 K erreicht. Weiterhin führt die hohe Dichte der ungesättigten Ag-Stellen, die durch Austausch der hohen Konzentration aktiver Säurestellen des Zeoliths Y eingebracht wurden, zu einer hohen Gasaufnahme. Die Gasaufnahme an den starken Adsorptionsstellen entspricht näherungsweise einem Drittel der gesamten am Gerüst

physisorbierten Gasmenge. Diese Kombination von hoher Selektivität und Gasaufnahme macht Zeolith AgY zu einem vielversprechenden Kandidaten für praktische Anwendungen.

Das Potential des kinetischen Quantensiebens zur Wasserstoffisotopentrennung wird erstmals an porösen organischen Käfigen (POCs) mit unterschiedlichen Porenöffnungen untersucht. POCs sind diskrete Moleküle mit intrinsischen Hohlräumen, in die gezielt funktionelle Gruppen eingebaut werden können, um Porenvolumen und Öffnungsgröße graduell feineinzustellen. Dabei bleibt, im Gegensatz zu anderen porösen Gerüsten, die Festkörperpackung und die Kristallitstruktur unverändert. Ausgewählt werden Käfige mit Porenöffnungen größer (4,5 Å für CC3 und 3,4 Å für 6FT-RCC3) oder kleiner (1,95 Å für 6ET-RCC3) als der kinetische Durchmesser von Wasserstoff. Das kleine Porenfenster öffnet sich temperaturabhängig und ermöglicht mit steigender Temperatur ein Eindringen der Gasmoleküle in die Pore. Die Käfige mit den großen Poren zeigen eine große Gasaufnahme bei geringer Selektivität ($S_{D2/H2} \sim 1,2$), während der Käfig mit der kleinen Pore eine gute Selektivität mit jedoch sehr geringer Aufnahme besitzt. Konsequenterweise wird ein Kokristall für optimierte Trenn- und Adsorptionsleistungen entwickelt, der Käfige mit kleinen und großen Poren durch chirale Erkennung in einem porösen Netwerk miteinander verbindet. Hierbei wird der Käfig mit der feinsten Öffnung als Diffusionsbarriere eingesetzt, um die H_2-Diffusion wirksam zu limitieren und einen großen kinetischen Quantensiebeffekt zu erzeugen, während der Käfig mit dem großem Hohlraum genügend Platz für eine gute Durchmischung und Adsorption der Isotope bietet. Deshalb wird aufgrund der Diffusion durch die abwechselnd großen und kleinen Poren ein mehrstufiges KQS erreicht und bei 30 K eine Selektivität von 8 bei 4,5 mmol/g Deuteriumaufnahme erzielt.

Weiterhin wurde die Wasserstoffisotopentrennung in einem metallorganischen Gerüst (MOF) basierend auf Kupfer, das aufgrund teilweiser Fluorierung eine trimodale Porenstruktur verbunden durch enge Porenöffnungen besitzt, untersucht. Die beiden engen Porenfenster mit 3,6 und 2,5 Å zeigen eine temperaturabhängige Öffnungsdynamik, die die Hohlräume mit zunehmender Temperatur für Wasserstoff zugänglich machen. Diese dynamische Porenöffnung optimiert in verschiedenen Temperaturbereichen den KQS-Effekt. Bei 25 K wird eine hohe Selektivität von 14 beobachtet, während erst ab 70 K die verschlossene dritte Pore für Gasmoleküle zugänglich wird und eine Isotopentrennung bei Temperaturen von 100 K ermöglicht, was der bisher höchsten gemessenen Einsatztemperatur des KQS entspricht.

Abstract

Separating H_2/D_2 isotope mixtures is one of the most challenging tasks in modern separation science and technology, since the isotopes have identical size, shape and thermodynamic properties. Conventionally, H/D separation can be realized through cryogenic distillation or Girdler-sulfide process, however, the selectivity is less than 2.5 and these processes are intensively energy consuming, and therefore expensive. A promising alternative is the use of porous materials to separate directly gaseous mixture of isotopes. The efficient isotope separation can be realized by two different mechanisms: i) Chemical affinity sieving (CAS) on strong adsorption sites, where the heavier isotope has a stronger interaction due to its lower zero-point energy (*ZPE*); ii) Kinetic quantum sieving (KQS) in small pore apertures, which is based on the faster diffusion of the heavier isotope with lower *ZPE* under cryogenic conditions. Cryogenic thermal desorption spectroscopy (TDS) is used to measure directly the selectivity after exposure to an equimolar H_2/D_2 isotope mixture.

Separation by chemical affinity sieving has been investigated in zeolite Y exchanged by a series of ions, Co (II), Ni (II), Cu (II), Ni (II), and Ag (I), to establish the relationship between the type of cation used and their separation performance. The separation and adsorption performance are enhanced in all the ion-exchange zeolites due to the higher adsorption enthalpies and smaller cation volume, which leads to larger cavities in the porous structure. Among all the cations investigated, the unsaturated Ag^+, as strong binding site, shows the preferential adsorption of the heavier isotope even at temperatures above liquid nitrogen temperature. The highest D_2/H_2 selectivity of 10 is achieved at 90 K. Moreover, a high gas uptake can be achieved due to a high density of unsaturated Ag sites which have been exchanged owing to the high concentration of active acid sites in zeolite Y. The gas uptake on the strong adsorption sites makes up approximately 1/3 of the total physisorbed amount in the framework. The combination of high selectivity and gas uptake makes zeolite AgY a promising candidate for practical applications.

On the other hand, separation by kinetic quantum sieving has been investigated on porous organic cages (POCs) possessing different pore apertures. Different from other porous frameworks, POCs are discrete molecules with intrinsic cavities, in which different functional

groups can be placed inside the molecular structure to tune pore volume and aperture size, without altering its solid-state packing and the pore structure. The aperture size of the chosen cages is either larger (4.5 Å for **CC3** and 3.4 Å for **6FT-RCC3**) or smaller (1.95 Å for **6ET-RCC3**) than the kinetic diameter of hydrogen. The temperature-dependent gate opening effect of the small pore aperture enables the penetration of the gas molecules into the cavity with increasing temperature. The large pore cage exhibits large uptake with poor selectivity ($S_{D2/H2}\sim1.2$), while the small pore cage shows good selectivity but very little uptake. Thus, the cocrystal structure, a porous network possessing interconnected small and large cavities by chiral recognition, is designed for the optimal separation and adsorption performance. Herein, the cage with finest aperture is chosen as a diffusion barrier for effectively hindering H_2 diffusion, resulting in the kinetic quantum sieving, while the cage with large cavity provides enough space for high isotope gas adsorption. Therefore, a selectivity of 8 and 4.5 mmol/g deuterium uptake are obtained at 30 K due to the diffusion through the alternating large and small pores, where the isotopes can pass each other in the large pore and penetrate into the neighboring pore, resulting in a multiple-step KQS.

In addition, hydrogen isotope separation has been investigated on a metal-organic framework (MOF) based on copper, which possesses due to partial fluorination a tri-modal pore structure connected by narrow pore apertures. The two bottleneck apertures of 3.6 and 2.5 Å exhibit a temperature-dependent gate opening effect, which makes these cavities become accessible for hydrogen with increasing temperature. This dynamic pore aperture optimizes the KQS effect in different temperature regions. At 25 K a high selectivity of 14 is observed, whereas above 70 K the third closed cavity becomes accessible for gas molecules, resulting in isotope separation even at temperatures of 100 K, which is the highest operating temperature based on KQS.

List of Abbreviation

ITER	International thermonuclear experimental reactor
MOFs	Metal-organic frameworks
CAS	Chemical affinity sieving
KQS	Kinetic quantum sieving
POCs	Porous organic cages
PSA	Pressure swing adsorption
FAU	Faujasite
SSA	Specific surface area
HCPs	Hypercrosslinked polymers
PIMs	Polymers of intrinsic microporosity
CMPs	Conjugated microporous polymers
PPNs	Porous polymer networks
COFs	Covalent organic frameworks
BET	Brunauer–Emmett–Teller theory
GS	Girdler-sulfide process
ZPE	Zero-point energy in van der Waals forces
TDS	Thermal desorption spectroscopy
TPD	Temperature-programmed desorption
UHV	Ultrahigh vacuum
PID	Proportional–integral–derivative controller
QMS	Quadrupole mass spectrometer
TGA	Thermogravimetric analysis
DSC	Differential scanning calorimetry
S	Selectivity
PXRD	Powder X-ray diffraction
MD	Molecular dynamics simulation,
SEM	Scanning electron microscope
List of AbbreviationNPD	In-situ neutron powder diffraction

1. Introduction and Motivation

The world is facing a severe energy and environmental challenge – how to provide competitive and clean energy in light of the climbing global energy demands, concerns over climate changes and air pollution. More specifically, current energy consumption depends primarily on fossil fuels. The nonrenewable resources took millions of years to form and there is only a limited supply on earth. However, with continued growth of the world's population and industrial development, a growth in global demand for fossil fuels is expected for the future. In addition, burning of fossil fuels has been attributed to a key factor for climate change, since the worldwide emissions of CO_2 and other greenhouse gases have been growing for decades and decades. Burning of fossil fuels is not only related to the global warming, but also in response to air pollutions and acid rain. Given the current worldwide interest in sustainable resources and reducing CO_2 emissions, it is not surprising that the demand of hydrogen for energy applications is attracting a great deal of attention.

1.1 Hydrogen Fusion

As a new large-scale, inexhaustible and carbon-free form of energy resource, fusion has the following advantages making it worth pursuing: abundant energy, sustainability, no greenhouse gases, no long-lived radioactive waste, no risk of meltdown, low cost in long-term, and so forth[1].

Opposite to fission reaction, where heavy isotopes are split up, the fusion reaction is a nuclear process, where hydrogen nuclei collide to form the heavier helium atoms and release a tremendous amount of energy. Fusion is the process by which the light and heat are generated in the core of our Sun.
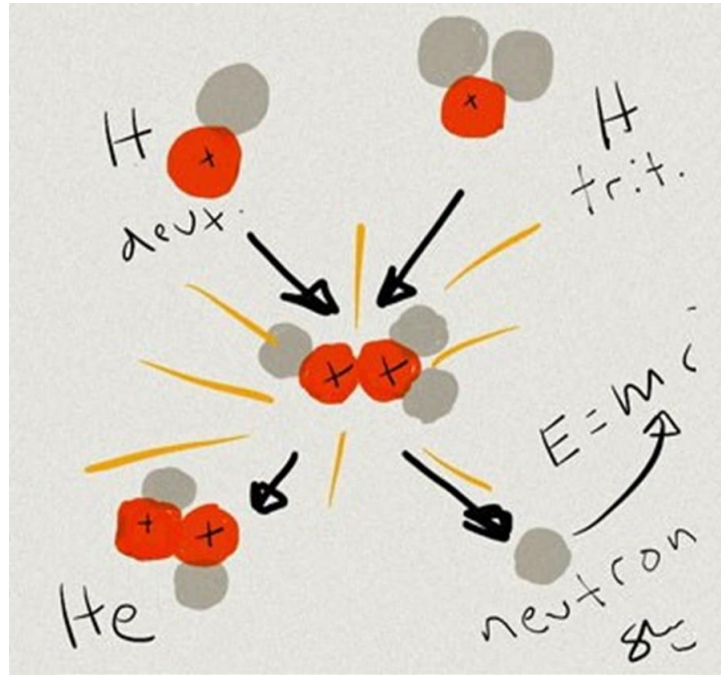
Figure 1.1 Schematic diagram of the DT fusion reaction via a compound nucleus[2].

The process can be achieved on earth by combining two isotopes of hydrogen: deuterium and tritium. Hydrogen is the first and lightest element in the periodic table, consisting of a single proton and an electron. Deuterium (D) has an extra neutron, while tritium (T) has two extra, making it three times heavier than protium (H). As shown in Figure 1.1, at very high temperature, the agitated deuterium and tritium collide at high speed that the repulsive electrostatic forces, which repel the two positive charged nuclei, can be overcomed to form a "compound nucleus", ^{5}He (helium). The extra mass of the resulting helium is leftover, converting into the kinetic energy of the neutron, based on the Einstein's famous formula: $E = mc^2$. The fusion of the deuterium (D) and tritium (T) according to the reaction

$$D + T \rightarrow {}^5_2He \rightarrow {}^4_2He + n$$
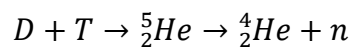
produces 17.6MeV of energy[3-4].

1.2 Hydrogen Isotope Separation

The isotopes of hydrogen, deuterium and tritium, play a key factor as the feedstock in the international thermonuclear experimental reactor (ITER), the most ambitious energy project in the world. However, the natural abundances of hydrogen isotopes are about 156 ppm for deuterium and only traces for tritium[5-6]. The separation of the heavier isotopes from hydrogen is a mandatory requirement for future fusion energy. In fact, the yield of hydrogen isotopes for nuclear feedstock is under 10%, so a fuel cycle loop of a fusion reactor is crucial to increase the efficiency and reduce nuclear residues. Additionally, the extraction of the heavier isotopes from hydrogen might be economically attractive or environmentally desired, adding on greater importance in hydrogen isotope separation[7].

In general, gaseous mixtures can be efficiently separated using porous materials as adsorption beds or membranes. The driving force in such molecular sieving is the discrimination of the size and shape of each component in a gas mixture. For a classical molecular sieve, only the gas molecules with smaller particle diameter than the pore diameters can penetrate, while the larger ones are obstructed. However, the identical kinetic diameter, shape, and similar chemical properties between hydrogen isotopes is an obstacle for the separation based on molecular sieving. Conventionally, H/D separation can be realized through cryogenic distillation or Girdler-sulfide process, however, the selectivity is less than 2.5 and these processes are intensively energy consuming, making them economically unfavorable. Thus, an alternative effective method in hydrogen isotope separation is highly desired.

A promising alternative utilizing porous materials to separate directly gaseous mixture of isotopes has been proposed by Beenakker et al.[8], which is called kinetic quantum sieving. The quantum effect takes place when the difference between the pore diameter and the kinetic diameter of the molecule becomes comparable to the molecule's de Broglie wavelength. Under this confinement, a greater repulsive interaction is generated for lighter isotopes, leading to faster diffusion rate of the heavier ones pores in porous materials. Another alternative for isotope separation is based on the differences in the attractive forces of isotope molecules on specific adsorption sites, called chemical affinity sieving. When the isotopes interact with strong adsorption sites, the isotope with heavier molecular mass has a lower zero-point energy,

resulting in higher adsorption enthalpy. The heavier isotope is therefore adsorbed preferentially on the strong adsorption sites, leading to the separation of isotopes.

The design of suitable porous materials is generally the first step in the development of the isotope separation process. A precisely tuned pore aperture or the embedded active sites are an essential prerequisite. Thus, functional porous materials, such as zeolites, metal-organic frameworks MOFs and porous organic cages show great prospects for addressing the challenges in isotopes separation, based on their properties of high porosity, ultra-small pore size and diverse functionality.

1.3 Aim of the Thesis

This work will focus on hydrogen isotope separation with nanoporous materials utilizing three different strategies: i) chemical affinity sieving (CAS) on strong adsorption sites, where the heavier isotope has a stronger interaction due to its lower zero-point energy; ii) kinetic quantum sieving (KQS) in small pore apertures, which is based on the faster diffusion of the heavier isotope with lower zero-point energy under cryogenic conditions; iii) dynamic transition of flexible nanoporous materials, which generates the pore aperture of the optimum size to maximize the KQS effect, as well as offer large storage capacity. Cryogenic thermal desorption spectroscopy (TDS) is used to measure directly the selectivity after exposure to an equimolar H_2/D_2 isotope mixture.

For chemical affinity sieving, zeolite Y exchanged by a series of ions, Co (II), Ni (II), Cu (II), Ni (II), and Ag (I), will be investigated to establish the relationship between the type of cation used and their separation performance. Based on the experimental results, the zeolite Y possessing unsaturated Ag^+ sites will be further studied. The effect of temperature and pressure on the adsorption and separation performance will be determined quantitatively. Even though zeolites are well-studied materials, the combination of high selectivity and gas uptake has never been obtained in such materials ever before.

On the other hand, kinetic quantum sieving will be investigated with porous organic cages (POCs) possessing different pore apertures. This is the first time to apply this novel molecular

material for hydrogen isotope separation. By fine-tuning the pore aperture of the cages, the correlation of separation performance and pore aperture size will be determined under proper experimental conditions. Furthermore, a cocrystal structure, a porous network possessing interconnected alternating small and large cavities, is studied under various operating conditions (temperature and time). The investigation provides a correlation of operating temperature and the flexibility of the aperture between the cavities, paving the path for optimal of separation and desorption performance in porous materials.

In addition, a strategy for effectively separating hydrogen isotopes utilizing the dynamic pore aperture change in a relatively flexible metal–organic framework (MOF) will be discussed. The effect of the dynamic pore aperture on the KQS will be evaluated under various experimental conditions. This investigation provides the correlation of operating temperature and the flexible aperture size, revealing the highest operating temperature based on KQS.

In all three strategies, a high selectivity as well as considerable high uptake amount have been achieved, revealing the potential for industrial applications of nanoporous materials to separate D_2/H_2 mixture more efficiently compared to conventional techniques.

2. Fundamentals

2.1 Physical Adsorption

Physical adsorption is be remarked as a phenomenon that an increase in density of a fluid near the surface of a solid or a liquid. The molecules/atoms in the adsorbed state are known as the adsorbate, while the adsorptive is the same component in the fluid phase. The adsorption space is the space occupied by the adsorbate[9].

The sorbent surface can be seen as a two-dimensional potential energy landscape, with wells possessing different depths relevant to different adsorption sites, as shown in Figure 2.1[10]. A gas molecule approaching a surface collides in two possible ways: i) elastically, where no energy exchange occurs, or ii) inelastically, where the gas molecule loses energy. In the elastically collision, the gas molecules tend to be reflected back to the gas phase, leaving the system unchanged; while in the latter case, the collision is likely leading to adsorption. If the trapped molecule lacks of energy to escape from the shallow potential well, which corresponds to weak interactions, such as van der Waals forces, it may diffuse from well to well across the surface, referred to as physical adsorption (physisorption). The physisorptive forces are usually characterized by interaction energies below 10 kJ/mol. In the case of deeper wells, the intermolecular forces lead to the formation of chemical bonds, resulting in chemical adsorption (chemisorption). Chemically bounded molecules require dissociation energies exceeding 50 kJ/mol.
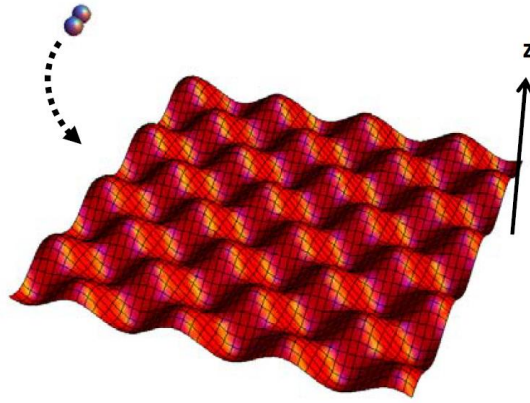
Figure 2.1 Potential energy landscape for adsorption of a diatomic molecule on a periodic two-dimensional surface. The depth of the energy well is shown in the z-axis[10].

In a system of the gas molecules and the solid surface where the chemisorption is absent, the weak physisorption occurs when the attractive dispersion forces overcomes the short-range repulsion forces. In addition, specific molecular interactions (e.g., polarization, field-dipole, field gradient quadrupole) are responsible for the adsorption. These forces collectively fall into the category of van der Waals forces[11-13]. These include: Keesom forces (permanent dipoles), Debye forces (permanent – induced dipoles), London dispersion forces (fluctuating induced dipoles).

The attractive potential arising from dispersion forces between a molecule and the adsorbate molecule can be given as,

$$\Phi_D = -\frac{A}{r^6} \tag{2.1}$$

where Φ_D is the dispersion energy, r is the distance between the two centers of the interacting pair, A is constant. This weak, long-range intermolecular interaction arises from the coupling between two temporary fluctuating and induced dipoles[14-15]. The short-range repulsion forces arising from the electron orbital overlapping is described by the Pauli Exclusion Principle,

$$\Phi_R = +\frac{B}{r^{12}} \tag{2.2}$$

where Φ_R is the repulsive energy, B is constant. Combining the inverse 6-order attraction and inverse 12-order repulsion leads to the Lennard-Jones potential[16-18],

$$\Phi = 4\epsilon \left[\left(\frac{\sigma}{r} \right)^{12} - \left(\frac{\sigma}{r} \right)^{6} \right] \tag{2.3}$$

where ϵ is the depth of the potential well, σ is the finite distance at which the inter-particle potential is zero. The Lennard-Jones potential function is schematically shown in Figure 2.2.
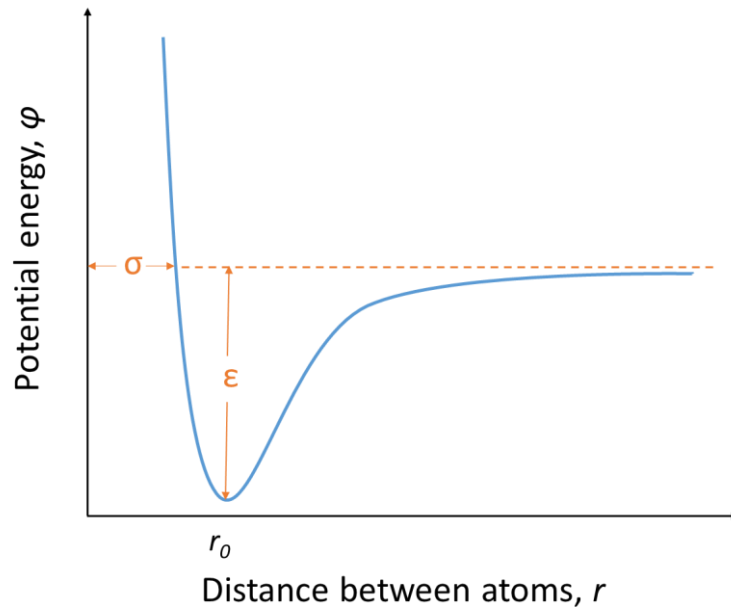

Figure 2.2 The Lennard-Jones 6-12 potential. The equilibrium distance between the interacting species is $r = r_0$.

2.2 Adsorptive Separation in Porous Materials

Separation can be defined as a process that transforms a mixture of substances into at least two products which possess different composition from each other. As an opposite process of mixing, favored by the second law of thermodynamics, separation is difficult to be achieved. As a worldwide used industrial process, particularly in chemistry, petrochemical and pharmaceutical industries, the separation steps often count as the major costs. The heart of high performance of any adsorptive separation process is usually a suitable adsorbent. In addition to a good selectivity, an adequate adsorptive capacity is required for practical separation processes. High adsorptive capacity can be achieved utilizing the high surface area or high micropore volume the microporous adsorbents provide. Adsorbents can be made with internal surface area

ranging from about 100 m^2/g to over 6000 m^2/g. This includes both the traditional microporous adsorbents such as activated carbon, carbon molecular sieve as well as zeolites, and the novel classes of materials such as metal-organic frameworks, microporous polymers and porous organic cages.

2.2.1 Porous Materials

Activated carbon

Activated carbon has been long used as an all-purpose sorbent and its first commercial application can be dated back to the 1930's[19]. The structure of active carbon consists of elementary microcrystallites of graphite stacked in random orientation, which form the micropores by the space in between[20]. A slight polarity may arise from surface oxidation of the nonpolar surface of the activated carbon, leading to hydrophobic and organophilic surfaces. It's therefore widely used in industrial applications including decolorizing sugar solutions, water purification, solvent recovery and hydrogen purification[21-22]. Activated carbon contains a wide distribution of pore size, from macropores greater than 50 nm to the micropores smaller than 2 nm. By controlling the pore sizes and their distribution, a board range of carbon adsorbents are available for various separation processes. In order to offer surfaces with appropriate wettability, activated carbons used for liquid phase applications have larger pore diameters, of the order of 3 nm or larger, than those used for the gas phase separations.

Carbon molecular sieves

Activated carbon generally shows little selectivity in the adsorption of molecules of different sizes because of its wide distribution of pore size. With special activation procedures, amorphous adsorbents can be obtained with a very narrow distribution of pore sizes with diameters ranging from 0.4 to 0.9 nm. Thus, carbon molecular sieves are characterized by the relatively high adsorptive capacity and selectivity to achieve a particular separation of a wide range of gases. For example, molecular sieves used for separation of nitrogen from air must have a pore size within the range 0.3 – 0.5 nm. In fact, carbon molecular sieves play a fundamental role in separation via pressure swing adsorption (PSA) of nitrogen from air[23]. The hydrophobic character of the surface and high resistance to acidic and basic media can also be

attributed to the use of these carbon molecular sieves as adsorbents for separation of gases, where the size of molecules differs only by 0.02 nm[24].

Zeolites

Another important class of solids used as widely as carbonaceous materials is zeolites, which can be found in nature or synthesized chemically. Zeolites are porous crystalline aluminosilicates consisting of tetrahedral SiO_4 and AlO_4, joined together with sharing oxygen atoms, at approximately 144° T-O-T angles (T represents Al/Si). The framework of zeolites contains cavities or cages which are connected by regular pores of molecular dimensions, allowing the adsorbate molecules to penetrate into. Considering that the micropore structure is determined by the crystal lattice, it is precisely uniform with no distribution of pore size. The pore size is determined by the number of the atoms forming the windows, which may be constructed from the rings containing 6, 8, 10, 12 oxygen atoms accompanied by the equal number of aluminium/silicon atoms. For windows formed by 6 oxygen atoms, it's only penetrable by small molecules such as water. For zeolites containing 8, 10, 12 oxygen atoms rings, the aperture size is determined to be 0.42, 0.57 and 0.74 nm, respectively. Due to the vibration of the crystal lattice and the diffusing molecules, the windows can be penetrated by molecules with a size slightly larger than the aperture.

The general formula of zeolite framework is $M_{x/n}[(AlO_2)_x(SiO_2)_y] \cdot m H_2O$, where y/x is never less than 1 with no upper limit. The water can be removed from the micropore structure by heating which in some cases occurring up to 50% of the pore volume. The ratio of oxygen to combine aluminium and silicon atoms is always two, therefore each aluminium atom introduce a negative charge which needs to be balanced by introducing a non-framework exchangeable cation M of valence $+n$. The additional cations are usually alkali and earth alkali ions. Due to the number and nature of the exchanged cations, the windows can be obstructed to some extent, since different cations show varying affinities for the window sites. The strong electrostatic forces produced by the non-framework ions result in strong polarizing sites inside the cavity, leading to the decrease in size. Thus, a wide range of different adsorptive and selective properties can be prepared by changing the position and type of cation on the framework to tune the pore size and chemical properties[25-27].

Among the over 150 synthetic zeolite types, based on Si to Al ratio, the most important commercially are type A, X and Y, and ammonium ZSM-5 zeolite, the schematic representation of the framework structures are shown in Figure 2.3.
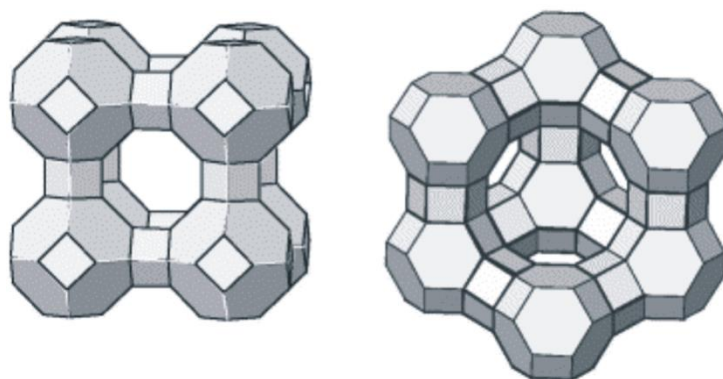

Figure 2.3 Schematic representation of the framework structure of (a) zeolite A and (b) zeolite X and Y, reproduced from Ruthven. The corners represent Al or Si atoms and in the middle of every line is one oxygen atom bridging two neighbouring Si or Al atoms[21].

The framework of zeolite A consists of eight polyhedral sodalite cages located at the corner of a cube, connected with each other through four membered oxygen rings, forming a large polyhedral cage with an eight-membered oxygen window of diameter 11.4 Å (Figure 2.3a). Si/Al ratio in zeolite A is close to 1 and there are 12 univalent exchangeable cations per unit cell. The positions occupied on the framework depend on the number and nature of the exchanged cations. Considering that calcium is the cation accommodated at sites within the cages, the number of cations per unit cell can be increased if Na^+ replaces Ca^{2+}. In this case, the sodium cation is located within the eight-oxygen rings and therefore the aperture is partially obstructed to 3.8 Å. If the Na^+ cations are exchanged for K^+, the channel size is further reduced to 3 Å due to the larger potassium cations.

The synthetic zeolite faujasite (FAU) X and Y have the same framework structure, sketched in Figure 2.3b. This zeolite has two independent networks which are interconnected. One network consists of a tetrahedral lattice of sodalite units connected through a six-membered oxygen hexagonal prism, which is called sodalite cage. The channel structure of the other network is highly opened with each cage connected with other four cages through twelve-membered oxygen rings, leading to a large cavity (supercage) of a diameter around 12.5 Å with a window size of 7.4 Å. Each supercage is connected to four others in a tetrahedral arrangement, resulting

in a relatively high surface area around 800 m^2/g[27]. The only difference between type X and Y possessing identical framework structure lies in the Si/Al ratio, which is in the range of 1 to 1.5 for type X and 1.5 to 3 for Y, corresponding to 10-12 and 6 exchangeable univalent cations per unit cell for type X and Y, respectively.
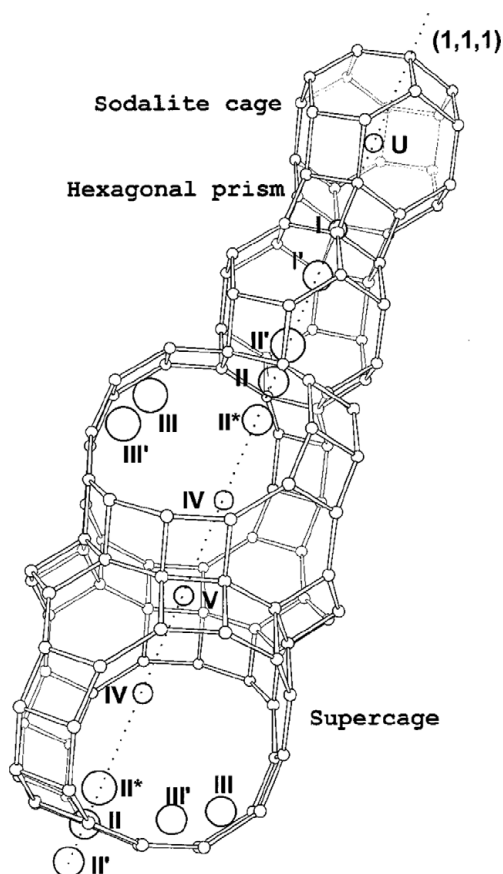

Figure 2.4 Illustration of the connectivity of cages in faujasite along with the Roman numeration of cation positions encountered in these hosts. Cation sites are labelled with the Roman number[28].

The cations sites have been identified to be five and illustrated in Figure 2.4[28]. Cation sites are site I in the centre of the hexagonal prism, site I' inside the sodalite cage close to the hexagonal window to the hexagonal prism, site II' in the sodalite cage close to the hexagonal window to the supercage, site II in the supercage on the hexagonal prism. Site III in the supercage near the four-rings and III' somewhat or substantially off III on the inner surface of the super cage. The primary cation sites for interaction with the adsorbed molecules are site II and III, since the other sites located in the cages are not accessible[29]. The distribution of cations between different sites depends on the number and nature of the exchanged cations and can be affected by the

moisture traces of the framework. For dehydrated Na-exchanged zeolites, the cations tend to occupy sites which can maximize their interaction with framework oxygen atoms and minimize cation-cation electrostatic repulsion. For example, The FAU unit cell contains 16 hexagonal prisms, eight sodalite cages and eight supercages. Sites I, I′, II′, II and III can accommodate 16, 32, 32, 32 and 96 cations, respectively. If sufficient Na cations have been located in zeolite Y, site II is always preferred to be completely occupied (32 cations) because distribution in site II minimizes cation-cation repulsion. Site I is the next preferred site, following site I' for the distribution of cations up to 64 per unit cell. Noted that the occupation of site I and I' cannot take place simultaneously, since the cation-cation distance in the same hexagonal prism is too small and the repulsion is too strong. Above 64 cations, site III in the supercage begins to be occupied. The case of hydrated samples is more complex because these water molecules can also access to the sodalite cage which can modify the cation site distribution.

Due to the homogeneously shaped and sized pores and openings, theses inorganic porous adsorbents have been widely applied for technical applications such as gas adsorption, separation, catalysis and ion-exchange. However, the pore size is restricted by the different crystal structure available, and therefore cannot be tuned continuously to match the precise aperture size desired in order to achieve effective separation of particular mixtures.

Metal-organic frameworks (MOFs)

With ultrahigh porosity (up to 90% free volume), low densities (0.21 to 1.00 g/cm^3) and surface areas exceeding 6000 m^2/g[30], metal-organic frameworks (MOFs) have emerged since the last two decades as a novel class of porous hybrid crystalline materials. They are generally built from inorganic metal/metal-containing cluster nodes connected by organic linkers. Considering the most well studied MOF-5 by Yaghi[31] for example, octahedral clusters formed by Zn^{2+} and 1,4-benzene-dicarboxylate are connected with each other by benzene groups to form a cubic network, as shown in Figure 2.5.

A variety of MOFs with a wide range of porosity and chemical functionality can be achieved utilizing appropriate organic ligands and metal-ions into the net-like materials with a targeted topology. The large number of possible organic likers combined in quasi-infinite way can be used to connect inorganic metal clusters, leading various porosity. The chemical features of the MOF pore system can be tuned via functionalization of the organic linker with polar functions, and incorporation of coordinative unsaturated metal sites, mainly transition metals, such as Co,

Cr, Ni, Zn, Cu, Fe[32-34]. When interacting with a gas or solute molecule, the metal ions can form the usual σ bonds with their s-orbitals. In addition, their d-orbitals can back-donate electron density to the antibonding π-orbitals of the molecule to be bonded[35]. This is the reason, MOFs with unsaturated metal ions have stronger interactions than materials which possess no such interaction sites. The synthesis of MOFs is usually carried out at mild conditions, which are easily controlled compared to the other porous materials such as zeolites. The extraordinary degree of variability of possible structures and properties offers MOFs the prospects for potential applications in gas adsorption and separation, sensor technology, drug delivery and catalysis.
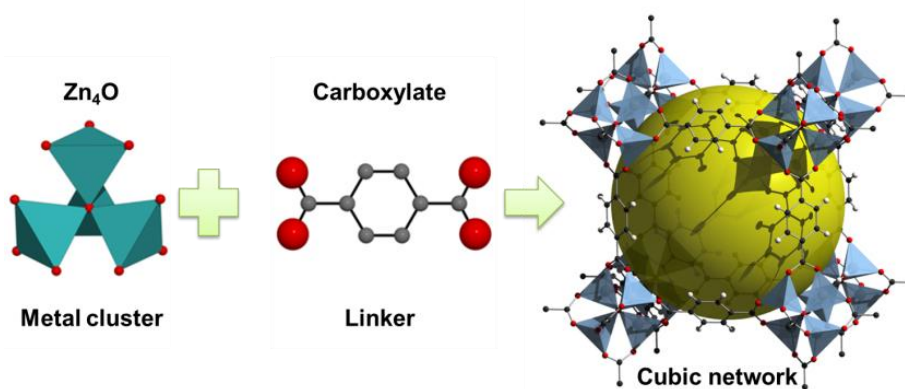

Figure. 2.5 Three-dimensional framework of MOF-5[31].

Microporous polymers

Microporous polymers have received an increased level of research interest due to their special properties achieved by combining the advanced properties of both porous materials and polymers. These polymers are represented by hypercrosslinked polymers (HCPs)[36], a series of permanent microporous polymer materials such as polymers of intrinsic microporosity (PIMs), conjugated microporous polymers (CMPs), and porous polymer networks (PPNs). Generally, HCPs can be produced in a large scale by a simple (Friedel-Crafts alkylation) reaction which provides a fast kinetics to form strong linkages between aromatic ring, preventing the polymer chains from collapsing into a dense, nonporous state, resulting in a highly crosslinked network, resulting in high surface area of up to 5600 m^2/g[37-38]. Such highly crosslinked nature of HCPs also enables the outstanding thermal stability superior to that of most organic polymers. Due to the simple and adaptable synthetic approach, a great variety of aromatic monomers can be

employed to develop polymer networks with various pore topology or unique functionalities[39]. These great advantages of this organic polymers, including low cost reagents, wide range of chemical functionality and tenability, make the porous materials of interest for competing with conventional microporous absorbents such as activated carbons.
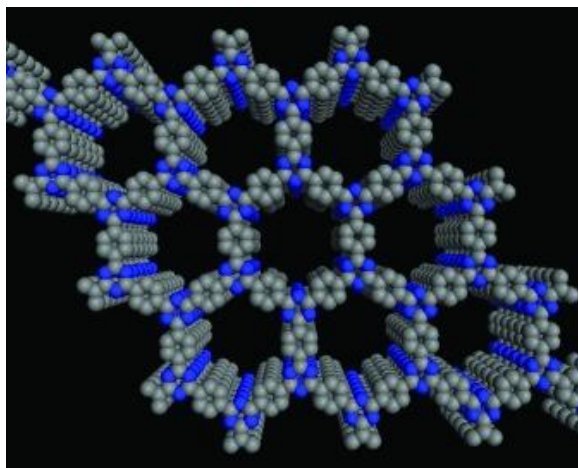

Figure. 2.6 Schematic representation of the structure of microporous polymers[40].

Porous organic cages (POCs)

Most microporous materials are extended networks, such as activated carbon, zeolites, MOFs, network polymers. The microporous materials with pores smaller than 2 nm have the potential in applications such as adsorption and separation[41]. Thus, the most attention has been focused on the control of the pore size and surface area. However, the external particle surface can also influence the sorption behaviour[42-43]. For porous materials, the interaction between sorption into micropores and interpaticle voids can be influenced by the particle size control[44-45]. In addition, the diffusion length can be reduced with nanosized particles. Substantial efforts have been made to achieve monodisperse nanoscale porous crystals with diameters below 100 nm. For porous solids such as MOFs and COFs, newly developed methods, including using surfactants, confined space synthesis and tuning of reaction conditions, still struggle to produce small particle size porous crystals. Not to mention that these methods require complex synthesis and purification procedures to remove the surfactant. Therefore, there is growing interest in porous materials composed of discrete organic molecules, known as porous organic cages, where fine control over particle size and morphology can be easily achieved.
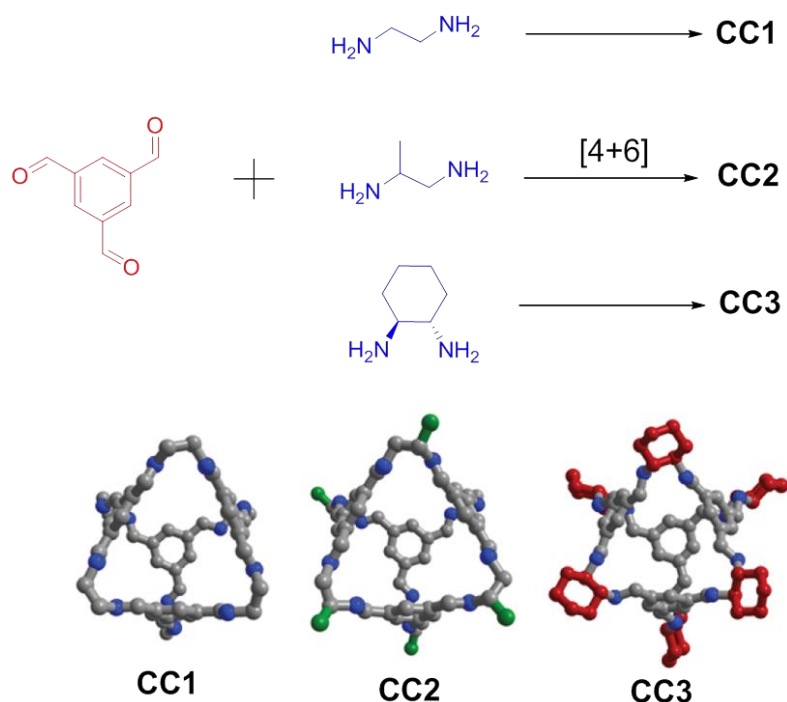
16

Figure. 2.7 Structures for cages 1–3 determined by X-ray crystallography for desolvated cages, as shown with one of the triangular pore windows facing[48].

Porous organic molecular materials are crystalline porous materials defined by their modular, molecular structures without extended covalent or coordination bonding in the solid-state. Unlike the extended frameworks, in particular metal-organic frameworks and covalent organic frameworks, where the synthesis and crystallization take place in the same step, the extended network of porous organic molecular materials is generally synthesized first and then assembled in the solid state in a separate step[46-47]. Thus, conventional permanent porosity in these structures is rare due to the preference for discrete molecules to pack efficiently with minimal void volume in solid-state. Nevertheless, a growing number of porous molecular materials have been reported recently. In particular, porous organic cages have been discovered with porosity that can compete with extended porous frameworks[48].

The first series of three porous organic cages has been reported by A. I. Cooper's group. This crystal porosity in these cages is a consequence of both the intrinsic porosity from molecular cavity in the cages and the extrinsic porosity from the inefficient packing of tetrahedrons. Three imine-linked tetrahedral cages were synthesized by the condensation reaction of 1,3,5-triformylbenzene with 1,2-ethylenediamine (cage **1**), 1,2-propylenediamine (cage **2**) and (R;R)-

1,2-diaminocyclohexane (cage **3**) in a [4 + 6] cycloimination, shown in Figure 2.7. The core cage structure for 1-3 shows tetrahedral symmetry and four approximately triangular windows. Cage **1** has unfunctionalized ethylene vertices, whereas **2** has one exo-methyl group per vertex. The vertices of **3** consist of relatively bulky cyclohexyl groups. The crystallographic packing and hence the pore structure in these materials is determined by the tetrahedral cage symmetry and by the functional groups on the cage vertices. Cage **1** packs in window-to-arene stacks and these stacks are arranged window-to-ethylene with respect to each other, resulting in a compact structure with no inter-cage window connectivity. Cage **2** packs in an analogous mode but the packing of stacks by the six vertex methyl groups leads to a one-dimensional pore channel running between the cages. Distinct from **1** and **2**, cage **3** packs in a window-to-window arrangement. The windows in **3** align due to the interlocking of three cyclohexyl groups (red). Combined with the tetrahedral cage symmetry, this results in an interconnected three-dimensional diamondoid channel (yellow) structure running through the cages (Figure 2.8a).
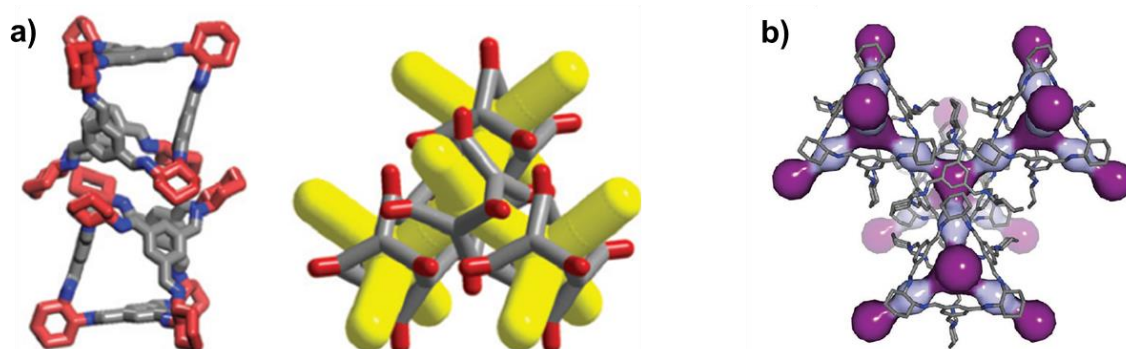

Figure 2.8 Schematic of a) cage-cage packing in the crystal structure of Cage **3**. b) Two pore cavities exist in the 3D pore structure of Cage **3**: a cage cavity inside the molecule itself (dark purple) and a window cavity between adjacent cage windows (light purple)[48].

However, due to the lack of extended covalent or coordination bonding in porous organic cages, the BET surface areas of cage **3**[47] is only up to 600 $m^2 \cdot g^{-1}$, which is much lower than that of MOFs[49], COFs[50-51], and polymer networks[38] (SSA_{BET}=5500–6200 $m^2 \cdot g^{-1}$)[52]. A further step has been made by Mastalerz and co-workers to develop porous organic molecules which could compete with frameworks for particular application[53]. Based on their earlier work of an *endo*-functionalized adamantoid cage compound **3**, a molecular organic crystal with an unprecedented surface area for cage compounds of SSA_{BET}=1375 $m^2 \cdot g^{-1}$ has been synthesized[54].

The exceptional surface area in this material was ascribed to the fact that no accessible molecular surface is lost by π–π stacking. Other researches have been carried out for promoting the properties of porous cages, summarized in Figure 2.9. It shows the development of various classes of porous materials over the past 25 years. The surface areas are compared with the newly developed organic molecules While surface area is already well catered for porous solids, such as carbons, polymers, MOFs, and COFs, the development of strategies to produce solids with larger pores and pore volumes is important if molecular crystals are to find applications, such as sorption of small atoms or molecules, such as Xe[55], SF_6[56] and carbon dioxide[57-59].
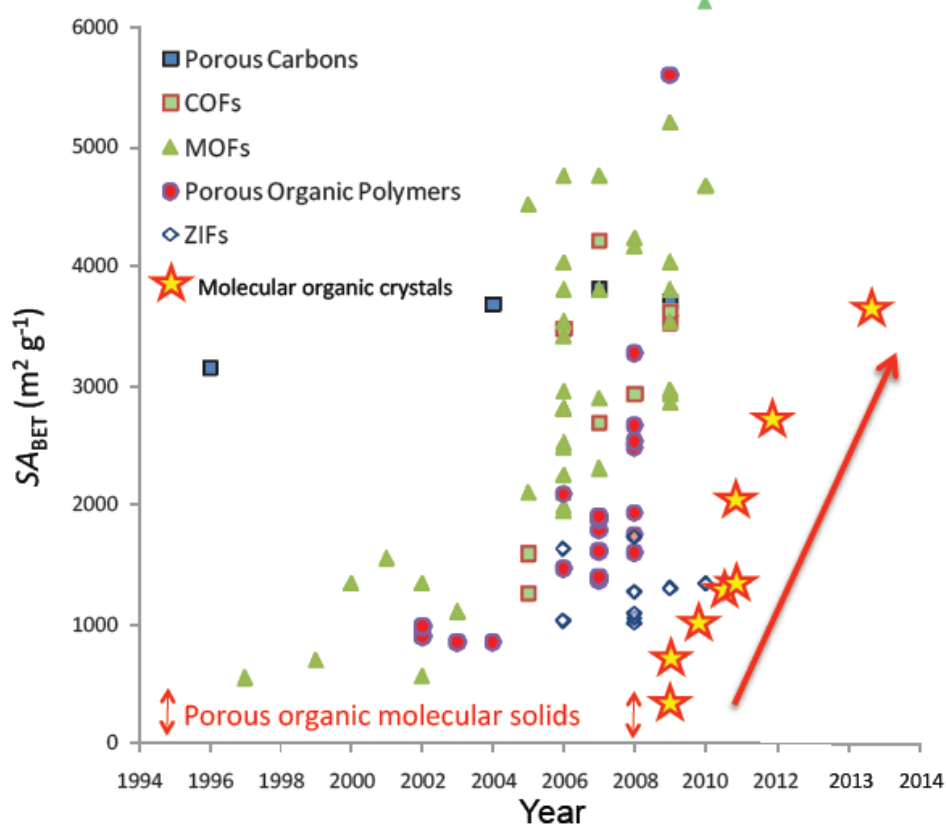
Figure 2.9 The rapid evolution in porosity in molecular crystals since 2009, illustrated with respect to the equivalent trend in extended networks and frameworks[47, 60-67].

Porous organic cages are also a potential energy-efficient alternative for molecular separation processes. MOFs have led the way for these molecular separations since small pores tends to perform better from a selectivity perspective. POCs might struggle to compete with the isosteric heats of adsorption reported for open metal site MOFs, but the chemistry of the pores are more

important than their surface areas, or the presence of open metal sites[68-71]. The properties design can be carried out at the molecular level based on the strategy to synthesize molecules with prefabricated pores, and then tune their functionalities, shapes, and sizes. For example, the POC CC3 tends to have the same limiting pore size irrespective of its crystal packing and therefore two adsorption sites from prefabricated porosity: the intrinsic cage cavity pore and the interstitial pore between two cage windows. CC3 has two adsorption sites: the intrinsic cage cavity pore and the interstitial pore between two cage windows. For adsorbed molecules to reach these sites in **3**, they must pass through the narrowest point in the pore network, which is the triangular shaped cage **3** windows (Figure 2.8b). These CC3 windows are dynamic in nature, which allows these windows to open and close during gas adsorption[47]. In addition, the pores can be postmodified to chemically alter the porous organic building blocks after they have been synthesized, prior to crystallization. For example, Mastalerz described a post-synthetic modification of the interior of a shape-persistent POC with six free hydroxy groups using a six-fold Williamson etherification[72]. Their pore structures and cavity properties can be therefore tuned to provide selective adsorption sites after being modified postsynthetically. Consequently, owing to their tunable apertures, designable functionality and good processibility, POCs have been successfully used for challenging separations such as xylenes isomers[73], noble gases[55] or chiral molecules[55].

2.2.2 Adsorptive Separation

Adsorptive separation refers to the process where the gas mixture is separated based on the differences in adsorption behavior of each component[74]. Depending on the properties of the adsorbents and adsorbates used, as well as the associated interactions, the adsorptive separation can be achieved based on three distinct mechanisms: steric, equilibrium and kinetics effect. The steric effect, also known as molecular sieve effect, is driven from molecular sieving properties of zeolites and molecular sieves. For porous adsorbents possessing pore system with specific dimension, the bulky molecules are excluded from entering the pore while the small ones can diffuse into. The largest application based on steric effect is the separation of paraffin from iso-paraffin utilizing zeolite 5A[75] (ref). In the equilibrium mechanism, the component having a stronger attachment to the porous materials is preferentially adsorbed from the mixture[76], based on the fundamental properties of the molecules: polarizability, magnetic susceptibility,

permanent dipole moment and quadrupole moment[77]. The kinetic mechanism is based on the differences in diffusion rate of different species within the porous materials. The pore size therefore needs to be tailored precisely to the extent between the kinetic diameters of the mixed components. In adsorption separation, adsorption capacity and selectivity are the primary properties of the adsorbents. Adsorption capacity is related to the nature of the adsorbate and the pore of the adsorbent, as well as the working conditions, such as temperatures and pressure in gas separation. The selectivity is the property based on the same prerequisites however more complicated. A promising adsorbent is the one which provides good adsorption capacity and selectivity. In the meantime, a favorable kinetics and regeneration need to be considered as an important issue in practical separation process to reduce cost for large-scale applications.

2.3 Hydrogen Isotope Separation

Adsorptive separation has been successfully applied to various industrial applications for gas separation, such as air separation by pressure swing adsorption. However, it cannot be applied to the separation of isotopes, since the traditional separation mechanisms are based on either size or chemical properties discrimination. However the chemical properties related to the interactions of protons with electrons of isotopes is almost the same. Separating H_2/D_2 mixtures is therefore one of the most challenging issues in modern separation science and technology since the isotopes have identical size, shape and thermodynamic properties. Thus, H/D separation can only be realized by techniques utilizing small difference in thermophysical properties, e.g. vapor pressure or molecular diffusion rate, which arises from the difference in isotope mass.

2.3.1 Current Technology for Industrial Separation of Hydrogen Isotopes

Currently, several techniques have been applied for hydrogen isotope separation based on the thermophysical differences, such as centrifugation[78], thermal diffusion[79-80], cryogenic distillation[81], proton exchange, diffusion through alloys, formation of hybrids[82], gas chromatography[83-84], electrolysis[85-86], and others[87-89]. However, most of these techniques

require hundreds of stages to achieve separation, resulting in huge energy consumption and high cost. Centrifugation requires simple device but only low efficiency can be achieved; Thermal diffusion has the disadvantage of small-scale and high energy consumption; Metal hydride absorption is not reliable in the regeneration and requires high temperatures; Chromatography is not a continuous process and the low capacity makes it impossible for industrial use. Among the methods mentioned above, feasible hydrogen isotope separation techniques on large-scale industrial application are cryogenic distillation and proton exchange between H_2O and H_2 or H_2S, so-called Girdler sulfide process.
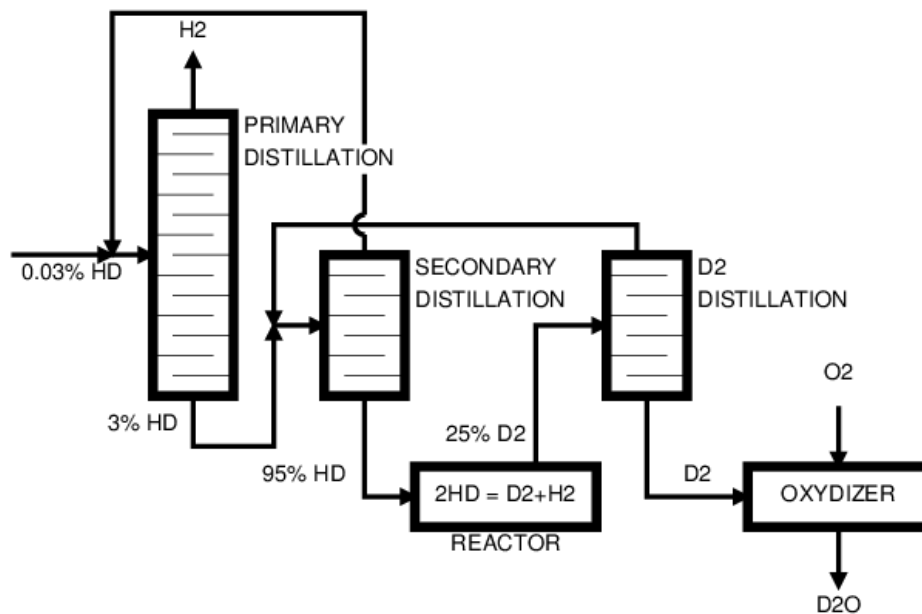

Figure 2.10 Process flow diagram of deuterium separation by way of a three-stage distillation at low temperature[90].

The cryogenic distillation is a widespread technique in chemical industry for liquid mixture separation. The method is based on the differences in saturation vapor pressure of the species above the surface of the liquid mixture. For the case of H_2/D_2 mixture, the gas must be cooled to 20.4 K, the boiling point of liquid hydrogen. Lighter components are those characterized by higher vapor pressures, hence higher volatility and lower boiling points; vice versa, heavier by lower vapor pressures, hence lower volatility and higher boiling points[91]. By utilizing the minor difference between the boiling temperatures of the isotopes: 20.4 K for H_2 and 23.7 K for D_2, resulting in a separation factor of 1.5 at 24 K[92]. The distillation of liquid hydrogen, is considered a multi-stage fractionation and the schematic diagram is shown in Figure 2.10.

The Girdler sulfide (GS) process is a chemical exchange technique based on the difference between the chemical reaction rates of isotopes. Deuterium can be transferred from a water molecule to a hydrogen sulfide molecule based on a reversible reaction: $H_2O + HDS \rightleftharpoons HDO + H_2S$. The separation factor is roughly equal to the equilibrium constant for this reaction. At 303 K, the equilibrium favors the concentration of deuterium in water, while at 403 K in the hydrogen sulfide. Thus, the concentration of deuterium is increased in the cold section of the separation tower, following to be used as a feed for the hot section, where the exchange further promotes enrichment, as shown in Figure 2.11, making it possible to separate D from H. The final product is 20% D_2O which needs to be separated by electrolysis to obtain deuterium[92-93].
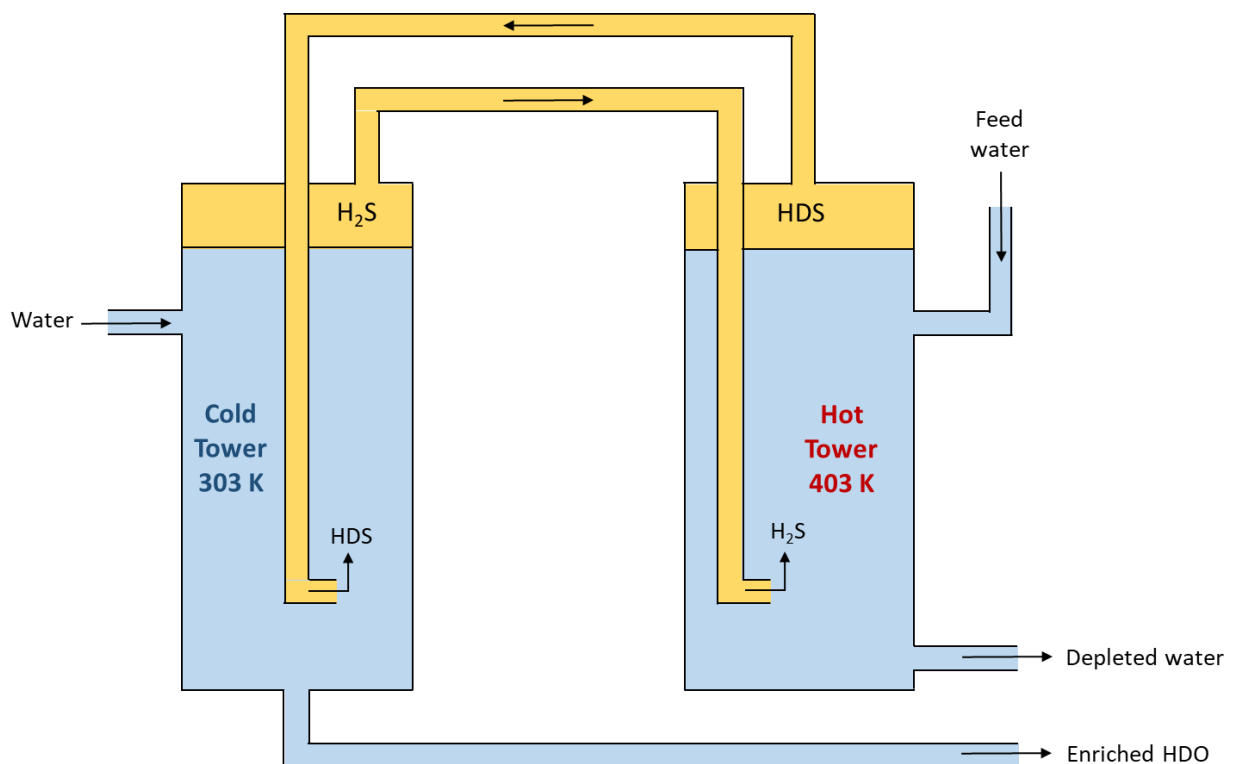

Figure 2.11 Production of heavy water by Girdler sulfide (GS) process.

However, these techniques are highly energy- and time intensive with a low separation factor. Therefore, an alternative efficient method in hydrogen isotope separation should be exploited to replace the energy-intensive techniques with a relatively low energy demanding.

2.3.2 Kinetic Quantum Sieving (KQS)

Quantum sieving in nanopores emerges as one promising avenue to separate H_2/D_2 isotope efficiently and effectively. Introduced by Beenakker et al.[8] in 1995, the quantum sieving is characterized by faster diffusion and preferred adsorption of the heavier isotope confined in pores, resulting in isotope separation. The quantum effect takes place in microporous materials when the difference between the diameter of a cylindrical pore (d) and the molecular hard core (σ) is comparable to the de Broglie wavelength of isotope molecules of radial motion (λ).

$$\lambda \approx d - \sigma \tag{2.4}$$

The model is based on the following assumptions: i) the pores are considered to be cylinders with constant diameter d; ii) the density of molecules in the pores is low enough to neglect the molecule-molecule interaction; iii) no molecule-surface interactions are stronger than van der Waals type. The motion of the molecules can therefore be separated into two independent components, the axial and radial. The motion in the axial direction is free, while it's restricted[94-95] in the radial direction by the potential well created by the interaction with the wall of the pore. The potential of a particle in a cylindrical pore as a function of the distance between the two opposite surfaces is demonstrated in Figure 2.12. For sufficiently large d, the potentials of the opposite walls do not influence each other, the walls therefore can be considered as two single flat surfaces, with the potential depth ε_{fs}. With decreasing d, the potential overlap gets stronger, exhibiting two minima. The two minima increase and coalesce with further reduced d, giving a single minimum of sharpening curvature. The overlap of the repulsive parts of the potential cause the potential depth decreases sharply when $d \leq \sigma$.
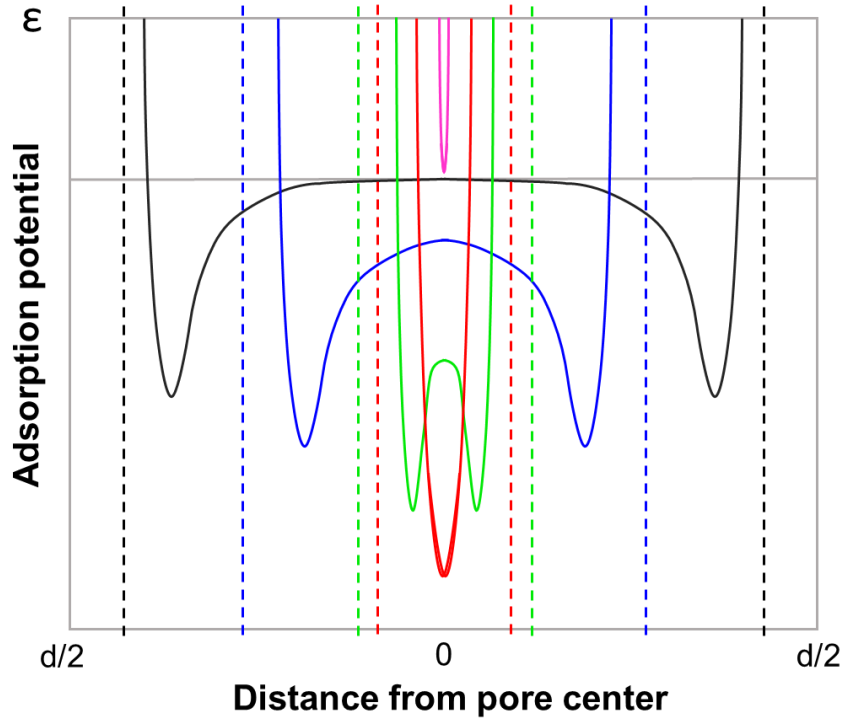
Figure 2.12 Adsorption potential depth as a function of pore diameter[96].

The energy levels of a circular square well in a cylinder are given in the following equation[97],

$$E_i = \frac{2\gamma_i^2 \hbar^2}{(d-\sigma)^2 m} \tag{2.5}$$

where γ_i are zeros of Bessel function, m is the molecular mass. When $i=0$, E_0 increases with the decreasing molecular mass, as well as the difference between pore diameter and molecular size. The quantization of the transverse motion of light particles in confined channels therefore cannot be neglected. The zero-point energy (*ZPE*) in van der Waals well corresponds to the interaction potential for the radial motion by a circular square well with the depth ε, which depends on the d due to the overlap of the opposite wall of the pore, as shown in Figure 2.13.

Based on the assumption of the equilibrium with the gas in free space, the density of the molecules inside the pores per unit length is denoted in,

$$n = n_v \frac{\pi}{4} (d - \sigma)^2 \sum_i exp\left(\frac{\varepsilon - E_i}{kT}\right) \tag{2.6}$$

where n_v is the gaseous molecules outside the channel, k the Bolzmann constant and T the absolute temperature. $\frac{\pi}{4}(d - \sigma)^2$ is the free volume per unit length of the channel.

The adsorption of a molecule on a surface can be characterized by the E_0/ε, the magnitude of the zero-point energy of the molecule with respect to the potential well from molecule-wall interaction. In region 4, where $E_0/\varepsilon < 1$, the molecule can be attracted by the wall since the potential well overcompensate the *ZPE*. In the situation $E_0/\varepsilon > 1$, the *ZPE* overcompensates the attractive molecule-wall interaction, thus the energy barrier for molecules to enter the pore can only be overcome by thermal excitement. Moreover, the density of the molecules inside the pore is reduced since the Bolzmann factor $(\varepsilon - E_0)/kT < 1$ due to equation 2.3.
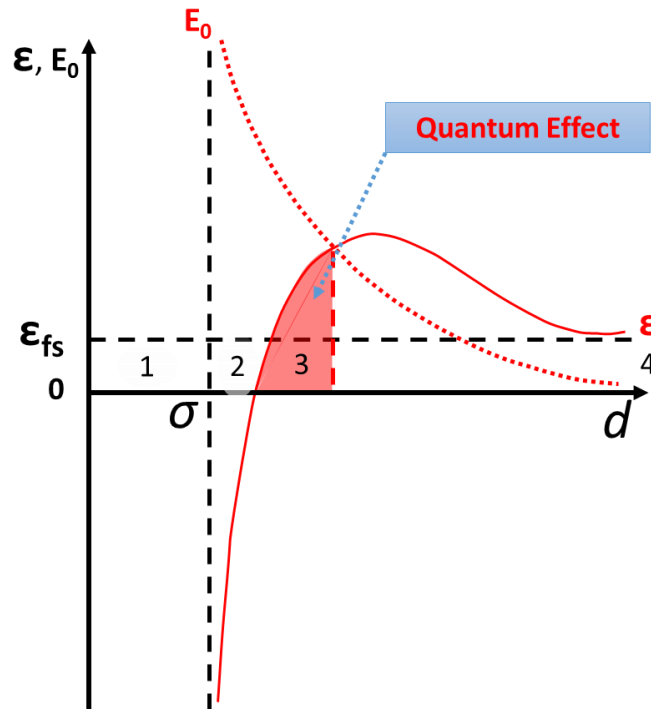
Figure 2.13 The potential well depth ε and zero-point energy E_0 as a function of the pore diameter d, where represents the depth of flat surface[8].

In region 2, the binding energy becomes negative before the situation $d = \sigma$ is reached, indicating that strong electrostatic repulsion of the electron shells of the molecule and the wall of pore occurs. For small pores $d \leq \sigma$, the molecular density inside the pore can be close to 0, indicating no molecule entering the pore (region 1). The quantum effect only takes place where the adsorption is dominated by *ZPE* in region 3, where the potential well is attractive but the

molecule faces penetrating barrier due to the stronger *ZPE*. As the isotopes have the same ε and σ, the quantum effect differs from their mass difference. Assuming that both isotopes occupy the lowest energy level, the adsorption in the pore is determined by their respective E_0. Therefore, the ratio of the densities inside the pore can be estimated as

$$\alpha = \frac{n_1}{n_2} = exp\left(\frac{E_{01}-E_{02}}{kT}\right) \tag{2.7}$$

where E_{01} and E_{02} are the zero-point energy of isotope 1 and 2, respectively. According to equation 2.5, the E_0 of the lighter isotope is higher than the heavier one, the molecular density of the lighter isotope is therefore lower than the heavier one.

Hence, the hydrogen molecule has a higher *ZPE* than its heavier isotope deuterium, resulting in a stronger diffusion barrier when entering into a confined pore. According to this quantum sieving effect, an efficient separation of hydrogen isotopes can be achieved.

2.3.3 Chemical Affinity Sieving (CAS)

Besides kinetic quantum sieving, the thermodynamic effects can be employed to separate hydrogen isotope mixture. Chemical affinity sieving is commonly observed in molecular sieving, which is based on the difference in molecule-surface interactions, leading to the preferential adsorption of certain species on the specific adsorption sites[98-99]. The kinetic quantum sieving discussed above is based on the confinement of the pore aperture, while the chemical affinity sieving dominates when the pore size is large enough for gas molecules to penetrate without diffusion barrier.

In general, a diatomic molecule possesses six degrees of freedom contributing to the *ZPE*, *x*, *y*, and *z* transitional, two rotational, and one vibrational. Once the molecule is absorbed on the surface with affinity strength, the two transitional degrees of freedom parallel to the surface are hindered[100]. In this situation, the transitional motion of the molecule towards the surface can be considered as molecule-surface vibrational motion, which is strongly influenced by the *ZPE*. The strength of the specific adsorption site of the host materials has a great impact on the *ZPE*[101]. Considering hydrogen isotopes, the difference between their *ZPE* depends on the depth of potential energies of different adsorption sites, as shown in Figure 2.14. The depth of the potential energy represents the strength of the adsorption sites respectively. For the steeper

potential energy, which means a strong binding sites, the difference between the *ZPE* of H_2 (black) and D_2 (red) is much larger compared to that of the weak binding sites. Consequently, the heavier isotope has a lower *ZPE* when adsorbed on the strong adsorption sites, which leads to a difference in adsorption enthalpies, resulting in the preferential adsorption of the heavy isotope. Notably, the deeper the potential well is, the higher desorption temperature can be realized. The isotope separation can be therefore achieved at increased temperatures via chemical affinity sieving.
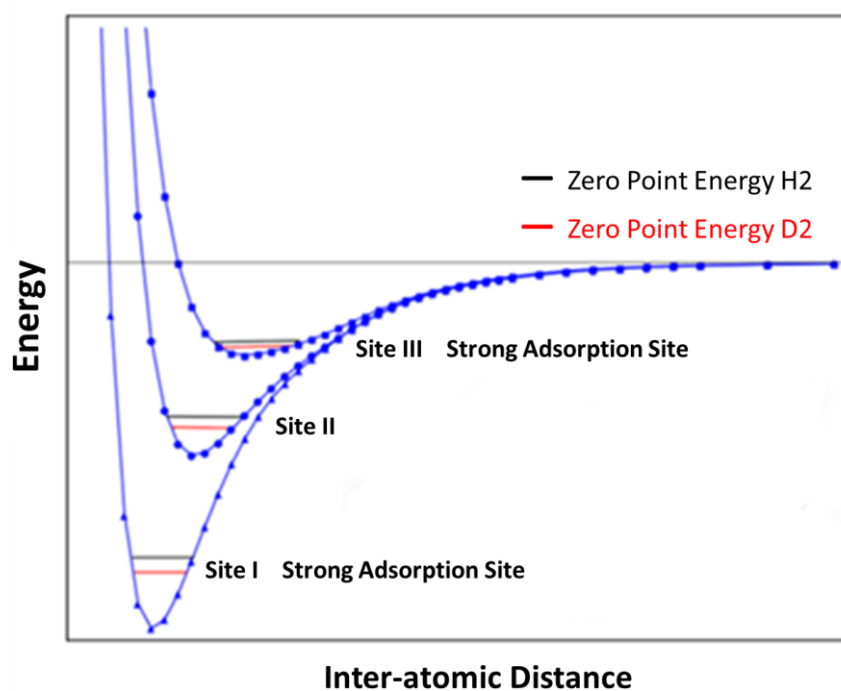

Figure 2.14 Schematic diagram of the zero-point energy on adsorption sites possessing different potential energy. The depth of the potential well represents the strength of distinct adsorption sites. The black and red lines represent the zero-point energy of H_2 and D_2 respectively.

3. Experimental Methods

3.1 Thermal Desorption Spectroscopy (TDS)

Thermal desorption spectroscopy (TDS), which is also known as temperature-programmed desorption (TPD), is an important technique for studying the kinetic and thermodynamic parameter of desorption of gases from solid surfaces[102-105].

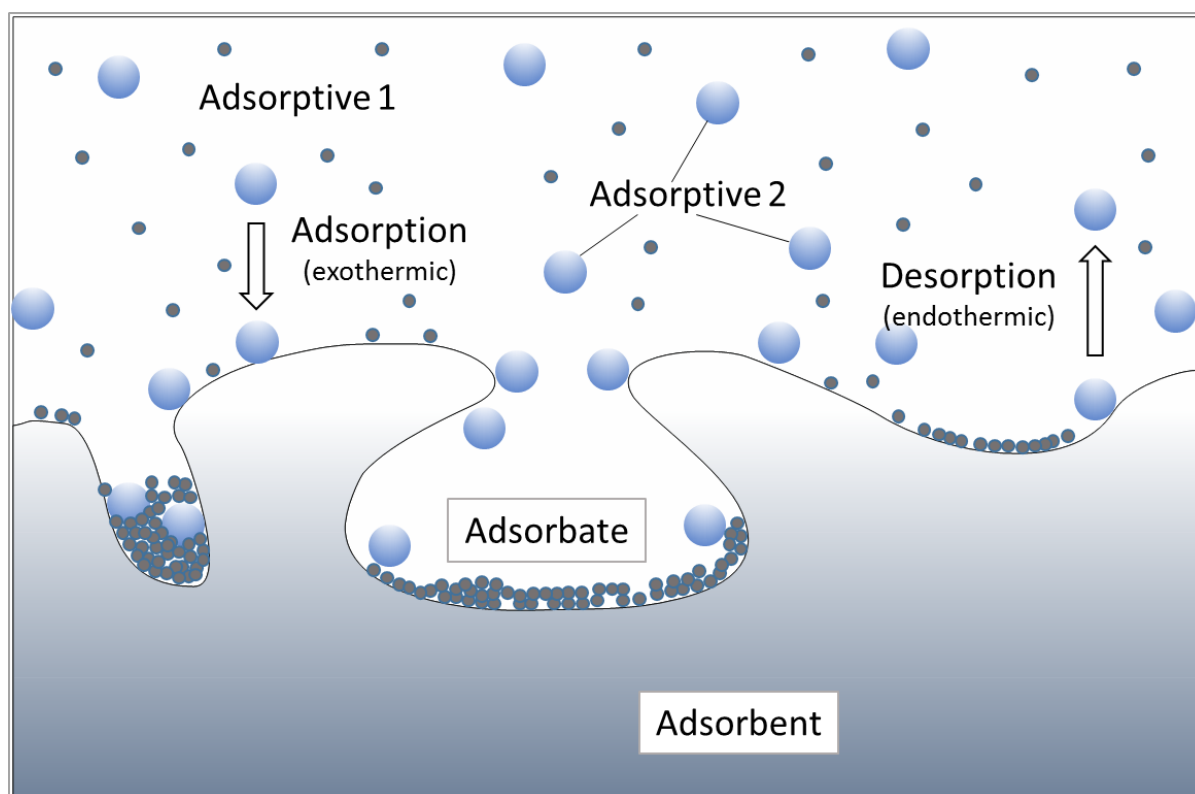Figure 3.1 Illustrated adsorption and desorption system consisting of a two component adsorptive gas. An adsorbate leaves the substrate and enters the gas phase by transferring the thermal energy to the adsorbed species when the surface is heated[106].

The basic process of studying the thermal desorption is illustrated in Figure 3.1. When the attractive interaction between molecules and surface is strong enough to minimize the

disordering effect of thermal motion, adsorption occurs. When the sample is heated, the desorption will take place when the adsorbed molecules get enough thermal energy to overcome the activation barrier to be released from the surface[106]. Therefore, the desorption temperature is related with binding strength of the adsorbed molecules to the specific surface.

3.1.1 TDS setup

The in-house designed TDS apparatus for measuring desorption spectra of adsorbed hydrogen isotopes under cryogenic conditions is shown in Figure 3.2. The setup consists four main parts.
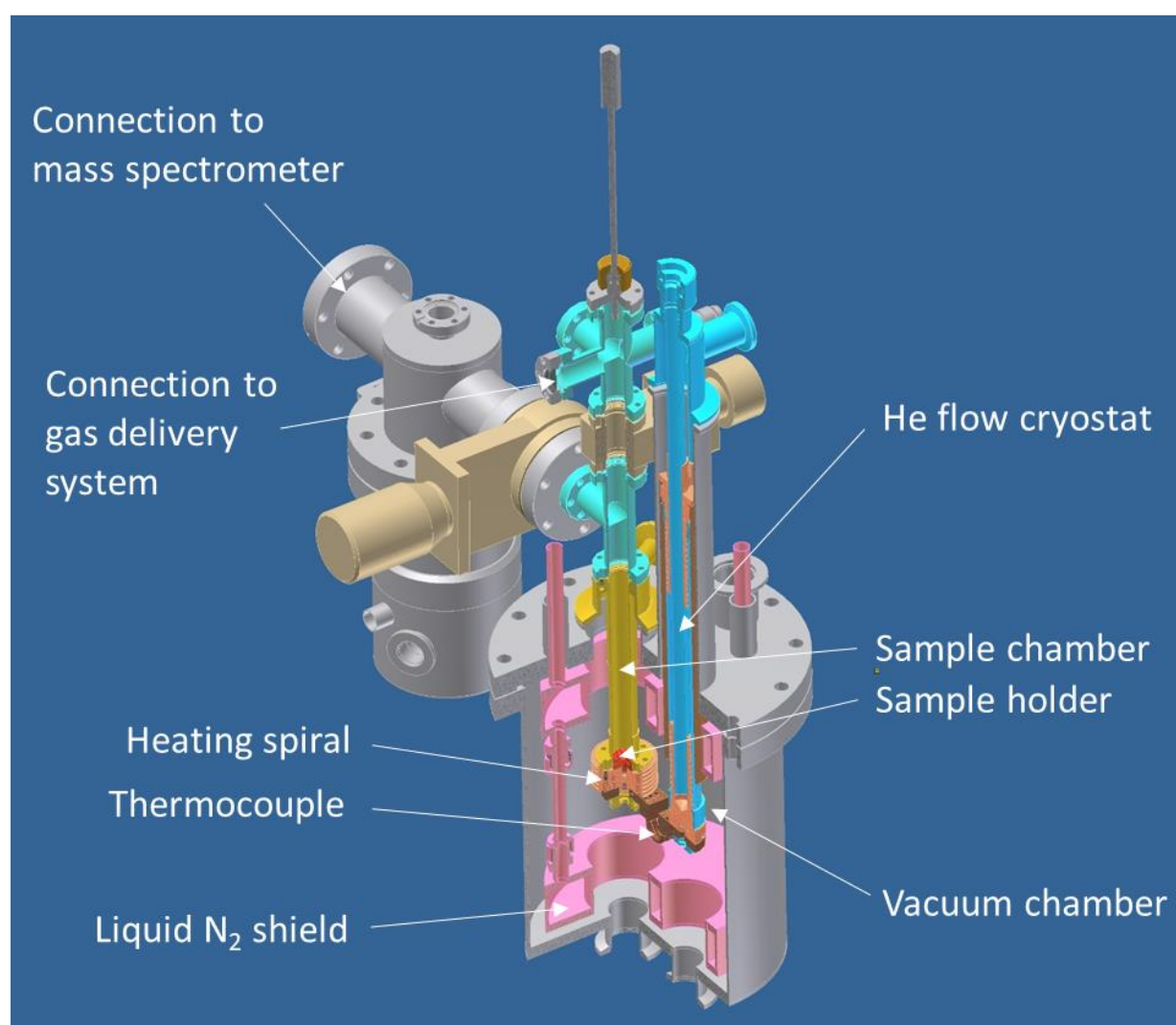

Figure 3.2 Schematic diagram of thermal desorption spectroscopy.

1. Ultrahigh vacuum (UHV) chamber

Made of stainless steel, the sample chamber is located in the central part of the setup. The UHV system consists of a pumping system and the vacuum vessel to make sure the chamber is under high vacuum (10^{-6} mbar). The sample holder is made by Cu and can be screwed tightly to the bottom of the sample chamber with the help of a removable rod. This ensures good thermal contact to the cooling-heating stage holder.

2. Temperature controlling system

The temperature of the sample is regulated by the coordination of a resistive heater and a helium flow cryostat. The heating spiral is wrapped around the copper block, and the temperature is detected by a pair of CrNi thermocouples and Pt resistance sensor. The copper block can be coupled to the cryostat when temperatures between 300 and 20 K are needed. Inside the cryostat, the temperature is measured by another pair of CrNi thermocouple which is located at the bottom. With a PID temperature control program, the temperature of sample can be increased with different heating rates, usually 0.01 to 0.1 K/s.

3. Gas delivery system

The gases dosing into the chamber is achieved by leak valves, which are connected to the hydrogen and deuterium tanks. The equimolar isotope gas mixture was produced directly from the connected gas line into the TDS pre-chamber. In order to minimize the velocity effect from different isotopes, here a new pre-mixing chamber with a large volume was added. A connected pressure trasducer allowed the preparation of a 1:1 equimolar isotope mixture.

4. Quadrupole mass spectrometer (QMS)

A QMS is placed to analyze the desorbed gas molecules, which detects masses in the range from 1 to 100 amu with the resolution of 10^{-11} torr. When the temperature increases, the partial pressure of different desorbing gases can be detected by QMS which is evacuated continuously with a constant pumping rate. The partial pressure is plotted versus temperatures, resulting in a TDS spectrum.

3.1.2 Theoretical Description

As a basic assumption of TDS, the desorption rate of a specific adsorbed species is proportional to the partial pressure which can be directly detected by a QMS. On this point, the pumping rate of the QMS system should be high enough to prevent possible re-adsorption of the desorbing gas molecules.

Considering adsorption and desorption pass through exactly the same states, the principle of microscopic reversibility can be included. Thus, adsorption and desorption can be described by the same set of rate equations. The desorption rate is normally described by a rate law of nth order:

$$r_{des} = -\frac{d\Theta}{dt} = k_n \cdot \Theta^n \tag{3.1}$$

where Θ is the referred to as the surface coverage, n is the kinetic order or desorption order, and k_n is the rate constant. If the rate constant k_n is described by the *Arrhenius* equation:

$$k_n = v_n \cdot exp\left(-\frac{E_{des}}{RT}\right) \tag{3.2}$$

where v_n is the frequency factor, E_{des} is the activation energy for desorption, R is referred to the gas constant and T the measured temperature.

Then the desorption spectral interpretation can be described by combining equation 3.1 and 3.2, which is usually referred to as the *Polanyi-Wigner* equation:

$$r_{des} = -\frac{d\Theta}{dt} = v_n \cdot exp\left(-\frac{E_{des}}{RT}\right) \cdot \Theta^n \tag{3.3}$$

Considering the sample is heated linearly during a TDS measurement,

$$T(t) = T_0 + \frac{dT}{dt}t = T_0 + \beta t \tag{3.4}$$

in which β is the heating rate, T_0 is the initial temperature. Therefore, substituting the time t in *Polanyi-Wigner* equation by $dt = (1/\beta) \cdot dT$, the equation can be interpreted as,

$$-\frac{d\Theta}{dT} = \frac{v_n}{\beta} \cdot exp\left(-\frac{E_{des}}{RT}\right) \cdot \Theta^n \tag{3.5}$$

The measured desorption rate of a TDS spectrum contains the fractional coverage term $\Theta(T)$ and the rate constant $k_n(T)$, which indicates the activation energy can be dependent on the temperature and heating rate, as shown in Figure 3.3[105, 107-110].
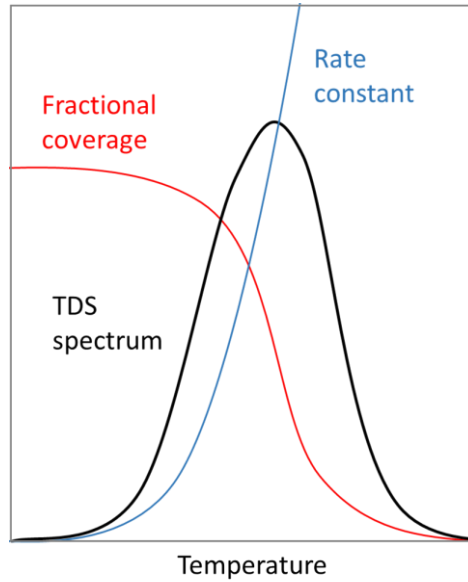

Figure 3.3 Correlation between surface coverage, desorption signal and rate constant as a function of temperature.
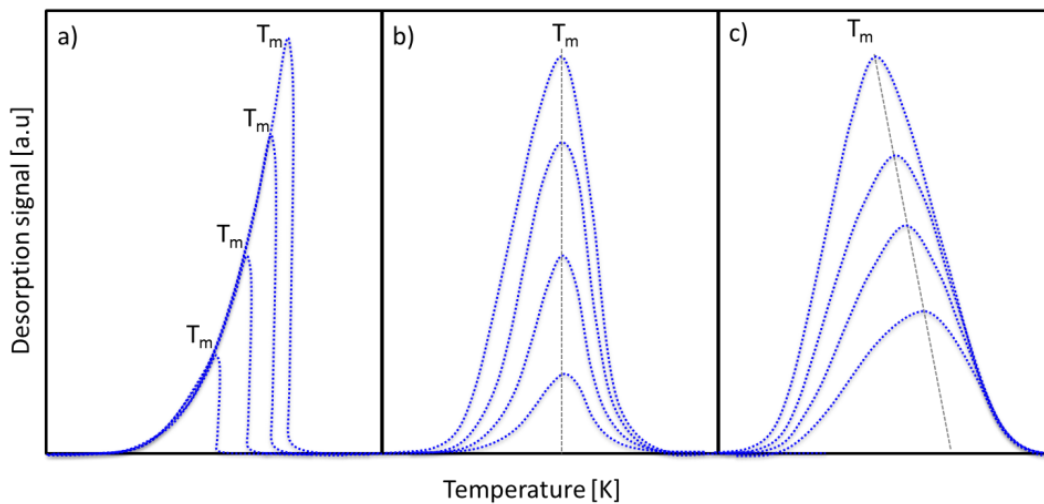

Figure 3.4 Schematic examples for different initial coverage of a) zero-order desorption kinetic, b) first-order desorption kinetic and c) second-order desorption kinetic[111].

As mentioned, the basic condition for determination of the data with *Polanyi-Wigner* equation is that the partial pressure is proportional to the desorption rate based on the sufficiently high pumping rate. Moreover, the other important element of the desorption process is the rate-limiting, which must be slower than all other reactions involved. The activation factors, such as v_n, activation energy E_{des} and desorption order n, are only applicable to a certain rate-limiting step[111]. Most importantly, the desorption rate can be strongly affected by different desorption order, illustrated in Figure 3.4.

Zero-order desorption kinetics ($n = 0$):

$$-\frac{d\Theta}{dT} = \frac{v}{\beta} \cdot exp\left(-\frac{E_{des}}{RT}\right) \tag{3.6}$$

In a zero-order desorption process, the desorption rate is independent on coverage and increases exponentially with temperature and drops rapidly exceeding T_{max}, where all adsorbed molecules have been desorbed. The temperature of the maximum can move to higher temperatures with increasing initial coverage. The zero-order kinetics can be observed in thick multilayers.

First-order desorption kinetics ($n = 1$):

$$-\frac{d\Theta}{dT} = \frac{v_1}{\beta} \cdot exp\left(-\frac{E_{des}}{RT}\right) \cdot \Theta \tag{3.7}$$

In this equation, the desorption rate is proportional to the fractional coverage. The maximum temperature is constant with initial coverage, while increases with higher E_{des}. This is the desorption order which represents non-dissociative molecular adsorption.

Second-order desorption kinetics ($n = 2$):

$$-\frac{d\Theta}{dT} = \frac{v_2}{\beta} \cdot exp\left(-\frac{E_{des}}{RT}\right) \cdot \Theta^2 \tag{3.8}$$

In case of a reaction rate proceeding the desorption process, e.g. the recombination desorbing atoms into a molecule, the second-order desorption process can be observed. The temperature of the peak maximum moves to lower temperature with increasing initial coverage. A more symmetric desorption peak can also be observed with regard to T_{max}.

3.1.3 Analysis of TDS

In order to extract the desorption energy from TDS measurements, *Kissinger* method[112] is exploited by employing desorption spectra recorded with different heating rates. Considering the assumption that the surface coverage at the maximum temperature is independent of the heating rate, the temperature of the maximum desorption rate $T_{max} = T(\max r_{des})$ is determined. The activation energy derivated from a plot $ln(T_{max}^2/\beta)$ vs. $1/T_{max}$, described as follows[113-116].

For $T = T_{max}$, the following condition must be fulfilled,

$$\left.\frac{dr_{des}}{dT}\right|_{T_{max}} = 0 \tag{3.9}$$

Because of,

$$r_{des} = -\frac{d\Theta}{dT} = -\beta \cdot \frac{d\Theta}{dT} \tag{3.10}$$

The equation 3.9 can be rewritten as

$$0 = \left.\frac{dr_{des}}{dT}\right|_{T_{max}} = n \cdot \Theta^{n-1} \cdot \frac{d\Theta}{dT} + \Theta^n \cdot \frac{E_{des}}{RT_{max}^2} \tag{3.11}$$

substituting $d\Theta/dT$ by equation 3.5, and solving for E_{des}/RT_{max}^2 obtains

$$\frac{E_{des}}{RT_{max}^2} = \frac{v_n}{\beta} \cdot n \cdot \Theta^{n-1} \cdot exp\left(-\frac{E_{des}}{RT_{max}}\right) \tag{3.12}$$

For the first-order desorption process ($n = 1$), equation 3.12 can be specified to

$$\frac{E_{des}}{RT_{max}^2} = \frac{v_1}{\beta} \cdot exp\left(-\frac{E_{des}}{RT_{max}}\right) \tag{3.13}$$

where the T_{max} is independent of the coverage Θ but dependent on heating rate β. Taking the logarithm and rearrangement of the equation 3.13 yields

$$\ln\frac{\beta}{T_{max}^2} = -\frac{E_{des}}{RT_{max}} + \ln\frac{v_1 \cdot R}{E_{des}} \tag{3.14}$$

Desorption energy can be obtained from the slope by plotting $\ln(\beta/T_{max}^2)$ vs. $1/T_{max}$ for a series of heating constant.

If the second-order desorption ($n = 2$) takes place, the equation 3.12 becomes

$$\frac{E_{des}}{RT_{max}^2} = \frac{v_2}{\beta} \cdot n \cdot \Theta \cdot exp\left(-\frac{E_{des}}{RT_{max}}\right) \tag{3.15}$$

The desorption peak is symmetric as mentioned, leading T_{max} half the value of the initial coverage. Thus equation 3.15 can be rearranged as

$$\ln\frac{\beta}{T_{max}^2} = -\frac{E_{des}}{RT_{max}} + \ln\frac{v_2 \cdot R \cdot \Theta_0}{E_{des}} \tag{3.16}$$

By plotting $\ln(\beta/T_{max}^2)$ versus $1/T_{max}$ as a function of heating rate, desorption energy can be obtained from the slope and the frequency factor v_2 from the intercept if the initial coverage is known. In this regard, the determination of desorption energy is independent of the reaction order.

3.1.4 Experimental Procedure of TDS

Calibration of TDS setup

The mass spectrometer measures the partial pressure of the desorbing gas molecules. The desorbed amount can be quantified by careful calibration of the signal from mass spectrometer. A solid polycrystalline piece of a diluted Pd alloy Pd$_{95}$Ce$_5$ is usually used for calibration. By introducing Ce into Pd lattice as trapping sites, the diatomic molecules of hydrogen/deuterium dissociate on the surface of Pd and form up the H-Ce complex, which can sustain under ambient conditions[117-119]. Therefore, the relatively stable Pd-H-Ce system allows the alloy to be handled for a few minutes to obtain the adsorbed mass of hydrogen by weighing. The calibration procedure is performed as follows.

Prior to the calibration, the Pd$_{95}$Ce$_5$ alloy (~ 0.5 g) is etched with aqua regia in order to remove the oxide layer and it is then annealed up to 600 K under high vacuum to remove any hydrogen that might be absorbed during the etching procedure. Afterwards, it is weighted and inserted into the sample chamber. At 350 K, 40 mbar pure H$_2$ or pure D$_2$ is loaded on the alloy for 1.5–2.5 h. After loading, the alloy is cooled down to room temperature and then weighed. Afterwards, it is placed back in the sample chamber and a normal TDS measurement till 600 K with 0.1 K/s heating rate performed. After desorption, the alloy is cooled back to RT and weighted again. The weight difference between unloaded state and loaded state equals to the mass uptake of H$_2$ or D$_2$, respectively, which is proportional to the area under the desorption

peak. In order to obtain reliable data, this sequence should be repeated at least for three times. The average of several runs with H_2 or D_2 yields a calibration constant for the mass spectrometer channels $m/z = 2$ and $m/z = 4$, respectively.

In this work, the calibration constant for mass 3 has been also performed. Instead of pure gas, an equimolar H_2/D_2 mixture is exposed on the alloy at 350 K for 2.5 h. When the sample is cooled down to room temperature, it is removed from the sample chamber and weighed. Then the alloy is replaced into the chamber before a heating ramp of 0.1 K/s is applied. The alloy is then weighed again without any gas absorbed. Since the D_2/H_2 mixture can be catalyzed to form HD, the weight difference between the two state equals to the total uptake amount of H_2, HD and D_2, which is proportional to the areas under corresponding desorption curves. With the help of the calibration constant obtained from pure gas calibration, the weight of H_2 and D_2 can be calculated from their desorption area. HD uptake weight can therefore be determined by subtracting the H_2 and D_2 from the total weight, and the HD calibration constant can be further calculated by establishing the correlation of weight and the area under desorption peak.

Instructions for the TDS experiments

For a typical TDS measurement process, about 2-6 mg sample is loaded in the sample holder and activated under vacuum in order to remove possibly adsorbed molecules such as impurities from sample loading or solvent from synthesis. The activation temperature and time is determined by the TG-DSC data collected from the specific sample. The sample mass should be restricted to the moderate gas uptake to prevent partial pressures higher than 10^{-5} mbar to enable the accurate results.

The pure gas desorption study is carried out for a new sample, for the purpose of obtaining an overview of the adsorption behavior. The sample is exposed to a certain pressure of pure H_2 or D_2 at room temperature and cooled down to around 20 K. Adsorption can take place during the cooling process. Afterwards, the remaining gas molecules are removed by evacuation of the sample chamber to achieve high vacuum condition again. Finally, a linear heating ramp (0.1 K/s) is applied to activate desorption and the desorbing molecules are detected continuously by the mass spectrometer. The pure gas measurement as room temperature helps to obtain the further exposure parameters of the given sample, such as exposure temperature and pressure for the mixture separation measurements. The pure gas measurement procedure is illustrated in Figure 3.5.
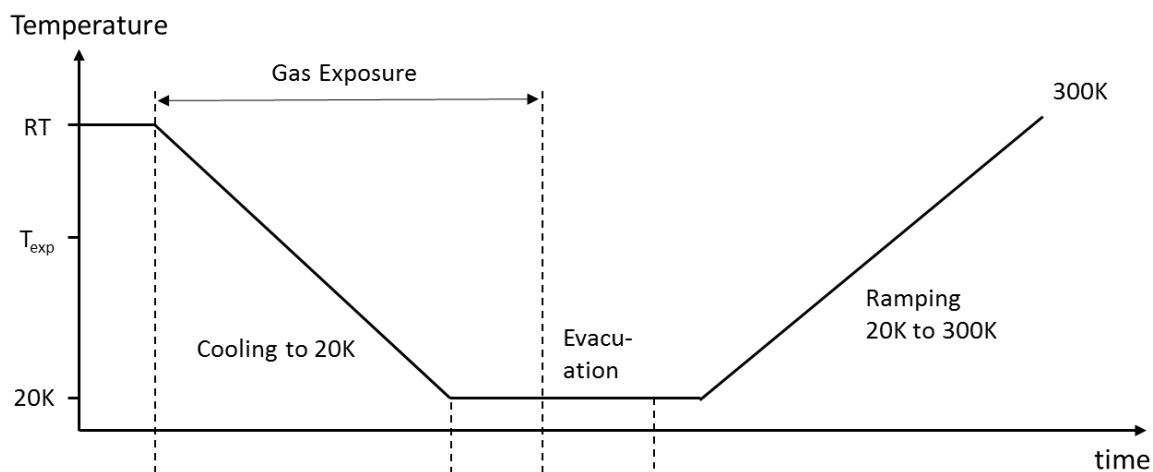
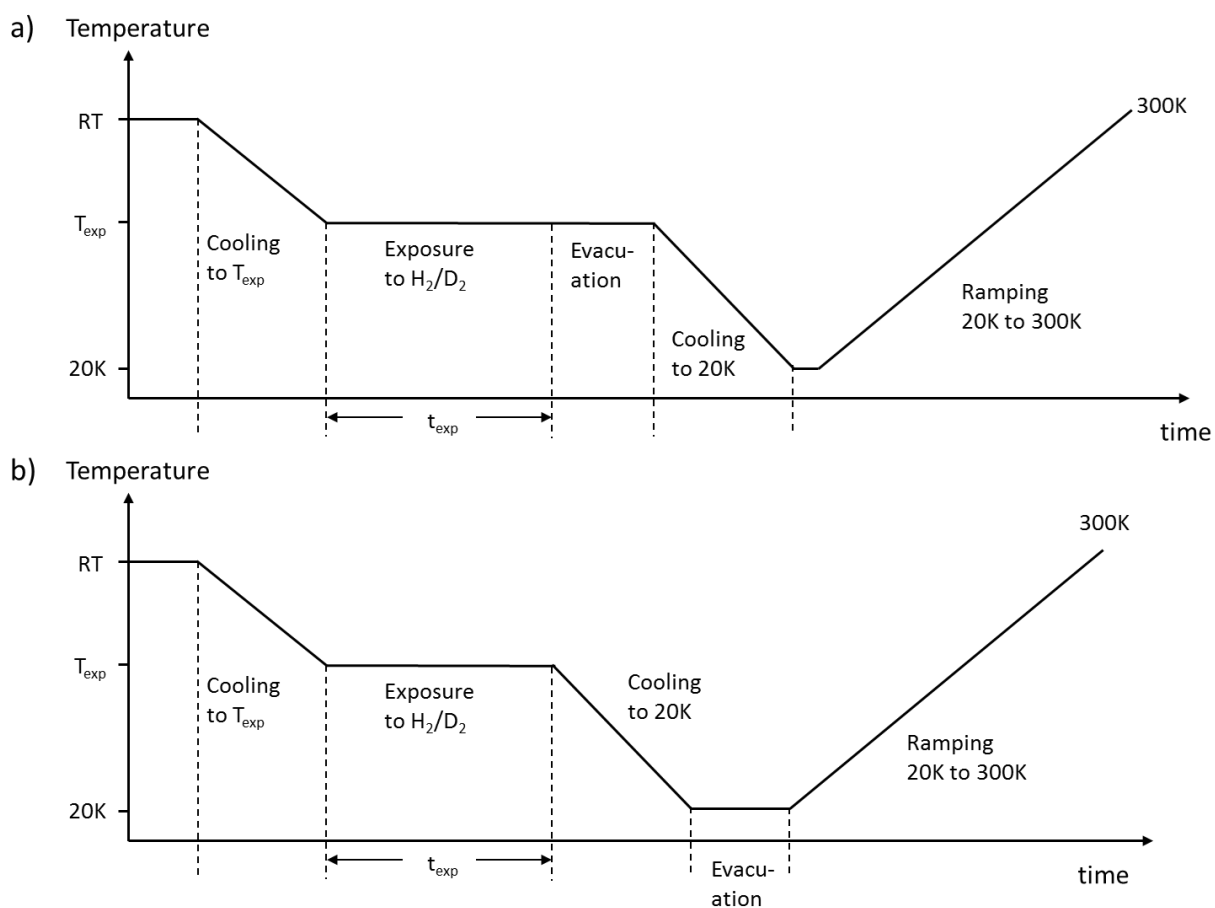Figure 3.5 TDS measurement procedure with pure gas.

Figure 3.6 TDS measurement procedure with isotope mixture, a) adsorbent possessing strong adsorption sites; b) adsorbent possessing small pore apertures.

In a series of isotope mixture measurements, two procedures are carried out depending on the pore aperture size or the existence of the strong adsorption sites. An equimolar D_2/H_2 isotope mixture is loaded on the sample at a fixed exposure temperature for a chosen exposure time. For materials possessing strong adsorption sites, the free gas molecules are evacuated and then the sample is cooled down to 20 K in order to preserve the adsorbed state, Figure 3.6a. While for materials possessing small pore apertures, the sample is cooled down directly to 20 K before the sample chamber is evacuated to remove the remaining gas. Finally, during heating from 20 K to room temperature with a heating rate of 0.1 K/s, the desorbing gas is continuously detected using a mass spectrometer, recognizing a pressure increase in the sample chamber when gas desorbs Figure 3.6b.

H_2/D_2 mixture selectivity

The separation performance of a material for an equimolar gas mixture can be obtained by the difference in the desorbing amount of each species, which is related to the different adsorption energy. Thus, the selectivity of the component A to B is defined as the ratio of the mole fraction in the adsorbed phase (x) and gas phase (y).

$$S(A.B) = \frac{x(A)/x(B)}{y(A)/y(B)} \tag{3.17}$$

Considering the volume of the sample chamber is much larger than the adsorbed gas volume, the 1:1 ratio of the gas mixture remains constant during adsorption process, leading to the mole fraction of gas phase $y(A)/y(B) \approx 1$. Therefore, the selectivity is given by the ratio of desorbed amount of A over B. Meanwhile, the amount of desorbed gas molecules is proportional to the area under the desorption peak after calibration of TDS, shown in Figure 3.7. The selectivity can be further determined by

$$S(A.B) = \frac{A_{Area} \cdot C_A}{B_{Area} \cdot C_B} \tag{3.18}$$

where A_{Area} and B_{Area} are referred to as the area under the desorption peak of each component, and C_A and C_B represent the calibration constant of the corresponding component.
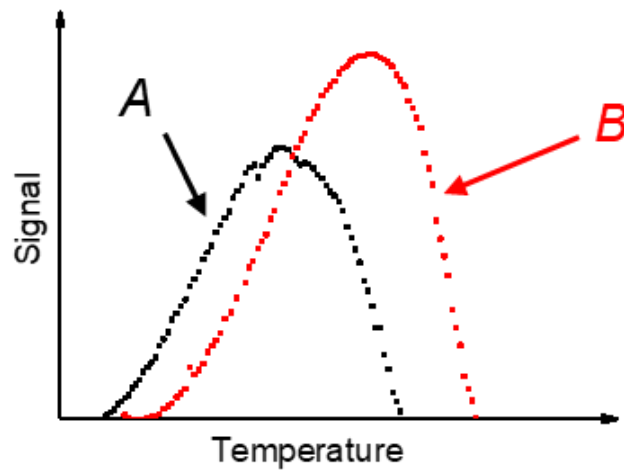
Figure 3.7 Thermal desorption spectrum from gas mixture of two species *A* and *B*.

3.2 Sieverts' apparatus

The most common laboratory technique for measuring adsorption of gaseous hydrogen by porous materials is the Sieverts method, resulting in sorption isotherms, which are plots of hydrogen uptake versus pressure at a fixed temperature[120-121]. A schematic diagram of a basic Sieverts system is shown in Figure 3.8. The device uses two well-known volumes, reservoir (V1) and sample cell (V2), connected through a valve. The calibrated reference volume (V1) is filled with gas to a certain pressure at room temperature, and then is connected to the sample chamber, the gas uptake by the sample can be calculated from the change in the gas pressure in the system.

The device used is a fully-automated Sieverts' apparatus of iQ_2 Autosorb (*Quantachrome Instruments*), coupled with a cryocooler that allows the control the sample temperature between 19.5 and 300 K with a temperature stability of $\pm$ 0.05 K. Additionally, the device has an ultra-low pressure transducer allowing the high-resolution isotherms to be collected even at pressure of $1 \cdot 10^{-8}$ mbar, which enables to use small amount of material ~20 mg[106, 121-122].
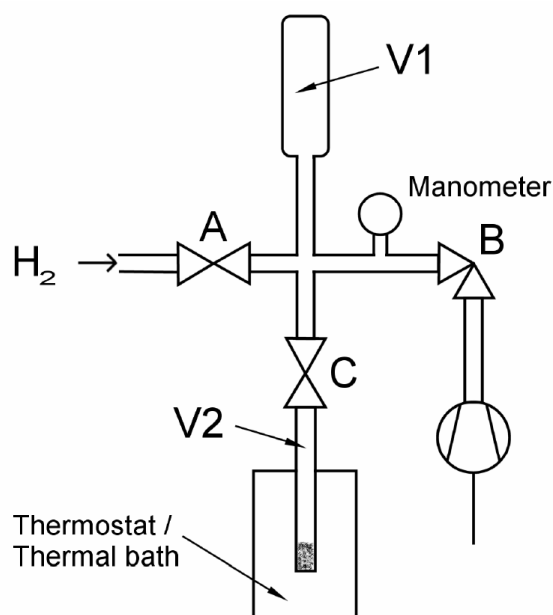
Figure 3.8 Schematic diagram of the Sieverts' apparatus[121].

Prior to the measurement, all samples were heated for several hours at higher temperatures under vacuum to remove moisture and any gases adsorbed on the surface. A calibration specific for each temperature and gas is subtracted from the measurement to account for the non-adsorbed gas in the empty space of the sample cell. Such calibrations can be performed in an individual gas volume versus pressure analysis of the empty sample cell at the same temperature and pressure range of each experiment. An example of hydrogen calibration is given in Figure 3.9 for an empty sample cell at 20.37 K, where the gas volume of the empty cell plotted versus the absolute pressure. For the masses typically used ($\sim$20 mg), the sample volume is nearly zero and the corrections related to the sample volume are neglected. For larger amounts of material, the differences in the volume can be automatically corrected from the calibration accounting for the non-linearity of the adsorbate and the sample volume, measured by an independent He expansion test.
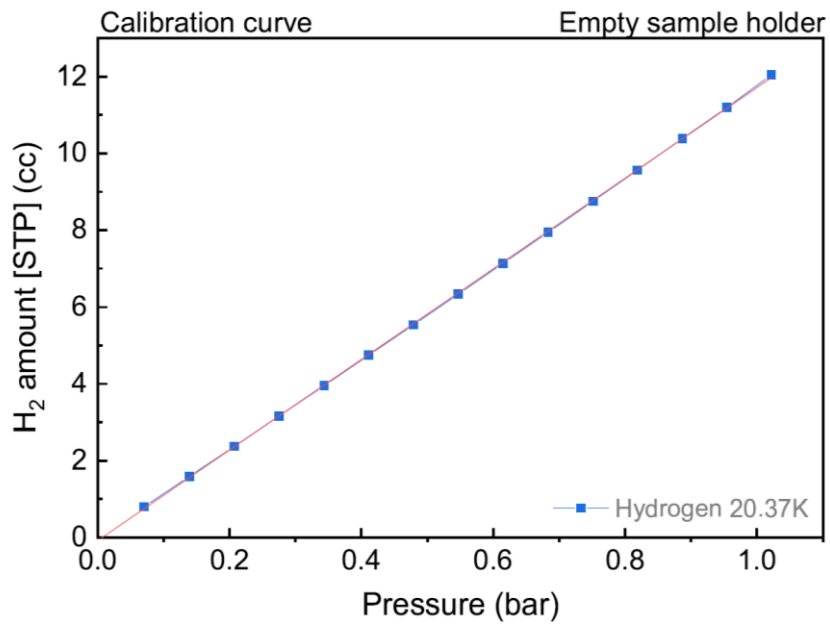
Figure 3.9 Hydrogen calibration for empty sample cell at 20.37 K[123]

4. Hydrogen Isotope Separation in Zeolites

In order to develop feasible nanoporous sieves for large-scale industrial application in hydrogen isotope separation, numerous studies have been carried out for increasing efficient hydrogen gas uptake as well as isotope selectivity. Thus, one fundamental approach is to increase the heat of adsorption on the surface via implementing sufficient unsaturated metal centers. Various metal-organic frameworks (MOFs) with metal centers have been investigated, such as M (Fe, Co and Ni)-MOF-74 systems and Cu(I)-MFU-4l, which show high D_2/H_2 selectivity. However, the technological drawbacks of most MOFs containing open metal sites are their limited thermal stability and the low density of these metal centers, which prohibit their industrial application. Therefore, ion-exchanged zeolites are chosen as a candidate for hydrogen isotope separation since zeolites are well-established in many large scale applications due to their advantageous properties, e.g. low cost, good thermal and radiation stability and well-defined pore structure. In addition, high-density unsaturated metal sites can be easily inserted into zeolite structures due to its acidic property.

In this chapter, the hydrogen isotope separation and efficient gas uptake of metals in zeolites have been studied thoroughly. Different types of cations have been compared based on solid state ion exchange: Co (II), Ni (II), Cu (II), Ni (II), and Ag (I) in zeolite Y. Various techniques have been employed in characterization, such as powder X-ray diffraction, nitrogen BET and cryogenic thermal desorption spectroscopy. Through these investigation, a relationship between the type of cation used and their separation performance has been established. Moreover, a high gas uptake along with high selectivity can be achieved, making ion-exchanged zeolites a promising candidate for practical applications.

4.1 Materials

4.1.1 Ion-Exchanged Zeolite Y

Sample preparation

The ion-exchanged zeolites used in this study have been synthesized by the group of Dr. W. N. Schmidt (Max-Planck-Institut für Kohlenforschung). The synthesis is described as follows. The starting material NaY is a commercial product purchased from Aldrich Chemical Company Inc. Cationic variants of zeolite Y (NaY, CoY, NiY, CuY, ZnY, and AgY) were prepared via conventional ion-exchange methods using aqueous nitrate solutions, as shown in scheme 4.1. 100ml nitrate solution containing 0.1 mol·l^{-1} of the exchanging cations and 1 g of NaY powder were mixed and stirred at 80 °C for 6 h. After each ion exchange step, the partially ion exchanged zeolite was filtered and washed using deionized water. This procedure was typically repeated three to six times to achieve a higher degree of ion exchange.
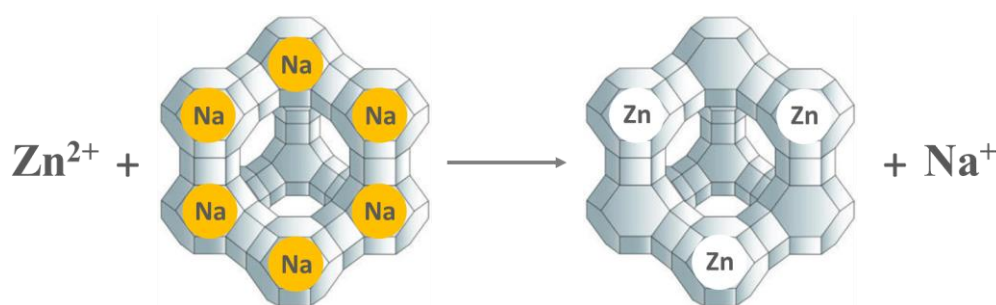
Scheme 4.1 Schematic representation of Zn^{2+} ions distribution on the extra-framework sites in the Zn(II)–NaY zeolites[124].

Characterization

X-ray powder diffraction (XRD) data were measured using CuKα radiation (λ=1.5406 Å) at a setting of 40 kV and 40 mA. The samples were scanned from 2 to 50° 2θ with a step of 0.01° and a step time of 30 s. Nitrogen adsorption measurements were performed on a Micromeritics ASAP 2010 having a 1000 mmHg transducer, using nitrogen adsorption at -196 °C for calculating the BET surface area.

Powder XRD patterns of ion-exchanged zeolite samples are shown in Figure 4.1. It was reported that the main diffraction peaks should appear approximately at 2θ of 6.31°, 10.31°, 12.10°, 15.92°, 20.71°, 24.06°, and 31.95°. It clearly reveals that all the zeolites were obtained in a pure and crystalline form[125]. The similarity in the XRD patterns of CoY, NiY, CuY, ZnY to the original NaY indicates that the original zeolite structure is retained without any significant change upon ion exchange treatment.
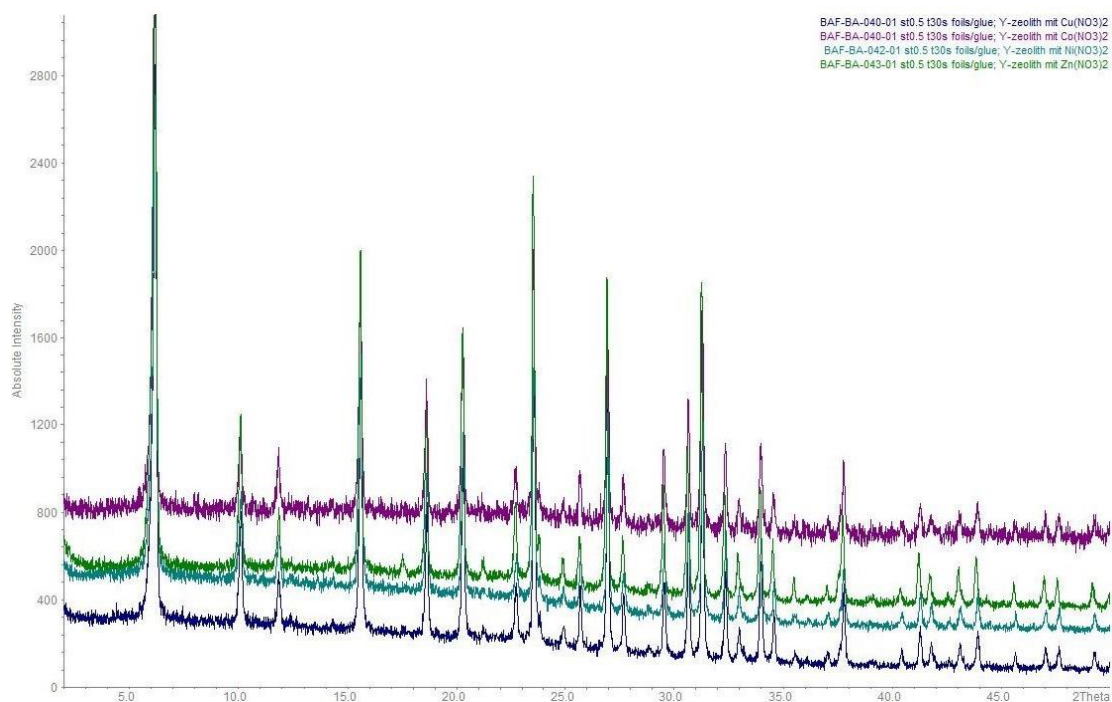
Figure 4.1 XRD patterns of (a) ZnY-zeolite, (b) NiY-zeolite, (c) CoY-zeolite, (d) NiY-zeolite (CuKα radiation). Provided by the group of Dr. W. N. Schmidt.

The synthesized ion-exchanged zeolite powders show distinct colors. The Co-exchanged zeolite has a pinkish color at the end of ion-exchange and calcination process. NiY-zeolite shows a light greenish color, while CuY-zeolite is in light blue color. In the case of Zn-exchanged adsorbent, the color remains white. The color behavior of the zeolites agrees with that reported in the literature[126-127].

The chemical compositions and physical properties of original and ion-exchanged zeolites are summarized in Table 4. 1. The molar ratio M^{n+}/Al^{3+}, where M^{n+} is the exchanged ion, indicates the number of ion exchange per ion-exchangeable site. In case of Co^{2+} exchange in CoY zeolite, if one Co^{2+} compensates for two aluminum tetrahedral sites, the ratio $2Co^{2+}/Al^{3+} = 0.77$

indicates the ion-exchange capacity achieved in the exchange with Co^{2+} are 77%. In the ion exchange with Ni^{2+}, Cu^{2+}, Zn^{2+}, and, Ag^+, the ion exchange results in 76 %, 91 %, 74 %, and 58%, respectively. Overall, high percentages of ion exchange were achieved in all materials.

Table 4.1 Chemical and physical properties of ion-exchanged Y-zeolites.

Zeolite	Chemical composition (wt%)			Molar ratios		BET area (m²/g)	Porous volume (cm³/g)	Pore radius (nm)
	Al	Si	M^{n+}	Na/Al	M^{n+}/Al			
NaY	10.85	27.01	/	1.02	/	624	0.41	0.67
CoY	10.84	26.77	9.12	0.28	0.77	712	0.27	0.64
NiY	10.85	27.01	8.96	0.29	0.76	611	0.26	0.65
CuY	10.14	25.27	10.87	0.25	0.91	478	0.20	0.57
ZnY	10.89	27.08	9.77	/	0.74	604	0.26	0.59
AgY	10.83	26.89	29.00	0.04	0.58	513	0.32	0.66

Both the BET area and pore volume decrease in all zeolites after the exchange of Na^+ by various cations. The mean pore radius is around 0.6 nm, regardless of the kind of metal and the amount of metal ion exchange.

4.2 TDS Results for Hydrogen Pure Gas

Five different ion-exchanged Y zeolites (CoY, NiY, CuY, ZnY, AgY zeolite) and the commerical NaY zeolite are used to investigate the relationship between the type of cation used and their separation performance for H_2/D_2. The ion-exchanged ratio of the corresponding zeolite (Co^{2+}, Ni^{2+}, Cu^{2+}, Zn^{2+}, Ag^+) is 77 %, 76 %, 91 %, 74 %, and 58%, respectively. Note that the BET area and pore volume remain similar regardless of the kind of metal and the amount of metal ion exchange.

Prior to the measurements, each ion-exchanged Y zeolite has been activated in the sample chamber of the TDS device under high vacuum (10^{-5} mbar) at 500 K for 2 h. Specific care has been taken for zeolite AgY: not to expose the sample to light, i.e., transfer in a darkroom. NaY, CoY, NiY, CuY, ZnY, and AgY zeolites have been exposed to a 10 mbar pure H_2 and pure D_2 gas atmosphere at room temperature. After cooling below 20 K, the unabsorbed gas molecules were evacuated, then the desorption spectra were recorded with a linear heating ramp of 0.1 K/s. The H_2 and D_2 spectra in the desorption temperature range of 17 – 170 K, collected from each sample, are shown in Figure 4.5.

The desorption spectra for all zeolites exhibit a desorption peak centered 45 K for hydrogen and 50 K for deuterium approximately. For zeolites NaY, CoY, NiY, CuY, and ZnY, only one maximum at low temperature with a shoulder at higher temperature appears in the corresponding desorption spectrum. In contrast, for zeolite AgY, a second distinct desorption peak in the high-temperature regime, with the maximum for H_2 at 82 K and for D_2 at 87 K, can be observed. Furthermore, for all zeolite samples, the D_2 spectrum is slightly shifted to higher temperature compared to that of H_2, indicating a higher D_2-surface interaction compared to H_2.

The area under the desorption curve is proportional to the adsorbed amount of molecules. Based on the calibration procedure shown in chapter 3.3, the adsorption amount can be quantitatively calculated. The original zeolite NaY shows an equal isotope uptake of 6.3 mmol/g for both H_2 and D_2. Among the ion-exchanged samples, the NiY, CuY, ZnY zeolites show a comparable adsorbed gas amount, 4.7, 4.8, 4.5 mmol/g for hydrogen, respectively. The corresponding adsorbed D_2 exceeds H_2 in all investigated samples. Note that the gas uptake of AgY which corresponds to 8.8 mmol/g of H_2 and 9.3 mmol/g of D_2, respectively, considerably exceeds that of the original zeolite NaY. The exceeding amount correlates with the additional high-temperature desorption peak an uptake of 3.0 mmol/g for both H_2 and D_2. The maximum temperature and the adsorbed gas amount in the individual samples have been summarized in Table 4. 2.
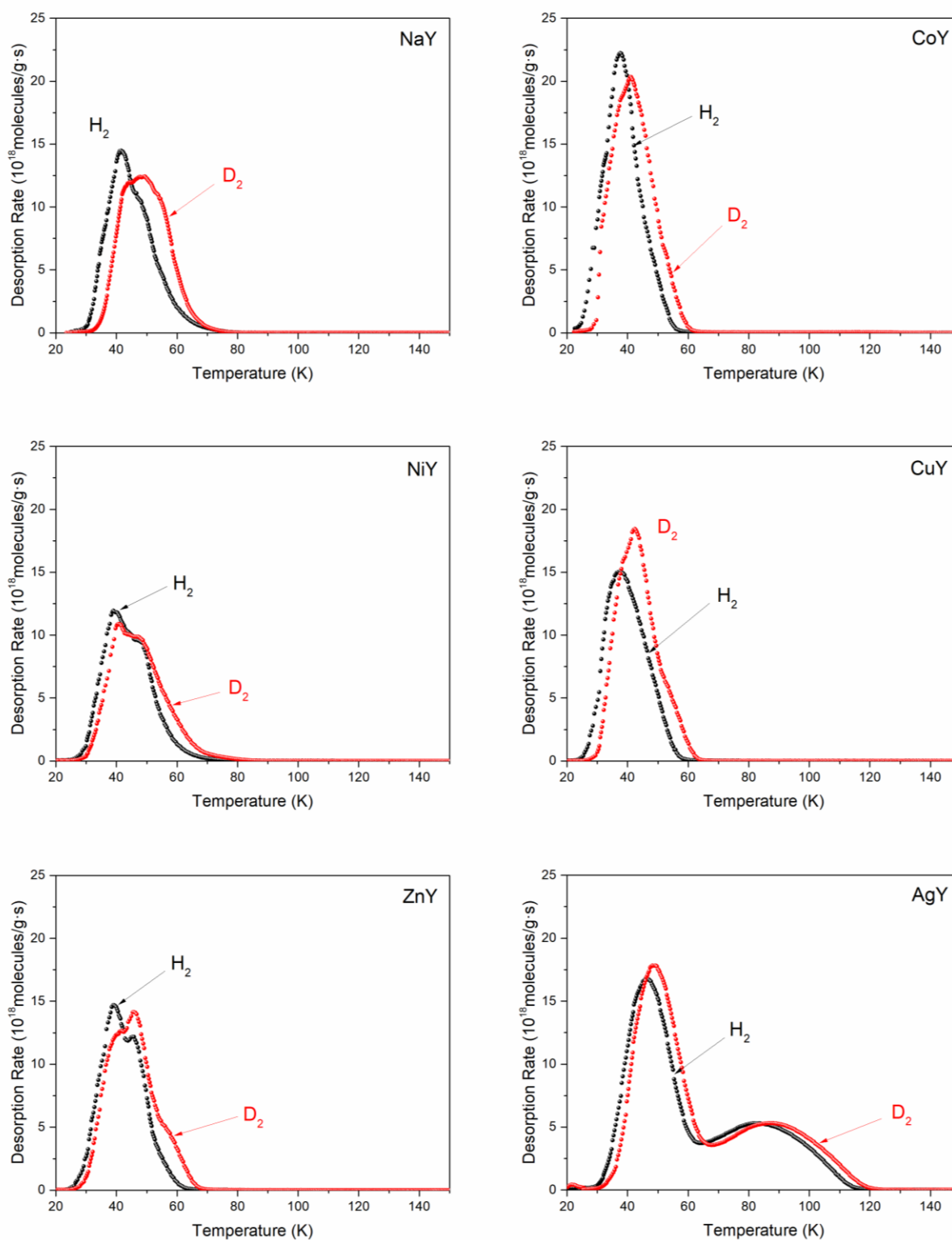
Figure 4.5 Thermal desorption spectra (TDS) of pure H_2 (black) and D_2 (red) gas from ion-exchange Na, Co, Ni, Cu, Zn, and Ag Y zeolites and exposed at 10 mbar and an exposure temperature of room temperature cooling to 20 K.

In addition, in the TDS measurements, a typical sequential filling from strong to weak adsorption sites can be observed. In other words, the molecules having strong interactions with the surface desorb at relatively high temperature, while molecules with weak interactions desorb at lower temperature. Thus, the two desorption maxima correspond to two different activation energies of desorption, indicating at least two energetically different adsorption sites in the framework of AgY zeolite, which possess different adsorption potentials, namely, the open metal site and the weaker adsorption sites in the supercages. However, the second desorption peak can be hardly observed in other ion-exchanged zeolites, and the low desorption temperatures indicates no strong open metal sites in these zeolites.

Considering the two distinct types of desorption spectra of hydrogen isotopes on ion-exchanged zeolites: two well separated desorption peaks centered around 45 and 85 K for zeolite AgY, and a single desorption peak with a maximum at approximately 45 K for other ion-exchanged zeolites (NaY, CoY, NiY, CuY, and ZnY), the main difference of ion-exchanged zeolites occurs at the temperatures above 60 K. Therefore, the ion-exchanged zeolites have been divided into two catagories to be investigated in this work, namely ion-exchanged zeolites i) NaY, CoY, NiY, CuY, and ZnY and ii) zeolite AgY.

Table 4.2 The total adsorbed gas amount and the temperature of the desorption maximum of the investigated ion-exchanged zeolites.

	Zeolites	**NaY**	**CoY**	**NiY**	**CuY**	**ZnY**	**AgY**
H$_2$	Uptake (mmol/g)	6.3	6.3	4.7	4.8	4.5	8.8 (3.0*)
	T$_{max}$ (K)	41.5	36.7	39.1	36.7	39.1	46.3 (81.9*)
D$_2$	Uptake (mmol/g)	6.3	6.9	4.9	5.3	4.9	9.3 (3.0*)
	T$_{max}$ (K)	48.9	39.5	40.9	42.7	41.3	48.8 (87.5*)

* The adsorbed isotope amount and the desorption maxima at open metal sites.

4.3 Influence of Cations in Zeolite Y on H_2/D_2 Separation
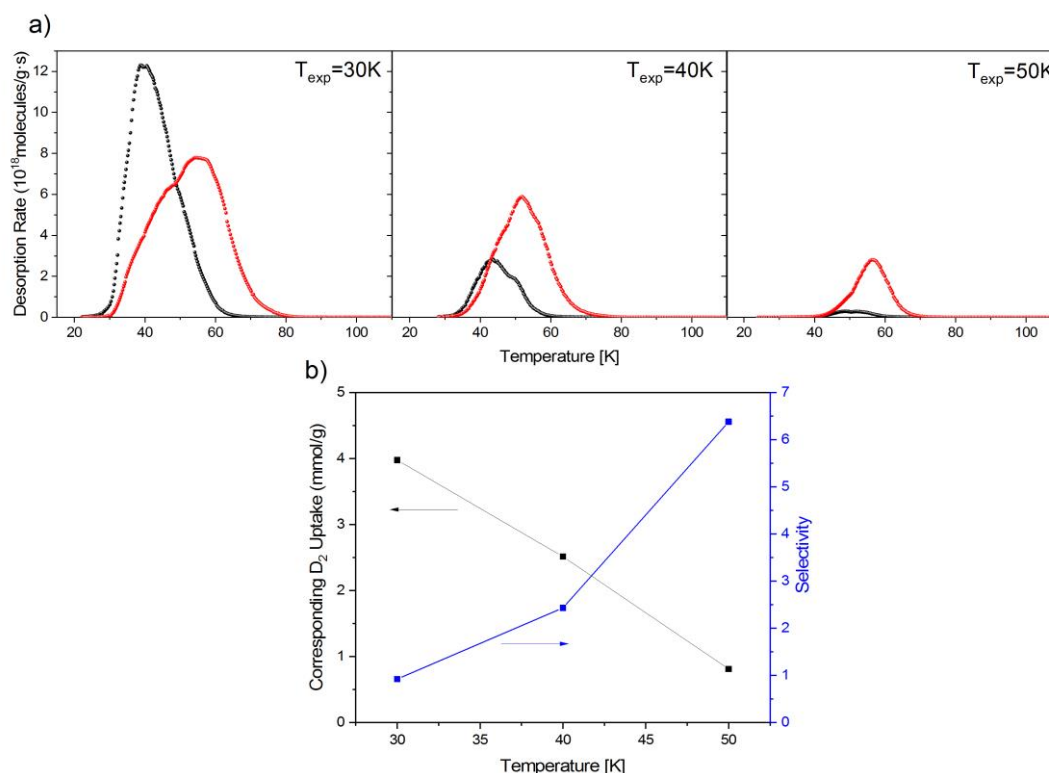

Figure 4.6 Original zeolite NaY a) H_2 (black) and D_2 (red) desorption spectra of 10 mbar 1:1 D_2/H_2 mixture exposure at exposure temperatures of 30, 40 and 50 K. b) D_2/H_2 selectivity (blue) and corresponding D_2 adsorbed amount (black) as function of exposure temperature.

The pristine sample, commercial zeolite NaY, was exposed to a 10 mbar equimolar D_2/H_2 isotope mixture at exposure temperature (T_{exp}) of 30 - 50 K. The H_2 and D_2 TDS spectra are presented in Figure 4.6a. The desorption peaks of H_2 and D_2 mainly occur below 60 and 80 K, respectively. Furthermore, the desorption temperature of D_2 is higher than that of H_2, indicating an enthalpy difference between D_2 and H_2 at the corresponding adsorption sites. The selectivity and the corresponding adsorbed D_2 uptake as a function of T_{exp} is shown in Figure 4.6b. The selecvitity rises from 0.9 to 6.5 with increasing T_{exp}, while the corresponding D_2 uptake drops from 4.0 to 0.8 mmol/g. One should note that zeolite NaY adsorbs slightly more H_2 than D_2 at 30 K.
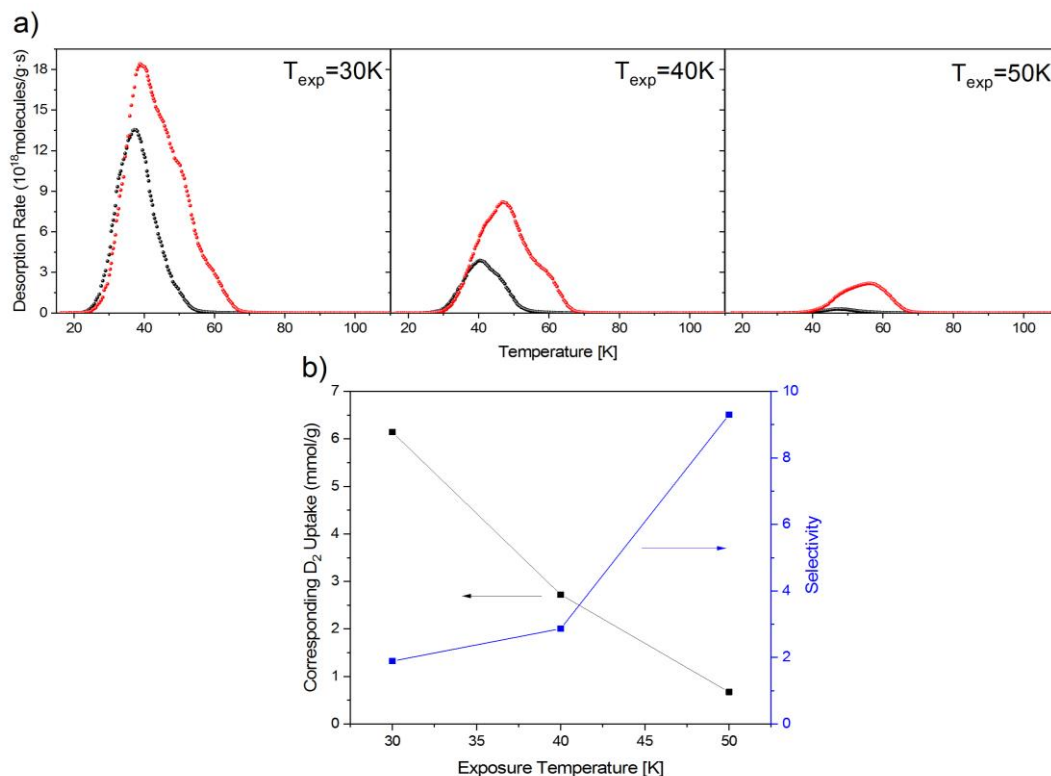
Figure 4.7 Zeolite ZnY a) H_2 (black) and D_2 (red) desorption spectra of 10 mbar 1:1 D_2/H_2 mixture exposure at exposure temperature of 30, 40, and 50 K for 10 min. b) D_2/H_2 selectivity (blue) and corresponding D_2 adsorbed amount (black) as function of exposure temperature.

As mentioned previously, the ion-exchanged sieves have been divided into two groups to study the correlation of the ions and separation performance based on direct equimolar isotope mixture measurements, namely, Ag and other transition metals. 10 mbar equimolar H_2/D_2 isotope mixture has been exposed on ion-exchanged zeolites CoY, NiY, CuY, and ZnY for 10 min at different exposure temperatures, 30, 40, and 50 K. For all samples, similar spectra have been recorded, indicating similar adsorption behavior. Thus, the TDS spectra and selectivity of zeolite ZnY have been shown as an example in Figure 4.7. All the other spectra for zeolites CoY, NiY and CuY have been included in Appendix A.

As shown in Figure 4.7, only one desorption maximum appears for both isotopes at all exposure temperatures. One should note that the maximum temperature as well as the ending temperature for D_2 desorption are much higher than that for H_2, demonstrating higher interaction of deuterium-surface/metal than hydrogen-surface/metal, which is similar to what has been observed in zeolite NaY prior to ion-exchange. In addition, the area under the desorption peak

51

of D_2 is much higher than H_2 in all the measurements. The selectivity calculated from the ratio of the areas under the curves of the isotopes and the corresponding adsorbed D_2 amount in zeolite ZnY have been shown in Figure 4.7b. The highest gas uptake appears after T_{exp} of 30 K and then decreases with increasing exposure temperature. However, the selectivity increases with exposure temperature, showing the highest value of 9.3 at 50 K, and has been enhanced compared with zeolite NaY ($S_{D2/H2} = 6.5$).

Figure 4.8 Zeolite ZnY a) H_2 (black) and D_2 (red) desorption spectra of 1:1 D_2/H_2 mixture exposure at exposure temperature of 30 K for 10 min for various exposure pressure. b) The adsorbed amount of isotope gases (H_2 black, D_2 red) and their total amount (blue) as function of exposure pressure. c) The D_2/H_2 selectivity as function of exposure pressure.

Furthermore, the influence of the exposure pressure (P_{exp}) on H_2/D_2 mixture separation has been studied by applying different exposure pressure (P_{exp}) of 5 to 60 mbar at low T_{exp} of 30 K on zeolite ZnY, shown in Figure 4.8a. Similar results are obtained for NiY and CuY, see Figure A4 and A5, respectively. The D_2 signal gets stronger with increasing P_{exp} while the H_2 signal gets weaker. The total amount of adsorbed isotopes remains approximately constant (average 9.0 mmol/g) for all the exposure pressures, see Figure 4.8b. Whereas, the desorbed D_2 amount is increasing while H_2 is decreasing with increasing P_{exp}, leading to an increased selectivity from 1 to 3 (Figure 4.8c). Since the total amount of H_2 and D_2 remains constant, this phenomenon indicates a partial exchange of H_2 by D_2 molecules.
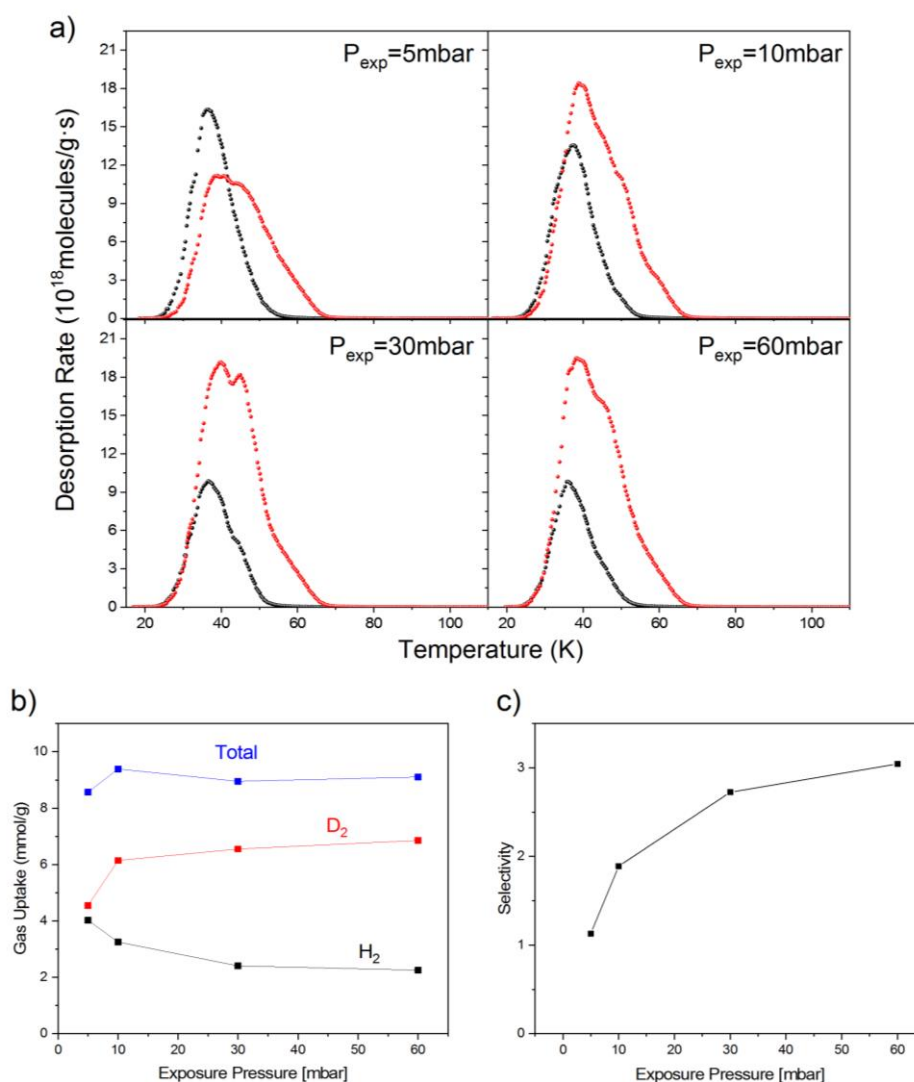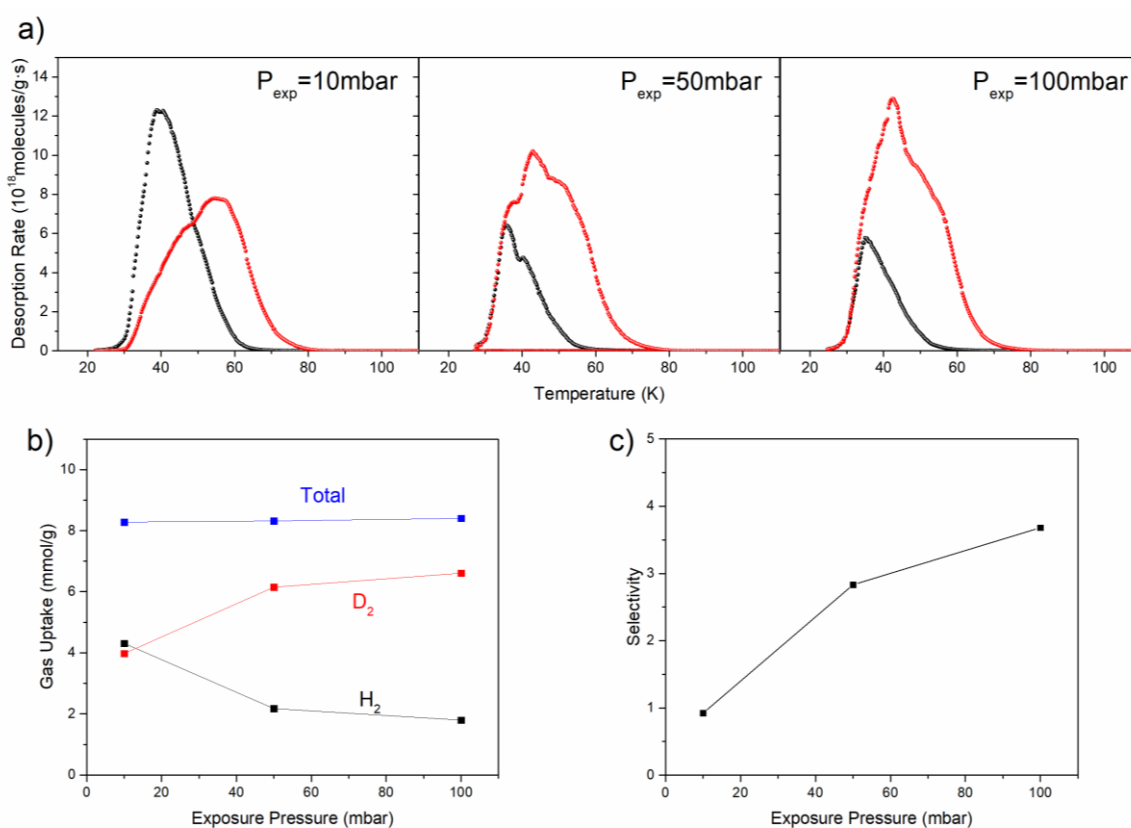

Figure 4.9 Zeolite NaY a) H_2 (black) and D_2 (red) desorption spectra of 1:1 D_2/H_2 mixture exposure at exposure temperature of 30 K for 10 min for various exposure pressure. b) The adsorbed amount of isotope gases (H_2 black, D_2 red) and their total amount (blue) as function of exposure pressure. c) The D_2/H_2 selectivity as function of exposure pressure.

Interestingly, the phenomenon has not only been observed in the transition metal ion-exchanged zeolites, but also in the pristine zeolite NaY. Figure 4.9 shows the D_2/H_2 selectivity is increasing

from 0.9 to 3.7 when the exposure pressure rises from 10 to 100 mbar. The slightly preferential uptake of H_2 at low exposure pressure reverses at higher exposure pressures, with a constant total gas uptake of 8.3 mmol/g, indicating an exchange of H_2 by D_2 with increasing pressure.

Figure 4.10a shows the H_2 and D_2 spectra obtained for various exposure times at (t_{exp}) at low T_{exp} of 30 K. The adsorbed amount of hydrogen isotopes remains approximately the same, 2.9 mmol/g for H_2 and 5.8 mmol/g for D_2, respectively, for all the exposure times, showing that an equilibrium uptake has already been reached after exposure for 10 min. The selectivity obtained from the TDS spectra is presented in Figure 4.10b and shows a constant value at 2 with longer t_{exp}, indicating no diffusion limitation in zeolite ZnY.
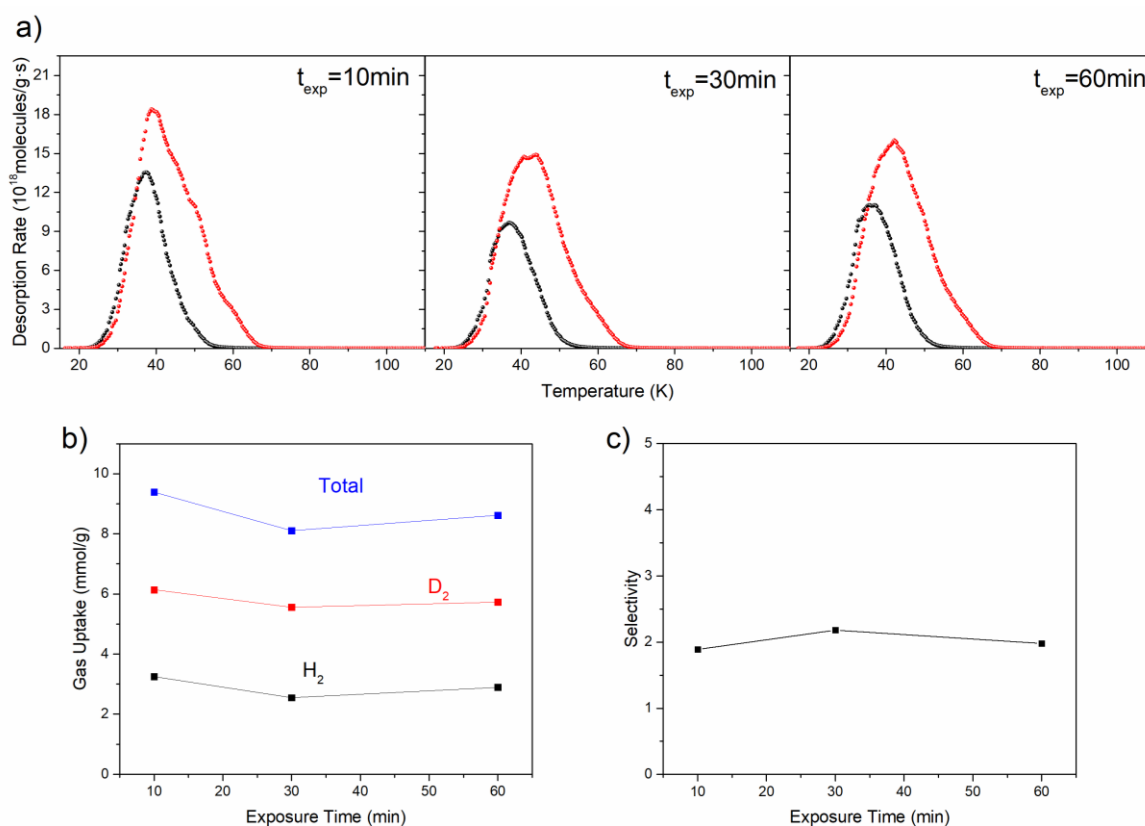

Figure 4.10 Zeolite ZnY a) H_2 (black) and D_2 (red) desorption spectra of 10 mbar 1:1 D_2/H_2 mixture exposure at exposure temperature of 30 K for various exposure time. b) The adsorbed amount of isotope gases (H_2 black, D_2 red) and their total amount (blue) as function of exposure time. c) The D_2/H_2 selectivity as function of exposure time.

4.4 Influence of Open-Metal-Sites in Zeolites on Hydrogen Isotope Separation

Even though the hydrogen isotope separation has been slightly enhanced by some transition metal exchanged in FAU type zeolite, almost all these examined porous sieves exhibit a low gas adsorption at higher temperatures. Hence, to achieve an efficient gas adsorption along with a good separation performance, open metal sites have been exploited in Ag(I)-Y zeolites.

As discussed above in Figure 4.5f, in order to identify the preferred adsorption sites and to estimate the adsorption strength at these sites on zeolite AgY, TDS measurements haven been performed for pure H_2 and D_2. The desorption spectra can be divided into a low-temperature regime with the maximum at 46 and 49 K for H_2 and D_2, respectively, and a high-temperature regime with the maximum for H_2 at 82 K and for D_2 at 88 K, indicating the existence of open metal sites. Typically, the open metal sites in porous materials, showing adsorption enthalpies higher than 10 kJ/mol, are expected to exhibit the strongest quantum sieving effect, as the difference of *ZPE* between adsorbed H_2 and D_2 molecules is the highest, therefore, high selectivity.
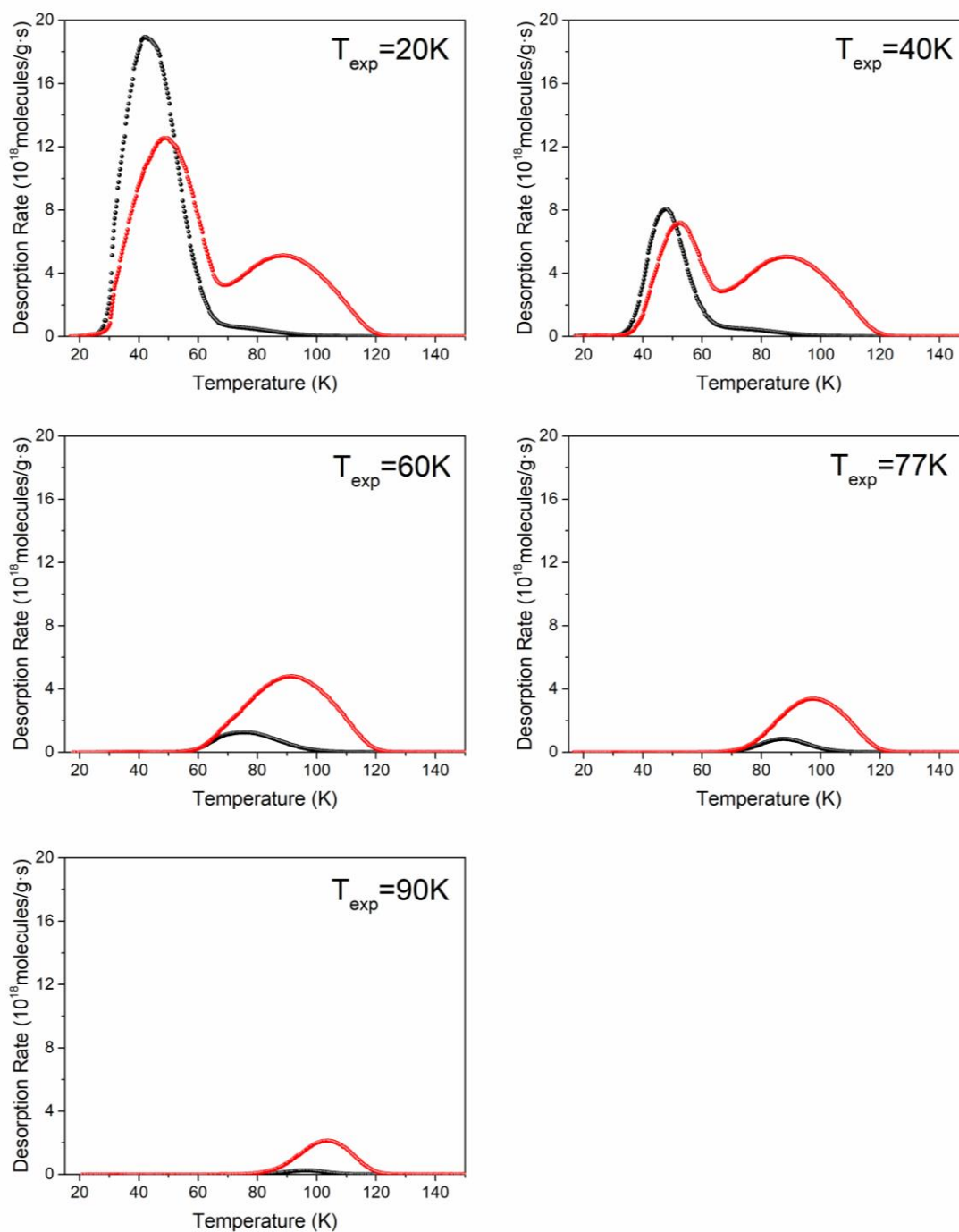
Figure 4.11 Zeolite AgY H_2 (black) and D_2 (red) desorption spectra of 10 mbar 1:1 D_2/H_2 mixture exposure at exposure temperature of 20, 40, 60, 77, and 90 K.

Thus, we further investigate the direct D_2/H_2 selectivity with TDS experiments. The sample was exposed to a 10 mbar equimolar hydrogen isotope mixture at T_{exp} of 25 - 90 K. One should

note that, the open metal sites have been reported as capable of hydrogen isotope exchange reactions. Thus, the D_2/H_2 mixture can be partially catalyzed to HD molecules at sufficiently high temperature, therefore the signal of m/z value 3 (HD) was monitored during the entire measurement. The value 3 intensity is negligible compared to the m/z values of 2 (H_2) and 4 (D_2) under our experimental conditions, i.e. exposure at temperatures below 100 K. The resulting H_2 and D_2 TDS spectra are presented in Figure 4.11 for different exposure temperatures. The desorption peaks of H_2 and D_2, which mainly occur below 60 K are attributed to the weak binding enthalpy of the adsorption sites in supercages, while the ones above 60 K are ascribed to the molecules desorbing from the stronger adsorption sites. When exposed to an equimolar mixture, the strong sites are predominately occupied by D_2, therefore, D_2 desorption curve is remarkably higher than that of H_2 counterpart, indicating a high D_2/H_2 selectivity at the open metal sites. Figure 4.12 shows the overall selectivity ($S_{D2/H2}$) and the corresponding amount of adsorbed D_2 as function of T_{exp}. It is obvious that $S_{D2/H2}$ is less than 2 at T_{exp} lower than 50 K due to the isotopes adsorption at weak and strong binding sites, whereas when T_{exp} is higher than 60 K, attributed to the strong binding sites, $S_{D2/H2}$ dramatically increases and reaches the highest of 10 at 90 K, while the adsorbed gas amount is still 1 mmol/g.
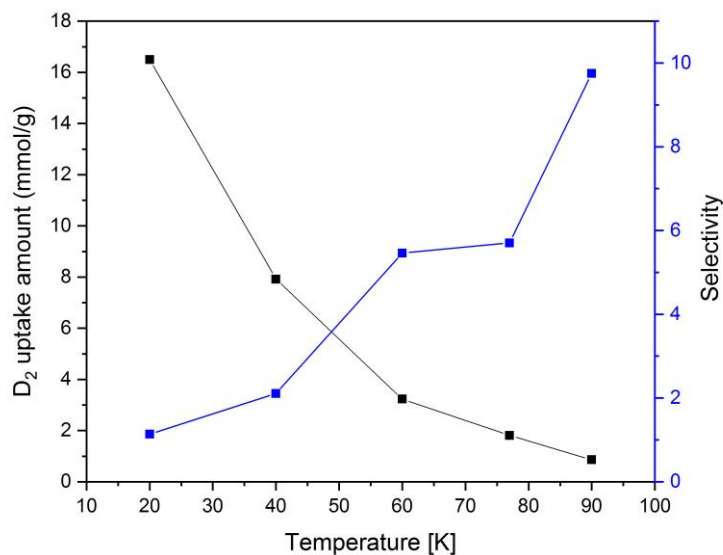

Figure 4.12 For zeolite AgY D_2/H_2 selectivity (blue) and corresponding D_2 adsorbed amount (black) as function of exposure temperature.
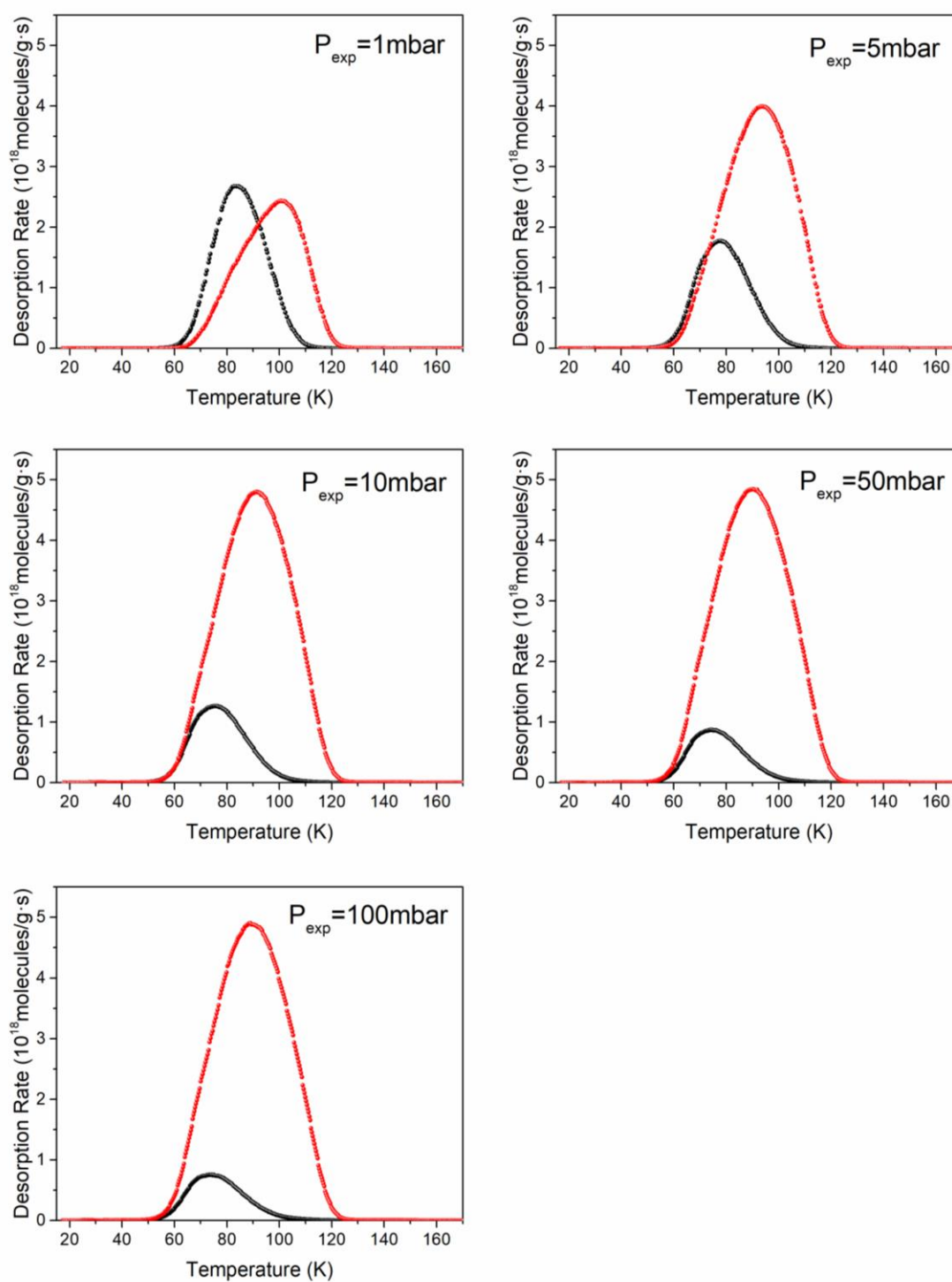
Figure 4.13 Zeolite AgY H_2 (black) and D_2 (red) desorption spectra of 1:1 D_2/H_2 mixture exposure at exposure temperature of 60 K for various exposure pressure (1, 5, 10, 50, and 100 mbar).

In order to observe the influence of exposure pressure on isotope separation, TDS spectra (see Figure 4.13) are collected after exposure to a 1 – 100 mbar equimolar D_2/H_2 mixture for 10 min at the exposure temperature of 60 K, at which only open metal sites remain occupied. At low P_{exp}, the adsorbed amount of H_2 and D_2 is nearly identical. As P_{exp} increases from 1 to 100 mbar, the selectivity increases dramatically from 1 to 9, meanwhile the corresponding adsorbed D_2 amount is enhanced from 1.4 to 2.8 mmol/g, see Figure 4.14. Interestingly, the number of adsorbed molecules of isotope gases remains constant when P_{exp} reaching 10 mbar, indicating the surface coverage, in other words, the occupied adsorption sites remains the same during adsorption processes. For higher exposure pressure than 10 mbar, the ration between D_2 and H_2 increases, ascribing to an exchange of H_2 by D_2, which enables an equilibrium distribution between the two hydrogen isotopes.

Figure 4.14 a) The adsorbed amount of isotope gases (H_2 black, D_2 red) and their total amount (blue) as function of exposure pressure obtained at T_{exp} of 60 K. b) The D_2/H_2 selectivity as function of exposure pressure.

The sample of zeolite AgY also has been exposed to a 10 mbar 1:1 H_2/D_2 mixture for different exposure times (1–120min) and pressures at a fixed exposure temperature of 60 K. Figure 4.15 shows the TDS spectra, and Figure 4.19 presents the uptake amount of the isotope gases and the D_2/H_2 selectivity as function of exposure time. After exposed to the equimolar isotope mixture, the desorption spectra of both isotopes exhibit one single desorption maximum. The maximum of this desorption peak shifts from 76.7 to 75.4 K for H_2 with increasing exposure

time, while fro, 93.2 to 91.1 for D_2. The adsorbed amount of H_2 decreases with increasing time, while that of D_2 increases. As shown in Figure 4.16a, the total gas adsorbed remains nearly constant of 3.2 mmol/g, while the selectivity rises from 3.9 to 6.3.
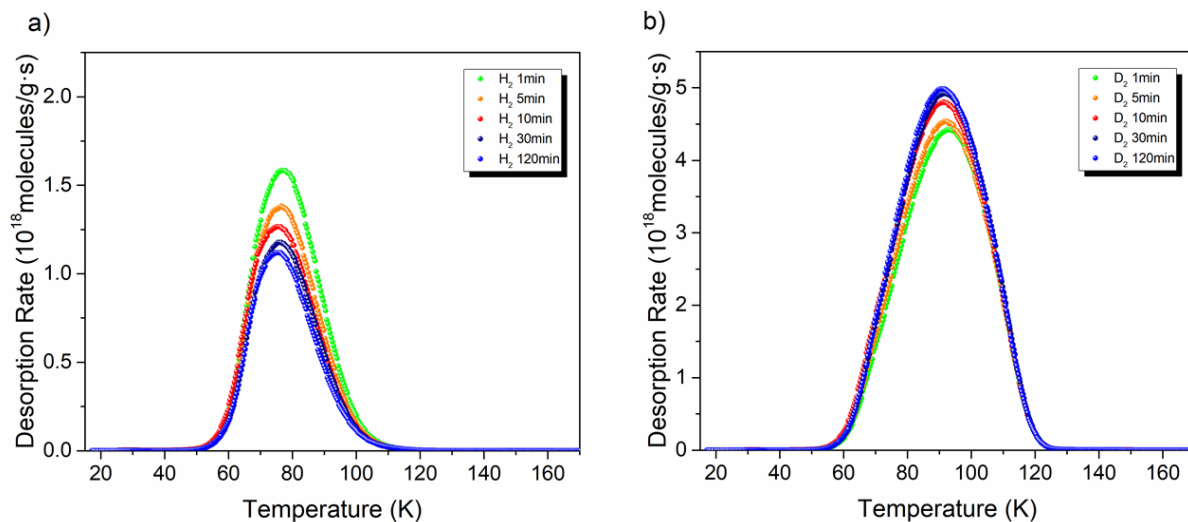
Figure 4.15 a) Hydrogen and b) deuterium desorption spectra of a 10 mbar 1:1 D_2/H_2 mixture exposure on zeolite AgY at exposure temperature of 60 K for various exposure time, 1 (green), 5 (orange), 10 (red), 30 (navy), and 120 (blue) min.
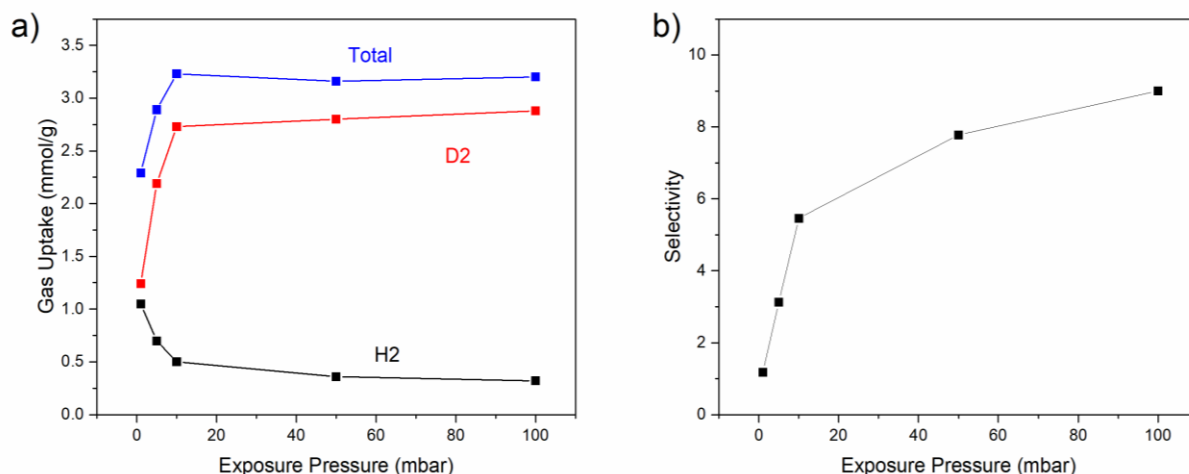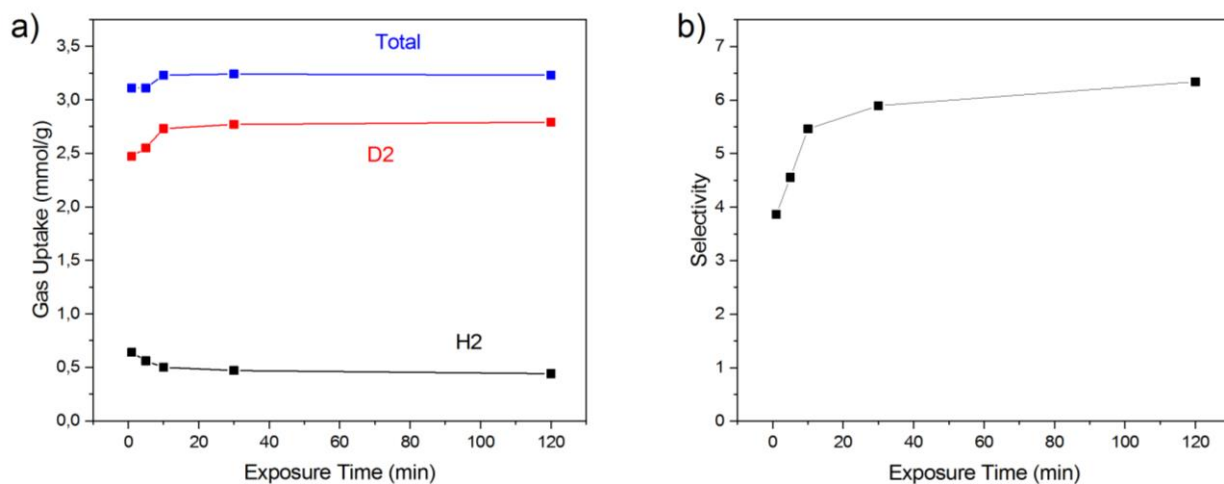

Figure 4.16 a) The adsorbed amount of isotope gases (H_2 black, D_2 red) and their total amount (blue) as function of exposure time obtained at T_{exp} of 60 K. b) The D_2/H_2 selectivity as function of exposure time.
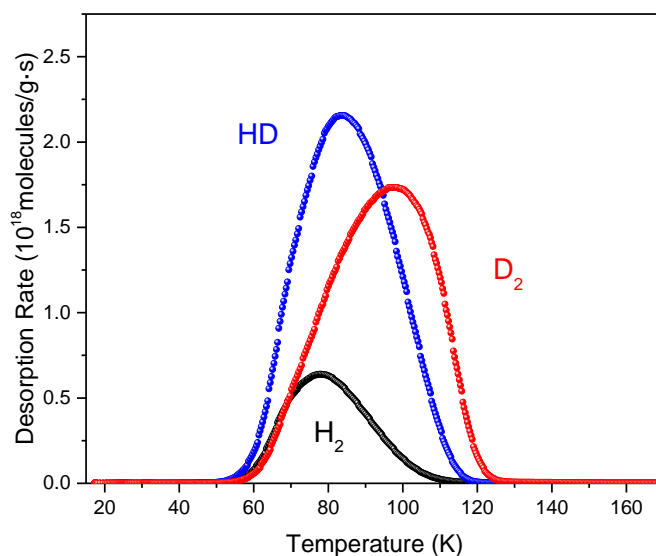
Figure 4.17 H_2 HD, and D_2 desorption spectra of 10 mbar 1: 3.5: 11 D_2/HD/H_2 mixture exposure on zeolite AgY at T_{exp} of 60 K for 10 min.

Motivated by the enhanced selectivity, the separation of D_2/HD/H_2 mixture has been experimentally investigated. Since deuterium mainly occurs natually in Earth's ocean, it is extracted for industrial by starting with heavy water. After electrolysis of the enriched heavy water, the final production can be a mixture of not only H_2 and D_2, but HD as well. Therefore, the D_2 enrichment process could be applied to exposure to the three hydrogen isotopologue mixture. The D_2 selectivity is directly measured by TDS measurement. Figure 4.17 shows H_2, HD, and D_2 spectra of zeolite AgY after exposure to a 10 mbar 1/3.5/1 D_2/HD/H_2 isotope mixture at T_{exp} of 60 K. The desorption spectra exhibit the maximum of 80 K for H_2, 82 K for HD, and 100 K for D_2. The D_2 spectrum is shifted to much higher temperature compared to that of H_2 and HD, indicating a stronger binding energy between the molecules and the host surface. The selectivity of D_2 over HD exhibits a value of 3.3, considering the smaller difference in *ZPE* of D_2 and HD compared to that of D_2 and H_2, due to a smaller mass difference.

4.5 Discussion

4.5.1 Hydrogen adsorption in ion-exchanged Zeolite Y

The H_2 desorption peaks, occurring approximately at 45 K, are present for commercial zeolite NaY and all the ion-exchanged zeolites (Na, Co, Ni, Cu, Zn, and Ag), as shown in Figure 4.5. Meanwhile, two well separated desorption maxima can be observed only in zeolite AgY, corresponding to different desoption energies. The presence of the second desorption peak clearly shows additional adsorption sites, possessing stronger adsorption potentials that exist in zeolite AgY for hydrogen.

The hydrogen adsorption properties of zeolites are known to depend on the framework structure, composition, and the acidic-basic nature of zeolites[128-130]. Two types of interaction mode are reported for hydrogen on cationic zeolites[131]. The first mode is related to a strong electrostatic interaction of the adsorbed H_2 molecules with the exposed metal-cation centers which act as the favored gas adsorption sites, resulting in polarization of the adsorbed molecules[132-134]. In addition, the basic oxygen of the zeolite framework has also been reported a minor contribution to the interaction with hydrogen[128, 132]. The other adsorption mode, which refers to delocalized adsorption, involves the filling of the zeolite pores, which takes place once all the cation sites are saturated.
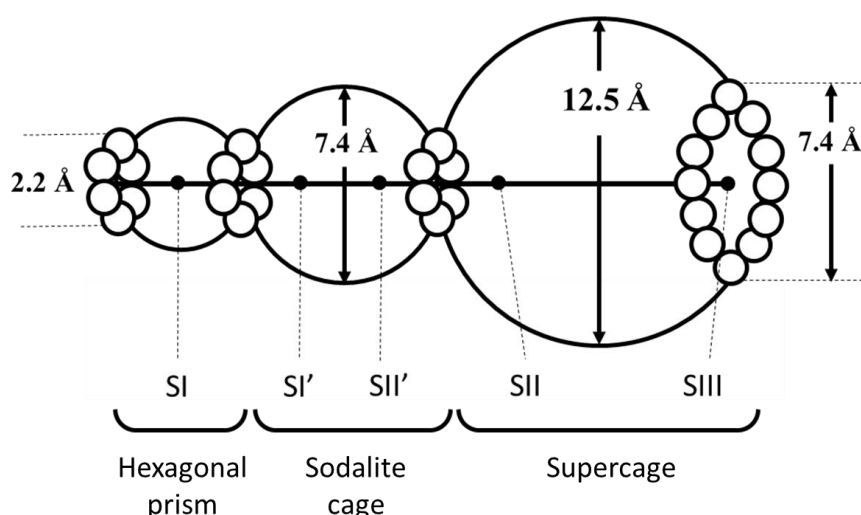
Figure 4.18 The adsorption sites for non-framework atoms in zeolite Y.

As presented in Figure 4.18, four distinct pore adsorption sites have been reported in faujasite - type zeolite $Y^{29, 135}$: site I', the most stable site inside sodalite cage; site II in the supercage on the hexagonal prism, and III and III' in the supercage. However, in the case of sodium distribution in supercages of zeolite Y, the molecular hydrogen adsorbed on exchanged cations in zeolites results in formation of 'T-shape' adsorption complex, due to its quadrupole moment[136-138]. According to the precise XRD and inelastic neutron scattering data[139-141], the sodium ions mainly occupy site II, while site III is partially occupied or remains free[133]. The calculated adsorption energies are reported to decrease in the sequence of III > I' > II[135]. Site I' is not taken into consideration in our case due to the inaccessible aperture of the sodalite cage (2.2 Å), unless some defects allow access to hydrogen molecules.
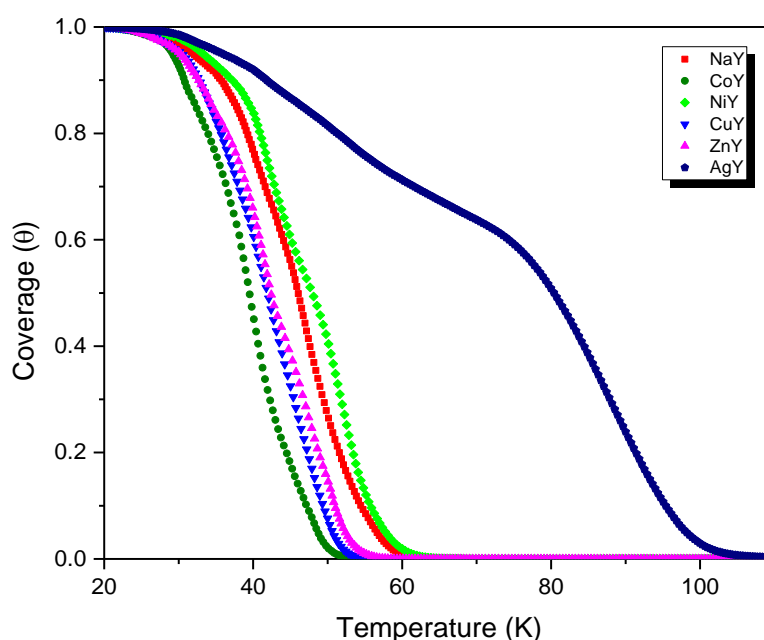
Figure 4.19 Coverage of hydrogen adsorbed on zeolite Y with different ions as function of desorption temperature.

In general, a sharp desorption peak indicates the molecules are adsorbed on the surfaces with similar energies. The broad peaks observed in these zeolites can be ascribed to the overlap of different desorption peaks from different interaction energies between the adsorbed molecules and the surfaces. Considering this order of energies, the hydrogen desorption peak observed in

all zeolites at 45 K which correspond to low adsorption energy can be assigned to pore filling and the adsorption on II sites in all tested ion-exchanged zeolites Y (Co, Ni, Cu, and Zn). Meanwhile, the desorption peak observed at 80 K in zeolite AgY indicates that the hydrogen molecules adsorb on site III.

In addition, the samples possess very similar specific surface area of 478-712 m^2/g measured with N_2 gas, shown in Table 4.2, corresponding to the reported values from various ion-exchanged FAU zeolites. However, the hydrogen uptake investigated by TDS shows no correlation with the surface area for different exchanged cations (Figure 4.5). The experimental results can be explained as follows: Considering the pore filling mode, the hydrogen uptake in zeolites is related to the available void volume of zeolite which decreases with the increasing size and number of the exchanged cations. However, as zeolite Y has a rather open structure, it is unlikely the cationic pore blocking effect will affect the hydrogen uptake observed. It is possible that a small amount of structural imperfection, which cannot be detected by XRD, may be responsible for this uptake variation[142-143].

A comparison among the desorption behaviors of ion-changed zeolites is presented in Figure 4.19, showing the relation between the surface coverage (θ) as a function of desorption temperature. At temperatures lower than 30 K the desorption behaviour of hydrogen is similar for all the ion-exchanged zeolites (Na, Co, Ni, Cu, Zn, and Ag). The low desorption temperatures can be attributed to the weakly adsorption in the pores of the zeolites. The voids of zeolite Y are large enough that the size of cations can be neglected. Therefore the interaction of hydrogen inside pores is almost equal for all six samples. The isosteric heat of adsorption for the pore filling mode has been reported to be in the range of 4.5 – 5.5 kJ/mol in zeolite Y[131]. For desorption temperatures in the range of 30 and 60 K, the adsorption energy is highly related to the cations exchanges on site II, which is different for ion exchanged zeolites. The coverage of hydrogen decreases with the increasing temperature in the following order: from the lowest Co, Cu and Zn, Na, Ni, to the highest Ag. The higher desorption temperature indicates a stronger interaction with H_2 molecules adsorbed on the cations. At a temperature of 60 K, all hydrogen is desorbed from zeolite Na, Co, Ni, Cu, and Zn. At higher temperatures, hydrogen molecules remain adsorbed on the open metal sites in zeolite AgY, revealing a much higher adsorption energy.

4.5.2 Separation of hydrogen isotopes on exchange ions

As discussed above, the adsorption capacity varies with the pore voids as well as density and distribution of different exchange cations. However, the surface area is not a crucial factor for hydrogen isotope separation, but the pore structure and cations in zeolites[144-146]. As shown in Figure 4.7 and Appendix A, for all investigated zeolites (Co^{2+}, Ni^{2+}, Cu^{2+}, and Zn^{2+}), the desorption spectra of H_2 and D_2 from exposure of 30 K mainly takes place in the temperature range between 25 and 50 K for H_2, and between 20 and 70 K for D_2, respectively. This low temperature is attributed to the weak binding enthalpy of the weaker adsorption sites. The desorption spectra exhibit a single hydrogen desorption peak at approximately 35 K which is independent from the exchanged cations. The D_2 desorption spectra show either two desorption peaks centered at 42 and 50 K in zeolite NiY or one desorption peak at 42 K along with an additional shoulder around 50 K for all others. The presence of the two desorption maxima clearly shows that at least two adsorption sites, possessing different adsorption energy, exist for deuterium. As shown in the previous section, these ion-exchanged zeolites possesses two different desorption energies: pore filling and site II. The desorption peak at 42 K therefore corresponds to the adsorption on cations sitting at site II. Since the desorption spectra of H_2 ends approximately at 50 K, whereas D_2 desorbs up to 70 K, indicating a preferential adsorption of deuterium on the stronger adsorption sites. When the exposure temperature increases, the gas uptake decrease, while the selectivity of D_2 over H_2 increases, reaching the maximum at T_{exp} = 50 K. Note that all the hydrogen and deuterium desorption start close to the T_{exp} since all the non-adsorbed gas molecules are evacuated at this temperature. Only site II contributes to the adsorption of hydrogen isotopes at exposure temperature of 50 K. D_2 predominately occupies these sites and therefore only a D_2 desorption curve can be observed, resulting in an increasing selectivity. Therefore, the heat of adsorption of D_2 on ion-exchanged zeolites is larger than that of H_2. However, it is difficult to estimate this activation energy of desorption from TDS, due to the weak interaction between the adsorbate and adsorbent.

4.5.3 The Influence of Open Metal (Ag$^+$) Sites

Separation of hydrogen isotopes on open metal sites

The D_2/H_2 selectivity of zeolite AgY in equimolar isotope mixture is directly measured in TDS experiments. The resulting TDS spectra for H_2 and D_2 after an exposure to 10 mbar of a 1:1 H_2/D_2 mixture at T_{exp} of 20 K to 90 K are shown in Figure 4.11. All the desorption spectra start closely to the exposure temperature due to the release of the weakly binded molecules during the evacuation process carried out at the same temperature. At exposure temperature lower than 40 K, two desorption maxima can be observed indicating at least two adsorption site with different binding enthalpies. As discussed in previous section, the first desorption maximum below 60 K is corresponding to the pore filling and adsorption on sites II simultaneously, since the binding enthalpies of H_2 and D_2 are rather weak. The second maximum observed at higher desorption temperatures above 60 K implies higher enthalpy at strong adsorption sites (unsaturated Ag located at site III), at which D_2 molecules predominantly occupy as necessary for chemical affinity sieving. TDS experiments also show a high $S_{D2/H2}$ at high exposure temperature, $T_{exp} \geq 60$ K, see Figure 4.12. The selectivity as function of exposure temperature clearly shows that $S_{D2/H2}$ at $T_{exp} \leq 40$ K is less than 2 due to the little difference between D_2 and H_2 adsorption enthalpies at weak binding sites, whereas $S_{D2/H2}$ at $T_{exp} \geq 60$ K, thus governed by the strong binding sites, increases dramatically and reaches the highest values of 10 at $T_{exp} = 90$ K. Even though the uptake is greatly reduced with increasing temperature, the adsorbed amount of D_2 still gets close to 1 mmol/g, it is one of the best combination of selectivity and adsorption above liquid nitrogen temperature making it an interesting material for practical isotope separation application. For comparison, CPO-27-Co, which is reported by Oh et al.[147], exhibits a selectivity of 6 at liquid nitrogen temperature, combined with D_2 uptake of 1 mmol/g.. Moreover, the study on MFU-4*l*-Cu from Weinrauch et al.[148] can also be mentioned, since the selectivity of 11 has been reported at T_{exp} of 100 K.

Desorption energy of the open metal sites

The desorption energy is determined by applying the Kissinger method to thermal desorption spectra. This method is based on the assumption that the adsorption and desorption are reversible processes, and the desorption energy is independent of the coverage or temperature. The desorption energy for H_2 and D_2 for zeolite AgY was measured directly from TDS of the

hydrogen isotopologue mixture at exposure temperature of 60 K. Different heating rates of 0.1, 0.05, and 0.01 K/s have been applied, the resulting TDS spectra are shown in Figure 4.20. The desorption maximum is shifted to lower temperatures for slower heating rate, indicating the released isotopes are thermally activated. The obtained desorption energies at silver sites for H_2 and D_2 are 6.0 and 8.5 kJ/mol, respectively, which are in good agreement with the TDS measurements. The heavier isotope has a higher desorption energy, higher D_2 desorption maximum can be therefore expected and thus a high selectivity.
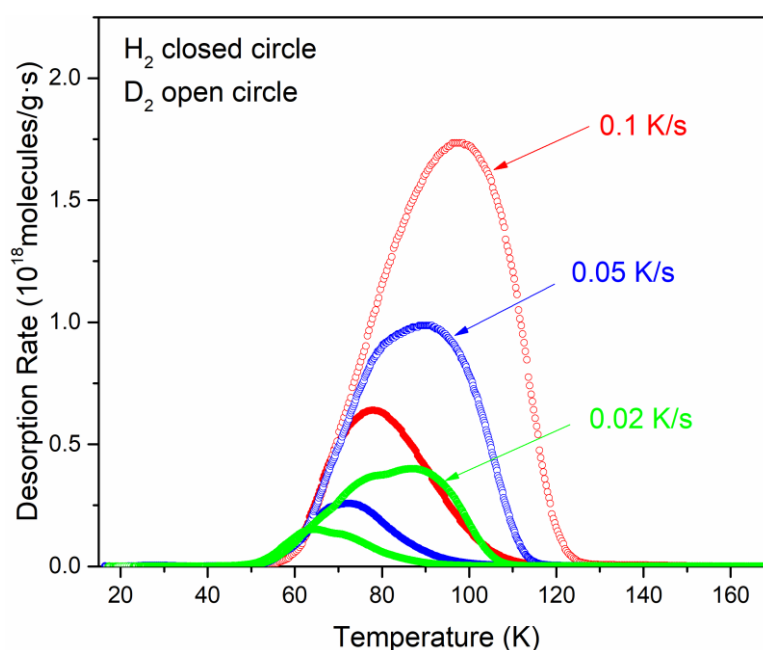
Figure 4.20 H_2 (closed circle) and D_2 (open circle) TDS spectra recorded for zeolite AgY at the exposure temperature of 60 K which has been loaded with a 10 mbar equimolar isotope mixture for 10 min, with different heating rates: 0.1 (red), 0.05 (blue), 0.02 (green) K/s.

Isotope exchange on metal-cation sites

The TDS spectra of zeolite AgY collected after exposure at different pressures 1-100 mbar to an equimolar D_2/H_2 mixture for 10 min at the exposure temperature of 60 K are shown in Figure 4.13. At $P_{exp} = 1$ mbar, the D_2/H_2 selectivity is close to 1 (Figure 4.14), where the D_2 and H_2 are equally adsorbed on the open metal sites, since at the given temperature of 60 K, only strong adsorption sites can be occupied by gas molecules. This clearly shows the comparable number of open metal sites to a consequently very small gas loading, thus, D_2 and H_2 can simultaneously occupy the empty strong sites without competition. For higher exposure pressure $P_{exp} \geq 5$ mbar,

the area under the D_2 desorption curve is remarkably higher than that of H_2, indicating the preferential occupation of open metal sites by D_2, resulting in high selectivity. In addition, the adsorbed gas amount is increased with higher exposure pressure. As P_{exp} increases from 1 to 10 mbar, the total adsorbed amount of the isotope gases increase from 2.2 to 3.4 mmol/g, and then stays constant with increasing P_{exp}. Interestingly, the selectivity is still increasing after the P_{exp} reaches 10 mbar, even the total uptake remains constant. This can be explained as follows: with a loading of 10 mbar, the isotope gas molecules are sufficient to occupy all the open metal sites available. Thus, for a loading with higher pressure on the fixed number of open metal sites, the D_2 is more favorably adsorbed and will replace the adsorbed H_2 with higher exposure pressure. Moreover, for longer exposure times at a fixed exposure pressure of 10 mbar, the intensity of D_2 desorption peak is increasing while that of H_2 is decreasing, leading to a rise in selectivity, but the total gas uptake remains constant (Figure 4.16), implying fully occupied of the open metal sites.

The highest adsorbed gas amount is 3.25 mmol/g for both measurements either with long exposure time at lower pressure (10 mbar, 120 min) or with the high pressure at shorter time (100 mbar, 10 min), denoting that all the accessible adsorption sites at 60 K are fully occupied and the largest adsorbed number of gas molecules is therefore equal to the existing Ag sites. Since the adsorbed D_2 amount is increasing, while H_2 is decreasing, but the total adsorbed molecules is independent from exposure time or pressure, the replacement of H_2 by D_2 can be clearly observed on open metal sites, resulting in an increasing selectivity.

For comparison, the isotope-exchange during the exposure times has been studied in this work on another porous materials possessing open metal sites MFU-4*l*-Cu(I). This MOF was synthesized by the group of Prof. Dr. D. Volkmer based on the metal-organic-framework MFU-4*l*, approximately 30% of the Zn (II)-Cl units are postsynthetically replaced by Cu (I) ions[148]. The unsaturated Cu (I) sites exhibit the highest heat of adsorption for H_2 molecules so far, leading to the largest difference in zero point energies of hydrogen isotopes. A clear correlation between the selectivity and exposure time observed, presented in Figure 4.21. At the fully occupied (1.5 mmol/g) strong binding Cu (I) sites, a time-dependent isotope exchange process can be observed. It means, that heavier isotopes are preferentially adsorbed and can substitute adsorbed molecules of those lighter ones over time, even though the adsorption sites are initially occupied by an isotope mixture of ratio 1:1. The highest D_2/H_2 separation factor can be achieved

after the isotope exchange occurred and an equilibrium state of the Cu (I) sites is reached for the occupation by H_2 and D_2 molecules.
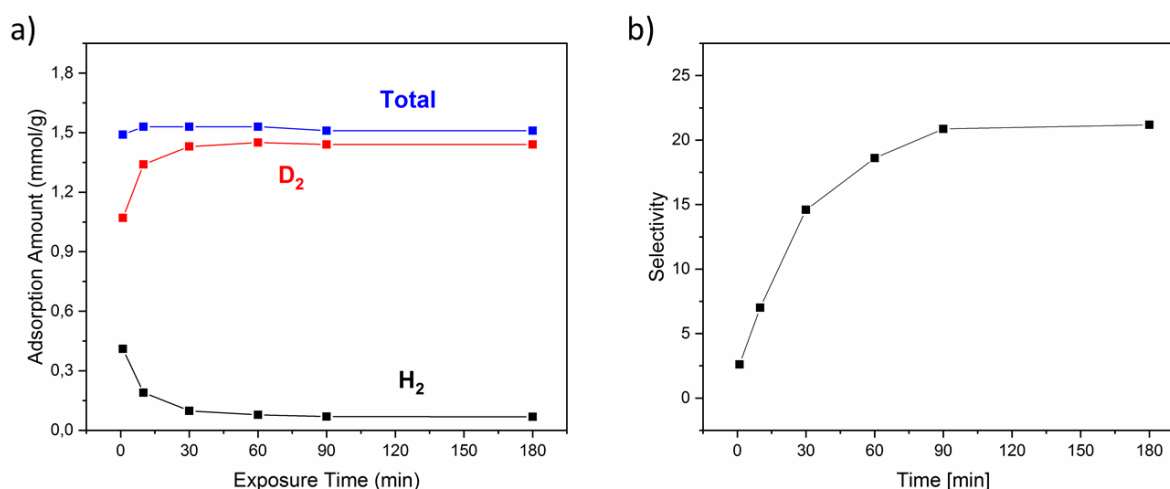
Figure 4.21 a) The adsorbed amount of isotope gases (H_2 black, D_2 red) and their total amount (blue) as function of exposure pressure for MFU-4*l*-Cu(I) exposed to a 1:1 H_2/D_2 mixture at 90 K for various exposure time. b) The D_2/H_2 selectivity as function of exposure time.

4.6 Summary

A series of ion-exchanged zeolite Y has been investigated for hydrogen isotope separation. Five different transition metal cations have been compared: Co (II), Ni (II), Cu (II), Ni (II), and Ag (I). The separation and adsorption performance can be slightly enhanced in all the ion-exchange zeolites due to their higher adsorption enthalpies and small cation volume, which leads to larger voids of the structure. Among all the cations investigated, the unsaturated Ag^+, as strong binding site, shows the preferential adsorption of the heavier isotope even at temperatures above liquid nitrogen temperature. In contrast, no such strong adsorption site has been found in other transition metal cation-exchanged zeolites.

In ion-exchanged zeolite Y without open metal sites (Co^{2+}, Ni^{2+}, Cu^{2+}, and Ni^{2+}), two different adsorption sites possessing different adsorption enthalpy were observed. All hydrogen molecules desorbed from the material at 50 K, due to the small adsorption enthalpy of pore filling, while deuterium molecules desorbed till 70 K, corresponding to a stronger site II in

supercages. Therefore, the D_2 over H_2 selectivity was increased with higher exposure temperature and pressure in all cases, reaching the maximum at 50 K. However, the gas uptakes dropped dramatically with increasing temperature.

In contrary, a clearly stronger adsorption site was observed in zeolite AgY. The desorption spectra showed a desorption maximum for H_2 and D_2 at 82 and 88 K, respectively, which can be ascribed to unsaturated Ag sites. On the open metal site, a large difference in *ZPE* between the two isotopes can be expected and therefore the heavier D_2 molecules were adsorbed stronger. At these strong binding sites, the separation of heavier isotopes from the gas phase is pronounced at temperatures above 77 K. The D_2/H_2 selectivity increased with higher exposure temperature, and the highest number of 10 is achieved at 90 K. In addition, the selectivity increases with longer exposure time and higher exposure pressure, revealing an isotope-exchange process. Moreover, the gas uptake on the strong adsorption sites makes up approximately 1/3 of the total physisorbed amount, due to a high density of unsaturated Ag sites contributed by the high concentration of active acid sites in zeolite Y. The combination of high selectivity and gas uptake makes zeolite AgY a promising candidate for practical applications. For the first time, the separation of D_2 from H_2 and HD has been performed since the final product from the industrial production is a mixture of the three isotopes. The desorption spectra exhibit maxima temperatures of 80 K for H_2, 82 K for HD, and 100 K for D_2, and such high desorption temperature leads to a selectivity of D_2 over HD with a value of 3.3.

5. Hydrogen Isotope Separation in Porous Organic Cages

Quantum sieving in nanopores emerges one promising avenue to separate H_2/D_2 isotope efficiently and effectively. When isotopes are adsorbed in a framework under cryogenic conditions, where the difference between the molecular size and the pore size becomes comparable to the de Broglie wavelength, the heavier isotope is more favorably adsorbed and can diffuse faster compared with respect to the lighter one. Thus, to optimize the pore aperture size plays a fundamental role in effective and efficient quantum sieving. Many experimental investigations concerning quantum sieving have been carried out on porous materials, such as MOFs and COFs, possessing a uniform and well-defined pore structure. Despite of the highly tunable properties of the pore structure in MOFs and COFs, it is not feasible to systematically tune the pore size. Moreover, the very small pores for efficient separation and the large inner surface for sufficient adsorption are often the two sides of the coin, which cannot be fulfilled at the same time. Porous organic cages (POCs), an emerging porous material with designable functionality, tunable pore size and good processibility, are one the most promising candidates for effective quantum cryo-sieving, since their pore apertures can be tuned precisely, even at atomic level.

In this chapter, POCs with different pore apertures have been studied by various techniques such as powder X-ray diffraction, low-pressure hydrogen and nitrogen BET and cryogenic thermal desorption spectroscopy. The kinetic quantum sieving has been experimentally observed and the hydrogen isotope separation is further enhanced by combining both high selectivity and high gas capacity within a single solid. This combination of improved gas capacity and high D_2/H_2 selectivity in POCs can be a huge step towards practical applications.

5.1 Influence of Pore Apertures in POCs on Hydrogen Isotope Separation

Three different organic cages (**CC3**, **6FT-RCC3**, and **6ET-RCC3**) have been selected for studying the H_2 isotopes adsorption and the quantum sieving effect. Pore size envelope analysis

suggests that the diameters of the pore aperture are around 4.5 Å, 3.4 Å, and 1.9 Å for **CC3**, **6FT-RCC3**, and **6ET-RCC3**, respectively. Notably, **6ET-RCC3** possesses smaller pore apertures compared to the kinetic diameter of a hydrogen molecule (2.83 - 2.89 Å), however it remains accessible to hydrogen isotopes due to flexibility.

5.1.1 Fine-Tuning of Pore Apertures in POCs

The materials are kindly provided by the group of Prof. A. I. Cooper (Liverpool University). Porous organic cages are discrete molecules with intrinsic cavities, which can form a three dimensional interconnected pore network via van der Waals forces by a window to window packing mode, as shown in Figure 5.1, for more detailed information please refer to section 2.2.1. The pore can be precisely tailored by post-synthetic installation of multiple functional groups only in the interior of the cage molecule without altering the solid-state packing and the cage structure itself. A series of internally post-functionalized porous organic cages that crystallized in an isostructural way have been synthesized by a protection-deprotection strategy, in which the five out of the six internal reaction sites in cages are functionalized by means of a formaldehyde "tying" method[149] (Scheme 5.1).
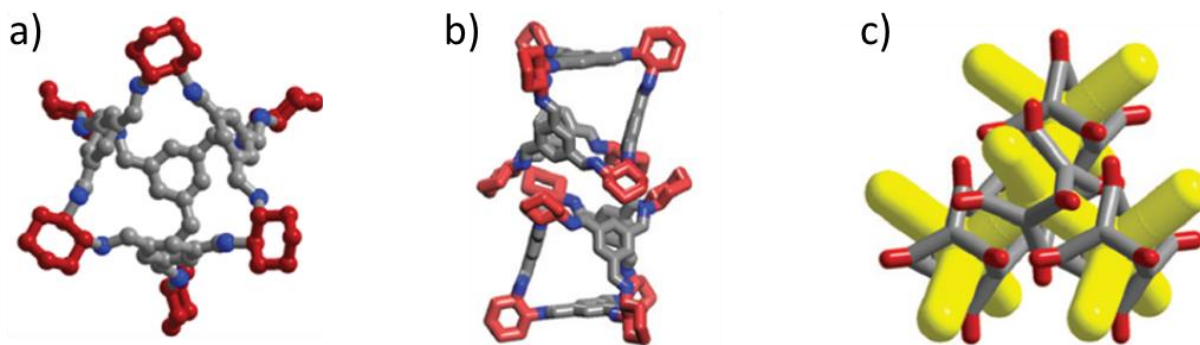

Figure 5.1 Schematic of cage-cage packing in the crystal structure of a) Cage **3** by the cyclohexyl groups (red) to pack b) window-to-window, generating c) an interconnected diamondoid-pore network (yellow)[149].

Synthesis

The materials were synthesized by Dr. M. Liu from group of A. I. Cooper[150]. The starting material 1,3,5-Triformylbenzene was purchased from Manchester Organics, UK. All other chemicals were purchased from Sigma-Aldrich and used as received.
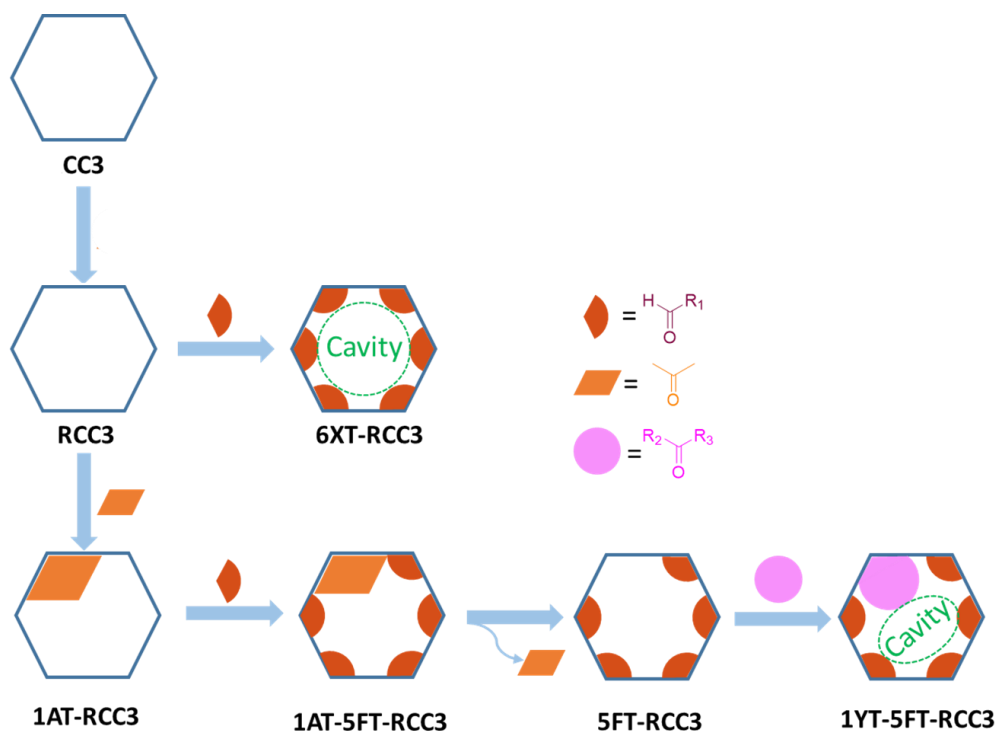
Scheme 5.1 Scheme showing the protect-functionalize-deprotect strategy for internal cage cavity modification, adapted from Ref. 150.

(i) Synthesis of CC3

As reported[64], dichloromethane (100 ml) was layered slowly onto solid triformylbenzene (TFB, 5 g, 30.86 mmol) without stirring at room temperature. Trifluoroacetic acid (1 mL) was added directly to this solution as a catalyst for the imine bond formation. Finally, a solution of (R,R)-1,2-diaminocyclohexane (5 g, 44.64 mmol) in dichloromethane (100 mL) was added to this, again without mixing. The reaction was covered and left to stand. Over 5 days, all of the solid triformylbenzene was used up and octahedral crystals of **3**-*R* grew on the sides of the glass reaction vessel. The crystalline product was removed by filtration and washed with 95 % ethanol / 5 % dichloromethane.

(ii) Synthesis of RCC3

The imine cage **CC3-*R*** (926 mg, 0.83 mmol) was dissolved in a $CHCl_3$ / methanol mixture (1:1 v/v, 50 mL) by stirring. When this solution became clear, sodium borohydride (1.00 g, 26.5mol) was added and the reaction was stirred for a further 12 hours at room temperature. Water (2 mL) was then added, and the reaction stirred for a further 12 hours. The solvent was then removed under vacuum. The resulting white solid was extracted with chloroform (2×50 mL) and then the combined organic phase was washed by water (2×100 mL). The $CHCl_3$ phase was dried using anhydrous $MgSO_4$ before being removed under vacuum. The parent cage **RCC3** was obtained as a white solid.

(iii) Synthesis of 6FT-RCC3

Paraformaldehyde (52 mg, 20 eq.) dissolved in CH_3OH (10 mL) was stirred at 70 °C. To this clear solution was added **RCC3** (100 mg) dissolved in CH_3OH (10 mL). A white precipitate appeared upon addition of **RCC3**. The reaction was stirred for a further 2 h at 70 °C. The reaction was cooled to room temperature and the precipitate was collected by filtration. **6FT-RCC3** (52 mg, 70 %) was obtained after being washed with CH_3OH (3×10 mL) and dried under vacuum[150].

(iv) Synthesis of 6ET-RCC3

Acetaldehyde (52 mg, 20 eq.) dissolved in CH_3OH (10 mL) was stirred at 70 °C. To this clear solution was added **RCC3** (100 mg) dissolved in CH_3OH (10 mL). A white precipitate appeared upon addition of **RCC3**. The reaction was stirred for a further 2 h at 70 °C. The reaction was cooled to room temperature and the precipitate was collected by filtration. **6ET-RCC3** (52 mg, 70 %) was obtained after being washed with CH_3OH (3×10 mL) and dried under vacuum. In the new cage **6ET-RCC3**, the bulkier ethylidene bridges replaced the six methylene bridges in **6FT-RCC3**[150].

RCC3

6FT-RCC3, R1 = H
6ET-RCC3, R1 = Me
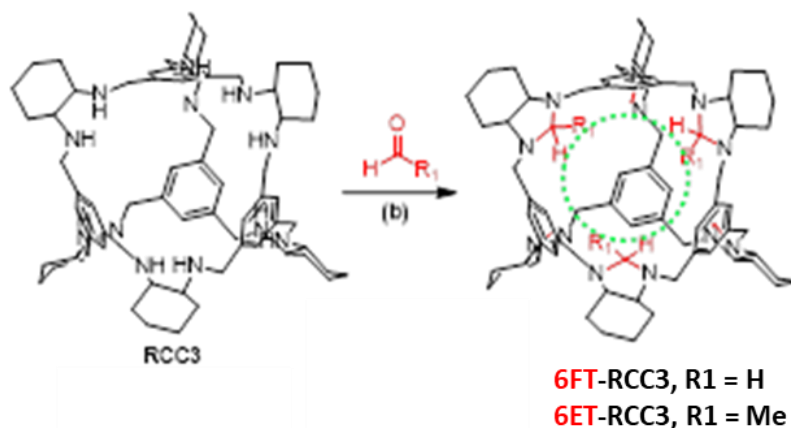
Scheme 5.2 Synthesis route for internal cage cavity modification, corresponding to scheme 5.1[150].

Characterization

Powder X-ray diffraction (PXRD) patterns were collected in transmission mode on samples held on thin Mylar film in aluminium well plates on a Panalytical Empyrean diffractometer, equipped with a high throughput screening (HTS) XYZ stage, X-ray focusing mirror, and PIXcel detector, using Cu-Kα (λ = 1.541 Å) radiation. PXRD patterns were measured over the 2θ range 5−50°, in ~0.013° steps, over 1 hour (Prof. A. I. Cooper group).

Materials

As presented in Schematic 5.1 and the synthesis procedure, by treatment with NaBH$_4$, the parent imine cage **CC3** can be chemically reduced to afford the corresponding dodecaamine cage **RCC3**, which has tetrahedral symmetry and is formed by cycloimination of 1,3,5-triformylbenzene and (1R,2R)-1,2-diaminocyclohexane. The cage packs through a window-to-window packing mode via van der Waals forces to give a 3D porous network. For guest molecules diffusing through this pore network, they must pass through the intrinsic cage cavities which act as the tetrahedral nodes (Figure 5.1c). A practical route to systematically tailor the pore aperture size without altering the structural shape and crystallization of the cage molecule is an internal functionalization of the cages. The flexible diamine groups in **RCC3** are reacted with six formaldehyde to afford the rigid 'tied' cage, **6FT-RCC3**, with a reduced pore aperture. One of the hydrogen atom in each formaldehyde group can be further replaced by methyl group to obtain a narrow pore cage **6ET-RCC3**, in which the windows are blocked by one or two methyl groups. The crystal structures of the as synthesized cages are shown in Figure 5.2.
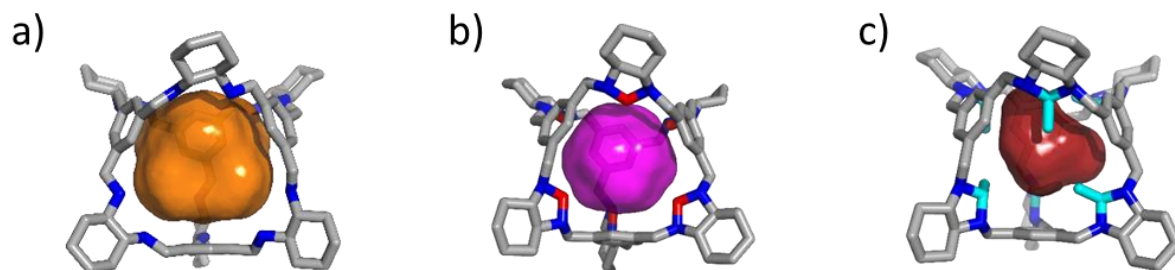
Figure 5.2 Molecular structures of a) **CC3**, b) **6FT-RCC3**, c) **6ET-RCC3**. Hydrogen atoms omitted for clarity. Carbon and nitrogen atoms are colored grey and blue, respectively. The formaldehyde molecule shown in red and the methyl groups in light blue. The colored bubbles inside the cages represent the internal volume[150].
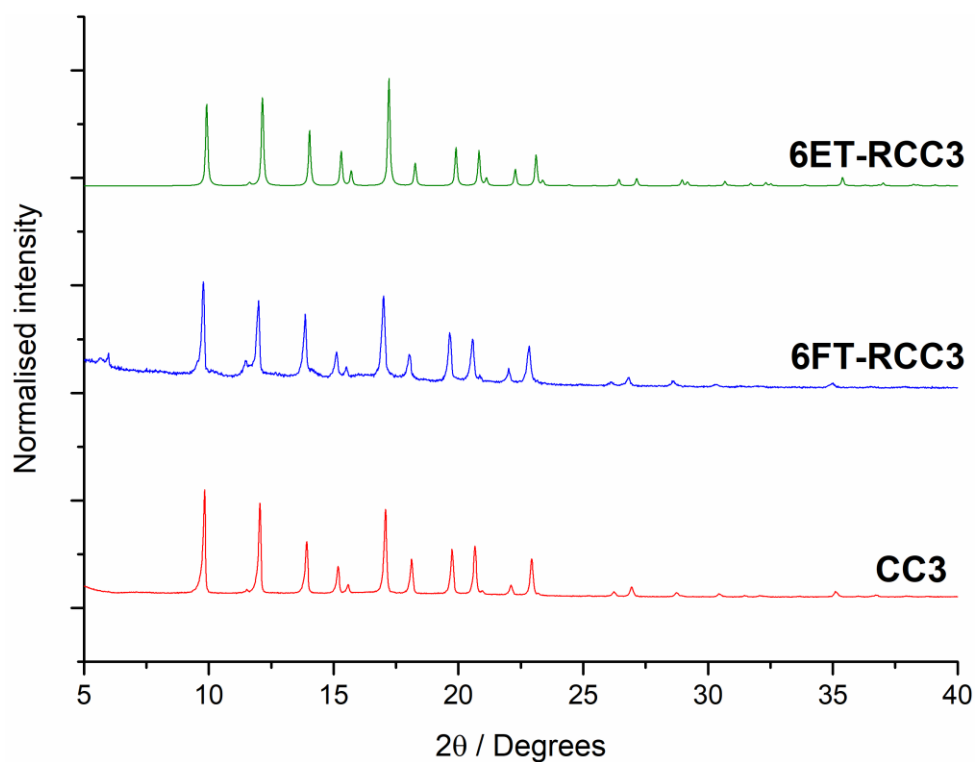
Figure 5.3 Experimental PXRD patterns (Cu-Kα) of the isostructural cages **CC3**, **6FT-RCC3**, and **6ET-RCC3**, as synthesized. Adapted from Ref. 150.

All the post-synthetically modified cages crystallizes in the cubic space group F4$_1$32, isostructural with the parent cage **CC3**, as determined by powder x-ray diffraction (PXRD), presented in Figure 5.3. It clearly reveals that all the cages were obtained in a pure and

crystalline form. The similarity in the XRD patterns indicates that the underlying shape and crystallization habit of the cage molecules. Therefore, the cavities are connected by the same diamondiod pore structure after implementing internal functionalization of the cage cavities. Noted that the high crystallographic symmetry of the structures does not allow to determine if the different functional groups are ordered in the microporous pore structures. The unit cell parameters and the calculated cavity volume determined by powder x-ray and single-crystal X-ray diffraction are summarized in Table 5.1.

Table 5.1 Unit cell parameters and cavity volume calculations for cage series. All X-ray data sets were recorded at 100 K after activating the crystals pores under dynamic vacuum at 353 K.

	CC3	6FT-RCC3	6ET-RCC3
a (Å)	25.711	25.316	25.216
V (Å^3)	16999	16225	16033
Cavity Volume (Å^3)*	186.9	129.6	29.5

* Calculated using *VOIDOO*, probe radius = 2.0 Å[151].

Instead of measuring a single, static pore diameter, molecular dynamics (MD) simulations to calculate the time averaged pore-limiting envelope (PLE), which allows for the effect of molecular flexibility on the diffusivity of small gas molecules through cage structures. These calculations show that postsynthetic modification allows the PLE to range from 1.95 Å (**6ET-RCC3**) to 3.50 Å (**6FT-RCC3**), while the PLE of the parent cage **CC3** is 4.50 Å. The MD simulation was performed by Dr. L. Chen from group of A. I. Cooper.

5.1.2 Results

Low-pressure, high-resolution H$_2$ and D$_2$ adsorption isotherms
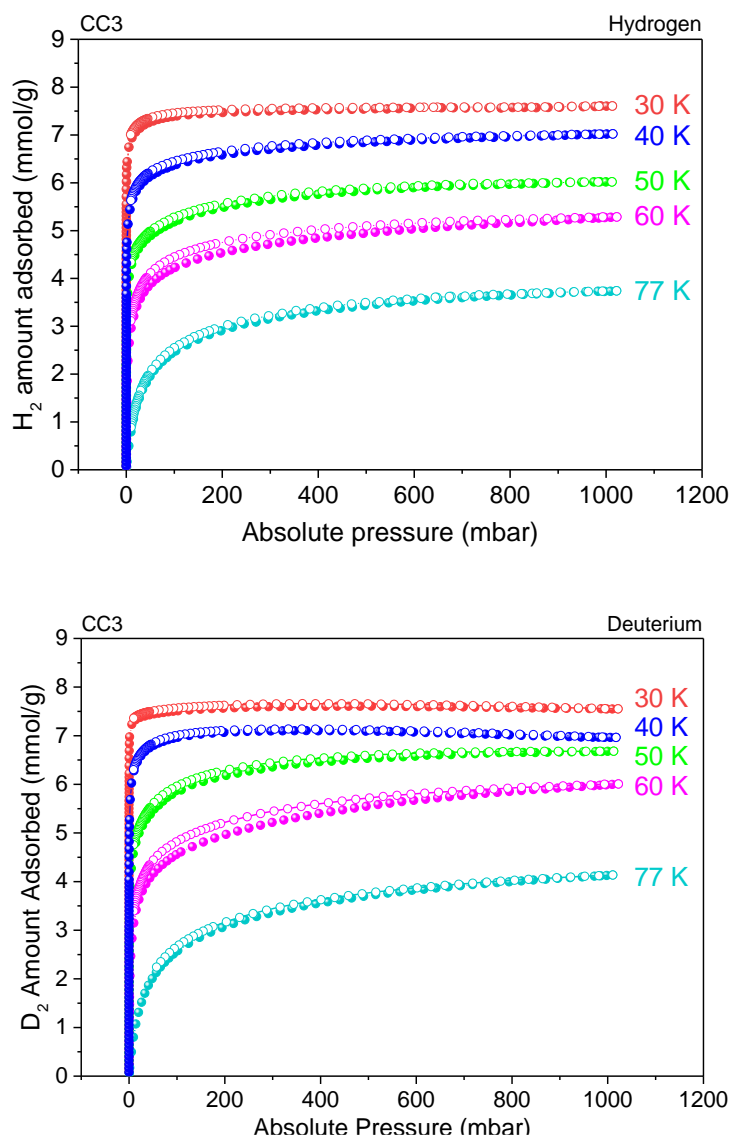
Figure 5.4 Hydrogen (upper) and Deuterium (bottom) adsorption (closed) and desorption (open) isotherms of **CC3** at various temperatures, 30 K (red), 40 K (blue), 50 K (green), 60 K (pink), and 77 K (turquoise).

Adsorption isotherms of H$_2$ and D$_2$ on **CC3**, **6FT-RCC3**, and **6ET-RCC3** are collected for various temperature between 30 K and 77 K. **CC3** and **6FT-RCC3** exhibit a type I adsorption isotherm, in the IUPAC classification, as shown in Figure 5.4 and 5.5, respectively. Typically,

physical type I adsorption is observed in microporous materials at the liquefaction point, in which an initial steep increase based on micropores filling occurs at relative pressure below 0.1, and the adsorption process is usually complete at a relative pressure of around 0.5[152].

Figure 5.5 Hydrogen (upper) and Deuterium (bottom) adsorption (closed) and desorption (open) isotherms of **6FT-RCC3** at various temperatures, 30 K (red), 40 K (blue), 50 K (green), 60 K (pink), and 77 K (turquoise).

The two cages exhibit increased H_2 uptake with decreasing temperature, with the highest uptake at 30 K of 7.4 and 7.6 mmol/g at 1 bar, representatively, indicating the accessible surface for H_2 is similar for both cages. The D_2 isotherms show a higher uptake compared to the H_2

isotherm at all temperatures, the corresponding values for D_2 adsorption at 30 K are 7.5 and 9.5 mmol/g for **CC3** and **6FT-RCC3**, respectively. The D_2 higher uptake is mainly attributed to the higher heat of adsorption of D_2.

Figure 5.6 Hydrogen adsorption (closed) and desorption (open) isotherms of **6ET-RCC3** at various temperatures, 30 K (red), 40 K (blue), 50 K (green), 60 K (pink), and 77 K (turquoise).

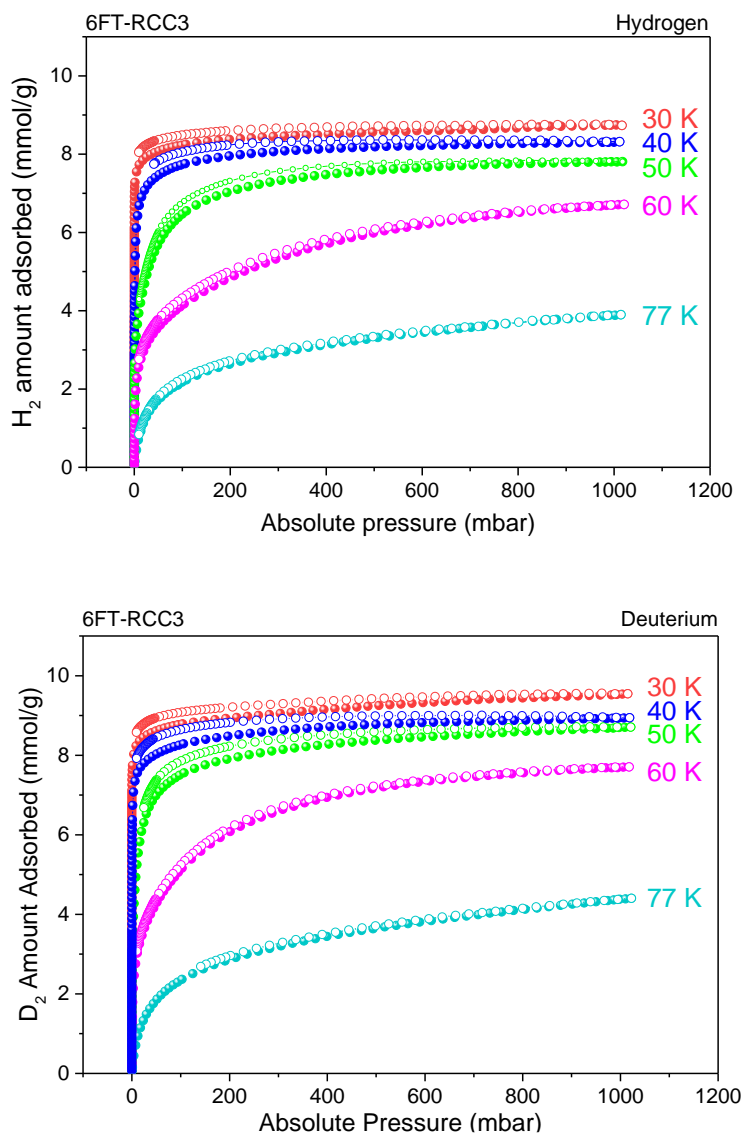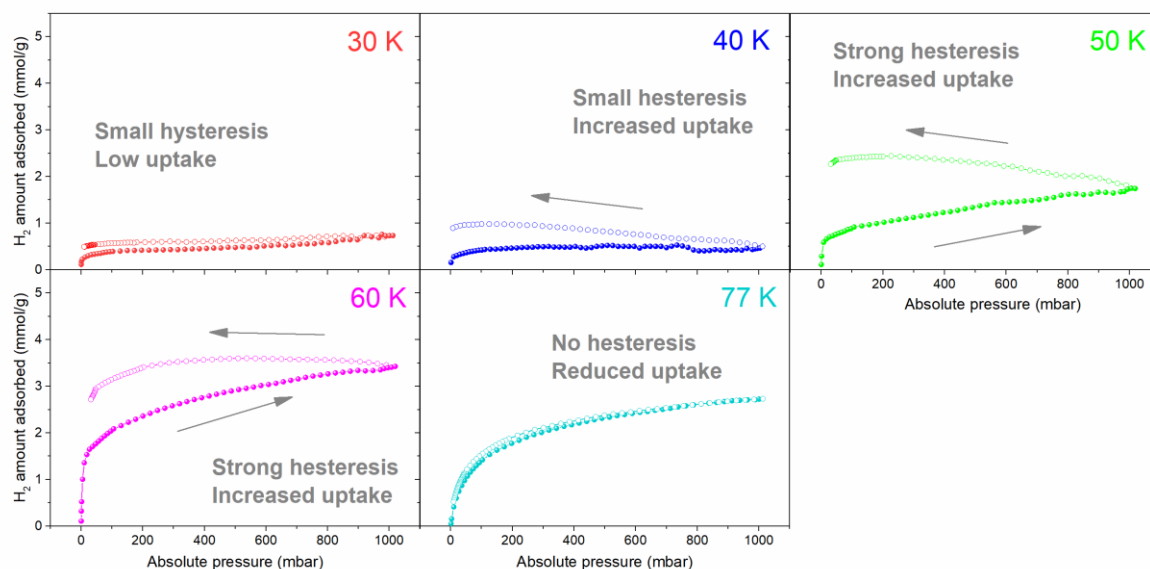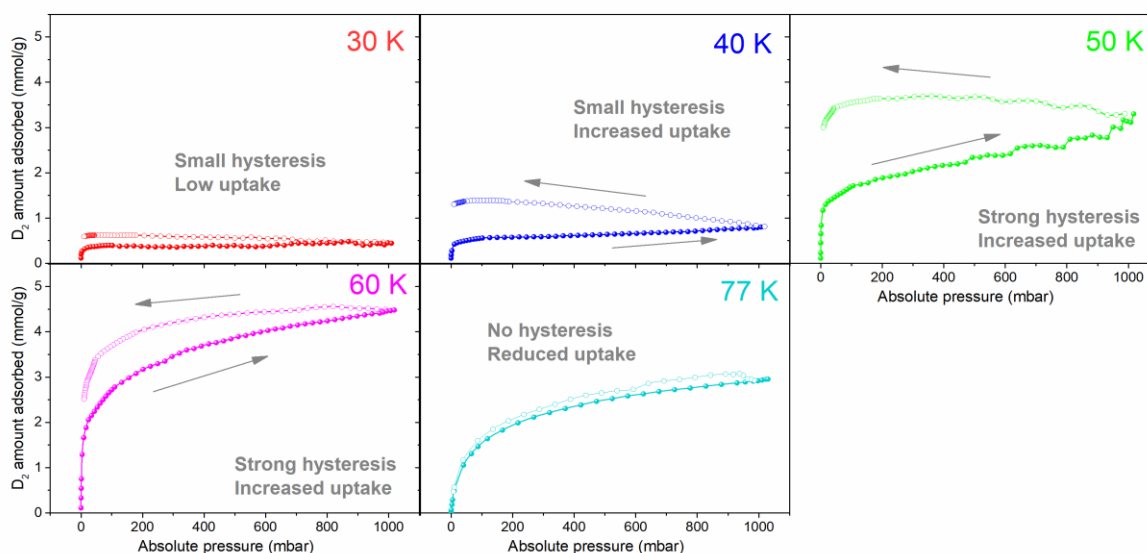Figure 5.7 Deuterium adsorption (closed) and desorption (open) isotherms of **6ET-RCC3** at various temperatures, 30 K (red), 40 K (blue), 50 K (green), 60 K (pink), and 77 K (turquoise).

Generally, the isotherms for hydrogen physisorption on porous materials exhibit increased uptake with decreasing temperature. However, a unique behavior can be observed in the isotherms of **6ET-RCC3**, as shown in Figure 5.6. Almost no uptake can be observed at 30 K and the uptake is increasing with temperature, reaching the maximum at 60 K (3.8 mmol/g at 1 bar). Compared with **CC3** and **6FT-RCC3**, the lower uptake of **6ET-RCC3** is attributed to the existence of functional groups, therefore, a smaller cavity. In addition, the observed hysteresis becomes stronger in the temperature range up to 50 K, then becoming weaker above 60 K, implying a better equilibrium at higher temperatures. With further increasing temperature, gas uptake decreased as typical type I sorption isotherms. Identical phenomena are also observed in case of D_2 adsorption, shown in Figure 5.7. The adsorption amount of D_2 is higher, with the maximum found at 60 K (4.5 mmol/g), and the hysteresis below 77 K is stronger than that of H_2. One should note that, in case of **6ET-RCC3**, H_2 or D_2 cannot penetrate the framework at 30 K due to the smaller size of the pore aperture than the kinetic diameter of the hydrogen isotope molecule. However, due to the larger pore aperture size of **CC3** and **6FT-RCC3**, adsorption and desorption are fully reversible.

TDS study for pure gas physisorption

Cryogenic TDS measurements have been carried out by applying H_2 or D_2 pure gas atmosphere, under identical experimental conditions. After degassing at 353 K for 2 h, all cage samples have been exposed to 10 mbar pure gas at room temperature. After cooling below 20 K, the unabsorbed gas molecules were evacuated, then the desorption spectra were recorded with a linear heating ramp of 0.1 K/s. The resulting TDS spectra obtained between 20 -120 K are shown in Figure 5.8.

For **CC3**, the desorption spectra show one maximum centered at 55 K with a small shoulder around 45 K. The area under the desorption peak is proportional to the desorbing amount of gas, which can be quantified with calibration, see Chap. 3.3. The uptake for H_2 and D_2 is determined to be 4.8 mmol/g and 5.0 mmol/g, respectively. The spectrum of D_2 of **6FT-RCC3** shows two desorption maxima, one sharp peak at the temperature of 34 K and a broad peak at around 48 K. In contrast, the H_2 spectrum shows a peak at 30 K with a broad shoulder centered at 48 K. The uptake for **6FT-RCC3** of H_2 and D_2 measured is 6.5 and 7.0 mmol/g, respectively.
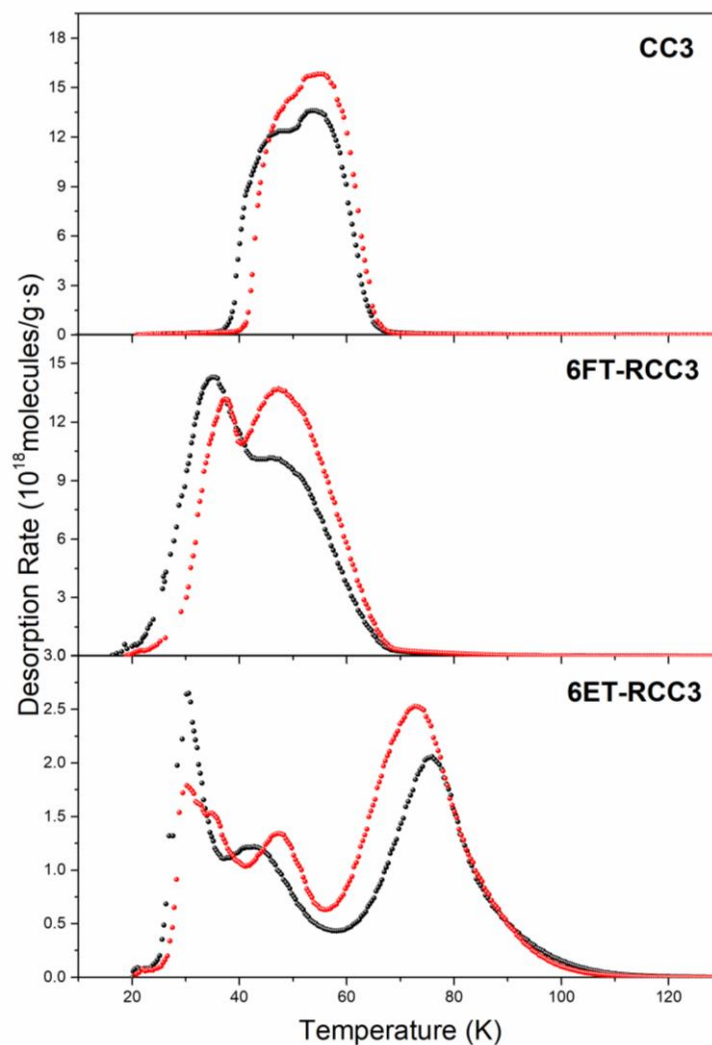
Figure 5.8 Pure gas H_2 (black) and D_2 (red) thermal desorption spectra of a) **CC3**, b) **6FT-RCC3**, and c) **6ET-RCC3** exposed to a 10 mbar pure isotope at room temperature, then cooling to 20 K.

The thermal desorption spectra of **6ET-RCC3** measured with H_2 show three desorption maxima centered at 30 K, 40 K, and 75 K, whereas for deuterium the maximum appeared at 30K, 45K, and 70K. The uptake for H_2 and D_2 yields a value of 1.0 and 1.5 mmol/g, respectively. In addition, the amount of hydrogen desorbed is negligible in **CC3** and **6FT-RCC3** above 75 K. In contrast, for **6ET-RCC3**, the desorption curve lasts till 115 K.

TDS study for hydrogen isotope separation

Isotope mixture TDS measurements have been carried out on **6ET-RCC3**. The H_2 and D_2 TDS spectra presented in Figure 5.9 have been collected after the sample was exposed to a 10 mbar equimolar D_2/H_2 isotope mixture at exposure temperature (T_{exp}) of 30 - 77 K. Note the different scales of y-axes. The adsorbed isotope gases and the corresponding selectivity as function of exposure temperature has been given in Figure 5.10.

Figure 5.9 H_2 (black) and D_2 (red) desorption spectra of 10 mbar 1:1 D_2/H_2 mixture exposure on **6ET-RCC3** at exposure temperatures of 30, 50, 60, and 77 K for 10 min.

TDS spectra show that the uptake in **6ET-RCC3** increased with increasing exposure temperature until a maximum for H_2 and D_2 is reached at T_{exp} of 60 K before decreasing again

at 77 K. The selectivity, $S_{D2/H2}$, decreases with increasing T_{exp} and exhibits a maximum of 3.9 at 30 K. The onset temperature of gas desorption is nearly identical to the exposure temperature, since after exposure the chamber is evacuated at T_{exp} prior to cooling to 20 K. No desorption peak can be observed above 60 K for $T_{exp} = 30$ K, the sample exhibits two desorption maxima centered at 35 and 45 K for D_2, while only one board peak with a maximum at 32 K for H_2. The desorption of the gases can be neglected above 60 K. When exposure temperature increases to 50 K, the first desorption maximum vanished. Instead, the TDS spectra show a maximum at 65 K for both isotopes, with a board shoulder till 90 K. As well as for the exposure at 60 K, and 77 K, the maximum shifts to higher temperatures of 75 and 105 K, respectively.
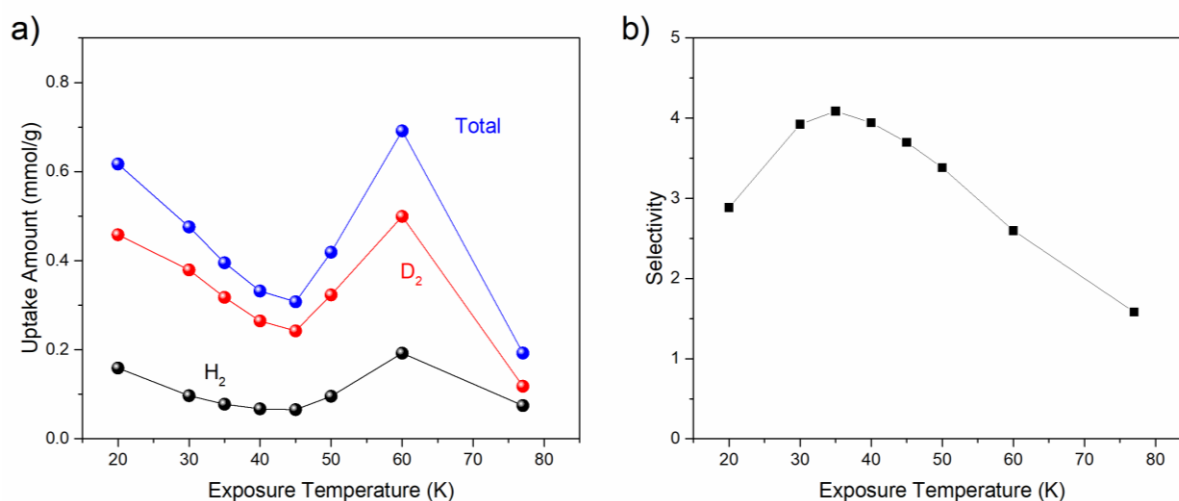
Figure 5.10 a) The adsorbed amount of isotope gases (H_2 black, D_2 red) and their total amount (blue) as function of exposure pressure on **6ET-RCC3**. b) The D_2/H_2 selectivity as function of exposure pressure.

The influence of exposure time has been investigated based on the results of the highest observed selectivity of **6ET-RCC3** at about 30 K. TDS measurements have been carried out for exposure under 1:1 isotope mixture at 30 K for 10 – 300 min. The H_2 and D_2 spectra for various exposure times are presented in Figure 5.11. TDS measurements have been applied to **CC3** and **6FT-RCC3** under identical condition as well. The corresponding desorption spectra are presented in Figure 5.12 and 5.13 for **CC3** and **6FT-RCC3**, respectively. The adsorbed gas amount and the corresponding selectivity as function of exposure time for three cages (**CC3**, **6FT-RCC3**, and **6ET-RCC3**) have been summarized in Figure 5.14.
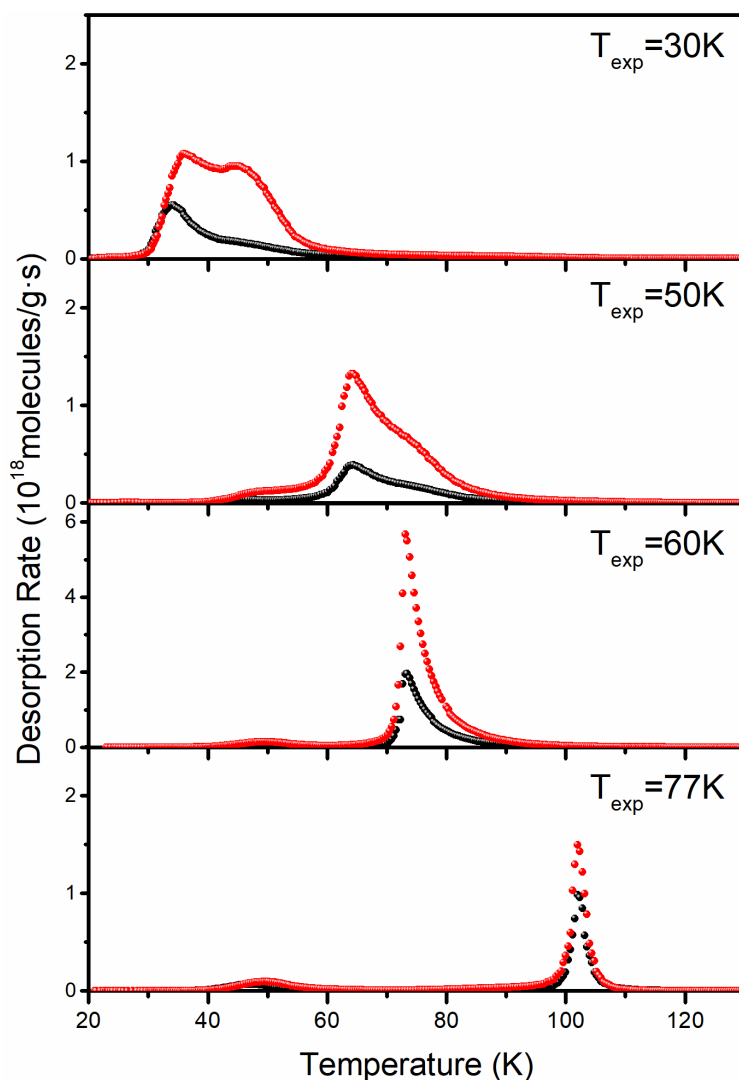
Figure 5.11 H_2 (black) and D_2 (red) desorption spectra of 10 mbar 1:1 D_2/H_2 mixture exposure on **6ET-RCC3** at exposure temperature of 30 K for various exposure times.

The total gas uptake dramatically decreased with decreasing pore aperture, that is 8.0, 8.3, and 0.7 mmol/g for **CC3**, **6FT-RCC3**, and **6ET-RCC3**, respectively. The uptake values are in good agreement with the uptake determined by the adsorption isotherms at 30 K. The number of gas molecules adsorbed on **6ET-RCC3** is rising with longer exposure time, from 0.4 to 0.7 mmol/g. In contrast, the gas uptake for the two cages with larger pore apertures is independent on exposure time. When the gas exposure is carried out at 30 K, the selectivity exhibits the highest value of $S_{D2/H2}$ = 3.9 for the shortest exposure time 10 min in **6ET-RCC3**. In addition, the selectivity decreases with increasing t_{exp}, from 3.9 to 3.3 in the range between 10 and 300 min, which can be attributed to kinetic quantum sieving. However, at 30 K, the D_2/H_2 selectivity for **CC3** and **6FT-RCC3** remains constant at 1.2 and 2.1 for different t_{exp}, respectively.
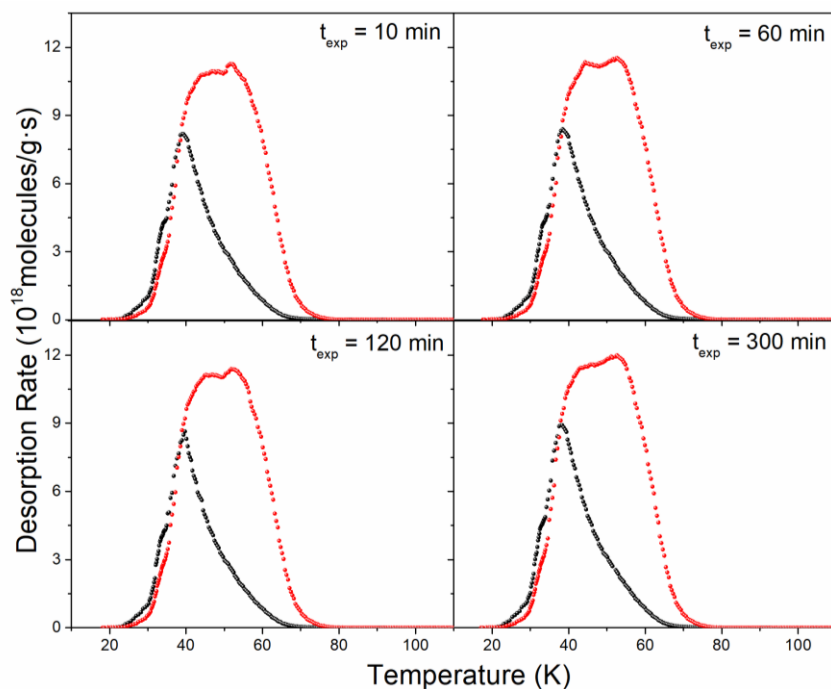
Figure 5.12 H_2 (black) and D_2 (red) desorption spectra of 10 mbar 1:1 D_2/H_2 mixture exposure on **CC3** at exposure temperature of 30 K for various exposure times.

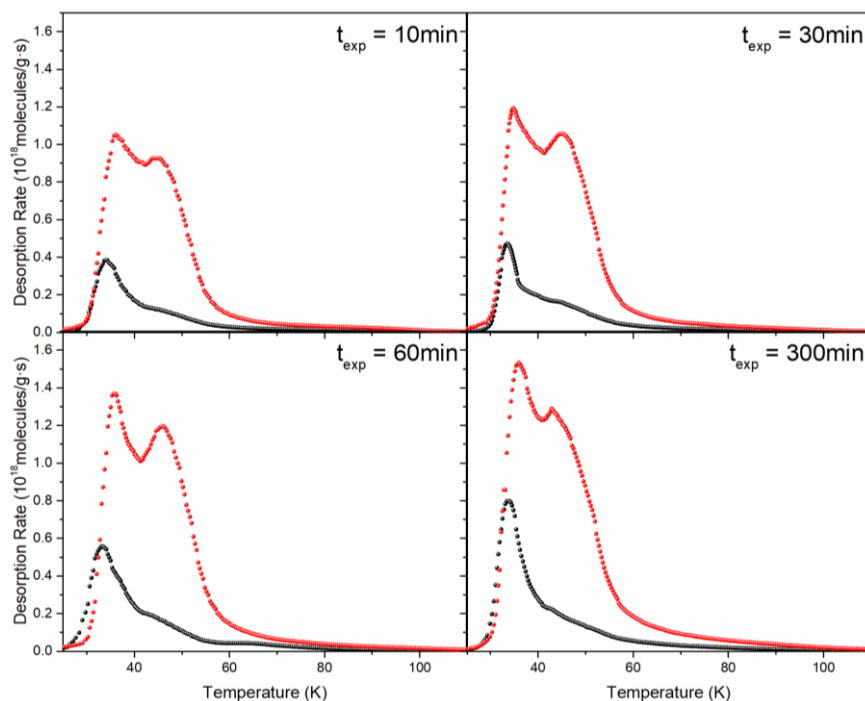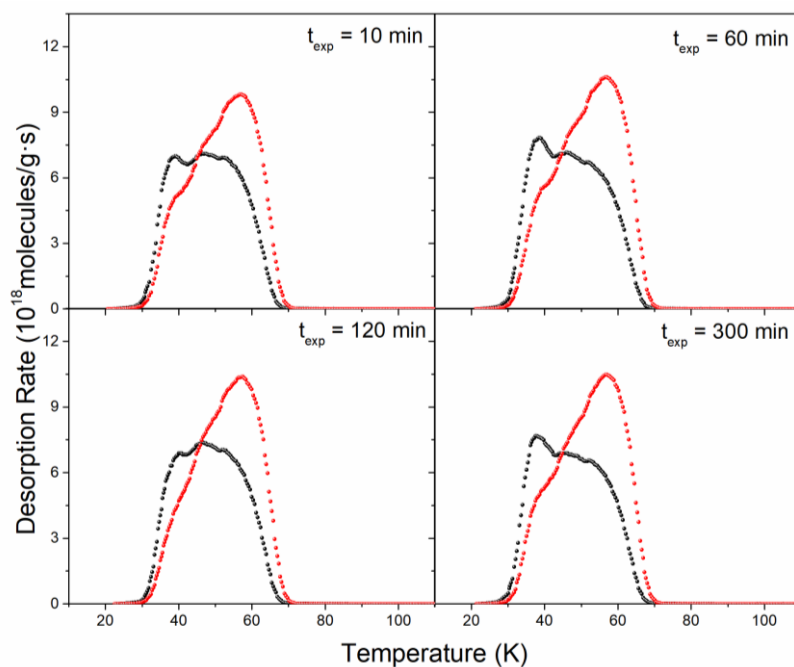Figure 5.13 H_2 (black) and D_2 (red) desorption spectra of 10 mbar 1:1 D_2/H_2 mixture exposure on **6FT-RCC3** at exposure temperature of 30 K for various exposure times.
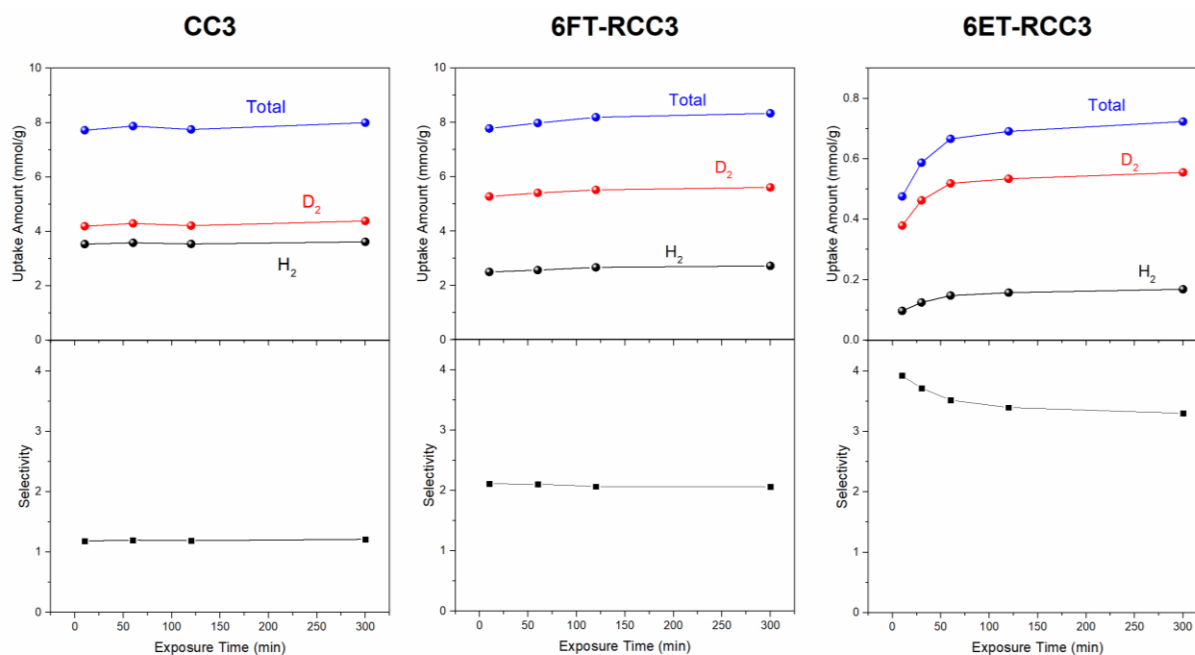
Figure 5.14 The adsorbed amount of isotope gases (H_2 black, D_2 red) and their total amount (blue) (upper) and the D_2/H_2 selectivity (bottom) as function of exposure time, obtained from TDS experiments using 10mbar 1:1 D_2/H_2 isotope mixture at 30 K for the samples **CC3** (left), **6FT-RCC3** (middle) and **6ET-RCC3** (right).

5.1.3 Discussion

Hydrogen isotope adsorption in cages possessing different pore apertures

Three porous organic cages with different pore apertures, **CC3**, **6FT-RCC3**, and **6ET-RCC3**, have been investigated. The parent cage CC3 reacts with six formaldehyde molecules to form **6FT-RCC3**, while with six equivalents of acetaldehyde to form a cage, **6ET-RCC3**, where bulkier ethylidene bridges replaced the six methylene bridges in **6FT-RCC3**. Thus, the cages have basically the same external cage shape and size and therefore crystalized in the same crystal packing. The placement of different functional groups inside the cage cavities allows the ultrafine control over the cavity size and the pore aperture. Consequently, the pore aperture of the cages are determined by molecular dynamics simulations to be around 4.5 Å, 3.4 Å, and 1.9 Å.

Hydrogen isotope adsorption measurements performed on the series of cages show distinct phenomena. The reversible type I adsorption isotherm reveals that the **CC3** and **6FT-RCC3** are fully accessible for hydrogen isotope molecules, indicating that the two materials have large enough pore apertures enabling free gas access. The two cages with the highest uptake at 30 K of 8 and 8.2 mmol/g at 1 bar indicate that the accessible surface for H_2 is similar for both cages.
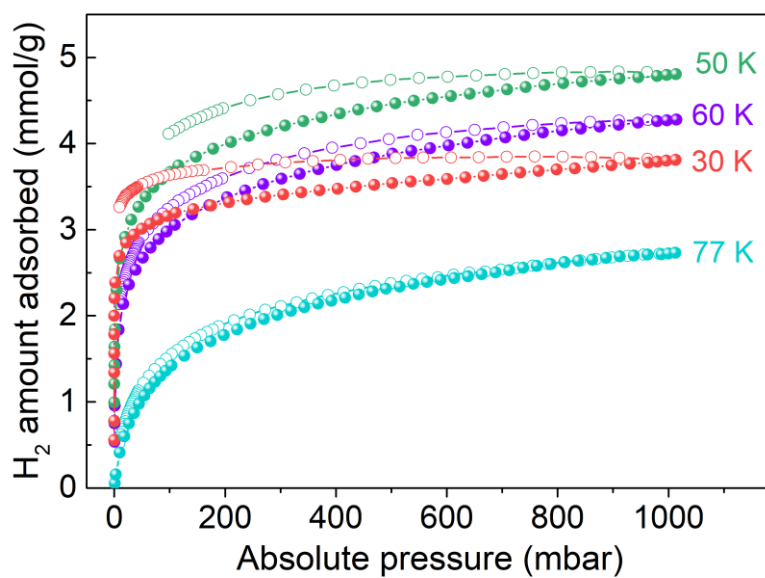
Figure 5.15 H_2 adsorption (closed) and desorption (open) isotherms of **6ET-RCC3** at different temperatures (equilibrium time 100 h).

In contrast, the H_2 sorption isotherms obtained from **6ET-RCC3** clearly show a different adsorption behavior. At low temperature 30 K, the H_2 and D_2 uptakes are close to zero, indicating that the isotope molecules cannot penetrate within a reasonable equilibrium time of approximately 20 h for the whole adsorption isotherm (Figure 5.7). This can be ascribe to the small effective aperture size at low temperature. At temperatures higher than 40 K, the gas molecules start to penetrate into the structure slowly with strong hysteresis, indicating that equilibrium is still not fully reached. One should note that, for desorption curves at 50 and 60 K, the amount adsorbed increase with decreasing pressure. This can be ascribed to the fact that the diffusion of gas molecules into material are still ongoing when the experiment is already decreasing the pressure. At higher temperature of 77 K, the gas molecules can penetrate the network more freely, then a typical type I isotherm can be observed without diffusion barrier.

The experiments have shown that a full-equilibrium isotherm at low temperatures cannot be collected for experimental times of 20 h. Therefore, a longer experimental time, around 100 h for each isotherm, has been applied for H_2 adsorption isotherms of **6ET-RCC3** (Figure 5.15). The gas uptake amount increases with increasing temperatures, reaching the maximum at 50 K (4.8 mmol/g at 1 bar), and then decreases again. The hysteresis is the largest at 30 K and decreases with increasing temperature, and the equilibrium is reached when the temperature increases to 77 K.

These experiments therefore indicate a full-equilibrium cannot be reached even for 100 h at low temperatures. In contrast, the equilibrium can be achieved within a short time (approximately 10 h) for **CC3** and **6FT-RCC3** at all temperatures. The gas molecules can penetrate the network freely, demonstrating no diffusion barrier in these two cages. This difference suggests that the methyl groups in the **6ET-RCC3** cavities can be responsible, since this is the only structural difference. Considering the window-to-window packing mode of **6ET-RCC3**, the pore aperture is defined by the methyl groups at the two windows, one has two methyl groups while the other has one. At temperature as low as 30 K, the effective pore aperture size is restricted by the rigid methyl groups which produce a strong diffusion barrier for hydrogen molecules. As temperature increasing, the thermally-induced flexibility of methyl groups leads to an effectively larger pore aperture size, leading to the decreasing diffusion barrier which enables the gas molecules to penetrate.

Temperature-dependent opening of the pore aperture of 6ET-RCC3

Notably, the pore size simulation shows that **6ET-RCC3** possesses far smaller pore apertures, 1.9 Å, compared to the kinetic diameter of a hydrogen molecule (2.83 - 2.89 Å), however it remains accessible to hydrogen isotopes at temperatures above 30 K. Even though the cages are relatively inelastic materials assembled from discrete molecules that are held together by weak intermolecular interactions, the local and molecular motions can play an important role in allowing the diffusion of guest molecules that are seemingly too large to diffuse. As discussed above, this can be attributed to the thermally-induced flexibility of methyl groups inside the cage.

The temperature-dependent gate-opening can also be observed by TDS measurements (see Figure 5.9). **6ET-RCC3** was exposed to a 10 mbar equimolar H_2/D_2 mixture for 10 min at various temperatures (20 – 77 K). The spectra at 30 K extended from 30 to 60 K, showing the

highest desorption rate at 35 and 45 K. For higher exposure temperatures the spectrum is shifted to higher desorption temperatures. When the exposure temperature is increased to 50 K, a new desorption peak extending to 80 K starts to appear, with a maximum at approximately 65 K. The intensity of the desorption peak grows with increasing exposure temperature. With the exposure temperature further increased to 60 K, a desorption peak centered at 75 K can be observed. The desorption spectrum collected at 77 K showed a maximum of 102 K for both isotopes.
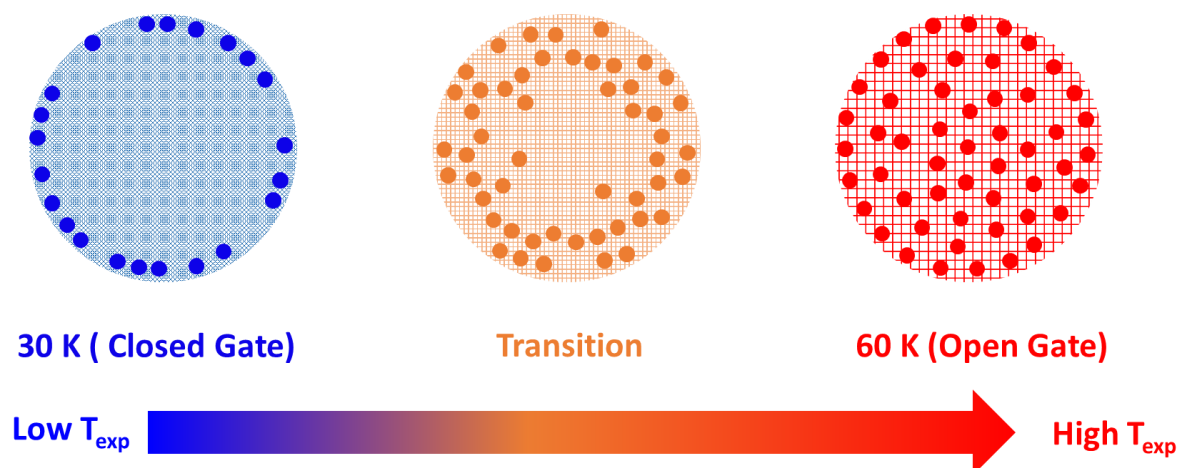
Figure 5.16 Schematic 2D representation of the distribution of gas molecules in a spherical crystal for different exposure temperatures. The larger effective apertures at higher exposure temperatures increase the accessibility for gas molecules (solid circle).

In general, thermal desorption spectra reflect the state created during the gas adsorption at a given exposure temperature and exposure time. For instance, the cages have been exposed to a given atmosphere at a given temperature and pressure. After being thus exposed, the sample chamber is evacuated directly at the exposure temperature, prior to cooling down to 20 K. The samples are then heated, and the desorption status can be recorded. For porous materials with large pore apertures, there is no diffusion limitation for the penetrating gas, and hence all adsorption sites are accessible during gas exposure. In this case, the desorption spectra will directly reflect the distribution of the energetically different adsorption sites. In other words, the desorption temperature reveals the interaction strength between the adsorbed hydrogen isotopes and the specific surfaces, for example **CC3** and **6FT-RCC3**.

By contrast, for materials with small pore apertures, the adsorption process is limited by the diffusion-limited process of gas penetration into the material. The desorption spectra demonstrate the diffusion barrier encountered by the gas molecules. Especially in the materials showing a thermally-activated gate-opening behaviour, the gas can typically penetrate into the cages and diffuse more deeply into the porous structure at higher exposure temperatures. Thus during desorption, the thermally-activated opening of the aperture again determines the desorption temperature at which the gas can leave the cages. Therefore, in the case of **6ET-RCC3** at $T_{exp} = 30$ K, the gas cannot penetrate far into the cage structure, resulting the TDS spectrum with the absence of desorption peaks at higher desorption temperatures. The TDS results suggest that there is only weakly adsorbed gas on the outer surface or inter-particle voids of the powder. With increasing exposure temperature, gases can penetrate into the cages and the desorption peaks in TDS spectra are shifted to higher temperatures. This is attributed by the following reasons:

(i) The TDS spectra always start approximately from the exposure temperature due to the evacuation of the unadsorbed gas molecules at the same temperature. Thus, the weakly bond gas molecules have been removed already during evacuation at the exposure temperature;

(ii) The desorption is governed by the temperature at which the aperture starts to open and the gas can leave the cage;

(iii) For even higher exposure temperatures, the gas penetrates deeper into the structure and needs a longer time to diffuse out via a random pathway, leading to an even higher desorption temperature.

Thus, in accordance with the observations of hysteresis in the pure gas isotherms, the desorption temperatures are shifting to higher temperatures with exposure temperature, indicating the adsorptions sites inside cages become more accessible at higher T_{exp}. The properties of **6ET-RCC3** can be attributed to the temperature-dependent opening of the pore aperture. The accessibility at different temperatures is illustrated in Figure 5.16.

One should note that, the flexibility is usually accompanied by the structural deformation. However, the flexibility described in cage **6ET-RCC3** only implies kinetic effects induced by the vibration of the methyl groups with temperature. Powder X-ray diffraction (PXRD) pattern of **6ET-RCC3** was measured after performing the TDS measurements. No change of the PXRD

pattern can be observed after the TDS measurements (Figure 5.17), despite carrying out repeated gas adsorption and desorption cycles.
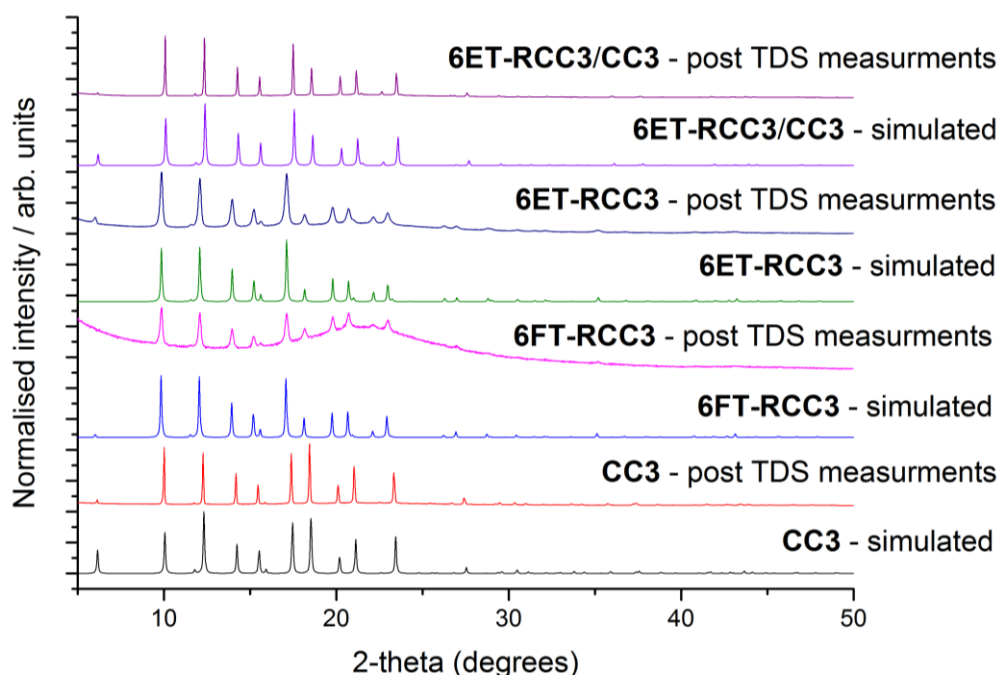
Fig. 5.17 PXRD data (Cu-Kα) recorded after TDS measurements for **CC3**, **6FT-RCC3**, and **6ET-RCC3**, shown above the simulated PXRD patterns for these structures. Only a slight loss in crystallinity for the **6ET-RCC3** cage materials can be observed during these measurements[150].

Separation of hydrogen isotopes

Kinetic quantum sieving has been observed experimentally in **6ET-RCC3**. As discussed above, for materials possessing confined apertures, diffusion limitation typically governs the adsorption/desorption process. In case of **6ET-RCC3** at low exposure temperatures, gas molecules can only be adsorbed weakly on the outer surface; at higher exposure temperatures, the gas can penetrate into the cages, resulting in TDS maxima centered at higher temperature. This flexible structure and dynamic properties of porous materials have been reported to enhance the operating conditions for hydrogen isotope separation. MIL-53 has been investigated by Kim et al. to effectively separate hydrogen isotopes, benefited from its breathing behavior of dynamic pore aperture. By tuning the pore state of this flexible MOF, the highest D_2 over H_2 selectivity of 13 was reached at 40 K[153]. Interestingly, the operating condition can be enhanced not only by typical flexible frameworks, where a volume or phase change occurs,

but also via structures whose flexibility originates from local deformations or vibrations. A temperature-triggered gate opening induced isotope separation was reported by Oh et al. in the flexible pyridine-decorated COF-1. The highest selectivity was 9.7 observed at 26 mbar and 22 K, which could be ascribed to the quantum isotope effect with cryogenic flexibility[154]. Another temperature-triggered gate opening was found by Teufel et al. in MFU-4, possessing a bimodal pore structure with alternating small and large cavities connected by narrow aperture (ca. 2.5 Å) formed by Cl atoms. Due to phonon-induced vibrations of the Cl atoms at the aperture, hydrogen isotopes (ca. 2.89 Å) could only penetrate into the internal pores at higher temperatures, resulting in a high selectivity of 7.5 at 60 K[155]. In addition, a partially fluorinated metal-organic framework FMOFCu, which possesses a unique a tri-modal pore system with large tubular cavities connected through a smaller cavity with bottleneck apertures of 3.6 Å plus a third hidden cavity connected by an even smaller aperture of 2.5 Å, was investigated within this thesis, see Chapter 6. Depending on the gate opening effect, the cavities get successively accessible for hydrogen isotopes with increasing temperature, yielding a selectivity of 14 at 25 K and 4 at 77 K[156]. Thus, it is evident that the hydrogen isotope separation performance can be improved by the gate-opening of the pore apertures.
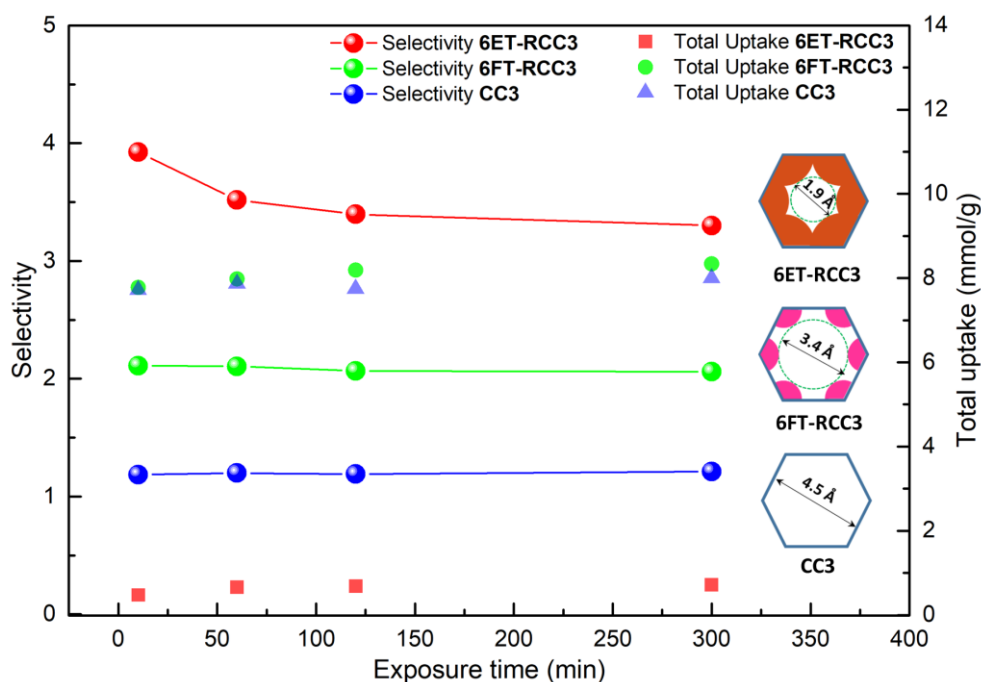

Figure 5.18 D_2/H_2 selectivities and gas uptakes as a function of exposure time at 30 K for **CC3**, **6FT-RCC3**, and **6ET-RCC3**[150].

TDS measurements (Figure 5.9) showed that the uptake in **6ET-RCC3** increased with increasing temperature until a maximum for H_2 and D_2 was reached at exposure temperature of 60 K before decreasing again at 77 K. The selectivity, $S_{D2/H2}$, decreased with increasing T_{exp} and exhibited a maximum of 3.9 at 30 K. In order to reveal the dependence of isotope separation performance on exposure time, TDS measurements have been performed at 30 K, where the highest selectivity has been achieved, and the desorption spectra have been presented in Figure 5.11 - 5.14. The selectivity and the total quantity of gas adsorbed for **6ET-RCC3**, **6FT-RCC3**, and **CC3** as a function of t_{exp} at $T_{exp} = 30$ K has been summarized in Figure 5.18. The total gas uptake obtained at 30 K for **CC3** and **6FT-RCC3** remains constant with longer exposure time (8.0 mmol/g), which is consistent with the adsorption results (Figure 5.4, 5.5). The selectivity, 1.2 for **CC3** and 1.8 for **6FT-RCC3**, which is also independent of the exposure time, are due to the larger pore aperture compared to the kinetic diameter of H_2 and D_2, which results in a rapid diffusion with no barriers through the channels. Differently, **6ET-RCC3** showed an increase in uptake for longer exposure time, indicating that diffusion was hindered and the adsorption process required sufficient time to reach equilibrium. The total uptake for **6ET-RCC3** at 30 K was only 0.8 mmol/g even after exposure for 300 min. At 30 K, the selectivity decreased with longer exposure time, from 3.9 to 3.3 between 10 and 300 min, which is typical for kinetic quantum sieving. In general, the kinetic quantum sieving effect is based on the diffusion limitation of the lighter isotope, but for longer exposure times, equilibrium can be approached for both isotopes. For **6ET-RCC3**, longer exposure time leads to an increase in gas uptake, but the selectivity decreases. At the beginning, D_2 is preferentially adsorbed by **6ET-RCC3**, but for longer exposure times when the equilibrium is approached, the saturation leads to a decrease in selectivity.

In summary, based on comparison of **CC3**, **6FT-RCC3**, and **6ET-RCC3** measured under identical experimental conditions, it has been shown that **6ET-RCC3** with the smallest pore aperture has the highest selectivity but small uptake while **CC3** and **6FT-RCC3** exhibit the high gas uptake amount but low selectivity due to the large cavity. Thus, an ideal structure should combine the two properties: large cavities offering the surface area for storing large amounts of deuterium combined with narrow pore aperture for increasing the separation effect via kinetic quantum sieving.

5.2 Enhanced Quantum Sieving in a Two-Component Cage Cocrystal

Single-component cage crystals either exhibited good selectivity but poor gas capacity (**6ET-RCC3**) or good gas capacity but poor selectivity (**CC3** and **6FT-RCC3**). For the optimal separation of isotopes, the ideal material should combine large cavities to store more D_2 along with a narrow pore aperture to increase the kinetic separation. Taking advantage of the chiral recognition assembly of discrete cage molecules, a cocrystal structure **Cocryst1** that combined two different cages (Scheme 5.3): **6ET-RCC3** chosen as the diffusion barrier, and **CC3** chosen as the partner cage to provide enough cavity for high gas adsorption has been designed.

5.2.1 Design of Cocrystal

Cocryst1（**CC3-*S*/6ET-RCC3-*R* Co-crystal**）**formation.**

CC3-*S* was dissolved in DCM (5 mg/mL) and added to an equivalent dichloromethane solution of **6ET-RCC3**-*R* at equal molar concentration (5.75 mg/mL). The solutions were mixed by direct addition at room temperature, with stirring. No precipitation was observed on mixing, but the solution became cloudy after approximately 10 minutes. The co-crystal, **Cocryst1**, was collected by filtration (Whatman® membrane filter PTFE, pore size 0.2 µm). Crystals suitable for single-crystal X-ray diffraction were cultured by vapor diffusion of acetone into the CHCl₃ solution of equal molar concentration **CC3**-*S* and **6ET-RCC3**-*R*.
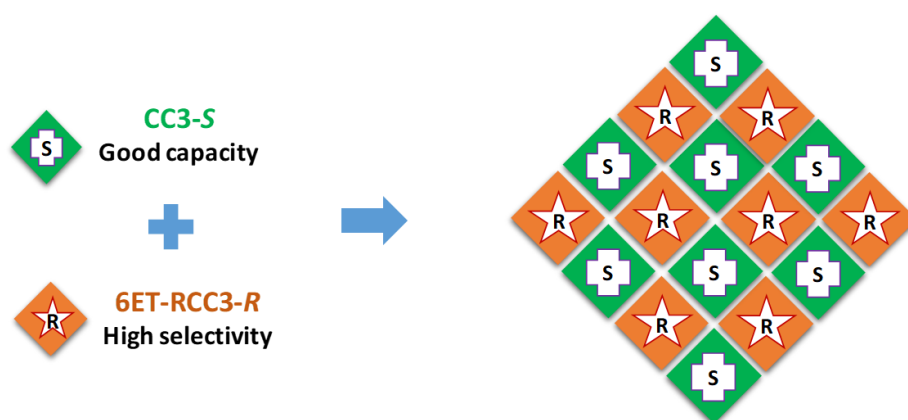
Scheme 5.3 2-dimensional scheme showing the cocrystal, **Cocryst1**, formed by chiral recognition between two cages **CC3** and **6ET-RCC3** to integrate capacity and selectivity in a single material.

Characterization

High-resolution synchrotron PXRD data for **Cocryst1**, (**CC3**-*S*/**6ET-RCC3**-*R*), was collected using the I11 beamline at Diamond Light Source (λ = 0.825015 Å), which is equipped with a Mython II position sensitive detector. This sample was loaded in a borosilicate glass capillary that was rocked to improve powder averaging during data acquisition. The crystal structure of Cocryst1 was determined by single-crystal X-ray diffraction. The characterization was performed by the group of Prof. A. I. Cooper.
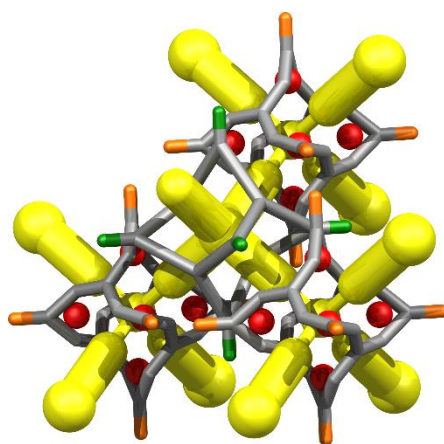
Figure 5.19 The simplified representation of the single-crystal structure of **Cocryst1**, with pore channels shown in yellow.
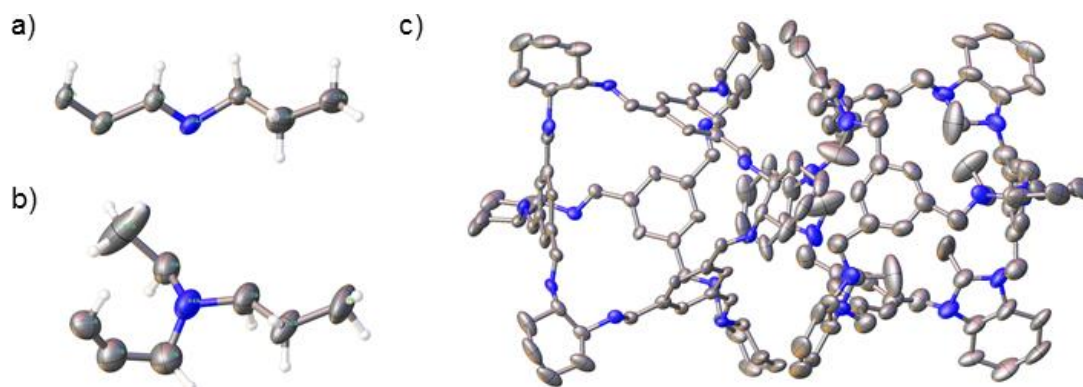
Figure 5.20 Displacement ellipsoid plots from the single crystal structure, **Cocryst1** (**CC3**-*S*, **6ET-RCC3**-*R*), showing the asymmetric units of a) **CC3**-*S* and b) **6ET-RCC3**-*R*. c) The window-to-window packing of **CC3**-*S* and **6ET-RCC3**-*R* cages (Grey, white, blue represent carbon, hydrogen, nitrogen atoms)[150].
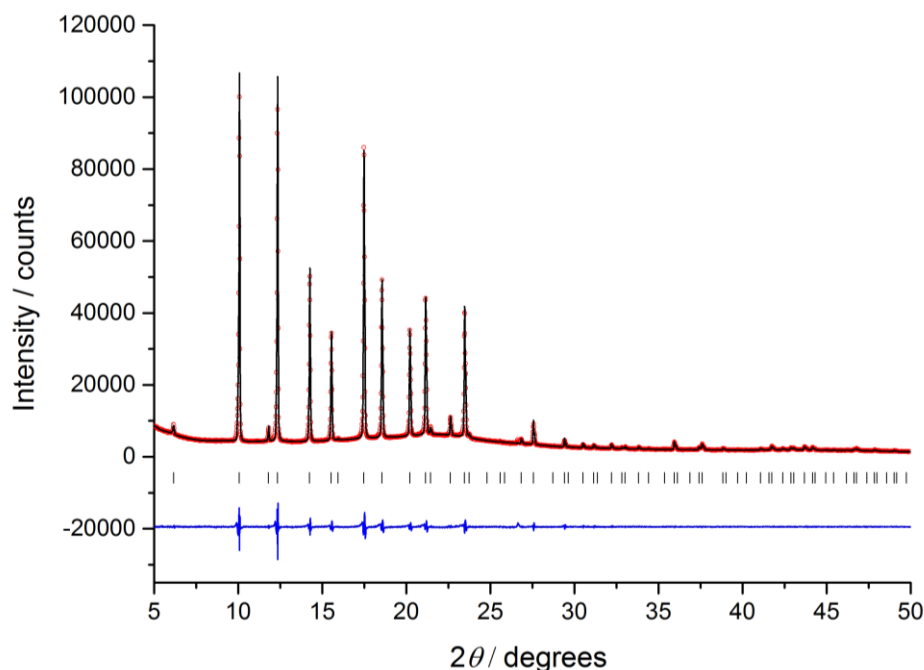
Figure 5.21 Le Bail fit for **Cocryst1** (**CC3**-*S*, **6ET-RCC3**-*R*) crystallised from CH_2Cl_2/acetone, activated under dynamic vacuum, and used for TDS measurements. X-ray diffraction (Cu-Kα) was recorded after removal of any adsorbed water from the crystal pores. The capillary was spun during the collection to improve powder averaging and the unit cell choice was based of refined single crystal data. Final observed (red), calculated (black) and difference (blue) PXRD profiles for Le Bail refinement ($Rwp = 3.857\%$, $Rp = 2.690\%$, $\chi^2 = 2.667$, $a = 24.846(2)$ Å, $V = 15338(2)$ Å^3, $T = 298$ K, $F4_132$)[150].

The crystal structure of the cocrystal is shown in Figure 5.19. The crystal structure was refined in the chiral cubic space group $F4_132$, and in the structure the *-R* and *-S* cage molecules are disordered over one position. Both cages were refined with site occupancies of 50%, and the idealized window-to-window packing of **CC3**-*S* and **6ET-RCC3**-*R* cages is shown in Figure 5.20. The Le Bail fit for determining the atomic structure and refining unit cell for **Cocryst1** has been carried out based on single-crystal X-ray diffraction data, shown in Figure 5.21. The cocrystal is characterized by the alternating small and large cavities. The methyl groups pointing the windows to restrict the pore diameter to around 2 Å in **6ET-RCC3**, whereas the storage cage offers a larger cavity size of 5.6-6.7 Å. The connection between the two cavities, formed by the window-to-window packing, consist of a large window of 4.5 Å followed by a small window of 1.9 Å. Since the cage cavities formed the nodes of the diamondoid pore network,

four **6ET-RCC3** cages surrounded each **CC3**. Guest molecules diffusing through the cocrystal are forced to traverse the small window of **6ET-RCC3**.

5.2.2 Results

Low-pressure, high resolution H_2 and D_2 adsorption isotherms

The **Cocryst1** has been studied using H_2 high-resolution adsorption experiments collected at 30, 40, 50, 60, 70 and 77K, presented in Figure 5.22. The H_2 uptake starts at 30 K with exhibiting a hysteresis. The amount absorbed at 1bar increases with temperature, reaching the maximum uptake at 40 K (6.6 mmol/g) and decreases again. The hysteresis becomes weaker with higher temperature. The typical type I isotherm showing no hysteresis can be observed at 50 K and above. Identical phenomena can be observed in D_2 isotherms, presented in Figure 5.23. The D_2 isotherms show in all cases a higher uptake compared to that of the H_2 due to the higher heat of adsorption of D_2.
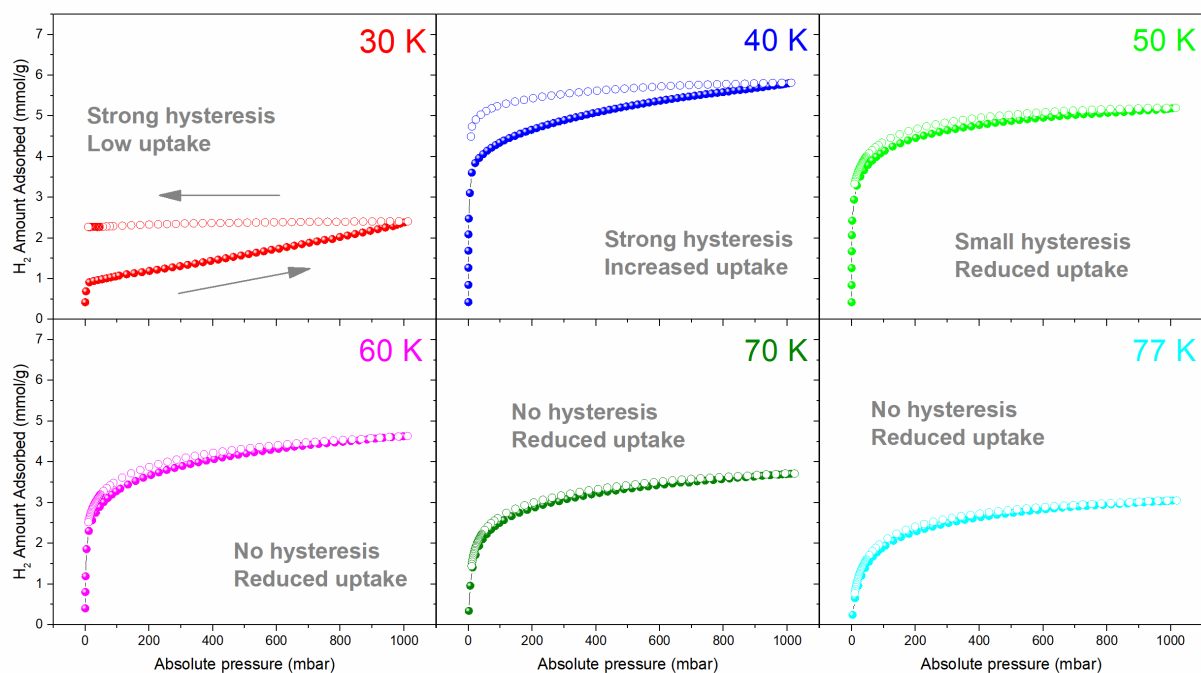
Figure 5.22 Hydrogen adsorption (closed) and desorption (open) isotherms of **Cocryst1** at various temperatures, 30 K (red), 40 K (blue), 50 K (green), 60 K (pink), 70 (olive), and 77 K (cyan).
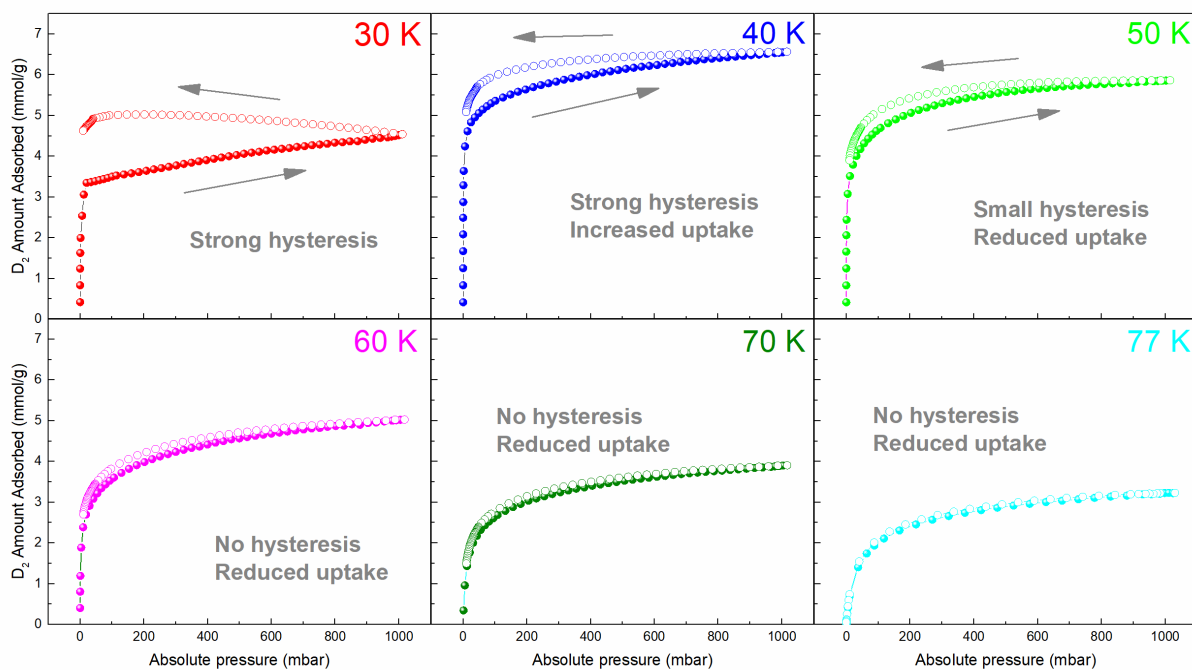
Figure 5.23 Deuterium adsorption (closed) and desorption (open) isotherms of **Cocryst1** at various temperatures, 30 K (red), 40 K (blue), 50 K (green), 60 K (pink), 70 (olive), and 77 K (turquoise).
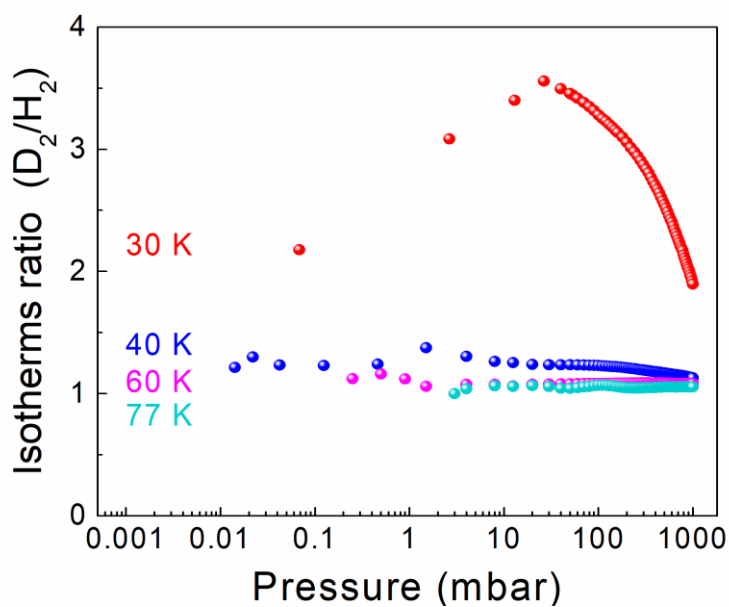
Figure 5.24 D_2/H_2 isotherm ratio as function of pressure for different temperatures, 30 K (red), 40 K (blue), 60 K (pink), and 77 K (turquoise).

The molar ratio of D_2/H_2 can be calculated from the pure gas isotherms. The D_2/H_2 ratio for each point of the isotherm as a function of the pressure is presented in Figure 5.24. **Cocryst1** exhibited a maximum value of 3.5 in the D_2/H_2 uptake ratio at 30 K and 25 mbar, which is one of the largest values ever measured by pure-gas-adsorption isotherms[154-155, 157-159].

TDS study for pure gas physisorption

Encouraged by the ratio of adsorbed amount of D_2 over H_2, directly separation is investigated by TDS. The selectivity determined by directly separating isotopes from a mixture is assumed to be larger than the D_2/H_2 uptake ratio from the adsorption experiments. This can be ascribed to favored adsorption of D_2 on the surface, as well as faster diffusion of heavier isotope into the nanopores.
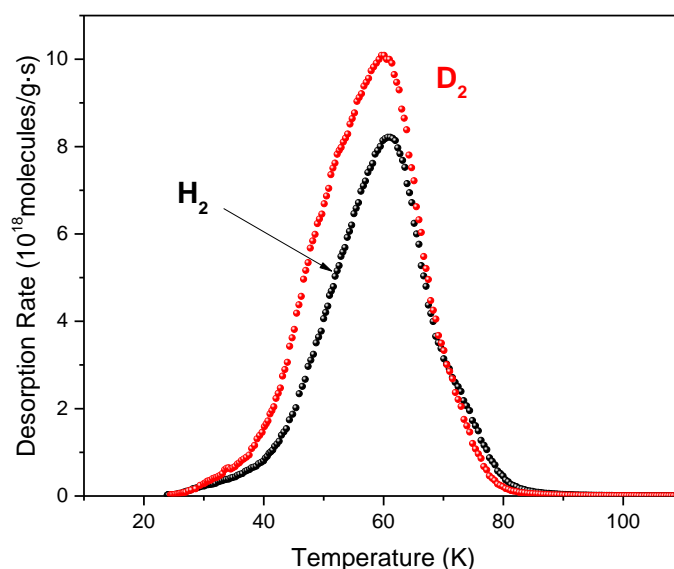
Figure 5.25 Pure gas H_2 (black) and D_2 (red) thermal desorption spectra of **Cocryst1** exposed to a 10 mbar pure isotope at room temperature, then cooling to 20 K.

Prior to the actual gas separation investigation, the H_2 and D_2 adsorption in the cocrystal cage has been applied to a pure gas of H_2 and D_2 atmosphere, utilizing cryogenic TDS measurements. All the degassed samples have been exposed to 10 mbar pure gas at room temperature. After cooling below 20 K, the unabsorbed gas molecules were evacuated, then the desorption spectra were recorded with a linear heating ramp of 0.1 K/s, resulting the TDS spectra shown in Figure

5.25. As a combination of **CC3** and **6ET-RCC3**, the resulting **Cocryst1** exhibits only one desorption peak with the maximum centered at 60 K for both isotope gases. In contrast, the **CC3** shows one maximum at 55 K, while the **6ET-RCC3** possesses there different desorption maxima. The gas molecules in the small and large cavities cannot desorb independently in cocrystal due to the existence of alternating cavity structure. The desorption spectra **Cocryst1** therefore exhibit only one desorption maximum.

TDS study for isotope separation
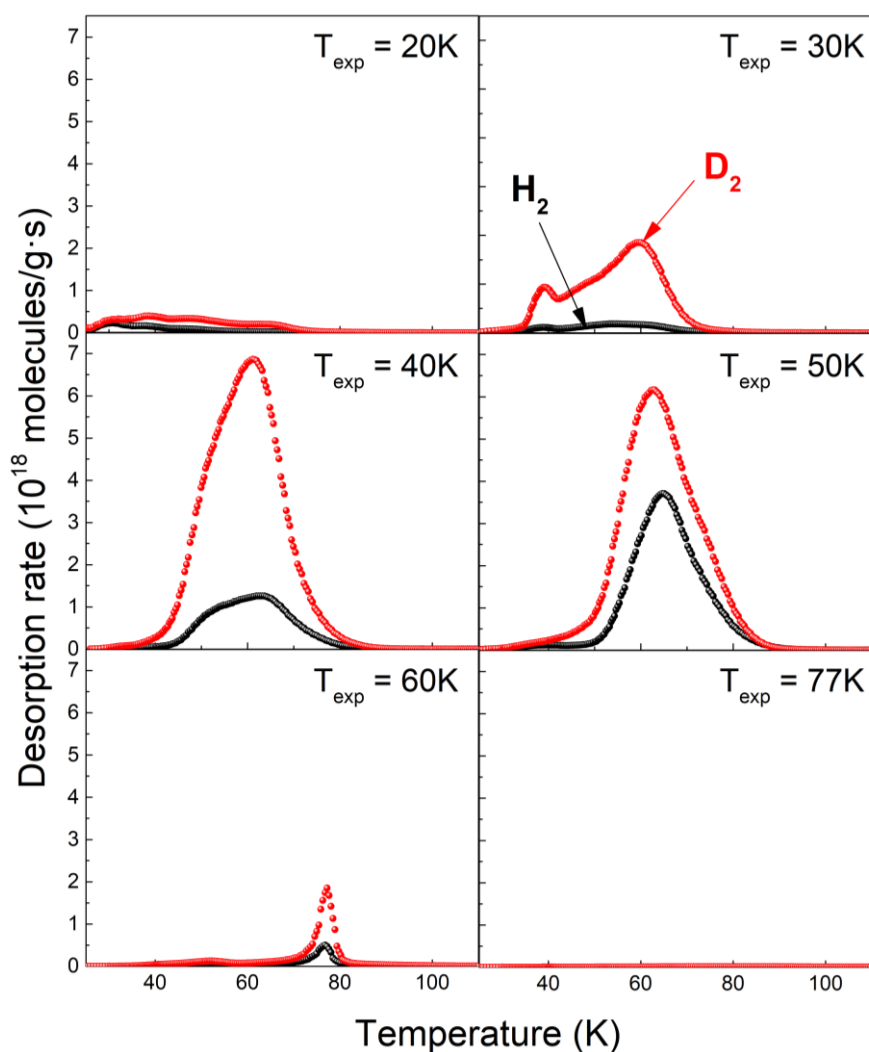
Figure 5.26 H_2 (black) and D_2 (red) desorption spectra of 10 mbar 1:1 D_2/H_2 mixture exposure on **Cocryst1** at exposure temperature of 20, 30, 40, 50, 60, and 77 K.

The **Cocryst1** was exposed to 10 mbar of 1:1 D_2/H_2 mixture for 30 min at various exposure temperatures of 20 to 77 K. The resulting TDS spectra are shown in Figure 5.26. The adsorbed isotope gases and the corresponding selectivity as function of exposure temperature has been given in Figure 5.27. Similar to the pure gas TDS spectra, only one maximum can be observed for each isotope. At T_{exp} = 20 K, nearly no desorption of hydrogen isotopes is detected. The uptake in the nanopores after exposure to a gas mixture then rises with increasing exposure temperature, until maximum of D_2 is reached at 40 K, meanwhile the maximum of H_2 uptake appears at 50 K. The uptake decreases again till no desorption peak can be observed at 77 K. The decreasing gas uptake at higher temperatures is due to the evacuation at the exposure temperature, releasing the molecules which are weakly attached on the surface. Meanwhile, the selectivity exhibits a maximum, where $S_{D2/H2}$ = 7.7, at 30 K, before it drops for higher exposure temperatures between 30 and 50 K.
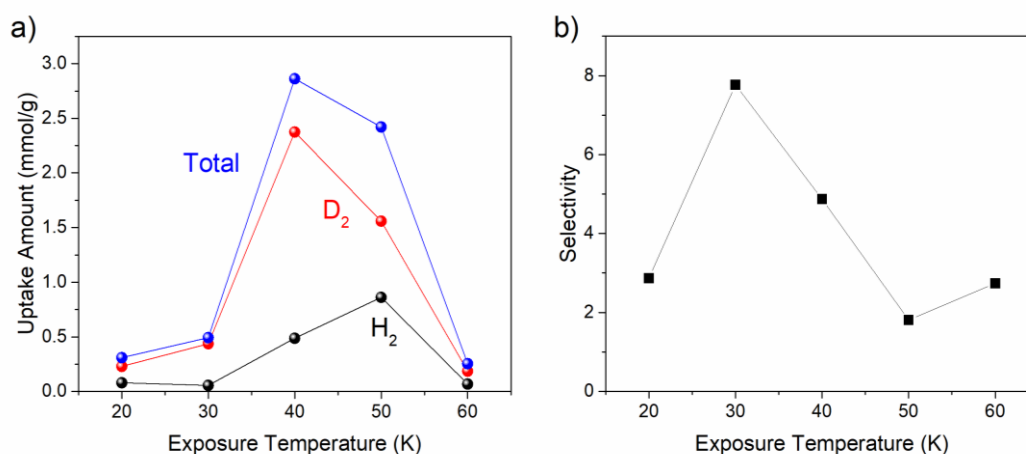
Figure 5.27 a) The adsorbed amount of isotope gases (H_2 black, D_2 red) and their total amount (blue) as function of exposure pressure on **Cocryst1**. b) The D_2/H_2 selectivity as function of exposure pressure.
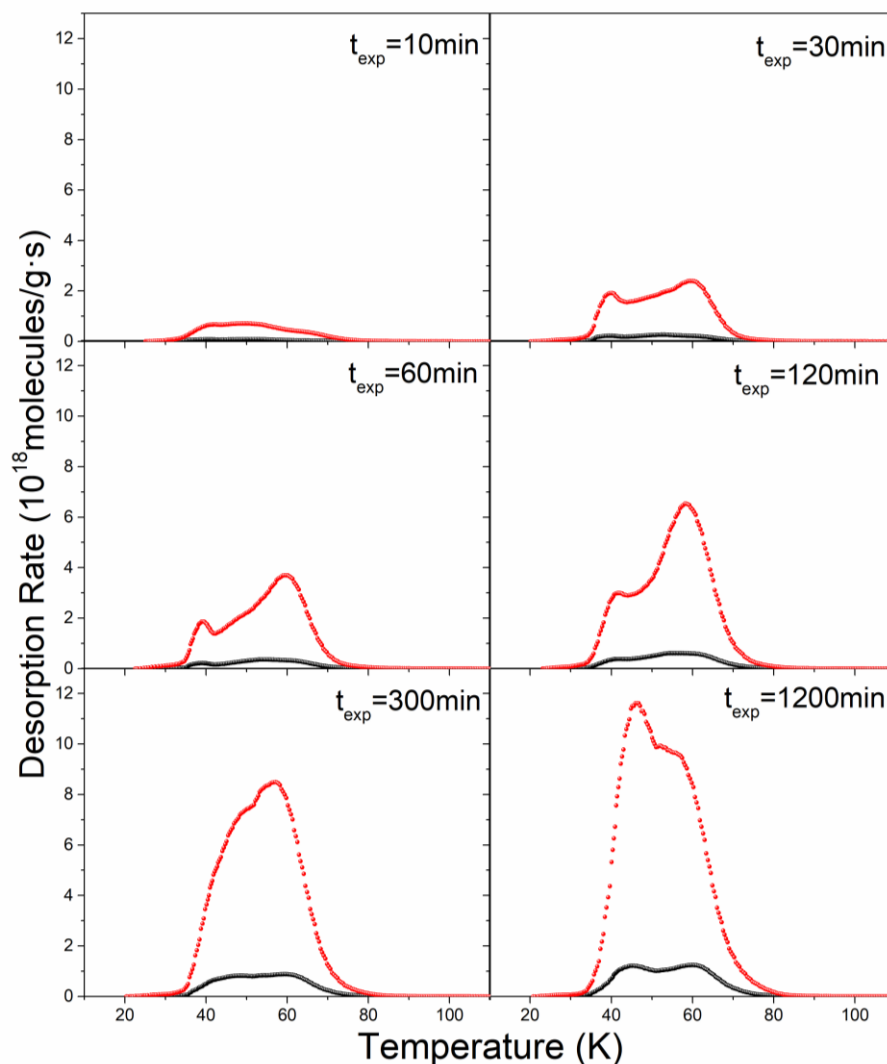
Figure 5.28 a) H_2 (black) and D_2 (red) desorption spectra of 10 mbar 1:1 D_2/H_2 mixture exposure on **Cocryst1** at exposure temperature of 30 K for various exposure time (10-1200 min).

According to the results obtained from adsorption isotherms and the TDS spectra, the **Cocryst1** shows the highest selectivity at low T_{exp} of 30 K. Thus, further TDS measurements have been carried out at 30 K and the H_2 and D_2 spectra for various exposure times have been presented in Figure 5.28 after the sample being exposed to 10 mbar equimolar hydrogen isotope mixture for 10 – 1200 min. The desorption spectra exhibit two desorption maxima for both isotopes centered at 35 and 60 K, respectively. The intensity of the D_2 desorption peak is rising dramatically compared to that of H_2 with longer exposure time. The observed dependence on exposure time reveals that the diffusion is hindered. As shown in Figure 5.29, the D_2 uptake is significantly enhanced from 0.40 to 4.71 mmol/g with exposure time increasing from 10 to 1200

min. In the meantime, the selectivity slightly drops with longer exposure time, from 8.2 to 7.8, revealing a kinetic quantum sieving effect. In addition, the total gas uptake remains approximately constant after exposure time of 600 min, indicating a complete penetration of the cocrystal particles. The H_2/D_2 separation properties of **Cocryst1** are excellent with the selectivity $S_{D2/H2} \sim 8.0$, combined with a greatly enhanced D_2 uptake with respect to **6ET-RCC3** (0.7 vs 4.7 mmol/g).
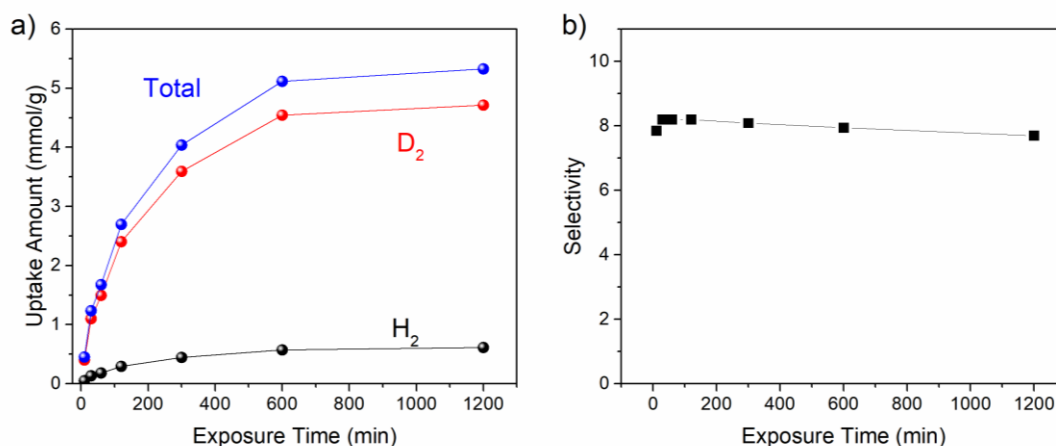
Figure 5.29 a) The adsorbed amount of isotope gases (H_2 black, D_2 red) and their total amount (blue) as function of exposure time on **Cocryst1**. b) The D_2/H_2 selectivity as function of exposure time.

5.2.3 Discussion

Hydrogen isotope adsorption in cocrystal cage

The cocrystal **Cocryst1** is a combination of the two single-component cages, **CC3** showing good adsorption capacity due to the large capacity, and **6ET-RCC3** possessing small pore aperture to enable the diffusion barrier for hydrogen isotopes, resulting in good selectivity.

The H_2 adsorption isotherm at 30 K shows a strong hysteresis, indicating the equilibrium is not fully reached within the measurement time, since the gas molecules cannot penetrate into the structure at such low temperature. For isotherms measured at higher temperatures, the hysteresis becomes weaker and eventually vanishes. The isotherms are fully reversible above 70 K, indicating that the isotherms are much closer to equilibrium at higher temperatures. This better

equilibrium denotes that both H_2 and D_2 molecules diffuse faster in the channels. Interestingly, the amount adsorbed increases with decreasing pressure during the desorption experiment at 30 K. This higher desorption curves compared to adsorption indicates that diffusion of gas molecules into material are still ongoing when the experiment is already decreasing the pressure. A similar behaviour can also be observed in **6ET-RCC3**, in the isotherms collected at 30, 40 and 50 K for both H_2 and D_2 gas, as shown in Figure 5.9 and 5.10.

The maximum uptake of **Cocryst1** is 5.2 mmol/g for H_2 and 6.5 mmol/g for D_2, respectively. Considering the maximum uptake corresponds to the crystalline pore volume available for adsorption, **Cocryst1** is supposed to have the averaged available voids from **CC3** and **6ET-RCC3,** as an assembled cocrystal with 1:1 ratio of the two component cages. The maximum uptake in **CC3** is 7.6 and 8.0 mmol/g for H_2 and D_2, and for the **6ET-RCC3** is 3.8 and 4.5 mmol/g for H_2 and D_2, respectively. The mean value of the uptake in these two cages is 5.7 mmol/g for H_2 and 6.3 mmol/g for D_2, which is in good agreement with the maximum uptake of **Cocryst1**. Noted the small variation of the uptake is mainly attributed to the lack of equilibrium in this cocrystal within experiment time, thus the maximum uptake can be affected.

Temperature-dependent opening of the pore aperture

As discussed above, the better equilibrium observed at higher temperatures indicates a faster diffusion of hydrogen molecules, denoting a temperature-dependent flexibility of **Cocryst1**, where the effective pore aperture becomes larger with higher temperature. Similar adsorption behavior has also been observed in **6ET-RCC3** (Figure 5.6, 5.7). The hysteresis is high at temperatures lower than 70 K, because of the large diffusion barrier; at higher temperatures, a temperature-dependent opening of the aperture allowed both H_2 and D_2 molecules to diffuse faster. The maximum is then reached at 60 K. However, the desorption part of the **Cocryst1** isotherms show a hysteresis much smaller compared to that of **6ET-RCC3**, with the maximum observed at 40 K, meaning a better equilibrium that implies a faster diffusion in the channels for this cocrystal, which is the result of the combination of the diffusion barrier of the **6ET-RCC3** with the high gas adsorption of the **CC3**.
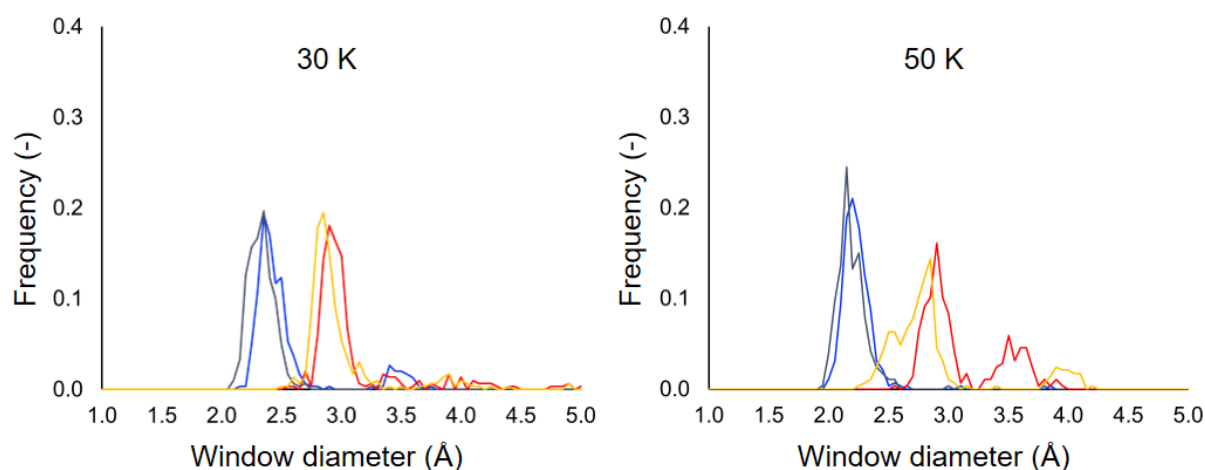
Figure 5.30 Time-averaged, window-size envelopes for all four windows of the same cage molecule obtained from a 300-ps MD trajectory, sampled every 1 ps, at 30 K or 50 K at 1 bar. Among the four cage windows, two have two methyl groups at the window (colored in grey and blue, respectively) and the other two have one methyl group at the window (colored in red and yellow, respectively)[150].

Based on the temperature-dependent gate-opening demonstrated from isotherms, the time-averaged window-size distributions for a cage molecule in the periodic cocrystal structure have been illustrated by Dr. L. Chen from Prof. Cooper's group, sampled from molecular dynamics trajectories at 30 K and 50 K. Presented in Figure 5.30, all four windows in one cage molecule exhibit an increase in the window size and flexibility, as the temperature increases. In time-averaged window-size distribution, the increase of the aperture size is demonstrated by the peaks i) shifting centers to a larger window diameter; ii) becoming broader and iii) appearance of additional new peaks. The window having one methyl group, colored in red and yellow at 30 and 50 K, respectively, becomes broader and shifts to larger window diameter at 50 K than 30 K. In addition, a new peak at 3.5 Å indicates an additional mode at 50 K, while the same window has only a narrow distribution of diameters centered at around 3.0 Å at 30 K.

Diffusion kinetics of hydrogen isotopes

The diffusion limitation governs the adsorption/desorption process in **Cocryst1**. TDS measurements have been applied to reveal the dependence of isotope separation performance on exposure time. The total gas uptake increases dramatically from 0.4 to 5.4 mmol/g with longer exposure time from 10 to 600 min. For longer exposure time in **Cocryst1**, the uptake

remains constant, implying that the gas molecules penetrate the structure, leading to a complete penetration into the structure.

Additionally, the kinetic quantum sieving effect and the selectivity decrease with time until the gas uptake is fully saturated. The kinetic quantum sieving effect is based on the diffusion limitation of the lighter isotope, but for longer exposure times, equilibrium can be approached for both isotopes as explained previously. For **Cocryst1**, longer exposure time leads to an intensive increase in gas uptake, while the selectivity decreases slightly. The TDS spectra of hydrogen and deuterium obtained after different exposure times and temperatures represent the adsorption process under those specific exposure conditions. Hence, the selectivity as a function of exposure time and temperature reflects the gas penetration and adsorption. The increasing selectivity with decreasing exposure temperature for **Cocryst1** indicates that the aperture is close to the optimal size for kinetic quantum sieving at 30 K.

The kinetics of pure H_2 and D_2 gas uptake at exposure temperature of 30 K can be studied by applying different exposure times, from 10 to 1200 min. The resulting spectra are shown in Figure 5.31. **Cocryst1** shows a more remarkable increase in D_2 uptake for longer exposure time, compared to that of H_2. The adsorbed amount of D_2 and H_2 for exposure of various times has been summarized and presented in Figure 5.32. The adsorption amount of D_2 is almost identical for loading times in the range from 600 min to 1200 min, which indicates that after 10 hours the voids are saturated, while the adsorbed amount of hydrogen obviously increases for longer exposure times, which implies a stronger diffusion barrier for hydrogen than deuterium. In other words, D_2 reaches saturation much faster, it likely has a much higher diffusion rate in the channel of cocrytal than H_2.
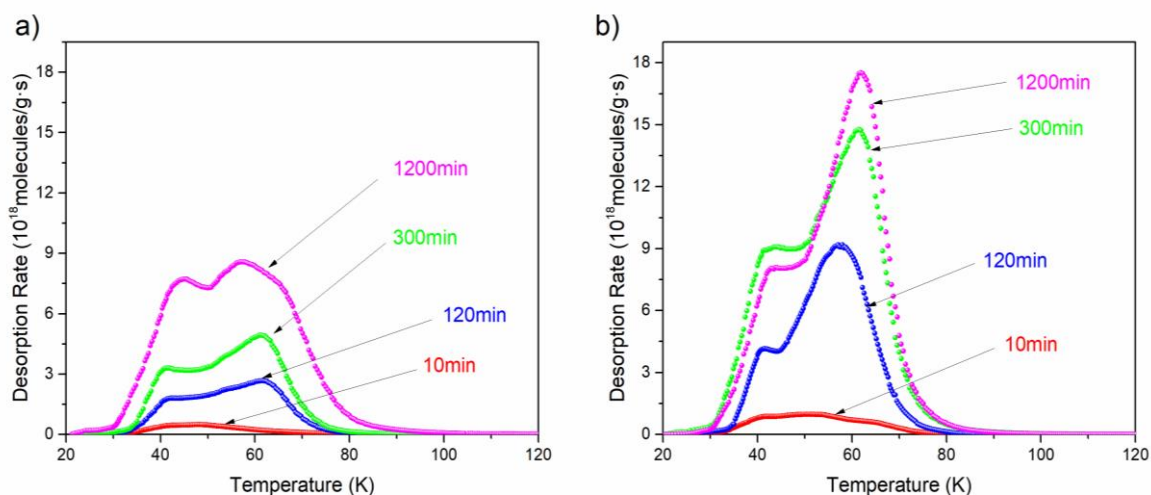
Figure 5.31 a) Hydrogen and b) deuterium desorption spectra obtained for different exposure times, 10 (red), 120 (blue), 300 (green) and 1200 (magenta) min. **Cocryst1** is exposed to 10 mbar hydrogen and deuterium pure gas separately at 30 K.
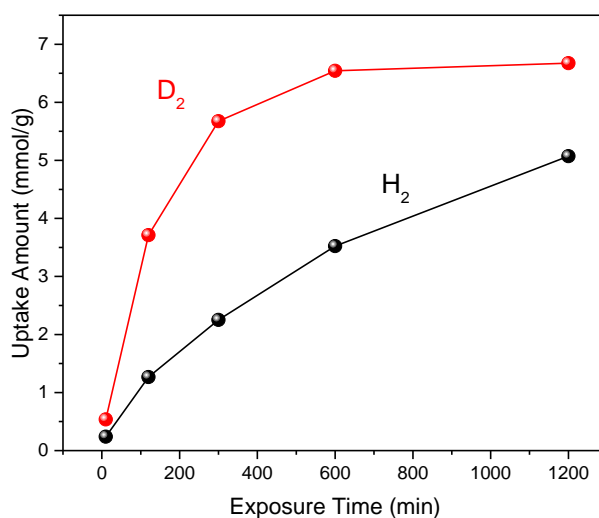
Figure 5.32 The corresponding amount of adsorbed H_2 (black), D_2 (red) pure gas at 30 K for **Cocryst1** as functions of exposure time.

Application for HD Separation

Additonally, HD separation, which is important for technique application, has been performed. At present, all of the isotope mixture separation studies are carried out only taking account of

H_2 and D_2 mixtures. However, deuterium is produced from heavy water which is separated out from water by GS process or distillation. The result is a mixture of H_2, D_2 and HD, which requires further purification. In addition, the naturally abundant deuterium appears mainly in the form of HD molecule[160]. Thus, based on the experimental results so far, the separation experiments are performed on an isotope mixture of H_2/HD/D_2 with a ratio 1:3:1. TDS measurements are carried out with this H/D of 10 mbar mixture at 30 K for 60 and 120 min, respectively. The resulting spectra are presented in Figure 5.33.
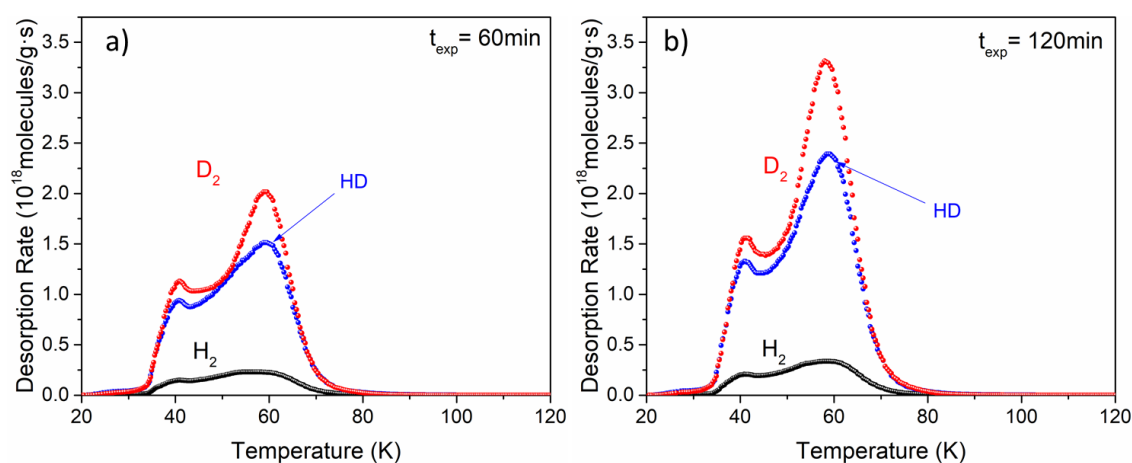
Figure 5.33 H_2 (black), HD (blue) and D_2 (red) desorption spectra of 10 mbar 1:3:1 D_2/HD/H_2 mixture exposure on **Cocryst1** at exposure temperature of 30 K for a) 60 min, b) 120 min.

Two desorption maxima can be observed, centered at 40 K and 60 K for all the three types of molecules. The desorption peak of D_2 is more intense than that of HD and H_2, even though the majority of the exposed mixture is HD. It clearly shows the faster diffusion kinetics of D_2, implying the lowest diffusion barrier. Based on quantum sieving, the heavier isotope is more favorably adsorbed and can diffuse faster compared with respect to the lighter ones. The selectivity $S_{D2/HD}$ is 4.6, while $S_{HD/H2}$ is 2.3. Furthermore, with longer exposure time of 120 min, the selectivity $S_{D2/HD}$ and $S_{HD/H2}$ remain 4.8 and 2.4, respectively, with an increase in total gas uptake from 1.6 to 2.3 mmol/g. The results imply that the cage cocrystal can also be a good candidate for D_2/HD/H_2 separation via kinetic quantum sieving.

5.2.4 Enhanced Quantum Sieving Performance

Comparison of the single-component and cocrystal cages

As discussed above, **Cocryst1** exhibits the combined adsorption and separation properties from both single-component cages **CC3** and **6ET-RCC3**. Simulations have been employed by Cooper Group to provide insights into the mechanism for hydrogen isotope separation by the porous organic cages. Diffusion of the hydrogen isotopes in **CC3**, **6ET-RCC3** and **Cocryst1** have been investigated and interpreted by comparison of the free-energy barriers for H_2 and D_2 in a given crystal structure at infinite dilution. In the transition state theory approximation, molecular diffusivity can be derived from a rate constant for the molecule hopping over the free-energy barrier.
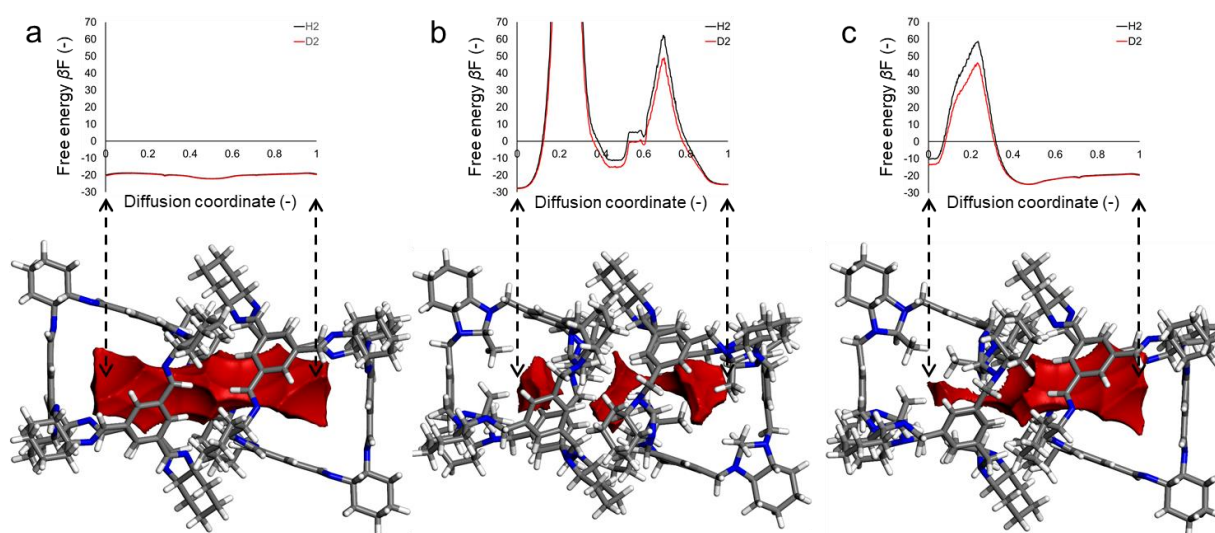
Figure 5.34 Simulated free energy profiles of a single H_2 or D_2 molecule diffusing between the centers of mass of two neighboring cage molecules for a) **CC3**, b) **6ET-RCC3**, and c) **Cocryst1**, respectively. Grey, white and blue atoms represent carbon, hydrogen and nitrogen, respectively; pore spaces inside the cage molecules, defined by a spherical probe with diameter 2.2 Å, are colored in red[150]. The simulation was conducted by Cooper Group.

Figure 5.34 shows the free-energy profile for a diffusion pathway between the center of mass of a cage molecule and the center of mass of a neighboring cage, travelling across two cage windows. The diffusion pathway in Figure 5.34b runs through a **6ET-RCC3** cage window with two methyl groups (left cage) and a second **6ET-RCC3** cage window with one methyl group

(right cage); the diffusion pathway in Figure 5.34c runs through a **6ET-RCC3** cage window with one methyl group (left cage) and a neighboring **CC3** cage window (right cage). In **CC3**, both H_2 and D_2 move easily between the two cage molecules in an almost barrier-free way. By contrast, in **6ET-RCC3**, the cage cavities are congested by the methyl groups and have narrow window apertures, which results in sharply peaked free-energy barriers, strongly decreasing the molecular diffusivity compared to **CC3**. Noted when two methyl groups are located in a single **6ET-RCC3** cage window, the pore space becomes disconnected and the diffusion barrier becomes too large to cross (off-scale in Figure 5.34; cage on the left). For windows with only one methyl group (Figure 5.34, cage on the right), the pore space runs through continuously between the cages and the free-energy barriers for H_2 and D_2 are lowered significantly. Crucially, **6ET-RCC3** cage windows containing one methyl group provide diffusion barriers that are different for D_2 and H_2, thus acting as a kinetic sieve; this feature is also carried over into **Cocryst1** (Figure 5.34). In **Cocryst1**, the large **CC3** cavities also provide good dynamical relaxation, resulting in improved D_2 kinetics and higher D_2 uptakes.

Enhancement of separation and adsorption

The strategy combining two porous cages in a cocrystal: the small-pore cage for good D_2/H_2 selectivity ($S_{D2/H2}$ = 3.9 at 30 K, **6ET-RCC3**), and a large-pore cage to increase gas capacity (8 mmol/g, **CC3**). This **Cocryst1** shows much improved gas capacity (4.7 mmol/g) compared to **6ET-RCC3** (0.8 mmol/g). Remarkably, however, the D_2/H_2 selectivity is also greatly enhanced to around 8 at 30 K. Since the selectivity is expected to be governed by the small pore apertures in **6ET-RCC3** due to the diffusion limitation, the enhancement in selectivity **Cocryst1** ($S_{D2/H2}$ = 8.2) compared **6ET-RCC3** ($S_{D2/H2}$ = 3.9) seems counterintuitive.

This can be ascribed to significant difference in the structure of the two materials. The small-pore materials permit only single-file gas diffusion, while the cocrystal allows mixing of the gas molecules in the alternating large and small pores. The small channels of **6ET-RCC3**, possessing the cavity volume of only 29.5 $Å^3$, lead to a single-file filling. Once a molecule penetrates in the pore, no exchange between the isotopes in the channels is possible. Hence, the desorption after exposure to a 1:1 mixture exhibits identical maximum temperatures for both isotopes (Figure 5.9)—the gas molecules leave in the order they entered—whereas the maximum for pure gas desorption appears lower for D_2 than for H_2 (Figure 5.8). This reveals that the KQS occurs only at the entrance of pore apertures on the cage crystal surface, without

further exchange once inside the channels. The single-file filling has been reported by Mondal et al[161]. on isostructural hexagonal metal-organic frameworks having 1-D channels, IFP-4 and -7. The hydrogen isotopes only enter the channel of IFP-4 and -7 with the pore aperture of 1.7 and 2.1 Å, respectively, due to a temperature dependent gate-opening. The poor selectivity less than 2 can be observed in both materials which can be explained by the 1-D channels structure: The small pore volumes prevent passing of hydrogen isotopes within the narrow channel, quantum sieving therefore only occurs at the outermost pore aperture.
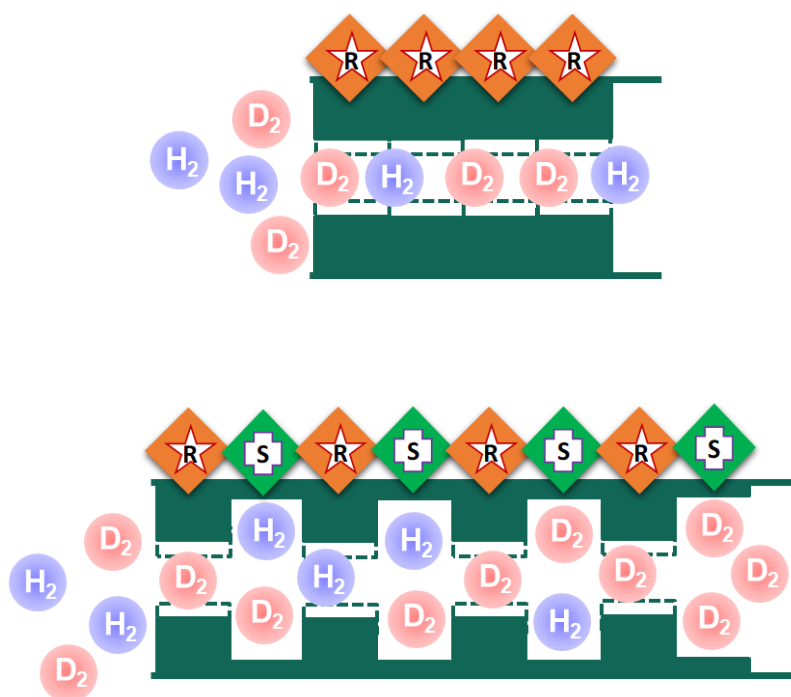
Scheme 5.4 Mechanisms for the isotope separation in cages, single-file kinetic quantum sieving in **6ET-RCC3** (upper), multiple kinetic quantum sieving in **Cocryst1** (bottom).

By contrast, **Cocryst1** consists of a combination of large storage pores and small separation pores, separated by a differential diffusional barrier, as shown by molecular simulation in Figure 5.34c. Penetration through the small apertures into the next larger cavity yields an additional sieving effect, whereby D_2 molecules can pass neighboring H_2 molecules inside the large cavity of 186.9 $Å^3$, unlike in the single-file pores of **6ET-RCC3**. As a result, although there were half as many small windows as in **6ET-RCC3**, **Cocryst1** has greatly enhanced D_2/H_2 selectivity, when both gases need to pass through the alternating small-pore-large-pore network to give the multiple sieving effect. Similar behavior has been observed in MFU-4 reported previously by

Teufel et al.[155], which possesses the characteristic framework topology of alternating small and large pores (inner diameters of 3.88 Å and 11.94 Å), connected by a narrow aperture (2.52 Å). The isotopes can pass each other in the large pore and penetrate into the neighboring pore, leading to a further sieving step. The two different separation mechanisms of single-file filling and multi-KQS are illustrated in scheme 5.4.

Comparison of the separation effectiveness via kinetic quantum sieving

The effective isotope separation in **Cocryst1** can be achieved in the presence of kinetic barriers that enable the separation by KQS. The additional presence of large cavities in the structure offers the required surface area for gas molecules adsorbed inside. The practical experimental selectivity of 8 for an equimolar isotope mixture obtained in **Cocryst1** (4.5 mmol/g D_2 uptake) is one of the highest reported $S_{D2/H2}$ experimental values among various porous adsorbents via KQS, as shown in Figure 5.35 and Appendix C, which indicates a possible alternative to the conventional isotope-separation techniques. All the data are collected from literatures where the selectivity is measured with 1:1 hydrogen isotope mixture, and the selectivities are plotted as a function of gas uptake amount. The results from this thesis are also included in the figure. Most of the investigated samples exhibit the D_2 uptake lower than 1 mmol/g and a selectivity less than 3, which is close to the separation performance from conventional techniques. For industrial usage of isotope separation, the nanoporous sieves should not only have a high selectivity but additionally large uptake amount of the obtained deuterium.
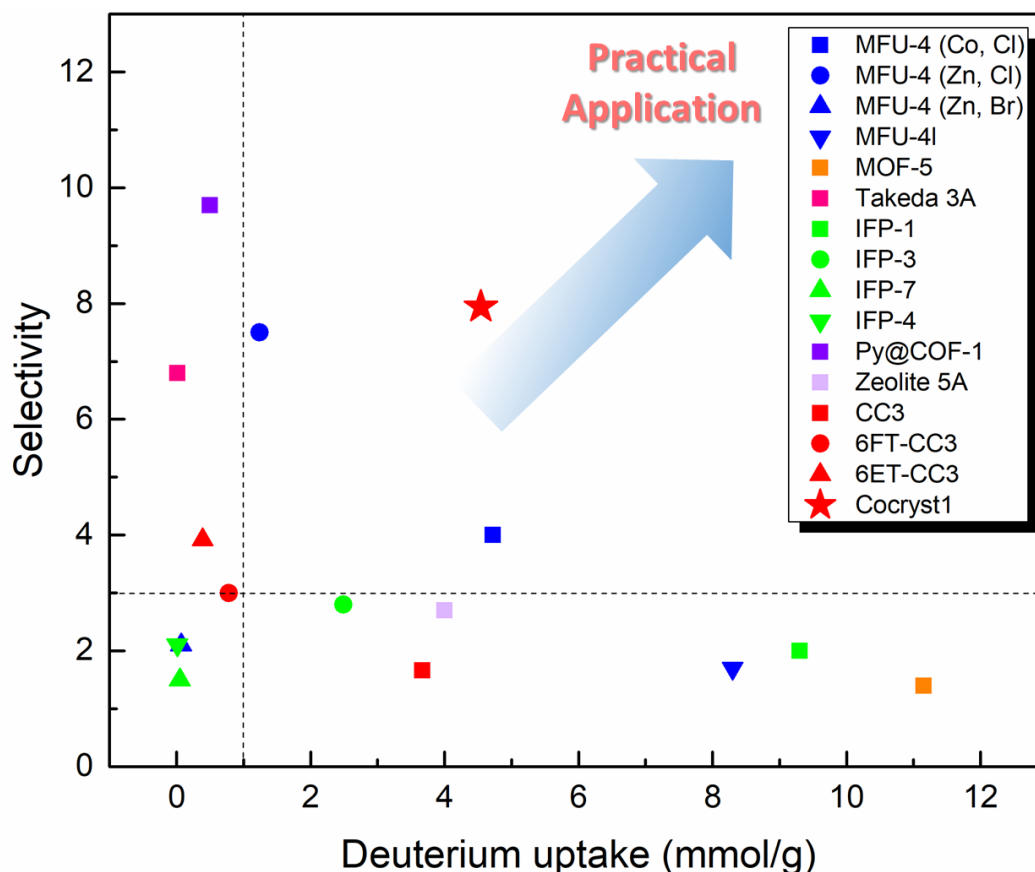
Figure 5.35 Summary of hydrogen isotope KQS selectivities and adsorption capacities for various porous materials. The list includes carbon (Takeda 3A[162], MOFs (MFU-4[155, 162-163], MOF-5[162], IFP[161]), COFs (Py@COF-1[154]), zeolite 5A[164], and porous organic cages (**CC3**, **6FT-CC3**, **6ET-CC3**, **Cocryst1**).

Taken individually, neither the uptake nor the selectivity value is highest reported value. However, the practical application of a KQS adsorbent will be a combination of its high selectivity and its high capacity at the same time. For various porous materials, the high selectivity can be achieved by the presence of kinetic barriers from small pore aperture that enable KQS effect, such as Py@COF-1. However, the small cavity cannot offer the required surface area for physisorption of gas molecules inside the framework, leading to a small uptake. On the other hand, for materials possessing large cavities, for example IFP-1 (4.2 Å), the gas uptake is capable for practical applications, while the poor selectivity prevents these adsorbents being used in isotope-separation. On this basis, the cage cocrystal therefore shows the most promising performance for technical applications.

5.3 Summary

In this chapter, the separation of hydrogen isotopes has been investigated for the first time on a novel class of nanoporous materials, porous organic cages. As discrete molecules with intrinsic cavities, the pore aperture size can be precisely tuned by placing different functional groups inside the molecular structure, without altering its solid-state packing and the pore structure.

For kinetic quantum sieving, well-defined pore aperture size in the range of the kinetic diameter of H_2 molecules plays an important role. The aperture size of the chosen series of cage structures can be fine-tuned in range between 3.5 to 1.95 Å, which is a desirable range for hydrogen isotope separation by KQS. The aperture size of the chosen cages is 4.5 Å, 3.4 Å, and 1.9 Å for **CC3**, **6FT-RCC3**, and **6ET-RCC3**, respectively. **CC3** and **6FT-RCC3** showed similar adsorption amounts for both H_2 and D_2, ~8 mmol/g. Both cages with large cavities presented poor D_2/H_2 selectivities of 1.2 and 1.8, respectively. For **6ET-RCC3**, even though the pore aperture is normally smaller than the kinetic diameter of hydrogen molecule, the temperature-dependent gate opening effect of the small pore aperture enabled the penetration of the gas molecules into the cavity with increasing temperature. The highest selectivity of 3.9 was observed at exposure temperature of 30 K and decreased to 3.3 for longer exposure time, revealing KQS effect. However, the small pore cage shows good selectivity but very little uptake.

For optimal separation and adsorption performance, a cocrystal structure, possessing alternating large and small cavities, was designed. By chiral recognition, **Cocryst1** was synthesized combining **CC3** and **6ET-RCC3**. The cage with finest aperture is chosen as a diffusion barrier for effectively blocking H_2 diffusion, resulting in the KQS effect, while the cage with large cavity provides enough space for high isotope gas adsorption. The experimental results show that the diffusivity of D_2 is much higher than that of H_2 at low temperatures which is attributed to quantum effects. Therefore a selectivity of 8 combined with 4.5mmol/g deuterium uptake is obtained at 30 K, which is the best combination of selectivity and gas uptake compared to other kinetic quantum sieves reported in literatures. Effective isotopes separation in the cocrystal structure was contributed by the presence of small apertures, while large cavities in the structure offer the required surface area for physisorption of gas molecules inside the cages. In addition, for the first time, HD separation from hydrogen isotopes has also been investigated. The

selectivity of $S_{D2/HD}$ and $S_{HD/H2}$ are 4.8 and 2.4, respectively, revealing that the cocrystal can be used for separating HD from H_2 and D_2.

The selectivity for **Cocryst1** is much larger than that for **6ET-RCC3**, even though good selectivity is typically related to a higher concentration of small pore apertures. Inside the narrow pore channel of **6ET-RCC3**, the selective adsorption only occurs at the entrance of the aperture and hydrogen isotopes cannot pass each other. Thus, the low selectivity is ascribed to this single-file filling. By contrast, **Cocryst1** consists of a combination of large storage cavities and small separation apertures. Penetration through the small apertures into the next larger cavity yielded an additional sieving step, whereby D_2 molecules can pass neighbouring H_2 molecules, unlike in the single-file pores of **6ET-RCC3**. As a result, **Cocryst1** had greatly enhanced D_2/H_2 selectivity, due to a multi-KQS effect from this alternating large and small pores.

6. Dynamic Opening of Apertures in MOFs for Enhancing Hydrogen Isotope Separation

For hydrogen isotope separation by kinetic quantum sieving, the aperture size plays a vital role in efficient separation. Among various porous matierials, metal-organic frameworks (MOFs), with exceptional surface area, tunability of pore size and functionality, has received increasing attention. However, due to the weak binding energies of hydrogen isotopes on the inner surface of porous materials, the high separation performance can only be observed at near zero-coverage pressure, which is not suitable for practical application. To enhance the operating pressure, MOFs with flexible structure and dynamic properties emerge as good candidates.

In this chapter, a hydrogen isotope separation strategy using a partially fluorinated MOF(Cu), FMOFCu has been studied via various techniques such as neutron powder diffraction, low-pressure high-resolution hydrogen and nitrogen BET and thermal desorption spectroscopy. The operating pressure and temperature are enhanced by using temperature-dependent flexibility of the unique tri-modal pore structure possessing two bottleneck of the FMOF, making it a good candidate for practical applications.

6.1 Materials and characterization

6.1.1 Sample Preparation

The partially fluorinated MOF(Cu) is kindly provided by the group of Prof. K. Choi from Sookmyung Women's University in Republic of Korea. The FMOFCu was prepared by a hydrothermal synthesis as follows: Copper nitrate trihydrate ($Cu(NO_3)_2 \cdot 3H_2O$ (0.024 g, 0.1 mmol, Sigma Aldrich) and 2,2-bis (4-carboxyphenyl) hexafluoropropane (CPHFP) (0.122 g, 0.31 mmol, TCI) were dissolved in deionized water (5ml) and reacted in a hydrothermal reactor at 150°C for 12 h. The molar ratio of the reaction was 1:3:2776. The product was repeatedly

washed with DMF (10 ml, Aldrich) and Methanol (10 ml, SAMCHUN) and dried with vacuum oven at room temperature[165].

6.1.2 Characterization

The characterization of the sample was performed by Choi group. The surface morphology and particle size were examined using a scanning electron microscope (Jeol, JSM-7600F). Powder X-ray diffraction (XRD) was performed on a diffractometer (D8 Advance, Bruker AXS) with Cu-Kα radiation and Bragg–Brentano focusing geometry was employed. Diffractograms were collected in the 5 to 40° 2θ-range with a step size of 0.01°. Fourier Transform Infrared Spectroscopy (FT-IR) spectra were collected on a Thermo Fisher Scientific Nicolet IS50 spectrometer. Samples were analyzed for ATR diamond mode measurement and 60 scans with a resolution of 4 cm^{-1}. Spectra were recorded in transmission mode.
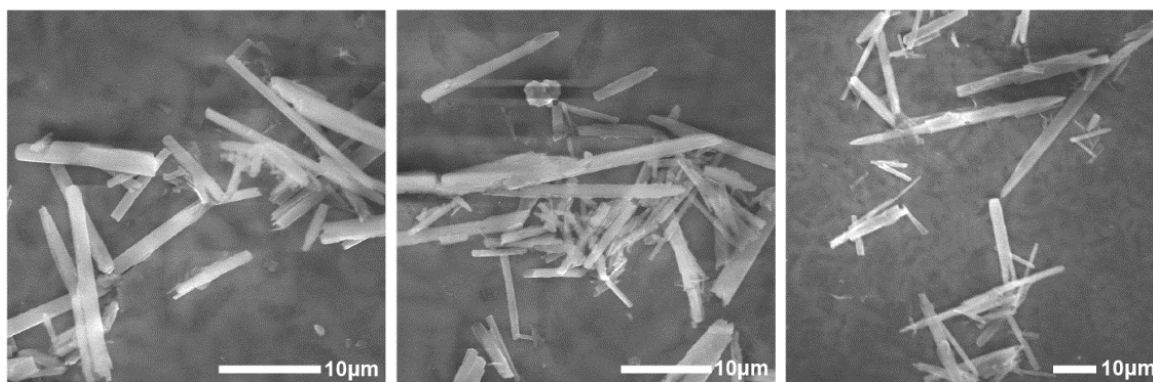
Figure 6.1 SEM image of FMOFCu framework[156].

The SEM image (Figure 6.1) reveals a well-spread whisker morphology. The XRD pattern also presents well-defined peaks, as shown in Figure 6.2, which match the simulated pattern, indicating the formation of pure crystalline FMOFCu. The crystal structure of FMOFCu, presented in Figure 6.3 was obtained by a single-crystal XRD analysis.
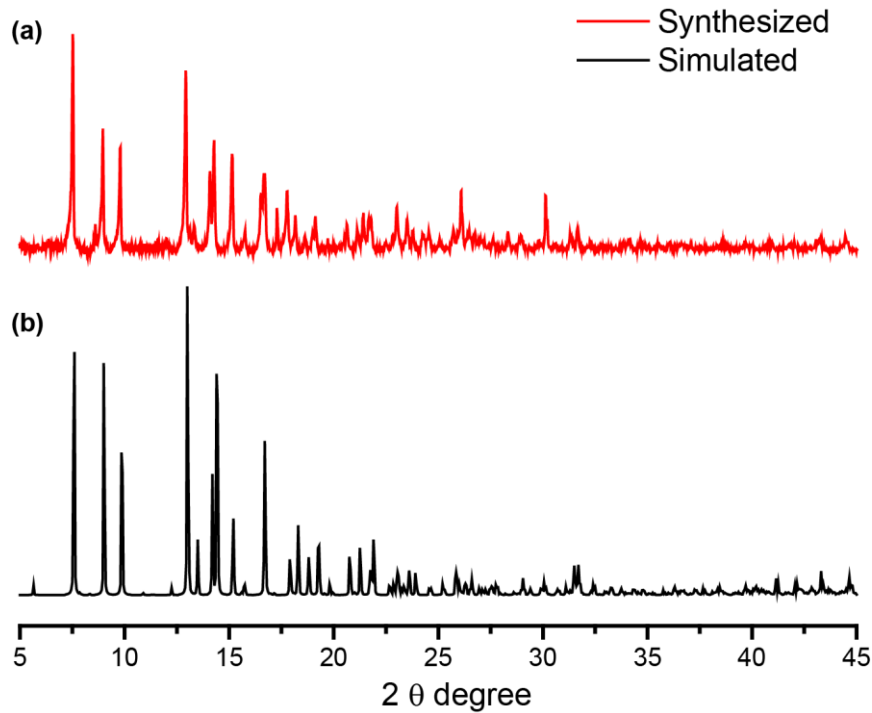
Figure 6.2 PXRD pattern of FMOFCu as a) synthesized, and b) simulated[156].

The unique structure contains a trimodal pore system with larger tubular cavities A (9.4×9.2 Å^2) and B (5.6×4.2 Å^2) connected by a small aperture of diameter 3.6 Å, and additionally a third hidden cavity C (8.8×4.7 Å^2) connected to the two tubular cavities by a 1D narrow channel consisting of fluorinated windows with a 2.5 Å wide aperture. On the basis of this structure, the pore network was analyzed by Choi Group with Mercury[166] software using a step size of 0.1 Å for the probe spheres. Three cavities (A, B, C) can be identified and are connected depending on the probe size. For a 3.6 Å effective probe size, cavities A and B are already connected while cavity C is completely isolated from the channel. However, when the effective probe size decreases to 2.6 Å, cavity C starts to get connected with cavity B and the channel.
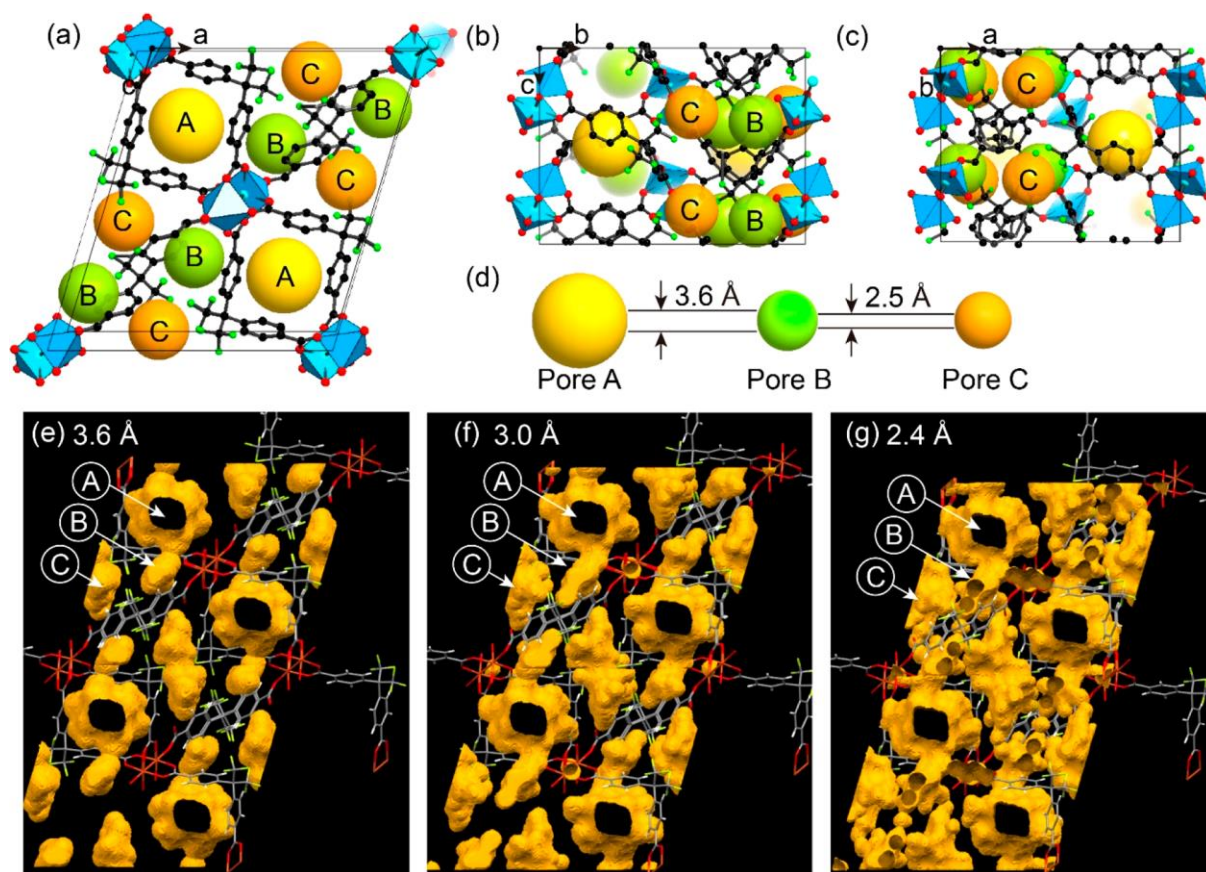
Figure 6.3 Unit cell (a-c) and crystal structure (e-g) of FMOFCu. The yellow, green, and brown spheres represent the volume of pores A, B, and C, respectively. a) *ac* plane, b) *bc* plane, and c) *ab* plane of the unit cell structure. (e−g) Pore network analysis with a grid space of 0.1 Å for the probe sphere. Red, black, and green represent copper, carbon, and fluorine atoms, respectively[156].
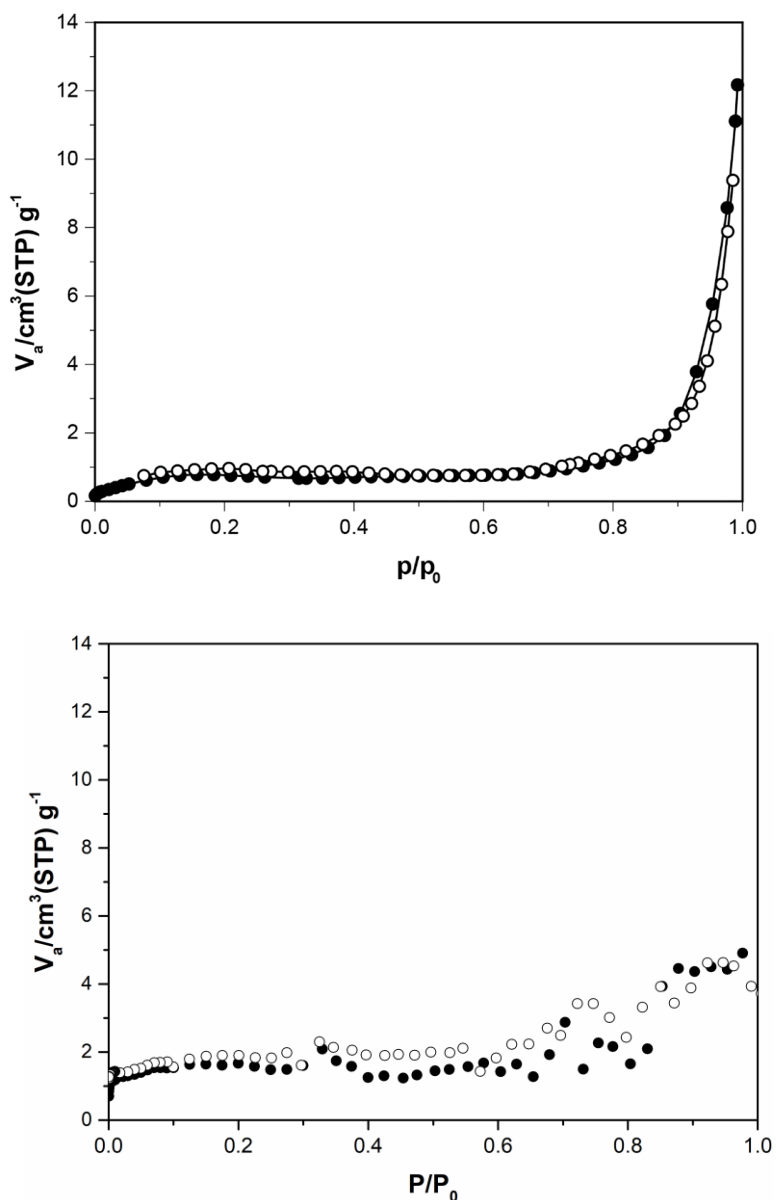
Figure 6.4 Adsorption isotherm of sample FMOFCu at 1 bar and 77K using N_2 (top) and 20 K using H_2 (bottom). Closed and open symbols represent the absorption and desorption of the sample.

Gas sorption measurements performed on FMOFCu possessing a bottleneck window (3.6 Å and 2.5 Å) show that neither N_2 at 77 K nor H_2 at 20 K can penetrate this partially fluorinated MOF due to the comparable size of the aperture and the kinetic diameter of probe molecules (3.64 Å N_2 and 2.89 Å H_2), presented in Fugure 6.4. The calculated BET surface area is very low which is within the measurement errors, implying the inaccessible aperture for both H_2 at 20 K and for N_2 at 77 K.

6.2 Results

Low-pressure, high resolution H$_2$ and D$_2$ adsorption isotherms
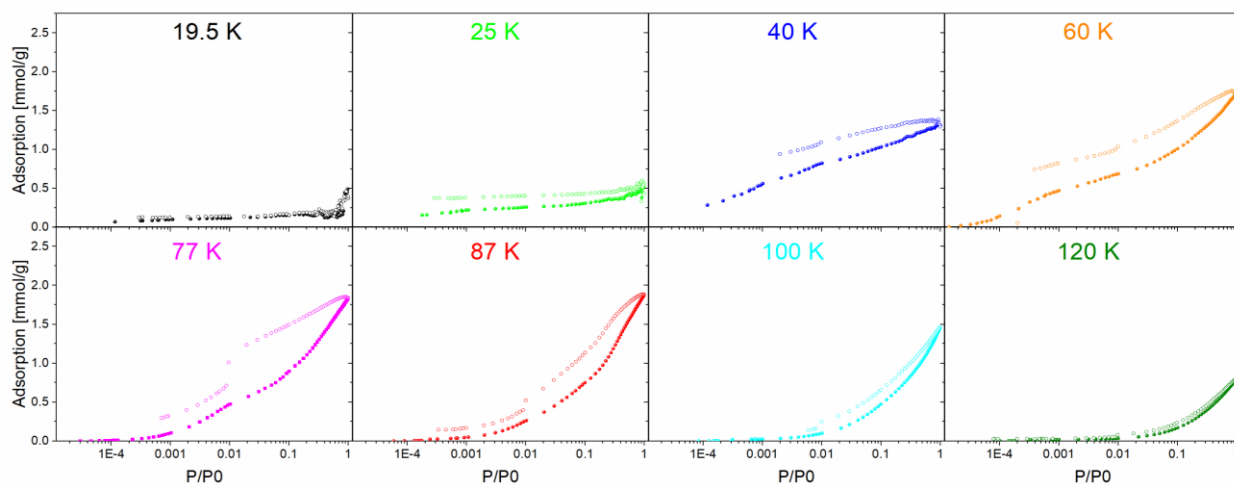
Figure 6.5 Hydrogen adsorption and desorption isotherms of FMOFCu at various temperatures: 19.5 K (black), 25 K (green), 40 K (blue), 60 K (orange), 77 K (magenta), 87 K (red), 100 K (cyan), and 120 K (olive). Closed and open symbols represent the absorption and desorption.
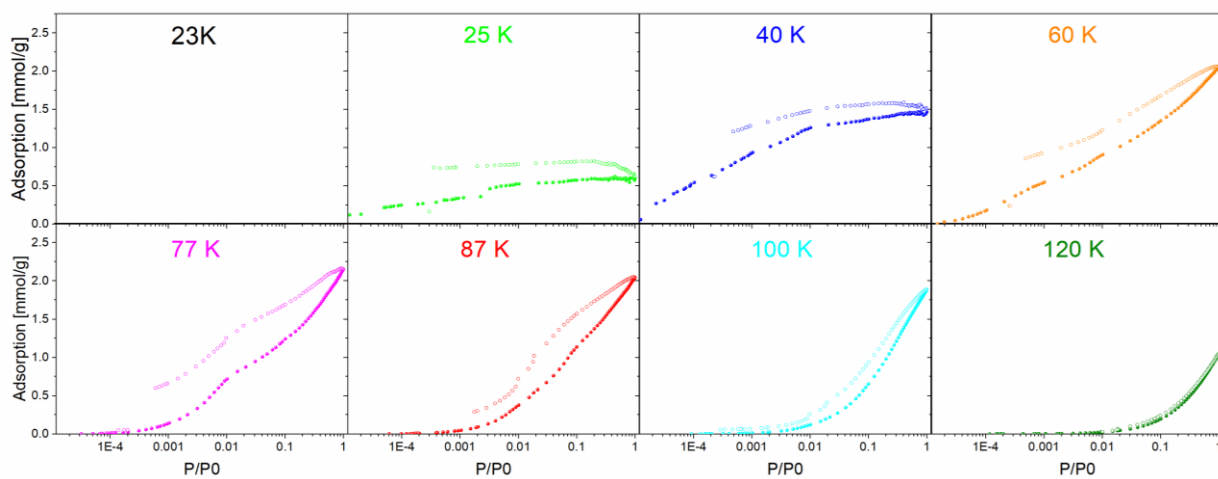
Figure 6.6 Deuterium adsorption and desorption isotherms of FMOFCu at various temperatures: 23 K (black), 25 K (green), 40 K (blue), 60 K (orange), 77 K (magenta), 87 K (red), 100 K (cyan), and 120 K (olive). Closed and open symbols represent the absorption and desorption.

The low pressure H_2 sorption isotherms obtained at various temperatures (20 – 120 K) are presented in Figure 6.5. Unlike typical isotherm characteristics of microporous materials (higher uptake with decreasing temperature), hydrogen uptake on FMOFCu starts at 25 K exhibiting a hysteresis and reaching the maximum uptake at 77 K (1.85 mmol/g at 1 bar). The observed hysteresis becomes stronger in the temperature range up to 77 K, then becoming weaker above 87 K, implying non-equilibrium isotherms within the measurement time, c.a. 10 h. Identical phenomena are also observed in the D_2 sorption, shown in Figure 6.6. The slightly higher D_2 uptake compared to H_2 is mainly attributed to the higher diffusion rate and the higher heat of adsorption of D_2.

TDS study for pure gas physisorption

Cryogenic TDS measurements have been carried out by applying a pure H_2 and D_2 atmosphere, respectively, on FMOFCu under identical experimental conditions.
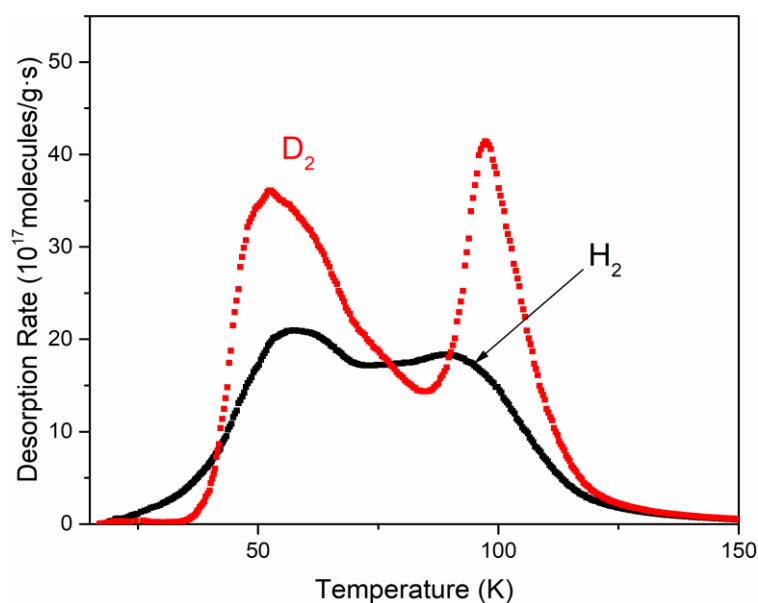
Figure 6.7 Pure gas H_2 (black) and D_2 (red) thermal desorption spectra of FMOFCu loaded at room temperature and evacuating at 20 K.

Degassed at 373 K for 10 h, the sample was exposed to 10 mbar pure gas at room temperature. After cooling down to 20 K, the unabsorbed gas molecules were evacuated. Then the desorption spectra were recorded with a linear heating of 0.1 K/s. The resulting H_2 and D_2 desorption spectra obtained in the range between 20 -150 K are shown in Figure 6.7. Both spectra show a

board peak centered approximately at 55 K. The second desorption peaks are different for both isotopes. For deuterium, the desorption curve exhibits one sharp peak at around 100 K, while the spectra of hydrogen shows a board shoulder with a maximum at 88 K. One should note that an additional smaller peak may exist in between of the two intensive peaks, but overlapping with the other two makes it look like a shoulder in the temperature range of 65-80 K. The area under the desorption peak is proportional to the desorbing amount of gas, which can be quantified with calibration. The uptake for H_2 and D_2 is determined to be 2.1 and 3.1 mmol/g, respectively.

TDS study for isotope separation

Direct separation for an isotopic mixture has been investigated. Figure 6.8 shows the TDS spectra collected after exposure of FMOFCu to a 10 mbar 1:1 H_2/D_2 isotope mixture for 10 min at different exposure temperatures (25, 40, 60, 77 and 87 K). The selectivity of D_2 over H_2 ($S_{D2/H2}$) can directly be calculated from the integrated amount of the desorption peaks after calibration. Figure 6.8f shows the D_2/H_2 selectivity and its corresponding D_2 uptake as a function of exposure temperature. The total uptake in the nanopores increases with rising temperatures, exhibiting a maximum for the H_2 uptake at T_{exp} of 60 K and D_2 uptake at T_{exp} of 40 K before it decreases again till 87 K. Meanwhile, the selectivity decreases with increasing T_{exp}, exhibiting the highest value $S_{D2/H2} = 14$ at 25 K. Interestingly, not only the lowest uptake with highest selectivity is observed for T_{exp} of 25 K, but also no desorption of any isotopes occurs above 80 K. Above T_{exp} of 60 K, the additional shoulder between desorption peak in the spectrum is getting larger and a new peak appears simultaneously. For even higher exposure temperatures, the desorption maximum shifts to higher temperature.
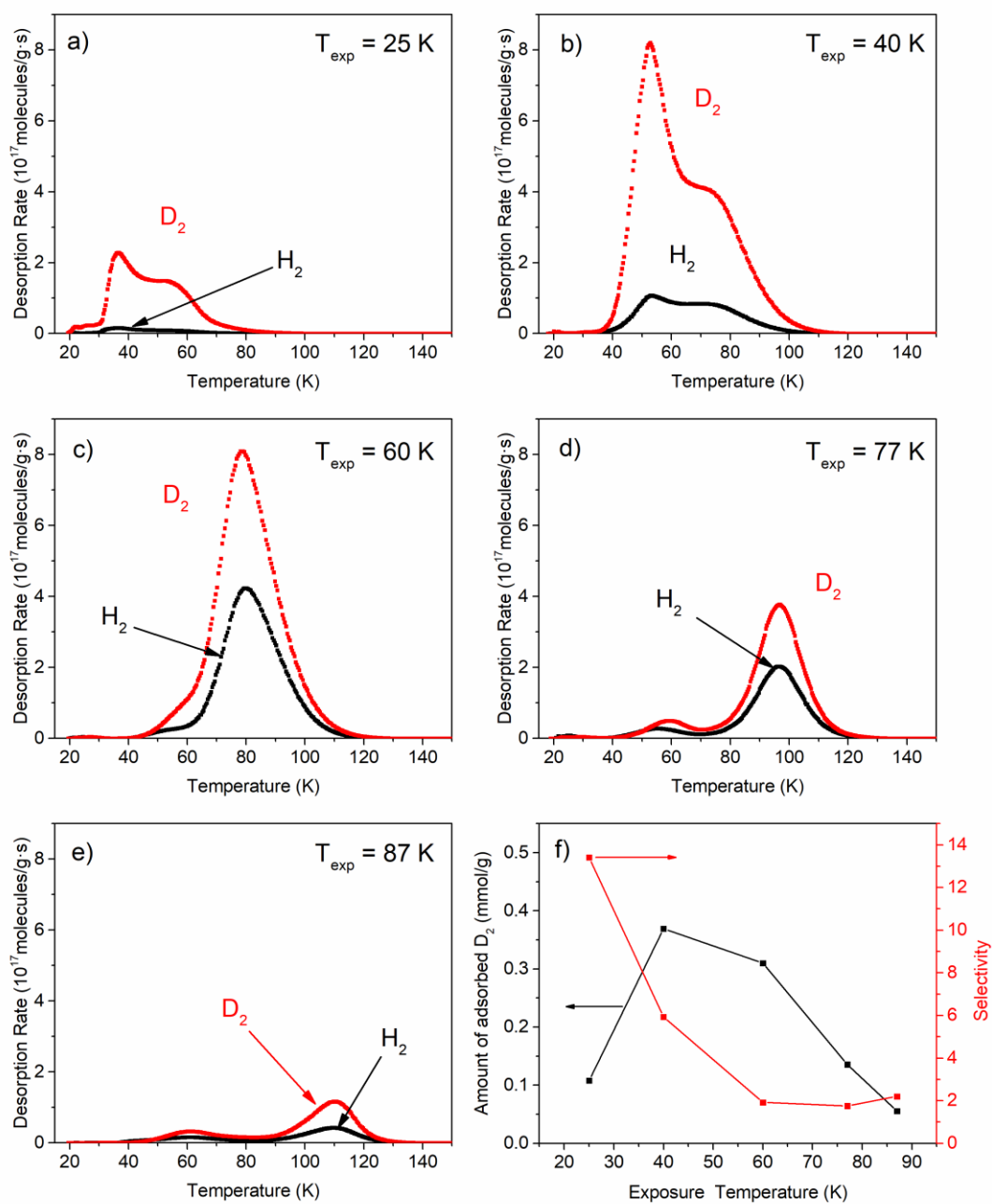
Figure 6.8 H_2 (black) and D_2 (red) thermal desorption spectra of 10 mbar 1:1 H_2/D_2 isotope mixture on FMOFCu for 10 min at various exposure temperatures (T_{exp}): a) 25 K, b) 40 K, c) 60 K, d) 77 K, and e) 87 K. f) The corresponding amount of adsorbed D_2 (black) and selectivity (red) as function of T_{exp}.
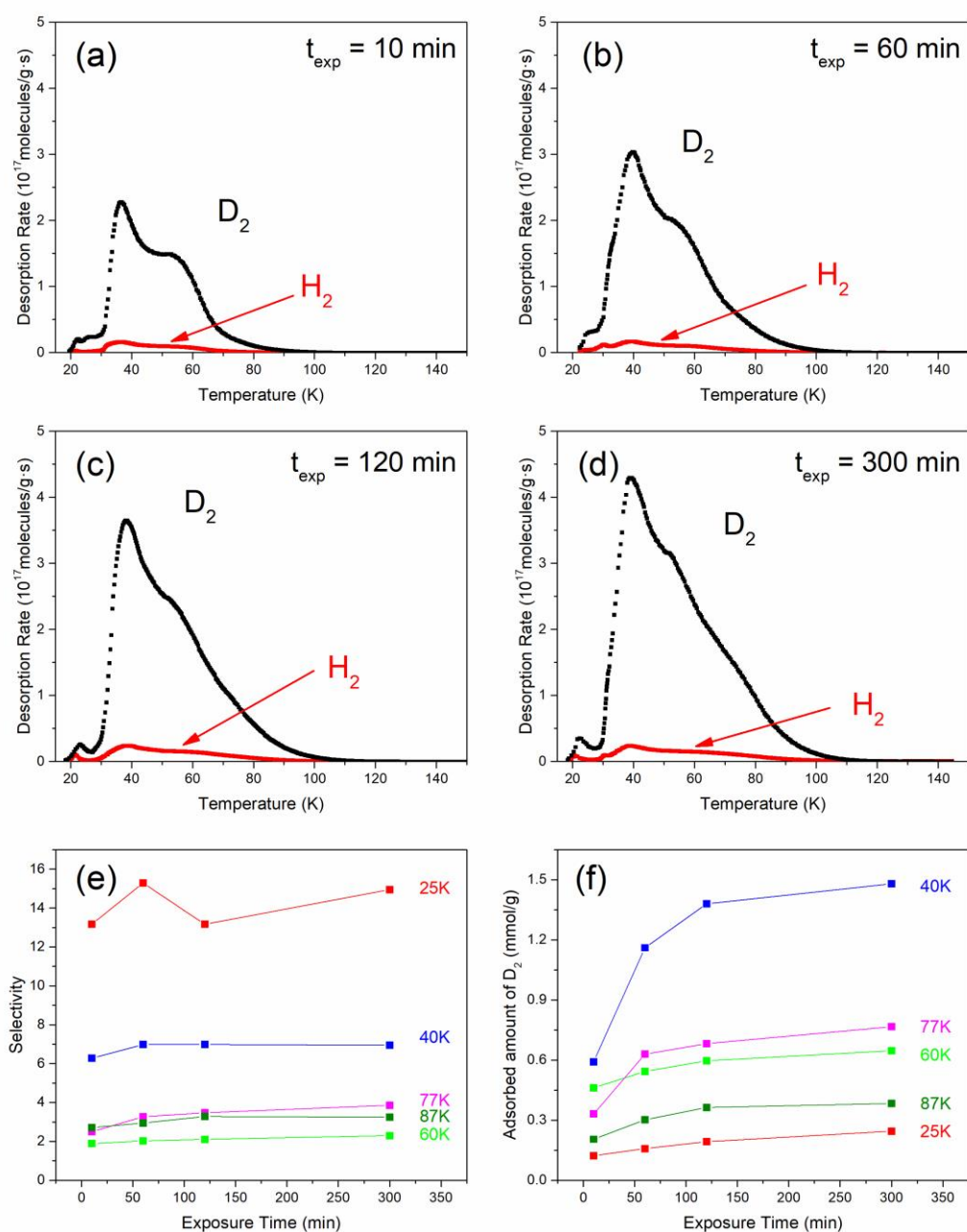
Figure 6.9 Kinetic effect of FMOFCu at 25 K. H_2 and D_2 desorption spectra of 50 mbar 1:1 isotope mixture loading for a different exposure time: (a) 10 min, (b) 60 min, (c) 120 min and (d) 300 min, and its corresponding (e) selectivity and (f) D_2 uptake.

Further TDS measurements have also been performed by applying a 50 mbar 1:1 isotope mixture at 25 K for different exposure time, since the highest selectivity is achieved at this low temperature. The desorption spectra shown in Figure 6.9(a-d) exhibit a sharp desorption peak

for deuterium centered at 35 K with a shoulder at approximately 55 K. The intensity of the D_2 desorption peak is much higher compared to that of H_2. Similar measurements have been carried out for higher exposure temperatures of 40-87 K, and the selectivity and the corresponding adsorption amount of D_2 are presented in Figure 6.9 (e,f). The selectivity remains approximately constant and the gas uptake increases with longer exposure time, the maximum uptake of 1.5 mmol/g can be observed at 40 K for 300 min.

6.3 Discussion

Temperature-dependent gating effect

FMOFCu possesses a unique temperature-dependence of the sorption behavior as presented previously in Figure 6.5. At low temperature of 19.5 K, the H_2 uptake is close to zero, indicating that the gas molecules cannot access the structure. The gas uptake is increasing at higher temperature, showing a strong hysteresis, and an equilibrium can only be achieved above 100 K. This phenomenon can be ascribed to the different effective aperture size at different temperatures. Below 77 K, a strong diffusion limitation is produced by the two small bottleneck windows, which does not allow to reach equilibrium in a reasonable time at low temperatures. Therefore, the increasing sorption amount and hysteresis observed between 25 and 77 K indicate that more H_2 molecules can access the pore system at higher temperatures due to thermally-induced gate opening of the two bottleneck windows.

In-situ neutron powder diffraction (NPD) experiments have been carried out to identify the possible structure changes of FMOFCu. The NPD experiments were performed by Prof. H. Oh at the E9 diffractometer of Helmholtz Center Berlin for Materials and Energy. 200 mg sample was activated at 400 K under vacuum for 12 h to remove the possible remaining solvent molecules. Deuterium was used as the adsorption gas to minimize the large incoherent neutron scattering cross-section of hydrogen which contributes to the signal background. Radiation with a wave length of 2.816 Å was chosen for the data collection. All diffraction data have been collected at 24 K for 16 h gas loading, presented in Figure 6.10. Although the statistics of the diffraction peaks is rather poor, the NPD pattern indicates no visible structural change in FMOFCu, which may support the local flexibility ascribed to thermal vibrations of CF_3 group

at the pore aperture. The CF_3 group features the unique tri-modal structure of FMOFCu. The larger tubular cavities A (9.4 × 9.2 Å^2) and B (5.6 × 4.2 Å^2) are connected by a small aperture of diameter 3.6 Å, and the additional hidden cavity C (8.8 × 4.7 Å^2) is connected to cavity B by a 1-D channel consisting of fluorinated windows with a 2.5 Å aperture. Hydrogen molecules thus can only access this cavity with higher temperatures, when the effective aperture becomes larger.
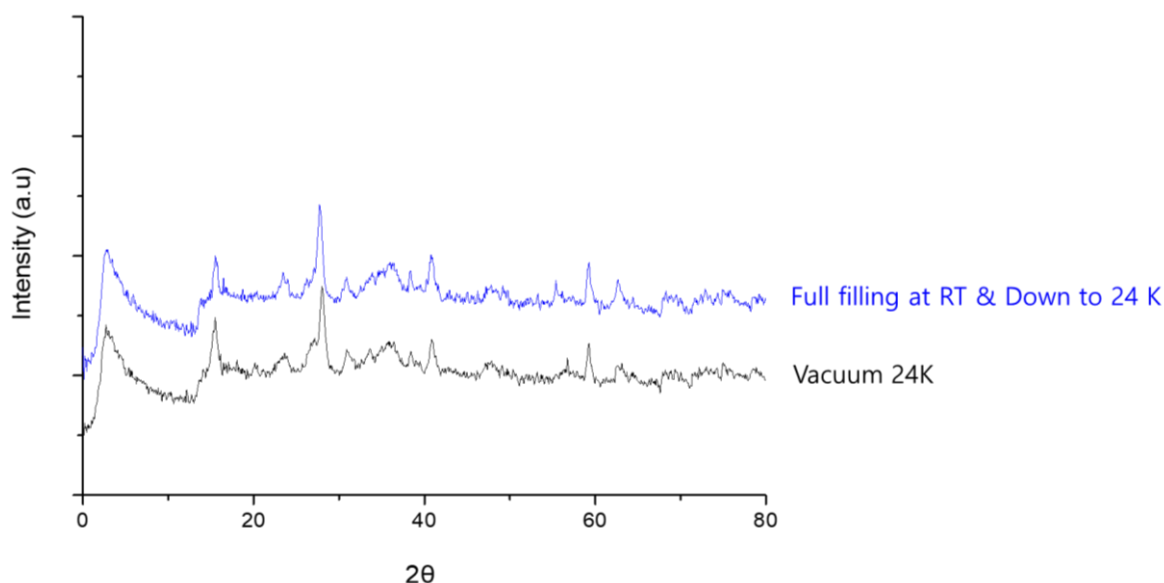
Figure 6.10 Neutron Powder Diffraction (NPD) measured at 24K under vacuum and fulling loading of D_2, showing no structural change by gas sorption[156].

This temperature-dependent gating effect can be ascribed to the thermal vibration of the flexible windows as gates in the framework. At lower temperatures, H_2 cannot penetrate the structure through the effectively small aperture. The gating effect has been similarly used by Fernandez et al.[167] to explain the increased Kr/Xe selectivity observed at low temperatures in FMOF. In addition, several porous materials possessing such temperature-dependent gate opening for hydrogen have been reported, such as the series of isostructural hexagonal MOFs possessing 1-D channel IFP-4 and -7[161], MFU-4 [155]with alternating small and large pores, Pyridine incorporated covalent organic framework COF-1[154], and porous organic cages **6ET-RCC3** with methyl groups inside the cavitydescribed in this work. All these materials possess pore apertures smaller than the kinetic diameter of hydrogen isotopes, which generally prevent the penetration of gas molecules into the structure. However, penetration can be observed with increasing

temperature due to the thermally induced opening of the pore apertures. These results also imply that the flexibility observed in FMOFCu is only local (no structural change), in contrast to the most well-known flexible (breathing) frameworks (e.g. MIL-53[153]), which show a volume change of the framework.

The H_2 and D_2 desorption spectra obtained on FMOFCu under pure gas atmosphere in Figure 6.7 show two desorption maxima for both isotopes, which can be therefore assigned to the two different effective apertures. The low-temperature peak is assigned to the larger alternating bi-modal cavity A and B, while the high-temperature peak is assigned to the diffusion into the small hidden pocket C, see Figure 6.11.
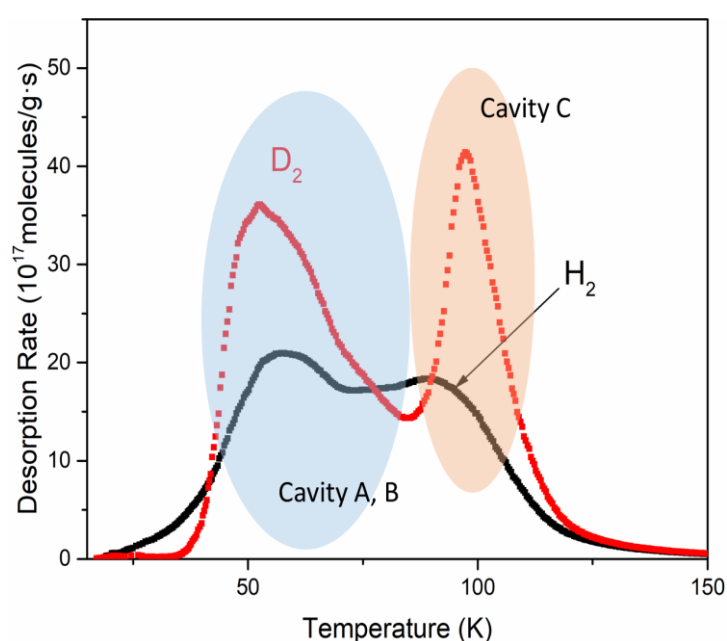
Figure 6.11 Pure gas H_2 (black) and D_2 (red) thermal desorption spectra of FMOFCu[156].

Note that the desorption maxima of the TDS spectra shift normally from weak to strong adsorption sites with rising temperatures if no diffusion barrier exists. However, the structure of FMOFCu possesses no strong adsorption sites and thus these two distinguishable peaks can be attributed to two (3.6 and 2.5 Å) narrow windows which cause a strong diffusion barrier. Hence, the thermally activated aperture becomes more open with increasing temperature, and this gate opening temperature may be different for the isotopes H_2 and D_2 due to quantum effects. Moreover, the lower H_2 uptake also implies a kinetic hindrance at the aperture where H_2 encountered larger diffusion barrier than D_2 under identical condition (exposure pressure,

temperature and time). Such narrow windows of cavity C produce a strong diffusion barrier which leads to a desorption spectrum extending up to high temperatures of ca. 130 K for both isotopes, which is due to the entrapment of molecules in the small cavity. The trapped gas molecules can be therefore released at high temperatures where the cavity is thermally opened.

Hydrogen isotope separation via dynamic opening

Normally, if different sorption sites exist inside porous media, the strongest site, yielding a high temperature desorption peak, is occupied firstly at very low loadings. Afterwards, the weaker site is occupied at higher gas loadings, resulting in additional low-temperature desorption peaks. TDS spectra therefore show a sequential filling from strong to weak adsorption sites, exhibiting 1, 2, or multiple maxima from high to low desorption temperature. However, H_2 and D_2 TDS spectra shift to higher desorption temperatures for higher exposure temperatures, which is contrary to the typical sequential filling behavior of accessible sites with different binding strength. At T_{exp} of 25 K, no desorption of either isotope occurs above 80 K, while above T_{exp} of 60 K, a new desorption peak appears. This can be attributed to the newly accessible cavity C due to local vibration of aperture at higher exposure temperature.

Moreover, for low exposure temperatures (T_{exp} of 25 K), the isotope separation is mainly governed by the faster diffusion of D_2 into cavity A and B independently or through the 3.6 Å bottleneck connecting cavity A and B, while cavity C is not accessible. As reported by Oh et al.[168], the D_2 diffusivity gets significantly faster than H_2 in porous materials with a pore aperture between 3.0-3.4 Å. Thus the confined aperture of 3.6 Å at 25 K produces a strong diffusion barrier, allowing D_2 to preferentially penetrate into the structure, leading to a high selectivity. However, for short exposure time of 10 min, the small gas uptake is due to the strong diffusion limitation. When T_{exp} increases to 40 K, the opening of the aperture by local vibrations contributes to better accessibility of both isotopes, thus the isotope uptake is increasing with decreasing selectivity. Above T_{exp} of 60 K, the 2.5 Å aperture connecting for cavity C opens thermally activated and the third desorption peak appears.

Despite low uptake and selectivity at $T_{exp} = 77$ and 87 K, the desorption maxima of both isotopes are centered at 96 and 110 K, respectively, which is a rare case exhibiting such high desorption temperatures without the existence of strong adsorption sites. In general, desorption peaks at such high temperatures indicate the existence of strong binding sites, such as the open metal sites in MOF-74[147]. Although there is a difference in total uptake, the high-temperature

desorption spectra (60, 77, and 87 K) of FMOFCu and MOF-74-Ni are compared in Figure 6.12. The FMOFCu even exhibits higher desorption maximum at all chosen exposure temperatures than MOF-74-Ni possessing unsaturated Ni sites. Since the isosteric heat of adsorption in FMOFCu was calculated to be 3 - 3.5 kJ/mol (see Figure 6.13) using the Clausius-Clapeyron equation, it is a clear evidence of the absence of any strong sorption site. Thus, the effective size of the bottleneck aperture is temperature dependent. Above certain gate-opening temperature, gas molecules can penetrate or leave the hidden cavity C. Cooling down below the opening temperature under gas atmosphere, gas will be entrapped in the small cavity and can be only released by heating above the opening temperature. Therefore, this thermally triggered local flexibility is responsible for the high-temperature desorption peak and gas release. Introducing bottleneck apertures into the MOF pore structure results in a diffusion barrier for hydrogen, which increases drastically the desorption temperature comparable or even higher than the desorption temperatures reached by open metal sites in other MOFs.
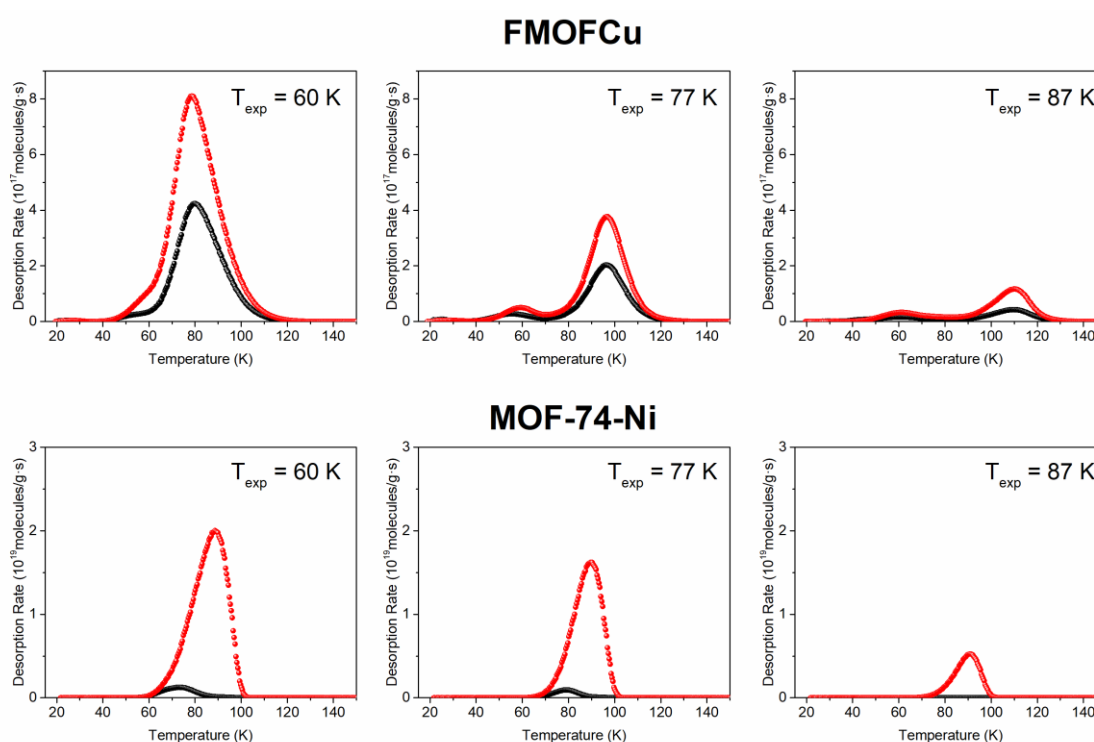
Figure 6.12 The comparison H_2 and D_2 desorption spectra of 10 mbar 1:1 isotope mixture loading for a different exposure temperature: 60K, 77K, and 87K, of FMOFCu and MOF-74-Ni. Note the different unit of desorption rate[156, 169].
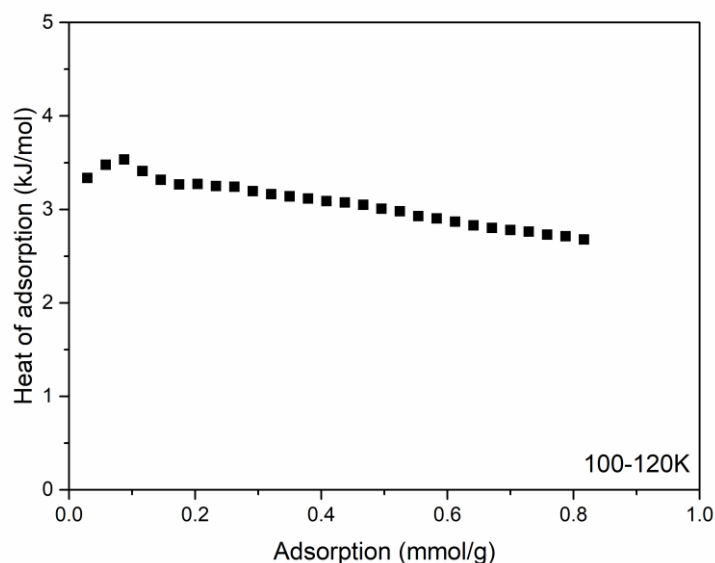
Figure 6.13 Isosteric heat of adsorption of hydrogen for FMOFCu as function of the adsorption amount[156].

TDS spectra obtained from measurements applying a 50 mbar 1/1 isotope mixture for different exposure temperatures 25-87 K and times t_{exp} 10 and 300 min have been compared with pure gas TDS spectrum, which has been obtained after room temperature exposure and cooling under gas atmosphere to 20 K, see Figure 6.14. The mixture measurement at a given t_{exp} and T_{exp} provides each hydrogen and deuterium signal individually, and the hydrogen (top in Figure 6.14.) and deuterium (bottom in Figure 6.14.) signals are presented separately to show the dependence of time and temperature. All black curves in the spectra represent the exposure to pure gas at room temperature, in which all cavities are assumend to be accessible through the different apertures during cooling down to 20 K. Thus, these black curves should be the envelope for all the spectra obtained at different temperatures. It is clear that 10 min exposure time (Figure 6.14 left) is not enough for reaching an equilibrium, while for 300 min (Figure 6.14 right) mixture exposure, the sum of all D_2 spectra collected at different T_{exp} between 25 and 87 K have as an envelope the pure gas TDS for RT exposure. This phenomenon can be explained by the successive filling of the different cavities by increasing the exposure temperature. At low exposure temperatures up to 40 K only the cavities A and B are accessible for gas molecules and the bottleneck aperture to cavity C is still closed. At higher exposure temperatures this small aperture opens thermally activated and gas can penetrate into cavity C.

132

Thus, the high selectivity is initially observed at $T_{exp} = 25$ K with low uptake due to the barely open aperture. Then, selectivity decreases with temperature due to opening the aperture, but increases again for 77 and 87 K compared to 60 K (Figure 6.9f) since the aperture of cavity C is opening and acting as another sieve. This successive filling of the different cavities by increasing the exposure temperature is schematically illustrated in Scheme 6.1. At low exposure temperatures up to 40 K only the cavities A and B are accessible for gas molecules and the bottleneck aperture to cavity C is still closed. At higher exposure temperatures this small aperture opens thermally activated and gas can penetrate into cavity C.
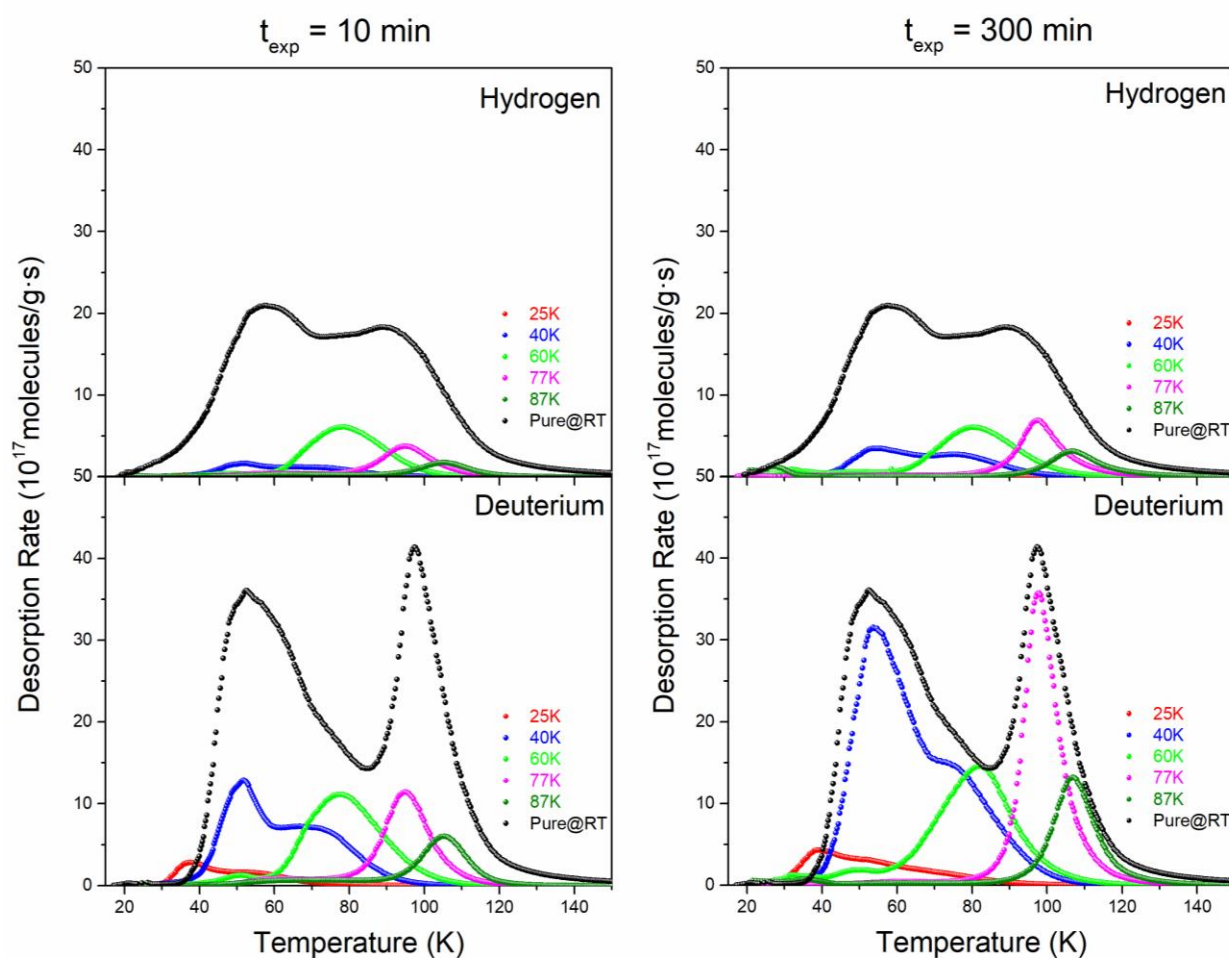
Figure 6.14 H_2 and D_2 thermal desorption spectra of 50 mbar 1:1 H_2/D_2 isotope mixture on FMOFCu for 10 and 300 min at various exposure temperatures (T_{exp}): 25 K (red), 40 K (blue), 60 K (green), 77 K (magenta), and 87 K (olive). Pure gas H_2 and D_2 thermal desorption spectra (black) as a comparison of accessible adsorption sites and gas uptake[156].
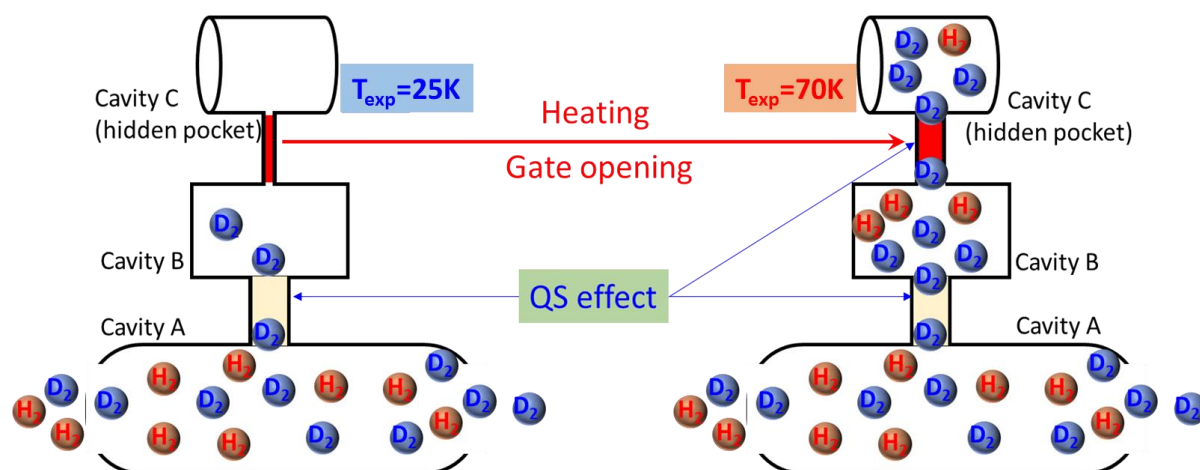
Scheme 6.1 Schematic filling of the cavities of FMOFCu at different temperatures[156].

6.4 Summary

Dynamic pore aperture opening has been investigated for optimizing KQS effect for hydrogen isotope separation. A partially fluorinated metal–organic framework (MOF) with copper, with an alternating small and large cavity structure forming a 1-D channel, was chosen. The unique structure of this porous material consists of a tri-modal pore system with large tubular cavities connected through a smaller cavity with bottleneck apertures with the size of 3.6 Å plus a third hidden cavity connected by an even smaller aperture of 2.5 Å. At low temperatures, the isotope separation is mainly governed by the faster diffusion of D_2 into cavity A and B, while cavity C is not accessible, leading to a high selectivity of ca. 14 at 25 K. With increasing exposure temperature of 77 K, an additional desorption peak centered around 100 K was observed, due to the opening of the hidden pocket. This additional presence of a hidden cavity in FMOFCu structure blocked by a small bottleneck aperture, which opens thermally activated, offers newly accessible inner surfaces for increasing adsorption of hydrogen isotopes inside the framework and a second narrow channel for quantum sieving. The gate opening behavior for the hidden cavity is related to the penetration barrier which is affected by the phonon frequencies of CF_3 groups (fluorinated windows). Thus, the gate can be opened by the assistance of low-energy vibrational modes. The aperture (2.5 Å) is getting wider by stretch or twist of CF_3 groups with increasing temperature. Thus, this penetration leads to an entrapment of molecules at lower

134

temperatures and a release at higher ones. The resulting desorption temperature of over 100 K is comparable to strong adsorption sites, even none are present in FMOFCu. Furthermore, a selectivity between 3 and 4 was achieved at an exposure temperature of 77 and 87 K, showing the potential of this material for isotope separation above liquid nitrogen temperature.

7. Conclusions

In this work, efficient hydrogen isotope separation has been systematically investigated on a great variety of nanoporous materials, including zeolite Y exchanged with various transition metal ions, porous organic cages possessing different pore apertures, and a flexible tri-modal metal-organic framework. Cryogenic thermal desorption spectroscopy (TDS) has been applied to measure directly the selectivity after exposure to an equimolar H_2/D_2 isotope mixture. Two different mechanisms can be exploited for separating gaseous mixture of isotopes. i) Chemical affinity sieving (CAS), where the heavier isotope has a stronger interaction with the adsorption sites due to its lower zero-point energy (*ZPE*) in van der Walls well; ii) Kinetic quantum sieving (KQS) in small pore apertures, which is based on the faster diffusion of the heavier isotope with lower *ZPE* in the confinement into the structure under cryogenic conditions.

Hydrogen isotope separation on open metal sites

A series of ion-exchanged zeolite Y has been selected for hydrogen isotope separation. Among five different cations exchanged: Co (II), Ni (II), Cu (II), Ni (II), and Ag (I), the best separation performance was observed in zeolite AgY due to the existence of strong open metal sites. Meanwhile, no such strong adsorption sites have been found in other transition cation-exchanged zeolites. Thus, the samples investigated have been divided into two categories.

- In zeolite Y with Co^{2+}, Ni^{2+}, Cu^{2+}, and Ni^{2+} TDS spectra show that the adsorbed amount of deuterium exceeds the one of hydrogen for all exposure temperatures. Due to the weak binding enthalpy, at low temperature around 50 K all hydrogen molecules have been desorbed from the materials, while for deuterium the desorption temperature is extended to 70 K. The desorption spectra of D_2 have also shown an additional desorption maximum centered approximately at 50 K, which is corresponding to a distinct adsorption sites, site II in supercages of zeolite Y. These second adsorption sites possess a higher activation energy of desorption and preferential adsorption of D_2, leading to an increasing selectivity with higher exposure temperature. The highest selectivities have been obtained for all zeolites exposed to the equimolar mixture at 50 K, where D_2

predominately occupies these adsorption sites. However, the gas uptakes drops with increasing temperature.

- In contrast to the other ion-exchanged zeolites, zeolite AgY shows an additonal desorption maximum for H_2 and D_2 at 82 and 88 K, respectively. These maxima are ascribed to the adsorption on the strong unsaturated Ag sites, where the large difference in *ZPE* between the isotopes can be expected. The heavier isotope is therefore bonded stronger and released at higher temperatures. The amount of gas at the open metal sites observed at temperatures above 60 K is about 1/3 of the total uptake in the structure, indicating a high density of open Ag sites which have been exchanged owing to the high concentration of active acid sites in zeolite Y.

- TDS measurements for isotope mixture on zeolite AgY show that the selectivity is increasing while the gas uptake is decreasing with increasing exposure temperatures from 20 to 90 K. The selectivity obtained below 40 K is less than 2, due to the small difference between D_2 and H_2 adsorption enthalpies at weak binding sites, whereas the selectivity above 60 K increases dramatically and reaches the highest values of 10 at 90 K, which is ascribed to the large difference in adsorption enthalpy between H_2 and D_2.

- For longer exposure time or higher exposure pressure at 60 K, the selectivity increases, while the total gas uptake remains constant. At this temperature, only open metal sites are occupied by hydrogen isotopes, and the largest adsorbed number of gas molecules is equal to the number of Ag sites. The D_2 uptake is increasing while H_2 is decreasing, clearly indicating that an isotope exchange is occurring, where H_2 molecules are replaced by D_2.

- Even though the uptake is greatly reduced with increasing temperature, the adsorbed amount of D_2 still gets close to 1 mmol/g, which is one of the best combinations of selectivity and adsorption above liquid nitrogen temperature, making AgY an interesting material for practical hydrogen isotope separation.

- In addition, considering the final product from the industrial production is a mixture of not only H_2 and D_2, but HD as well, the separation of D_2/HD/H_2 mixture has been performed experimentally for the first time. TDS spectra exhibit desorption maxima at 80 K for H_2, 82 K for HD, and 100 K for D_2. This high desorption temperature indicates a strong binding energy which is apparently increasing with the mass of the molecules. Thus, a selectivity of D_2 over HD exhibits a value of 3.3.

Hydrogen isotope separation via KQS

A novel class of porous materials, porous organic cages (POCs), has been explored for the first time with respect to hydrogen isotope separation. The pore aperture of these discrete molecules with intrinsic cavities can be precisely tuned, even at atomic level, without altering the pore structure. Three porous organic cages, **CC3**, **6FT-RCC3**, and **6ET-RCC3** have been investigated, with different pore apertures of 4.5 Å, 3.4 Å, and 1.9 Å, respectively.

- **CC3** and **6FT-RCC3** show fully reversible isotherms, indicating large enough pore apertures for fully free gas access. The highest H_2 uptake at 30 K for the two cages are 8 and 8.2 mmol/g at 1 bar. Isotope separation measurements show that the total gas uptake at 30 K (8.0 mmol/g) and the selectivity (1.2 for **CC3** and 1.8 for **6FT-RCC3**) are independent of the exposure time. These observations are due to the large pore aperture compared to the kinetic diameter of H_2 and D_2, which results in a rapid diffusion through the channels without any barriers.

- **6ET-RCC3** possesses far smaller pore apertures, 1.9 Å, compared to the kinetic diameter of a hydrogen molecule, making it geometrically not accessible for hydrogen isotopes. However, flexibility can allow penetration by a temperature-dependent gate opening effect. H_2 sorption isotherms obtained from **6ET-RCC3** clearly show a unique adsorption behavior. At low temperature 30 K, the H_2 and D_2 uptakes are close to zero, indicating no penetration into the cavities within a reasonable equilibrium time. The hysteresis observed in isotherms then gets stronger with increasing temperature till 77 K. The uptake is firstly increasing, reaching its maximum at 50 K (0.5 mmol/g), and then decreasing with higher temperature. It clearly shows that the gas molecules can penetrate into the network more deeply with increasing temperature, implying a larger effective pore aperture from the thermally-induced flexibility of methyl groups.

- TDS spectra show that the uptake in **6ET-RCC3** increases with increasing exposure temperature until a maximum for H_2 and D_2 is reached at 60 K. The selectivity exhibits a maximum of 3.9 at 30 K and decreases with increasing temperature. For longer exposure time at 30 K, the total gas uptake increases while the selectivity decreases from 3.9 to 3.3, revealing that kinetic quantum sieving is occurring at the small pore aperture. By contrast, the selectivity of **CC3** and **6FT-RCC3** has a constant value of 1.2 and 1.8,

respectively, for various exposure times, due to a rapid diffusion through the large appertures.

- **6ET-RCC3** with the smallest pore aperture has the highest selectivity but small uptake while **CC3** and **6FT-RCC3** exhibit a large gas uptake amount but low selectivity due to the large cavity and aperture. To optimize the separation and adsorption performance, a cocrystal possessing interconnected small and large cavities has been designed by crystal engineering. A porous network formed by chiral recognition between **CC3** and **6ET-RCC3** is named **Cocryst1**. The cage with small pore aperture acts as a diffusion barrier for effectively reducing H_2 diffusion, resulting in the KQS effect, while the cage with large cavity provides enough space for high isotope gas adsorption.

- The temperature-dependent gate opening effect can also be observed in **Cocryst1**. A strong hysteresis observed at 30 K with a moderate uptake shows that equilibrium is not fully reached, since that the gas molecules cannot penetrate into the structure at this low temperature. For higher temperatures, the hysteresis becomes weaker and eventually vanishes, denoting that both H_2 and D_2 molecules can diffuse faster in the channels. TDS spectra after isotope mixture exposure at 30 K reveal the highest D_2/H_2 selectivity of 8 in combination with considerable uptake amount (4.5 mmol/g for D_2). This combination is comparable with the best reported kinetic quantum sieves.

- For the first time, HD separation from hydrogen isotopes has been experimentally investigated in porous cages after exposure to a H_2/HD/D_2 mixture. The selectivity of $S_{D2/HD}$ and $S_{HD/H2}$ are 4.8 and 2.4, respectively, revealing that the cocrystal can be used for technical application for separation of HD from H_2 and D_2.

- The selectivity is greatly enhanced in **Cocryst1**, even though **6ET-RCC3** provides the diffusion barrier. **Cocryst1** consists of an alternating large storage pores and small separation pores. Penetration through the small apertures into the next larger cavity therefore yields each time an additional sieving step, whereby D_2 molecules can pass neighboring H_2 molecules inside the large cavity. As a result, **Cocryst1** has greatly enhanced D_2/H_2 selectivity, when both isotopes need to diffuse through the alternating small-pore-large-pore network resulting in a multiple sieving effect. By contrast, the small channels of **6ET-RCC3** lead to a single-file filling: Once a molecule penetrates in the pore, no exchange between the isotopes in the narrow channels is possible and KQS only occurs at the outmost pore aperture.

Hydrogen isotope separation by dynamic opening of aperture

A partially fluorinated metal–organic framework (MOF) with copper, FMOFCu, has been investigated. The unique structure of this porous material consists of a tri-modal pore system with large tubular cavities connected through a smaller cavity with bottleneck apertures with a size of 3.6 Å plus a third hidden cavity connected by an even smaller aperture of 2.5 Å.

- Hydrogen adsorption on FMOFCu starts at 25 K, exhibiting a hysteresis and reaching the maximum uptake at 77 K (1.85 mmol/g). The observed hysteresis becomes stronger in the temperature range up to 77 K and then weaker above 87 K, implying a faster equilibrium at higher temperatures. This unique behavior below 77 K can be ascribed to a strong diffusion limitation, produced by the two small bottleneck windows. The increasing adsorption amount and hysteresis observed between 25 and 77 K indicate that more H_2 molecules can access the pore system at higher temperatures due to thermally induced gate opening of the two bottleneck windows by the thermal vibration of the CF_3 groups.

- TDS measurements on isotope mixtures show increasing desorption maxima with higher exposure temperatures. At low exposure temperatures of 25 K, the isotope separation is mainly governed by the faster diffusion of D_2 into cavity A and B independently or through the 3.6 Å bottleneck connecting cavity A and B, while cavity C is not accessible. The small aperture of 3.6 Å produces a strong diffusion barrier at 25 K, allowing D_2 to preferentially penetrate into the structure, leading to a high selectivity of 14. At higher exposure temperature, the isotope uptake is increasing with decreasing selectivity due to a thermally activated opening of the aperture by local vibrations of CF_3 groups which enables a better accessibility. Above T_{exp} of 60 K, the 2.5 Å aperture connecting for cavity C opens thermally and gas can access. Cooling down results in an entrapment of gas molecules while they are released at high temperatures. This increases drastically the desorption temperature (up to 100 K) to values comparable to or even higher than the desorption temperatures reached by open metal sites in other MOFs. Furthermore, a selectivity between 3 and 4 is still achieved at exposure temperatures of 77 and 87 K, showing the potential of this material for isotope separation above liquid nitrogen temperature.

The current work reveals the potential of novel porous materials to separate D_2/H_2 mixtures compared to the conventional techniques. Chemical affinity sieving has been investigated for zeolites with unsaturated metal sites, showing for zeolite AgY a selectivity up to 10 and D_2 uptake of 3 mmol/g above liquid nitrogen temperature. Kinetic quantum sieving has been studied on nanoporous materials with reduced and flexible apertures. Porous organic cages with fine-tuned small apertures and a cocrystal with alternating small and large cavities are tested for the first time, exhibiting a selectivity of 8 and 4.5 mmol/g deuterium uptake at 30 K which is above hydrogen boiling point. A MOF with a trimodal pore structure connected by thermally-induced, flexible apertures shows the possibility of hydrogen isotope separation above liquid nitrogen temperature by kinetic quantum sieving. The present results combine a high selectivity with good gas uptake and show the potential of novel porous materials for industrial hydrogen isotope separation.

Appendix A
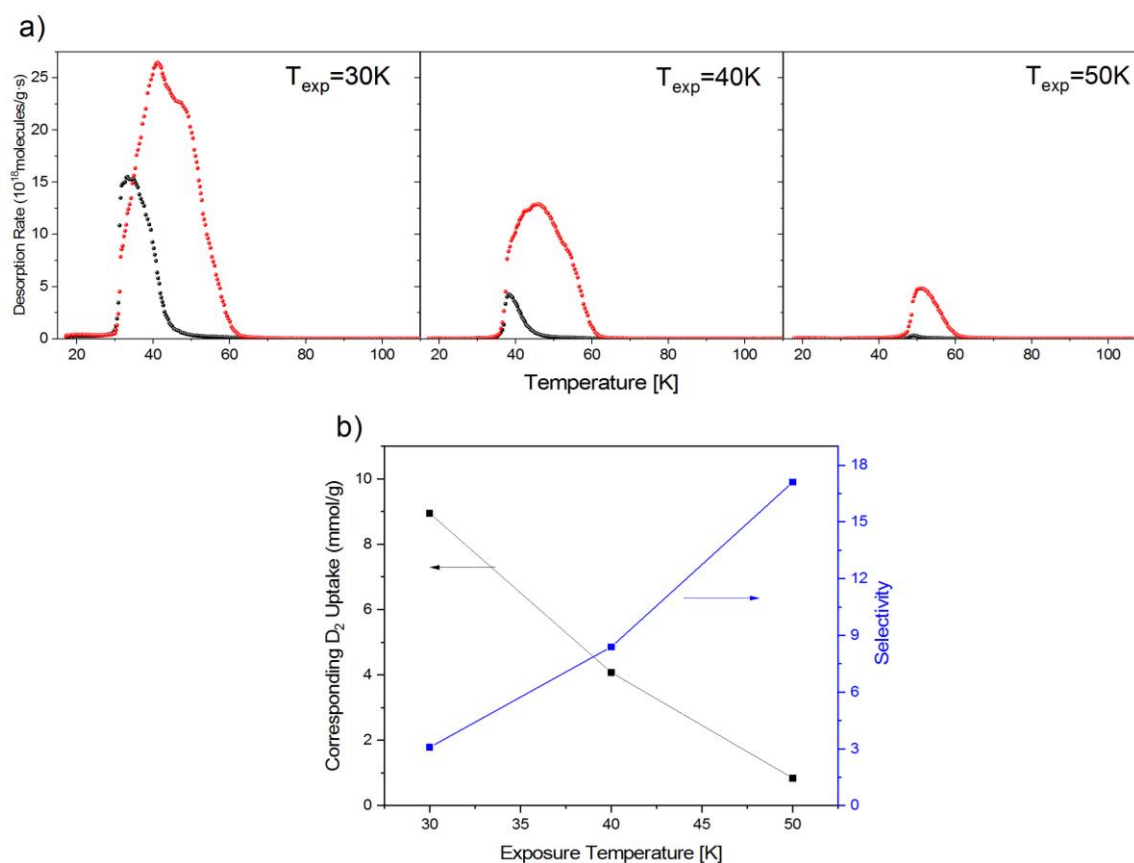
Figure A.1 Zeolite CoY a) H$_2$ (black) and D$_2$ (red) desorption spectra of 10 mbar 1:1 D$_2$/H$_2$ mixture exposure at exposure temperature of 30, 40, and 50 K for 10 min. b) D$_2$/H$_2$ selectivity (blue) and corresponding amount of adsorbed D$_2$ (black) as function of exposure temperature.
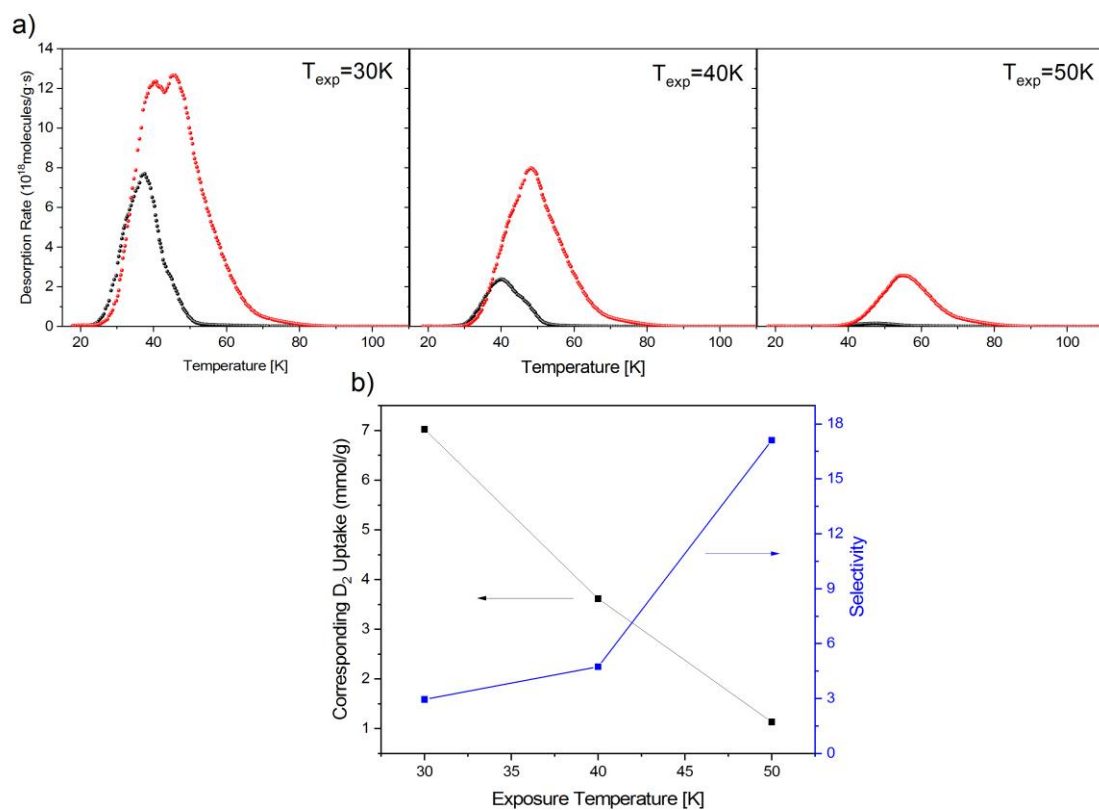
Figure A.2 Zeolite NiY a) H_2 (black) and D_2 (red) desorption spectra of 10 mbar 1:1 D_2/H_2 mixture exposure at exposure temperature of 30, 40, and 50 K for 10 min. b) D_2/H_2 selectivity (blue) and corresponding amount of adsorbed D_2 (black) as function of exposure temperature.
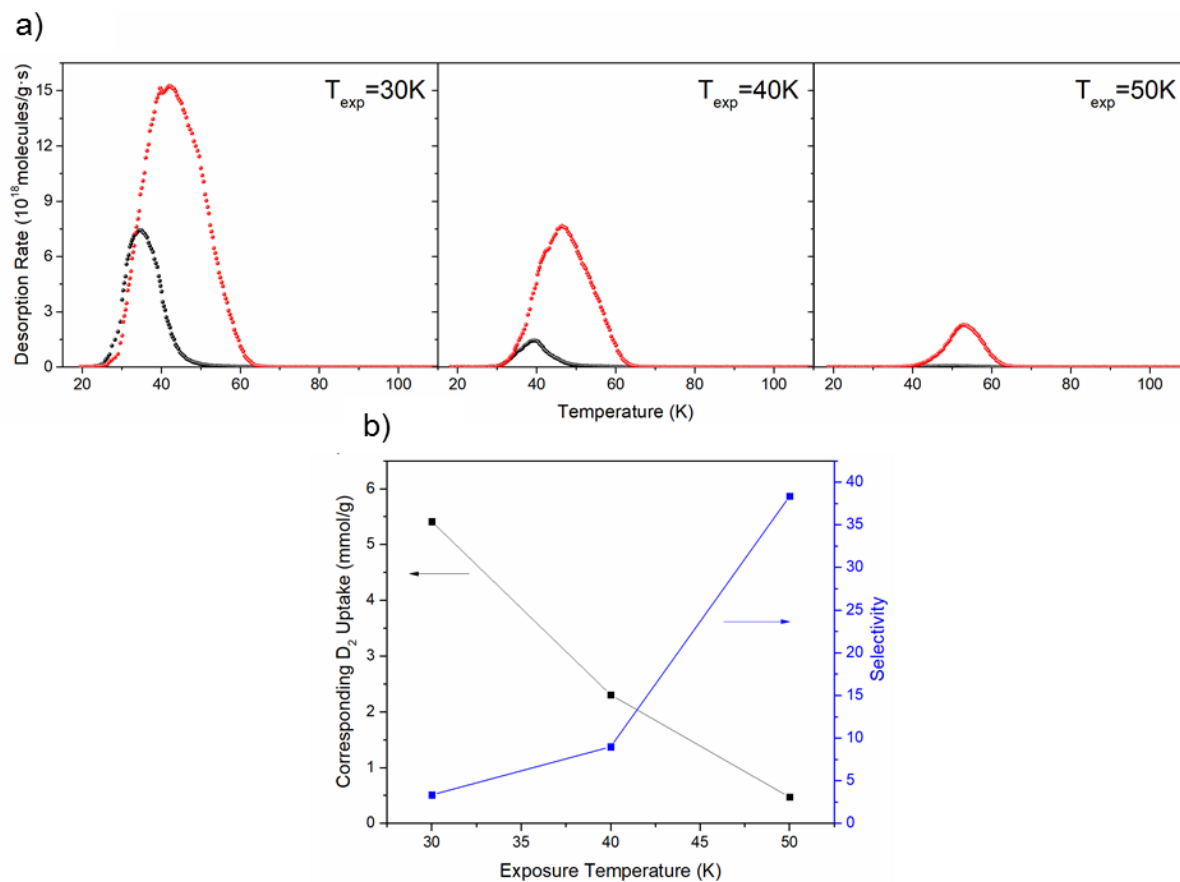
Figure A.3 Zeolite CuY a) H_2 (black) and D_2 (red) desorption spectra of 10 mbar 1:1 D_2/H_2 mixture exposure at exposure temperature of 30, 40, and 50 K for 10 min. b) D_2/H_2 selectivity (blue) and corresponding amount of adsorbed D_2 (black) as function of exposure temperature.
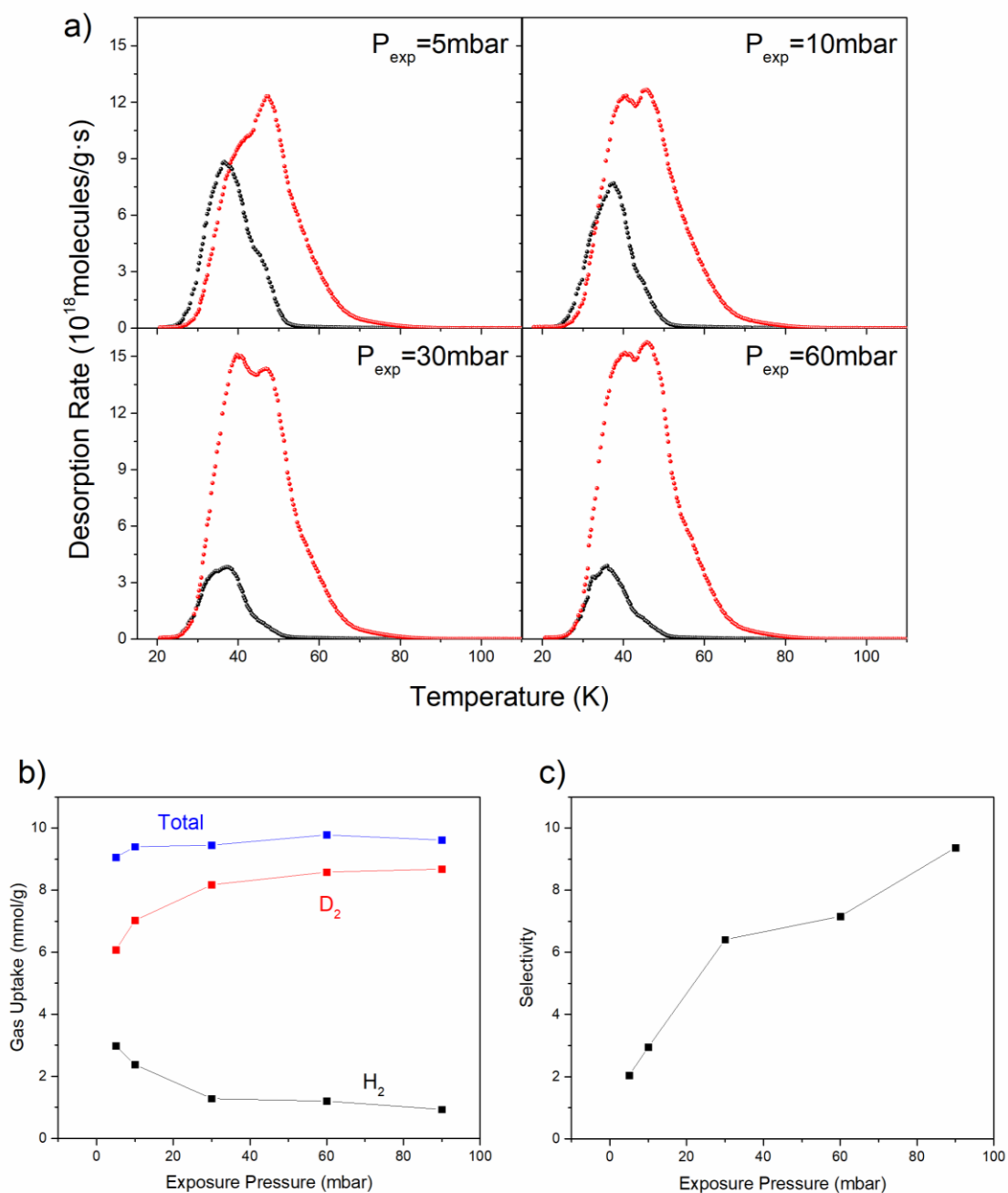
Figure A.4 Zeolite NiY a) H_2 (black) and D_2 (red) desorption spectra of 1:1 D_2/H_2 mixture exposure at exposure temperature of 30 K for 10 min of various exposure pressures. b) The adsorbed amount of isotope gases (H_2 black, D_2 red) and their total amount (blue) as function of exposure pressure. c) The D_2/H_2 selectivity as function of exposure pressure.
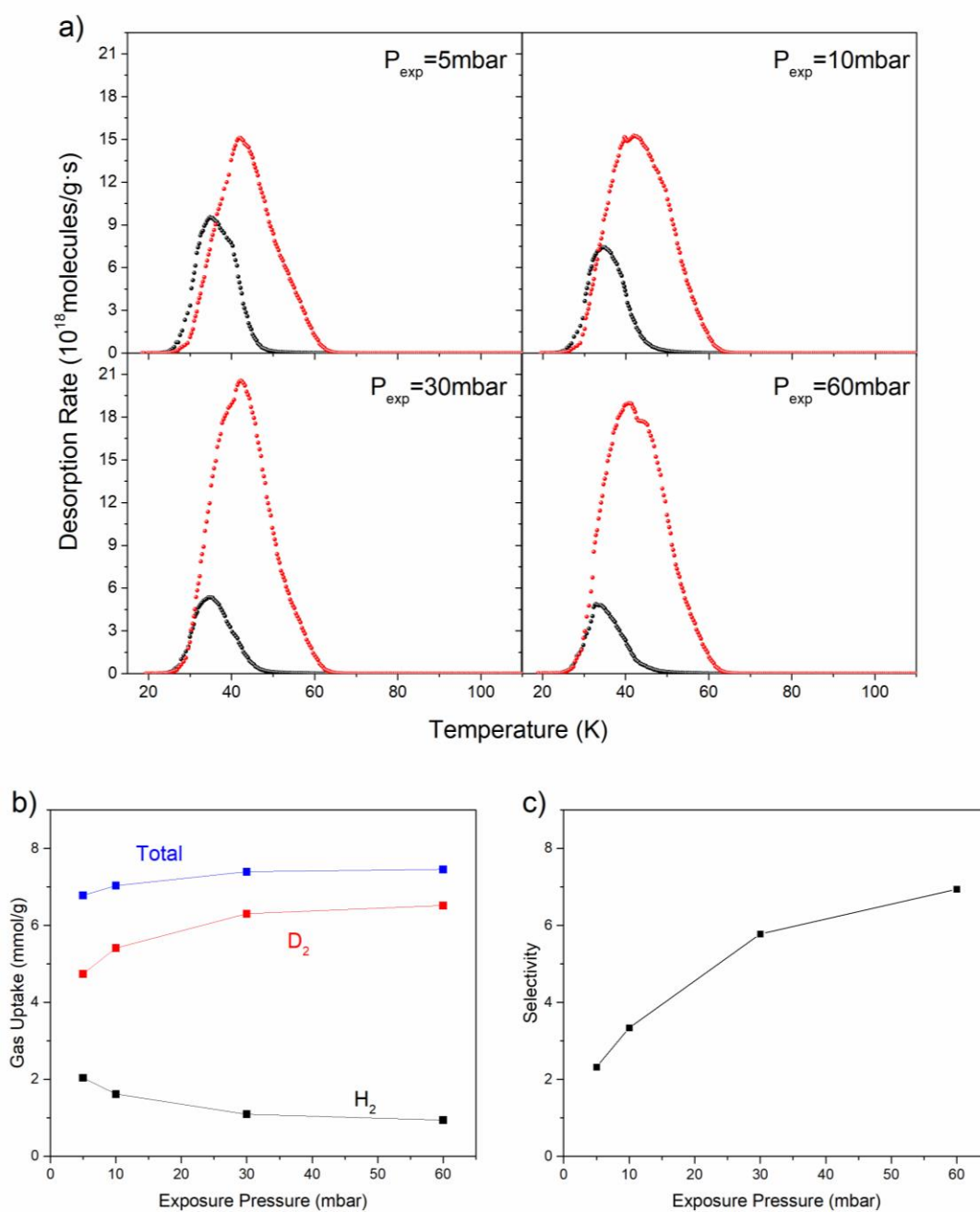
Figure A.5 Zeolite CuY a) H_2 (black) and D_2 (red) desorption spectra of 1:1 D_2/H_2 mixture exposure at exposure temperature of 30 K for 10 min of various exposure pressures. b) The adsorbed amount of isotope gases (H_2 black, D_2 red) and their total amount (blue) as function of exposure pressure. c) The D_2/H_2 selectivity as function of exposure pressure.

Appendix B

Table B.1 Summary of hydrogen isotope selectivities and adsorption amount for various porous materials via KQS (directly measured by TDS).

Compound	T_{exp}(K)	Selectivity (D$_2$/H$_2$) (1:1 Mixture)	Adosrbed D$_2$ amount (mmol/g)	Ref.
MFU-4 (Co, Cl)	30	4.0	4.72	162
	40	2.0	4.66	
MFU-4 (Zn, Cl)	40	6.9	0.02	155
	50	5.8	0.40	
	60	7.5	1.24	
MFU-4 (Zn, Br)	70	2.1	0.07	162
MFU-4*l*	40	1.7	8.30	163
Takeda 3A	40	6.8	0.01	162
	50	5.9	0.03	
MOF-5	70	1.4	11.15	
Py@COF-1	22	9.7	0.50	154
	30	7.9	0.60	
IFP-1	30	2.0	9.30	161
IFP-3	30	2.8	2.49	
IFP-7	77	1.5	0.05	
IFP-4	77	2.1	0.01	

Zeolite 5A	30	2.7	4	164
CC3	30	1.7	3.67	
	50	1.8	1.20	
6FT-RCC3	30	2.2	2.81	This work
	50	3.0	0.78	
6ET-RCC3	30	3.9	0.39	
	50	1.8	0.32	
Cocryst1	30	8.0	4.72	

Table B.2 Summary of experimentally measured hydrogen isotope separation performance on various porous materials via KQS.

Compound	Aperture (Å)	T (K)	P (mbar)	Selectivity (D_2/H_2) (1:1 Mixture)	Ratio (nD_2/nH_2) (Pure Gas Isotherms)	Ratio (kD_2/kH_2) (Rate constant)	Ref.
Breakthrough							
CMS	5-7/ 15-35	77	4000	1.53 ($H_2:D_2$=139:175)	-	-	170
Zeolite 5A	5	77		1.8 ($H_2:D_2$=99:1)	-	-	171
Zeolite 13X	8	77		1.9 ($H_2:D_2$=99:1)	-	-	
Zeolite Y	6-7	77	4000	Up to 1.52 ($H_2:D_2$=139:175)	-	-	172
Pure gas sorption							
CMS T3A	5.46	77	5-1000	-	1.063	-	171
PCS	5.66	77	50-500	-	-	Up to 1.9	
		77	5-1000	-	1.097	-	
		77	0-50	-	-	Up to 1.25	
3KT-172	4.9	77	20	-	-	1.86	173
1.5GN-H	4.6	77	100	-	-	5.83	
CNH	-	77	70-1000	-	1.09	-	174
HKUST-1	9/5	77	20	-	1.23	-	
SWCNT	13-14	77	10000	-	1.2	-	175
SG-SWCNT	28.5	40	0.1-10	Up to 5*	-	-	176
		77		Up to 3.8*			
LA-SWCNT	13.7	40	0.1-10	Up to 2.8*	-	-	
		77		Up to 1.5*			
Zeolite 5A	5	77	0.01-10	Up to 3.26*	-	-	177

Zeolite NaX	7.4	77	139	-	1.18	-	178
		30	Stand-ard pressure	-	1.06	-	
		40			1.03		
		50			1.43		
		77			1.33		
Zeolite 4A	4	77	150	2.09*	-	-	179
Zeolite 5A	5	77	150	2.48*	-	-	
Zeolite Y	6-7	77	150	1.32*	-	-	
Zeolite 10X	8	77	150	1.3*	-	-	
CMK-3	35	77	150	0.95*	-	-	
Zeolite 13X	8	77	0.1-1000	Up to 3.2*	-	-	180
CuBOTf	2×2 8.7×8.7	40	0.1-10	Up to 5.8*	-	-	157
		77	0.1-10	Up to 5.8*	-	-	
		77	50-1000	-	1.13	-	
M'MOF 1	5.6×12	77	5-1000	-	1.09	-	181
		87		-	1.11	-	
ZIF-7	3	20	Near-zero pressure	-	-	-	168
ZIF-8	3.4	20		-	11	-	
COF-1	9	20		-	7	-	
COF-102	12	20		-	1	-	
MFU-4 (Zn)	3.88/ 11.93/ 2.52	50	7	-	4.1	-	155
		60	4	-	2.3	-	
		70	1.8	-	1.7	-	
Fe-MOF-74	11	77	Near-zero pressure	2.5*	2.5	-	147
Co-MOF-74	11	77		3.2*	3.25	-	
Ni-MOF-74	11	77		5*	4.5	-	
VSB-5	11	140	0-1000	Up to 4*	-	-	182
12-Connected MOFs	10	77	1000	-	1.1	-	183
Cu2L2	7.3	77	100	-	1.2	-	34

Pseudoisobaric mixture gas sorption[184]

Zeolite 3A	3	77-130	85	4.33	-	-	185
		77-140		3.04	-	-	
		77-160		2.32	-	-	
		77-130	58	3.19*	-	-	
		77-140		2.60*	-	-	
		77-160		2.20*	-	-	
MS13X	8.6	77	-	3.05	-	-	186

* D_2/H_2 mixture selectivity calculated by IAST.

Appendix C
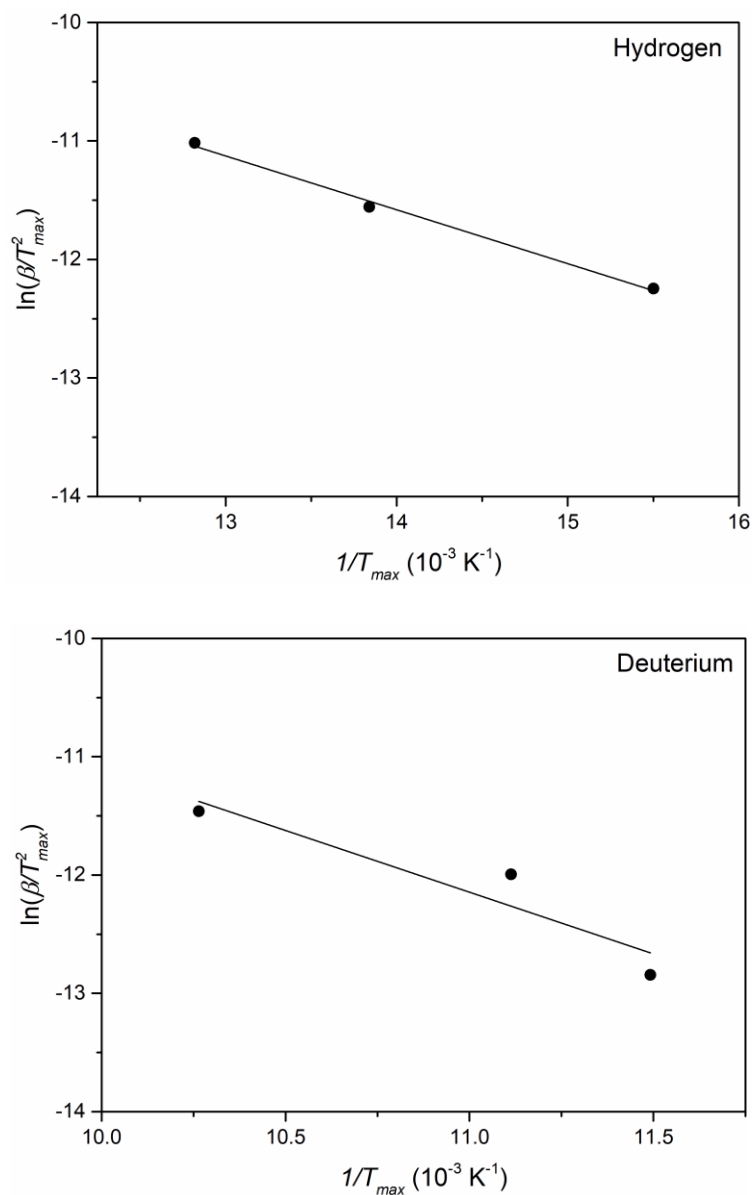
Figure C.1. The Kissinger plot for hydrogen (top) and deuterium (bottom) for determination of desorption energy of hydrogen isotopes adsorbed on zeolite AgY. The method has been described in section 3.1.3 and can be used according to equation 3.16. T_{max} is the maximum temperature while β is the heating rate. The desorption energy can be calculated from the slope by plotting $\ln(\beta/T_{max}^2)$ versus $1/T_{max}$

References

1.   Advantages of fusion. June 23, 2020.

2.   Fusion. https://www.iter.org/sci/whatisfusion. June 23, 2020.

3.   Kikuchi, M., Frontiers in Fusion Research: Physics and Fusion. Springer, London: 2011.

4.   Stacey, W. M., *Fusion: An Introduction to the Physics and Technology of Magnetic Confinement Fusion*. 2 ed.; Wiley-VCH: 2010.

5.   Greenwood, N. N.; Earnshaw, A., *Chemistry of the Elements*. Elsevier: 2012.

6.   Urey, H. C.; Brickwedde, F. G.; Murphy, G. M., A hydrogen isotope of mass 2 and its concentration. *Physical Review* **1932,** *40* (1), 1.

7.   Meija, J.; Coplen, T. B.; Berglund, M.; Brand, W. A.; De Bièvre, P.; Gröning, M.; Holden, N. E.; Irrgeher, J.; Loss, R. D.; Walczyk, T., Isotopic compositions of the elements 2013 (IUPAC technical Report). *Pure and Applied Chemistry* **2016,** *88* (3), 293-306.

8.   Beenakker, J.; Borman, V.; Krylov, S. Y., Molecular transport in subnanometer pores: zero-point energy, reduced dimensionality and quantum sieving. *Chemical Physics Letters* **1995,** *232* (4), 379-382.

9.   Thommes, M.; Kaneko, K.; Neimark, A. V.; Olivier, J. P.; Rodriguez-Reinoso, F.; Rouquerol, J.; Sing, K. S., Physisorption of gases, with special reference to the evaluation of surface area and pore size distribution (IUPAC Technical Report). *Pure and Applied Chemistry* **2015,** *87* (9-10), 1051-1069.

10.   Stadie, N. P. Synthesis and thermodynamic studies of physisorptive energy storage materials. California Institute of Technology, 2013.

11.   Clerk-Maxwell, J., On the dynamical evidence of the molecular constitution of bodies. Nature Publishing Group: 1875.

12.   Parsegian, V. A., *Van der Waals forces: a handbook for biologists, chemists, engineers, and physicists*. Cambridge University Press: 2005.

References

13. Dzyaloshinskii, I. E. e.; Lifshitz, E. M.; Pitaevskii, L. P., The general theory of van der Waals forces. *Advances in Physics* **1961,** *10* (38), 165-209.

14. London, F., Zur theorie und systematik der molekularkräfte. *Zeitschrift für Physik* **1930,** *63* (3-4), 245-279.

15. London, F., The general theory of molecular forces. *Transactions of the Faraday Society* **1937,** *33*, 8b-26.

16. Lennard-Jones, J., Processes of adsorption and diffusion on solid surfaces. *Transactions of the Faraday Society* **1932,** *28*, 333-359.

17. Lennard-Jones, J. E., Cohesion. *Proceedings of the Physical Society* **1931,** *43* (5), 461.

18. Jones, J. E., On the determination of molecular fields.—II. From the equation of state of a gas. *Proceedings of the Royal Society of London. Series A, Containing Papers of a Mathematical and Physical Character* **1924,** *106* (738), 463-477.

19. Jankowska, H.; Swiatkowski, V.; Choma, J., Active Carbon, Ellis Harwood Ltd., Chichester (1990). M. Jaroniec and R. Madey. *Carbon* **1988,** *26*, 107.

20. Bond, R. L., *Porous carbon solids*. Academic Press: 1967.

21. Ruthven, D. M., *Principles of adsorption and adsorption processes*. John Wiley & Sons: 1984.

22. W John Thomas, F.; Crittenden, B., *Adsorption technology and design*. Butterworth-Heinemann: 1998.

23. Reid, C.; Thomas, K., Adsorption of gases on a carbon molecular sieve used for air separation: linear adsorptives as probes for kinetic selectivity. *Langmuir* **1999,** *15* (9), 3206-3218.

24. Tascón, J. M., *Novel carbon adsorbents*. Elsevier: 2012.

25. Auerbach, S. M.; Carrado, K. A.; Dutta, P. K., *Handbook of zeolite science and technology*. CRC press: 2003.

26. Cejka, J.; Corma, A.; Zones, S., *Zeolites and catalysis: synthesis, reactions and applications*. John Wiley & Sons: 2010.

158

27.   Kärger, J.; Ruthven, D., Diffusion in zeolites. *Handbook of Zeolite Science and Technology* **1992,** *341*.

28.   Kirschhock, C.; Hunger, B.; Martens, J.; Jacobs, P., Localization of residual water in alkali-metal cation-exchanged X and Y type zeolites. *The Journal of Physical Chemistry B* **2000,** *104* (3), 439-448.

29.   Frising, T.; Leflaive, P., Extraframework cation distributions in X and Y faujasite zeolites: A review. *Microporous and Mesoporous Materials* **2008,** *114* (1-3), 27-63.

30.   Zhou, H.-C.; Long, J. R.; Yaghi, O. M., Introduction to metal–organic frameworks. ACS Publications: 2012.

31.   Li, H.; Eddaoudi, M.; O'Keeffe, M.; Yaghi, O. M., Design and synthesis of an exceptionally stable and highly porous metal-organic framework. *nature* **1999,** *402* (6759), 276-279.

32.   Eddaoudi, M.; Li, H.; Yaghi, O., Highly porous and stable metal− organic frameworks: structure design and sorption properties. *Journal of the American Chemical Society* **2000,** *122* (7), 1391-1397.

33.   Nouar, F.; Eubank, J. F.; Bousquet, T.; Wojtas, L.; Zaworotko, M. J.; Eddaoudi, M., Supermolecular building blocks (SBBs) for the design and synthesis of highly porous metal-organic frameworks. *Journal of the American Chemical Society* **2008,** *130* (6), 1833-1835.

34.   Adil, K.; Belmabkhout, Y.; Pillai, R. S.; Cadiau, A.; Bhatt, P. M.; Assen, A. H.; Maurin, G.; Eddaoudi, M., Gas/vapour separation using ultra-microporous metal–organic frameworks: insights into the structure/separation relationship. *Chemical Society Reviews* **2017,** *46* (11), 3402-3430.

35.   Chang, F.; Zhou, J. Chen, P.; Chen, Y.; Jia, H.; Saad, S. M.; Gao, Y.; Cao, X.; Zheng, T., Microporous and mesoporous materials for gas storage and separation: a review. *Asia-Pacific Journal of Chemical Engineering* **2013,** *8* (4), 618-626.

36.   Davankov, V.; Tsyurupa, M., Structure and properties of hypercrosslinked polystyrene—the first representative of a new class of polymer networks. *Reactive Polymers* **1990,** *13* (1-2), 27-42.

37.   Martín, C. F.; Stöckel, E.; Clowes, R.; Adams, D. J.; Cooper, A. I.; Pis, J. J.; Rubiera, F.; Pevida, C., Hypercrosslinked organic polymer networks as potential adsorbents for pre-combustion CO_2 capture. *Journal of Materials Chemistry* **2011,** *21* (14), 5475-5483.

38.   Ben, T.; Ren, H.; Ma, S.; Cao, D.; Lan, J.; Jing, X.; Wang, W.; Xu, J.; Deng, F.; Simmons, J. M., Targeted synthesis of a porous aromatic framework with high stability and exceptionally high surface area. *Angewandte Chemie International Edition* **2009,** *48* (50), 9457-9460.

39.   Tan, L.; Tan, B., Hypercrosslinked porous polymer materials: design, synthesis, and applications. *Chemical Society Reviews* **2017,** *46* (11), 3322-3356.

40.   Kuhn, P.; Antonietti, M.; Thomas, A., Porous, covalent triazine-based frameworks prepared by ionothermal synthesis. *Angewandte Chemie International Edition* **2008,** *47* (18), 3450-3453.

41.   Wright, P. A., *Microporous framework solids*. Royal Society of Chemistry: 2007.

42.   Ritchie, L. K.; Trewin, A.; Reguera-Galan, A.; Hasell, T.; Cooper, A. I., Synthesis of COF-5 using microwave irradiation and conventional solvothermal routes. *Microporous and mesoporous materials* **2010,** *132* (1-2), 132-136.

43.   Diring, S.; Furukawa, S.; Takashima, Y.; Tsuruoka, T.; Kitagawa, S., Controlled multiscale synthesis of porous coordination polymer in nano/micro regimes. *Chemistry of Materials* **2010,** *22* (16), 4531-4538.

44.   Larsen, S. C., Nanocrystalline zeolites and zeolite structures: synthesis, characterization, and applications. *The Journal of Physical Chemistry C* **2007,** *111* (50), 18464-18474.

45.   Holmberg, B. A.; Wang, H.; Norbeck, J. M.; Yan, Y., Controlling size and yield of zeolite Y nanocrystals using tetramethylammonium bromide. *Microporous and mesoporous materials* **2003,** *59* (1), 13-28.

46.   Hasell, T.; Cooper, A. I., Porous organic cages: soluble, modular and molecular pores. *Nature Reviews Materials* **2016,** *1* (9), 1-14.

47.   Tozawa, T.; Jones, J. T.; Swamy, S. I.; Jiang, S.; Adams, D. J.; Shakespeare, S.; Clowes, R.; Bradshaw, D.; Hasell, T.; Chong, S. Y., Porous organic cages. *Nature materials* **2009,** *8* (12), 973-978.

48.   Little, M. A.; Cooper, A. I., The Chemistry of Porous Organic Molecular Materials. *Advanced Functional Materials* **2020**.

49.   Furukawa, H.; Ko, N.; Go, Y. B.; Aratani, N.; Choi, S. B.; Choi, E.; Yazaydin, A. Ö.; Snurr, R. Q.; O'Keeffe, M.; Kim, J., Ultrahigh porosity in metal-organic frameworks. *Science* **2010,** *329* (5990), 424-428.

50.   Cote, A. P.; Benin, A. I.; Ockwig, N. W.; O'Keeffe, M.; Matzger, A. J.; Yaghi, O. M., Porous, crystalline, covalent organic frameworks. *science* **2005,** *310* (5751), 1166-1170.

51.   El-Kaderi, H. M.; Hunt, J. R.; Mendoza-Cortés, J. L.; Côté, A. P.; Taylor, R. E.; O'Keeffe, M.; Yaghi, O. M., Designed synthesis of 3D covalent organic frameworks. *Science* **2007,** *316* (5822), 268-272.

52.   Holst, J. R.; Stöckel, E.; Adams, D. J.; Cooper, A. I., High surface area networks from tetrahedral monomers: metal-catalyzed coupling, thermal polymerization, and "click" chemistry. *Macromolecules* **2010,** *43* (20), 8531-8538.

53.   Mastalerz, M.; Schneider, M. W.; Oppel, I. M.; Presly, O., A salicylbisimine cage compound with high surface area and selective CO_2/CH_4 adsorption. *Angewandte Chemie International Edition* **2011,** *50* (5), 1046-1051.

54.   Mastalerz, M., One-pot synthesis of a shape-persistent endo-functionalised nano-sized adamantoid compound. *Chemical Communications* **2008,** (39), 4756-4758.

55.   Chen, L.; Reiss, P. S.; Chong, S. Y.; Holden, D.; Jelfs, K. E.; Hasell, T.; Little, M. A.; Kewley, A.; Briggs, M. E.; Stephenson, A., Separation of rare gases and chiral molecules by selective binding in porous organic cages. *Nature materials* **2014,** *13* (10), 954-960.

56.   Hasell, T.; Miklitz, M.; Stephenson, A.; Little, M. A.; Chong, S. Y.; Clowes, R.; Chen, L.; Holden, D.; Tribello, G. A.; Jelfs, K. E., Porous organic cages for sulfur hexafluoride separation. *Journal of the American Chemical Society* **2016,** *138* (5), 1653-1659.

57.   Sozzani, P.; Bracco, S.; Comotti, A.; Ferretti, L.; Simonutti, R., Methane and carbon dioxide storage in a porous van der Waals crystal. *Angewandte Chemie International Edition* **2005,** *44* (12), 1816-1820.

58.   Bracco, S.; Miyano, T.; Negroni, M.; Bassanetti, I.; Marchio, L.; Sozzani, P.; Tohnai, N.; Comotti, A., CO_2 regulates molecular rotor dynamics in porous materials. *Chemical Communications* **2017,** *53* (55), 7776-7779.

59.   Lü, J.; Perez-Krap, C.; Suyetin, M.; Alsmail, N. H.; Yan, Y.; Yang, S.; Lewis, W.; Bichoutskaia, E.; Tang, C. C.; Blake, A. J., A robust binary supramolecular organic framework (SOF) with high CO_2 adsorption and selectivity. *Journal of the American Chemical Society* **2014,** *136* (37), 12828-12831.

60.   Cooper, A. I., Molecular organic crystals: from barely porous to really porous. *Angewandte Chemie International Edition* **2012,** *51* (32), 7892-7894.

61.   Msayib, K. J.; Book, D.; Budd, P. M.; Chaukura, N.; Harris, K. D.; Helliwell, M.; Tedds, S.; Walton, A.; Warren, J. E.; Xu, M., Nitrogen and hydrogen adsorption by an organic microporous crystal. *Angewandte Chemie International Edition* **2009,** *48* (18), 3273-3277.

62.   Bezzu, C. G.; Helliwell, M.; Warren, J. E.; Allan, D. R.; McKeown, N. B., Heme-like coordination chemistry within nanoporous molecular crystals. *Science* **2010,** *327* (5973), 1627-1630.

63.   Mastalerz, M.; Schneider, M. W.; Oppel, I. M.; Presly, O., Eine Salicylbisimin-Käfigverbindung mit großer spezifischer Oberfläche und selektiver CO_2/CH_4-Adsorption. *Angewandte Chemie* **2011,** *123* (5), 1078-1083.

64.   Jones, J. T.; Hasell, T.; Wu, X.; Bacsa, J.; Jelfs, K. E.; Schmidtmann, M.; Chong, S. Y.; Adams, D. J.; Trewin, A.; Schiffman, F., Modular and predictable assembly of porous organic molecular crystals. *Nature* **2011,** *474* (7351), 367-371.

65.   Schneider, M. W.; Oppel, I. M.; Ott, H.; Lechner, L. G.; Hauswald, H. J. S.; Stoll, R.; Mastalerz, M., Periphery-Substituted [4+6] Salicylbisimine Cage Compounds with Exceptionally High Surface Areas: Influence of the Molecular Structure on Nitrogen Sorption Properties. *Chemistry–A European Journal* **2012,** *18* (3), 836-847.

66.   Mastalerz, M.; Oppel, I. M., Rational construction of an extrinsic porous molecular crystal with an extraordinary high specific surface area. *Angewandte Chemie International Edition* **2012,** *51* (21), 5252-5255.

67.   Zhang, G.; Presly, O.; White, F.; Oppel, I. M.; Mastalerz, M., A permanent mesoporous organic cage with an exceptionally high surface area. *Angewandte Chemie International Edition* **2014,** *53* (6), 1516-1520.

68.   Bloch, E. D.; Queen, W. L.; Krishna, R.; Zadrozny, J. M.; Brown, C. M.; Long, J. R., Hydrocarbon separations in a metal-organic framework with open iron (II) coordination sites. *science* **2012,** *335* (6076), 1606-1610.

69.   Cui, X.; Chen, K.; Xing, H.; Yang, Q.; Krishna, R.; Bao, Z.; Wu, H.; Zhou, W.; Dong, X.; Han, Y., Pore chemistry and size control in hybrid porous materials for acetylene capture from ethylene. *Science* **2016,** *353* (6295), 141-144.

70.   Cadiau, A.; Adil, K.; Bhatt, P.; Belmabkhout, Y.; Eddaoudi, M., A metal-organic framework–based splitter for separating propylene from propane. *Science* **2016,** *353* (6295), 137-140.

71.   Barnett, B. R.; Gonzalez, M. I.; Long, J. R., Recent progress towards light hydrocarbon separations using metal–organic frameworks. *Trends in Chemistry* **2019**.

72.   Schneider, M. W.; Oppel, I. M.; Griffin, A.; Mastalerz, M., Post-Modification of the Interior of Porous Shape-Persistent Organic Cage Compounds. *Angewandte Chemie International Edition* **2013,** *52* (13), 3611-3615.

73.   Mitra, T.; Jelfs, K. E.; Schmidtmann, M.; Ahmed, A.; Chong, S. Y.; Adams, D. J.; Cooper, A. I., Molecular shape sorting using molecular organic cages. *Nature chemistry* **2013,** *5* (4), 276.

74.   Li, J.-R.; Sculley, J.; Zhou, H.-C., Metal–organic frameworks for separations. *Chemical reviews* **2012,** *112* (2), 869-932.

75.   Yang, R. T., *Gas separation by adsorption processes*. Butterworth-Heinemann: 2013.

76.   Kaneko, K.; Kanoh, H.; Hanzawa, Y., Fundamentals of Adsorption 7 Proceedings of FoA 7 Conference. *Nagasaki, May* **2001**.

77.   Yang, R. T., *Adsorbents: fundamentals and applications*. John Wiley & Sons: 2003.

78.   Vasaru, G., *Tritium isotope separation*. CRC press: 1993.

References

79.   Rutherford, W.; Lindsay, C., Separation of hydrogen isotopes by thermal diffusion. *Fusion Technology* **1985,** *8* (2P2), 2278-2284.

80.   Richter, F. M.; Watson, E. B.; Mendybaev, R.; Dauphas, N.; Georg, B.; Watkins, J.; Valley, J., Isotopic fractionation of the major elements of molten basalt by chemical and thermal diffusion. *Geochimica et Cosmochimica Acta* **2009,** *73* (14), 4250-4263.

81.   Timmerhaus, K.; Weitzel, D.; Flynn, T., Low Temperature Distillation of Hydrogen Isotopes. *Chem. Eng. Progr.* **1958,** *54*.

82.   Hu, S.; Hou, J.; Xiong, L.; Weng, K.; Yang, T.; Luo, Y., Hydrophobic Pt catalysts with different carbon substrates for the interphase hydrogen isotope separation. *Separation and purification technology* **2011,** *77* (2), 214-219.

83.   Degtyareva, O.; Bondareva, L., Gas-chromatographic analysis of mixtures of hydrogen Isotopes. *Journal of Analytical Chemistry* **2004,** *59* (5), 442-446.

84.   Ueda, S.; Nanjou, Y.; Itoh, T.; Tatenuma, K.; Matsuyama, M.; Watanabe, K., Development of advanced column material for hydrogen isotope separation at room temperature. *Fusion science and technology* **2002,** *41* (3P2), 1146-1150.

85.   Washburn, E. W.; Urey, H. C., Concentration of the H2 Isotope of Hydrogen by the Fractional Electrolysis of Water. *Proceedings of the National Academy of Sciences of the United States of America* **1932,** *18* (7), 496.

86.   Alekseev, I.; Bondarenko, S.; Fedorchenko, O.; Vasyanina, T.; Konoplev, K.; Arkhipov, E.; Voronina, T.; Grushko, A.; Tchijov, A.; Uborsky, V., Heavy water detritiation by combined electrolysis catalytic exchange at the experimental industrial plant. *Fusion engineering and design* **2003,** *69* (1-4), 33-37.

87.   Bernhardt, A. F., Isotope separation by laser deflection of an atomic beam. *Applied physics* **1976,** *9* (1), 19-34.

88.   Lis, G.; Wassenaar, L.; Hendry, M., High-precision laser spectroscopy D/H and $^{18}O/^{16}O$ measurements of microliter natural water samples. *Analytical chemistry* **2008,** *80* (1), 287-293.

89.   Perez-Carbajo, J.; Parra, J. B.; Ania, C. O.; Merkling, P. J.; Calero, S., Molecular Sieves for the Separation of Hydrogen Isotopes. *ACS applied materials & interfaces* **2019,** *11* (20), 18833-18840.

90.   Flynn, T.; Weitzel, D.; Timmerhaus, K.; Vander Arend, P.; Draper, J., Distillation of Hydrogen-Deuterium Mixtures. In *Advances in Cryogenic Engineering*, Springer: 1960; pp 39-44.

91.   Valenti, G., Separation of hydrogen isotopes by cryogenic distillation. **2017**.

92.   Rae, H. K. *Separation of hydrogen isotopes*; American Chemical Society, Washington, DC: 1978.

93.   Ragheb, M., Isotopic separation and enrichment. *Nuclear, plasma and radiation science. Inventing the future.* https://www. *researchgate. net/publication/242126786_ISOTOPIC_SEPARATION_AND_ ENRICHMENT. Accessed* **2015,** *15*.

94.   Beenakker, J.; Borman, V.; Krylov, S. Y., Molecular transport in the nanometer regime. *Physical review letters* **1994,** *72* (4), 514.

95.   Borman, V.; Krylov, S.; Prosyanov, A., Theory of Nonequilibrium Phenomena at a Gas/Solid Interface. *Sov. Phys. JETP* **1988,** *67* (10), 2110-2121.

96.   Everett, D. H.; Powl, J. C., Adsorption in slit-like and cylindrical micropores in the henry's law region. A model for the microporosity of carbons. *Journal of the Chemical Society, Faraday Transactions 1: Physical Chemistry in Condensed Phases* **1976,** *72*, 619-636.

97.   Nakamura, K.; Thomas, H., Quantum billiard in a magnetic field: chaos and diamagnetism. *Physical review letters* **1988,** *61* (3), 247.

98.   Jiao, Y.; Du, A.; Hankel, M.; Smith, S. C., Modelling carbon membranes for gas and isotope separation. *Physical Chemistry Chemical Physics* **2013,** *15* (14), 4832-4843.

99.   Kowalczyk, P.; Brualla, L.; Żywociński, A.; Bhatia, S. K., Single-walled carbon nanotubes: efficient nanomaterials for separation and on-board vehicle storage of hydrogen and methane mixture at room temperature? *The Journal of Physical Chemistry C* **2007,** *111* (13), 5250-5257.

100.   Waldmann, T.; Klein, J.; Hoster, H. E.; Behm, R. J., Stabilization of Large Adsorbates by Rotational Entropy: A Time-Resolved Variable-Temperature STM Study. *ChemPhysChem* **2013,** *14* (1), 162-169.

101. Müller, J., Role of zero-point energy changes in H_2-surface collisions: application to Cu (111) and Pt (111). *Surface science* **1992,** *272* (1-3), 45-52.

102. Falconer, J. L.; Schwarz, J. A., Temperature-programmed desorption and reaction: applications to supported catalysts. *Catalysis Reviews Science and Engineering* **1983,** *25* (2), 141-227.

103. Cvetanovic, R.; Amenomiya, Y., Application of a temperature-programmed desorption technique to catalyst studies. *Adv. Catal* **1967,** *17*, 103-149.

104. Collins, D.; Spicer, W., The adsorption of CO, O_2, and H_2 on Pt: I. Thermal desorption spectroscopy studies. *Surface Science* **1977,** *69* (1), 85-113.

105. King, D. A., Thermal desorption from metal surfaces: A review. *Surface Science* **1975,** *47* (1), 384-402.

106. Keller, J. U.; Staudt, R., *Gas adsorption equilibria: experimental methods and adsorptive isotherms*. Springer Science & Business Media: 2005.

107. Nagai, K., A simple rate equation useful for adsorption systems: Analyses of thermal desorption spectra. *Surface science* **1986,** *176* (1-2), 193-218.

108. Elliott, J.; Ward, C., Temperature programmed desorption: A statistical rate theory approach. *The Journal of Chemical Physics* **1997,** *106* (13), 5677-5684.

109. Katz, N.; Furman, I.; Biham, O.; Pirronello, V.; Vidali, G., Molecular hydrogen formation on astrophysically relevant surfaces. *The Astrophysical Journal* **1999,** *522* (1), 305.

110. Tomkova, E., TDS spectra analysis. *Surface science* **1996,** *351* (1-3), 309-318.

111. Parker, D. H.; Jones, M. E.; Koel, B. E., Determination of the reaction order and activation energy for desorption kinetics using TPD spectra: Application to D_2 desorption from Ag (111). *Surface science* **1990,** *233* (1-2), 65-73.

112. Kissinger, H. E., Reaction kinetics in differential thermal analysis. *Analytical chemistry* **1957,** *29* (11), 1702-1706.

113. De Jong, A.; Niemantsverdriet, J. Thermal desorption analysis: Comparative test of ten commonly applied procedures. *Surface Science* **1990,** *233* (3), 355-365.

166

114.   Piloyan, G.; Ryabchikov, I.; Novikova, O., Determination of activation energies of chemical reactions by differential thermal analysis. *Nature* **1966,** *212* (5067), 1229-1229.

115.   Redhead, P, Thermal desorption of gases. *Vacuum* **1962,** *12* (4), 203-211.

116.   Lord, F. M.; Kittelberger, J. On the determination of activation energies in thermal desorption experiments. *Surface Science* **1974,** *43* (1), 173-182.

117.   Coluzzi, B.; Biscarini, A.; Campanella, R.; Floridi, G.; Mazzolai, F.; Sakamoto, Y.; Lewis, F., Reorientation of the Ce–D pairs in a Pd95Ce5Dn alloy. *Journal of alloys and compounds* **1997,** *253*, 360-363.

118.   Yoshihara, M.; McLellan, R., Palladium-cerium-hydrogen solid solutions—I. Thermodynamic properties. *Acta Metallurgica* **1988,** *36* (12), 3217-3224.

119.   Cornell, D. A.; Seymour, E., Nuclear magnetic resonance study of hydrogen diffusion in palladium and palladium-cerium alloys. *Journal of the Less Common Metals* **1975,** *39* (1), 43-54.

120.   Broom, D, The accuracy of hydrogen sorption measurements on potential storage materials. *International Journal of Hydrogen Energy* **2007,** *32* (18), 4871-4888.

121.   Broom, D, Hydrogen sorption measurements on potential storage materials. *JRC Scientific and Technical Reports* **2008**.

122.   Blach, T; Gray, E. M., Sieverts apparatus and methodology for accurate determination of hydrogen uptake by light-atom hosts. *Journal of Alloys and Compounds* **2007,** *446*, 692-697.

123.   R.Balderas-Xicohtencatl. High-density hydrogen monolayer formation and isotope diffusion in porous media. Doctoral Thesis, University of Stuttgart, 2019.

124.   Sanaeepur, H.; Kargari, A.; Nasernejad, B.; Amooghin, A. E.; Omidkhah, M., A novel Co^{2+} exchanged zeolite Y/cellulose acetate mixed matrix membrane for CO_2/N_2 separation. *Journal of the Taiwan Institute of Chemical Engineers* **2016,** *60*, 403-413.

125.   Motazedi, K.; Mahinpey, N.; Karami, D., Preparation and application of faujasite-type Y zeolite-based catalysts for coal pyrolysis using sodium silicate solution and colloidal silica as silicon source. *Chemical Engineering Communications* **2016,** *203* (3), 300-317.

References

126.   Hernández-Maldonado, A. J.; Yang, F. H.; Qi, G.; Yang, R. T., Desulfurization of transportation fuels by π-complexation sorbents: Cu (I)-, Ni (II)-, and Zn (II)-zeolites. *Applied Catalysis B: Environmental* **2005,** *56* (1-2), 111-126.

127.   Xue, M.; Chitrakar, R.; Sakane, K.; Hirotsu, T.; Ooi, K.; Yoshimura, Y.; Toba, M.; Feng, Q., Preparation of cerium-loaded Y-zeolites for removal of organic sulfur compounds from hydrodesulfurizated gasoline and diesel oil. *Journal of colloid and interface science* **2006,** *298* (2), 535-542.

128.   Li, Y.; Yang, R. T., Hydrogen storage in low silica type X zeolites. *The Journal of Physical Chemistry B* **2006,** *110* (34), 17175-17181.

129.   Wang, L.; Yang, R. T., Hydrogen storage properties of low-silica type X zeolites. *Industrial & engineering chemistry research* **2010,** *49* (8), 3634-3641.

130.   Prasanth, K.; Pillai, R. S.; Bajaj, H.; Jasra, R.; Chung, H.; Kim, T.; Song, S., Adsorption of hydrogen in nickel and rhodium exchanged zeolite X. *International journal of hydrogen energy* **2008,** *33* (2), 735-745.

131.   Palomino, G.; Bonelli, B.; Areán, C. O.; Parra, J.; Carayol, M.; Armandi, M.; Ania, C. O.; Garrone, E., Thermodynamics of hydrogen adsorption on calcium-exchanged faujasite-type zeolites. *international journal of hydrogen energy* **2009,** *34* (10), 4371-4378.

132.   Kazansky, V.; Borovkov, V. Y.; Serich, A.; Karge, H., Low temperature hydrogen adsorption on sodium forms of faujasites: barometric measurements and drift spectra. *Microporous and mesoporous materials* **1998,** *22* (1-3), 251-259.

133.   Kazansky, V., Drift spectra of adsorbed dihydrogen as a molecular probe for alkaline metal ions in faujasites. *Journal of Molecular Catalysis A: Chemical* **1999,** *141* (1-3), 83-94.

134.   Regli, L.; Zecchina, A.; Vitillo, J. G.; Cocina, D.; Spoto, G.; Lamberti, C.; Lillerud, K. P.; Olsbye, U.; Bordiga, S., Hydrogen storage in chabazite zeolite frameworks. *Physical Chemistry Chemical Physics* **2005,** *7* (17), 3197-3203.

135.   Kang, L.; Deng, W.; Han, K.; Zhang, T.; Liu, Z., A DFT study of adsorption hydrogen on the Li-FAU zeolite. *International journal of hydrogen energy* **2008,** *33* (1), 105-110.

136.   Davies, J., *Spectroscopic and computational studies of supramolecular systems*. Springer Science & Business Media: 2013; Vol. 4.

137.   Karge, H. G.; Weitkamp, J., *Zeolites as catalysts, sorbents and detergent builders: applications and innovations*. Elsevier: 1989.

138.   Förster, H.; Schuldt, M., Studies of mobility and surface interaction of A_2 molecules in-zeolite A by IR spectroscopy. *Journal of Molecular Structure* **1980,** *61*, 361-364.

139.   Olson, D. H., Crystal structure of the zeolite nickel faujasite. *The Journal of Physical Chemistry* **1968,** *72* (13), 4366-4373.

140.   Eulenberger, G.; Shoemaker, D. P.; Keil, J., Crystal structures of hydrated and dehydrated synthetic zeolites with faujasite aluminosilicate frameworks. I. The dehydrated sodium, potassium, and silver forms. *The Journal of Physical Chemistry* **1967,** *71* (6), 1812-1819.

141.   Bosacek, V.; Beran, S.; Jirak, Z., Distribution of protons and cations in sodium HY zeolites. *The Journal of Physical Chemistry* **1981,** *85* (25), 3856-3859.

142.   Langmi, H.; Walton, A.; Al-Mamouri, M.; Johnson, S.; Book, D.; Speight, J.; Edwards, P.; Gameson, I.; Anderson, P.; Harris, I., Hydrogen adsorption in zeolites A, X, Y and RHO. *Journal of Alloys and Compounds* **2003,** *356*, 710-715.

143.   Langmi, H.; Book, D.; Walton, A.; Johnson, S.; Al-Mamouri, M.; Speight, J.; Edwards, P.; Harris, I.; Anderson, P., Hydrogen storage in ion-exchanged zeolites. *Journal of alloys and compounds* **2005,** *404*, 637-642.

144.   CHU, X.-Z.; XU, J.-M., Relationship Between the Adsorption Capacity of Hydrogen Isotopes and Specific Surface Area of Adsorbents. *Chemical Journal of Chinese Universities* **2008,** *4*.

145.   Chu, X.-Z.; Xu, J.-M.; Zhao, Y.-J.; Zhang, W.-G.; Chen, Z.-P.; Zhou, S.-Y.; Zhou, Y.-P.; Zhou, L., Monolayer adsorption behavior of hydrogen isotopes on microporous and mesoporous molecular sieves. *Journal of Chemical & Engineering Data* **2010,** *55* (7), 2512-2516.

146.   Chu, X.-Z.; Cheng, Z.-P.; Xiang, X.-X.; Xu, J.-M.; Zhao, Y.-J.; Zhang, W.-G.; Lv, J.-S.; Zhou, Y.-P.; Zhou, L.; Moon, D.-K., Separation dynamics of hydrogen isotope gas in mesoporous and microporous adsorbent beds at 77 K: SBA-15 and zeolites 5A, Y, 10X. *International journal of hydrogen energy* **2014,** *39* (9), 4437-4446.

References

147. Oh, H.; Savchenko, I.; Mavrandonakis, A.; Heine, T.; Hirscher, M., Highly effective hydrogen isotope separation in nanoporous metal–organic frameworks with open metal sites: direct measurement and theoretical analysis. *ACS nano* **2014,** *8* (1), 761-770.

148. Weinrauch, I.; Savchenko, I.; Denysenko, D.; Souliou, S.; Kim, H.; Le Tacon, M.; Daemen, L. L.; Cheng, Y.; Mavrandonakis, A.; Ramirez-Cuesta, A., Capture of heavy hydrogen isotopes in a metal-organic framework with active Cu (I) sites. *Nature communications* **2017,** *8* (1), 1-7.

149. Liu, M.; Little, M. A.; Jelfs, K. E.; Jones, J. T.; Schmidtmann, M.; Chong, S. Y.; Hasell, T.; Cooper, A. I., Acid-and base-stable porous organic cages: shape persistence and pH stability via post-synthetic "tying" of a flexible amine cage. *Journal of the American Chemical Society* **2014,** *136* (21), 7583-7586.

150. Liu, M.; Zhang, L.; Little, M. A.; Kapil, V.; Ceriotti, M.; Yang, S.; Ding, L.; Holden, D. L.; Balderas-Xicohténcatl, R.; He, D., Barely porous organic cages for hydrogen isotope separation. *Science* **2019,** *366* (6465), 613-620.

151. Kleywegt, G. J.; Jones, T. A., Detection, delineation, measurement and display of cavities in macromolecular structures. *Acta Crystallographica Section D: Biological Crystallography* **1994,** *50* (2), 178-185.

152. Lowell, S.; Shields, J. E., *Powder surface area and porosity*. Springer Science & Business Media: 2013; Vol. 2.

153. Kim, J. Y.; Zhang, L.; Balderas-Xicohténcatl, R.; Park, J.; Hirscher, M.; Moon, H. R.; Oh, H., Selective hydrogen isotope separation via breathing transition in MIL-53 (Al). *Journal of the American Chemical Society* **2017,** *139* (49), 17743-17746.

154. Oh, H.; Kalidindi, S. B.; Um, Y.; Bureekaew, S.; Schmid, R.; Fischer, R. A.; Hirscher, M., A cryogenically flexible covalent organic framework for efficient hydrogen isotope separation by quantum sieving. *Angewandte Chemie International Edition* **2013,** *52* (50), 13219-13222.

155. Teufel, J.; Oh, H.; Hirscher, M.; Wahiduzzaman, M.; Zhechkov, L.; Kuc, A.; Heine, T.; Denysenko, D.; Volkmer, D., MFU-4–A Metal-Organic Framework for Highly Effective H_2/D_2 Separation. *Advanced Materials* **2013,** *25* (4), 635-639.

156.	Zhang, L.; Jee, S.; Park, J.; Jung, M.; Wallacher, D.; Franz, A.; Lee, W.; Yoon, M.; Choi, K.; Hirscher, M., Exploiting Dynamic Opening of Apertures in a Partially Fluorinated MOF for Enhancing H_2 Desorption Temperature and Isotope Separation. *Journal of the American Chemical Society* **2019,** *141* (50), 19850-19858.

157.	Noguchi, D.; Tanaka, H.; Kondo, A.; Kajiro, H.; Noguchi, H.; Ohba, T.; Kanoh, H.; Kaneko, K., Quantum sieving effect of three-dimensional Cu-based organic framework for H_2 and D_2. *Journal of the American Chemical Society* **2008,** *130* (20), 6367-6372.

158.	FitzGerald, S. A.; Pierce, C. J.; Rowsell, J. L.; Bloch, E. D.; Mason, J. A., Highly selective quantum sieving of D_2 from H_2 by a metal–organic framework as determined by gas manometry and infrared spectroscopy. *Journal of the American Chemical Society* **2013,** *135* (25), 9458-9464.

159.	Xiao, B.; Wheatley, P. S.; Zhao, X.; Fletcher, A. J.; Fox, S.; Rossi, A. G.; Megson, I. L.; Bordiga, S.; Regli, L.; Thomas, K. M., High-capacity hydrogen and nitric oxide adsorption and storage in a metal− organic framework. *Journal of the American Chemical Society* **2007,** *129* (5), 1203-1209.

160.	Koppenol, W., Names for muonium and hydrogen atoms and their ions (IUPAC Recommendations 2001). *Pure and Applied Chemistry* **2001,** *73* (2), 377-379.

161.	Mondal, S. S.; Kreuzer, A.; Behrens, K.; Schütz, G.; Holdt, H. J.; Hirscher, M., Systematic Experimental Study on Quantum Sieving of Hydrogen Isotopes in Metal-Amide-Imidazolate Frameworks with narrow 1-D Channels. *ChemPhysChem* **2019,** *20* (10), 1311-1315.

162.	Teufel, J. S., Experimental investigation of H_2/D_2 isotope separation by cryo-adsorption in metal-organic frameworks. **2012**.

163.	Savchenko, I.; Mavrandonakis, A.; Heine, T.; Oh, H.; Teufel, J.; Hirscher, M., Hydrogen isotope separation in metal-organic frameworks: Kinetic or chemical affinity quantum-sieving? *Microporous and Mesoporous Materials* **2015,** *216*, 133-137.

164.	Xiong, R.; Xicohténcatl, R. B.; Zhang, L.; Li, P.; Yao, Y.; Sang, G.; Chen, C.; Tang, T.; Luo, D.; Hirscher, M., Thermodynamics, kinetics and selectivity of H_2 and D_2 on zeolite 5A below 77K. *Microporous and Mesoporous Materials* **2018,** *264*, 22-27.

References

165.   Liu, J.; Fernandez, C. A.; Martin, P. F.; Thallapally, P. K.; Strachan, D. M., A two-column method for the separation of Kr and Xe from process off-gases. *Industrial & Engineering Chemistry Research* **2014,** *53* (32), 12893-12899.

166.   Macrae, C. F.; Bruno, I. J.; Chisholm, J. A.; Edgington, P. R.; McCabe, P.; Pidcock, E.; Rodriguez-Monge, L.; Taylor, R.; Streek, J.; Wood, P. A., Mercury CSD 2.0–new features for the visualization and investigation of crystal structures. *Journal of Applied Crystallography* **2008,** *41* (2), 466-470.

167.   Fernandez, C. A.; Liu, J.; Thallapally, P. K.; Strachan, D. M., Switching Kr/Xe selectivity with temperature in a metal–organic framework. *Journal of the American Chemical Society* **2012,** *134* (22), 9046-9049.

168.   Oh, H.; Park, K. S.; Kalidindi, S. B.; Fischer, R. A.; Hirscher, M., Quantum cryo-sieving for hydrogen isotope separation in microporous frameworks: an experimental study on the correlation between effective quantum sieving and pore size. *Journal of Materials Chemistry A* **2013,** *1* (10), 3244-3248.

169.   Kim, J. Y.; Balderas-Xicohténcatl, R.; Zhang, L.; Kang, S. G.; Hirscher, M.; Oh, H.; Moon, H. R., Exploiting diffusion barrier and chemical affinity of metal–organic frameworks for efficient hydrogen isotope separation. *Journal of the American Chemical Society* **2017,** *139* (42), 15135-15141.

170.   Chu, X.-Z.; Cheng, Z.-P.; Zhao, Y.-J.; Xu, J.-M.; Li, M.-S.; Zhou, L.; Lee, C.-H., Adsorption dynamics of hydrogen and deuterium in a carbon molecular sieve bed at 77 K. *Separation and Purification Technology* **2015,** *146*, 168-175.

171.   Zhao, X.; Villar-Rodil, S.; Fletcher, A. J.; Thomas, K. M., Kinetic isotope effect for H_2 and D_2 quantum molecular sieving in adsorption/desorption on porous carbon materials. *The Journal of Physical Chemistry B* **2006,** *110* (20), 9947-9955.

172.   Chu, X.-Z.; Zhao, Y.-J.; Kan, Y.-H.; Zhang, W.-G.; Zhou, S.-Y.; Zhou, Y.-P.; Zhou, L., Dynamic experiments and model of hydrogen and deuterium separation with micropore molecular sieve Y at 77 K. *Chemical Engineering Journal* **2009,** *152* (2-3), 428-433.

172

173.   Xing, Y.; Cai, J.; Li, L.; Yang, M.; Zhao, X., An exceptional kinetic quantum sieving separation effect of hydrogen isotopes on commercially available carbon molecular sieves. *Physical Chemistry Chemical Physics* **2014,** *16* (30), 15800-15805.

174.   Tanaka, H.; Kanoh, H.; Yudasaka, M.; Iijima, S.; Kaneko, K., Quantum effects on hydrogen isotope adsorption on single-wall carbon nanohorns. *Journal of the American Chemical Society* **2005,** *127* (20), 7511-7516.

175.   Noguchi, D.; Hattori, Y.; Yang, C.; Tao, Y.; Konishi, T.; Fujikawa, T.; Ohkubo, T.; Nobuhara, Y.; Ohba, T.; Tanaka, H., Storage function of carbon nanospaces for molecules and ions. *ECS Transactions* **2007,** *11* (8), 63.

176.   Noguchi, D.; Tanaka, H.; Fujimori, T.; Kagita, H.; Hattori, Y.; Honda, H.; Urita, K.; Utsumi, S.; Wang, Z.-M.; Ohba, T., Selective D_2 adsorption enhanced by the quantum sieving effect on entangled single-wall carbon nanotubes. *Journal of Physics: Condensed Matter* **2010,** *22* (33), 334207.

177.   Kotoh, K.; Nishikawa, T.; Kashio, Y., Multi-component adsorption characteristics of hydrogen isotopes on synthetic zeolite 5A-type at 77.4 K. *Journal of nuclear science and technology* **2002,** *39* (4), 435-441.

178.   Salazar, J.; Lectez, S.; Gauvin, C.; Macaud, M.; Bellat, J.; Weber, G.; Bezverkhyy, I.; Simon, J., Adsorption of hydrogen isotopes in the zeolite NaX: Experiments and simulations. *International Journal of Hydrogen Energy* **2017,** *42* (18), 13099-13110.

179.   Chu, X.-Z.; Zhou, Y.-P.; Zhang, Y.-Z.; Su, W.; Sun, Y.; Zhou, L., Adsorption of hydrogen isotopes on micro-and mesoporous adsorbents with orderly structure. *The Journal of Physical Chemistry B* **2006,** *110* (45), 22596-22600.

180.   Kotoh, K.; Kudo, K., Multi-component adsorption behavior of hydrogen isotopes on zeolite 5A and 13X at 77.4 K. *Fusion science and technology* **2005,** *48* (1), 148-151.

181.   Chen, B.; Zhao, X.; Putkham, A.; Hong, K.; Lobkovsky, E. B.; Hurtado, E. J.; Fletcher, A. J.; Thomas, K. M., Surface interactions and quantum kinetic molecular sieving for H_2 and D_2 adsorption on a mixed metal− organic framework material. *Journal of the American Chemical Society* **2008,** *130* (20), 6411-6423.

182.   Sharma, A.; Lawler, K. V.; Wolffis, J. J.; Eckdahl, C. T.; McDonald, C. S.; Rowsell, J. L.; FitzGerald, S. A.; Forster, P. M., Hydrogen uptake on coordinatively unsaturated metal sites in VSB-5: Strong binding affinity leading to high-temperature D_2/H_2 selectivity. *Langmuir* **2017,** *33* (51), 14586-14591.

183.   Jia, J.; Lin, X.; Wilson, C.; Blake, A. J.; Champness, N. R.; Hubberstey, P.; Walker, G.; Cussen, E. J.; Schröder, M., Twelve-connected porous metal–organic frameworks with high H 2 adsorption. *Chemical communications* **2007,** (8), 840-842.

184.   Kim, J. Y.; Oh, H.; Moon, H. R., Hydrogen Isotope Separation in Confined Nanospaces: Carbons, Zeolites, Metal–Organic Frameworks, and Covalent Organic Frameworks. *Advanced Materials* **2019,** *31* (20), 1805293.

185.   Kotoh, K.; Kimura, K.; Nakamura, Y.; Kudo, K., Hydrogen isotope separation using molecular sieve of synthetic zeolite 3A. *Fusion science and technology* **2008,** *54* (2), 419-422.

186.   Niimura, S.; Fujimori, T.; Minami, D.; Hattori, Y.; Abrams, L.; Corbin, D.; Hata, K.; Kaneko, K., Dynamic quantum molecular sieving separation of D2 from H_2–D_2 mixture with nanoporous materials. *Journal of the American Chemical Society* **2012,** *134* (45), 18483-18486.

Acknowledgements

I credit the work in this presented thesis to many great people who supported and guided me throughout the past years for developing myself in science.

First and foremost, I would like to express my deep and sincere gratitude to my research supervisor, Dr. Michael Hirscher for his valuable guidance and constant support throughout this work. I will always feel fortunate to have had the opportunity to work in his laboratory where he has taught me the methodology to carry out research and to present the research works as clearly as possible.

This work would not have been possible without Prof. Dr. Gisela Schütz. I thank her acceptance of me as one of her member in the Department for Modern Magnetic Systems at Max Planck Institute for Intelligent Systems and her thoughtful guidance.

My special thanks also go to Prof. Dr. Dr. Guido Schmitz for his scientific assistance and insightful comments on this thesis. I'm very grateful to Prof. Dr.-Ing. Elias Klemm for accepting to be the chair of my examination committee.

I would like to thank all the members from hydrogen storage group. I am very grateful to Dr. Rafael Rafael Balderas-Xicohténcatl for his patient hours of advice, guidance and support in keeping me positive. I thank Dr. Ingrid Zaiser who helped me a lot with the experiments. I'm also grateful to Prof. Dr. Hyunchul Oh and Prof. Dr. Renjin Xiong for their genuine support and enlightenment of research, and the fruitful collaborations. I would also like to thank Nadine Kotzur and Linda Bondorf for sharing a pleasant time in the group.

My sincere gratitude goes to Bern Ludescher for his great technical support, this work could not have been made without his talents contributed to building the apparatus of TDS. Many thanks to Dr. Sapana Tripathi and Margarita Baluktsian for all the lunches, chats and discussions which bring a great joy in institute. Thanks for the help from our department secretary Monika Kotz, and all the members from Department Schütz.

Curriculum Vitae

Personal Data

Name	Linda Zhang
Birthday	Feb. 21, 1990
Place of birth	Xuzhou, P.R.China

Education

Max-Planck-Institute for Intelligent Systems   Feb. 2016 – present

Ph.D. candidate, Materials Science

Shanghai Jiao Tong University   Sept .2012 – Mar. 2015

MSc, Materials Science

Tianjin University   Sept. 2008 – Jun. 2012

BSc, Materials Science and Engineering

List of Publication

[1] R. Xiong, **L. Zhang**, P. Li, W. Luo, T. Tang, B. Ao, G. Sang, C. Chen, X. Yan, J. Chen, M. Hirscher. Highly effective hydrogen isotope separation through dihydrogen bond on Cu(I)-exchanged zeolites well above liquid nitrogen temperature. *Chem. Eng. J.* 2020, 391, 123485.

[2] J. King, **L. Zhang**, S. Doszczeczko, O. Sambalova, M. Meledina, T. Phillips, A. Borgschulte, M. Hirscher, M. Addicoat, P. Á. Szilágyi. How to functionalise metal-organic frameworks to enable guest nanocluster embedment. *J. Mater. Chem. A.* 2020, 8, 4889-4897.

[3] **L. Zhang**, S. Jee, J. Park, M. Jung, D. Wallacher, A. Franz, W. Lee, M. Yoon, K. Choi, M. Kyung, M. Hirscher, H. Oh. Exploiting dynamic opening of apertures in partially fluorinated MOF for enhancing H_2 desorption temperature and isotope separation. *J. Am. Chem. Soc.* 2019, 141, 19850-19858.

[4] M. Liu, **<u>L. Zhang</u>**, M. A. Little, V. Kapil, M. Ceriotti, S. Yang, L. Ding, D. L. Holden, R. Balderas-Xicohténcatl, D. He, R. Clowes, S. Y. Chong, G. Schütz, L. Chen, M. Hirscher, A. I. Cooper. Barely porous organic cages for hydrogen isotope separation. *Science*. 2019, 366, 613-620.

[5] R. Xiong, R. Balderas-Xicohténcatl, **<u>L. Zhang</u>**, P. Li, Y. Yao, G. Sang, C. Chen, T. Tang, D. Luo, M. Hirscher. Thermodynamics, Kinetics and Selectivity of H_2 and D_2 on Zeolite 5A below 77K. *Microporous and Mesoporous Materials.* 2018, 264, 22–27.

[6] J. Y. Kim, **<u>L. Zhang</u>**, R. Balderas-Xicohténcatl, J. Park, M. Hirscher, H. R. Moon, H. Oh. Selective Hydrogen Isotope Separation via Breathing Transition in MIL-53(Al). *J. Am. Chem. Soc*. 2017, 139, 17743−17746.

[7] J. Y. Kim, R. Balderas-Xicohténcatl, **<u>L. Zhang</u>**, S. G. Kang, M. Hirscher, H. Oh, H. R. Moon. Exploiting Diffusion Barrier and Chemical Affinity of Metal−Organic Frameworks for Efficient Hydrogen Isotope Separation. *J. Am. Chem. Soc*. 2017, 139, 15135-15141.

Erklärung über die Eigenständigkeit der Dissertation

Ich versichere, dass ich die vorliegende Arbeit mit dem Titel .

Experimental Investigation on Hydrogen Isotope Separation in Nanoporous Materials

selbständig verfasst und keine anderen als die angegebenen Quellen und Hilfsmittel benutzt habe; aus fremden Quellen entnommene Passagen und Gedanken sind als solche kenntlich gemacht.

Declaration of Authorship

I hereby certify that the dissertation entitled

Experimental Investigation on Hydrogen Isotope Separation in Nanoporous Materials

is entirely my own work except where otherwise indicated. Passages and ideas from other sources have been clearly indicated.

Name/Name: Linda Zhang_____

Unterschrift/Signed: _____

Datum/Date: _____